Evolution of microstructure and mechanical properties during linear friction welding of AD730^{TM} Ni-based superalloy

by

Fatemeh MASOUMI

MANUSCRIPT-BASED THESIS PRESENTED TO ÉCOLE DE TECHNOLOGIE SUPÉRIEURE IN PARTIAL FULFILLMENT OF THE REQUIREMENTS FOR THE DEGREE OF DOCTOR OF PHILOSOPHY
Ph.D.

MONTRÉAL, JULY 17, 2018

ÉCOLE DE TECHNOLOGIE SUPÉRIEURE
UNIVERSITÉ DU QUÉBEC

BOARD OF EXAMINERS

THIS THESIS HAS BEEN EVALUATED

BY THE FOLLOWING BOARD OF EXAMINERS

Dr. Mohammad Jahazi, Thesis Supervisor
Department of Mechanical Engineering at École de technologie supérieure

Dr. Simon Joncas, Chair, Board of Examiners
Department of Automated Production Engineering at École de technologie supérieure

Dr. Tan Pham, Member of the jury
Department of Mechanical Engineering at École de technologie supérieure

Dr. Vladimir Brailovski, Member of the jury
Department of Mechanical Engineering at École de technologie supérieure

Dr. Olanrewaju Ojo, External Evaluator
Department of Mechanical Engineering at University of Manitoba

THIS THESIS WAS PRESENTED AND DEFENDED

IN THE PRESENCE OF A BOARD OF EXAMINERS AND THE PUBLIC

JUNE 08 2018

AT ÉCOLE DE TECHNOLOGIE SUPÉRIEURE

ACKNOWLEDGMENTS

This research work would not have been possible without perspective on various aspects and continual guidance of my supervisor, Mohammad Jahazi. His kindness and positive attitude made this project a very enjoyable learning experience. I thank him for making my PhD study possible and for giving me the opportunity to explore many interesting aspects of materials characterization, welding, physical modeling and data analysis that were documented in this manuscript.

I am very grateful for the opportunity to work with Prof. Jonathan Cormier and learn from him. I owe many thanks to him for his continuous support during my thesis. I would like to extend my appreciation to Loius Thébaud for performing the mechanical tests.

I would like to express appreciation to Aubert & Duval Co. for providing AD730^{TM} samples and to TWI Ltd. for welding the samples especially Dr. Alexandre Deveaux and Mr. Bertrand Flipo for their invaluable discussions.

I would like to thank Dr. Hossein Monajati for helping and training on SEM and EBSD machine and Mr. Radu Romanica for providing facilities at the material laboratory.

I am gratefully acknowledging the financial support from the Natural Sciences and Engineering Research Council (NSERC) of Canada in the form of a Discovery Grant.

Finally, I am deeply indebted to my family for all their love and support.

Most of all, I would like to thank my supportive, patient, and encouraging husband Davood whose support and help during this Ph.D. is so appreciated.

ÉVOLUTION DE LA MICROSTRUCTURE ET DES PROPRIÉTÉS MÉCANIQUES DURANT LE SOUDAGE PAR FRICTION LINÉAIRE DU SUPER ALLIAGE BASE NICKEL AD730™

Fatemeh MASOUMI

RÉSUMÉ

Le soudage par friction linéaire (LFW) est une technologie de fabrication émergente d'une part pour l'assemblage des aubes aux disques et d'autre part pour la réparation des disques de turbine (Blisks) dans les turbines à gaz et des moteurs à réaction. Ce type de soudage a déjà été appliqué à des alliages de Ti pour des applications de fonctionnement de compresseur (c'est-à-dire à basse température) mais pas à des composants à haute température. Ainsi, de nombreux défis devaient être résolus avant une application industrielle complète. Certains de ces défis ont été pris en compte dans cette recherche. L'objectif de cette étude a été de développer, pour ce type de soudage, une meilleure compréhension des mécanismes fondamentaux régissant l'évolution de la microstructure et des propriétés mécaniques à haute température des superalliages base nickel et particulièrement dans le cas d'un alliage nouvellement introduit, AD730™.

Les expériences LFW ont été réalisées en utilisant différents paramètres de procédé. Une méthodologie a été développée pour déterminer les paramètres optimaux pour l'alliage étudié. Cette méthode peut être appliquée à d'autres alliages métalliques. Cela a consisté à estimer l'oscillation, la fréquence, le frottement et la force de forge en utilisant des contraintes plastique d'écoulement de matière, des données rapportées dans la littérature et la capacité de la machine. Le temps de frottement a été estimé sur la base d'un modèle analytique de distribution de température. Il a été déterminé que les échantillons obtenus, par ce type de soudage, avec un raccourcissement axial de 3.5 mm étaient exempts de défauts tels que couches d'oxyde ou microfissures.

Ce superalliage base nickel, AD730™, a subi des traitements de mises en solution à différentes températures. Dans le but de décrire les processus de dissolution des particules γ' et de quantifier leur fraction volumique des modèles semi-analytique ont été développés. Ces modèles ont été utilisés pour prédire la température ou la fraction volumique du γ' dans différentes zones de l'échantillon soudé par cette technique. Les mécanismes de re-précipitation et la cinétique de reprécipitation des particules γ' pendant le refroidissement des regions super-solvus et sub-solvus ont été étudiés. Suite à cela, un modèle cinétique a été proposé pour quantifier et prédire la fraction volumique de particules γ' reprécipitées à des vitesses de refroidissement élevées et faibles, représentant le refroidissement post-soudure à différentes distances de l'interface de soudure.

L'étude de la microstructure à l'aide de la microscopie électronique à balayage (MEB) a révélé que la fraction volumique et la taille de γ' augmentaient avec la distance de l'interface

de la soudure. Ces particules ont été totalement dissoutes à l'interface de la soudure, et seule une distribution de re-précipitée γ′ monomodale re-précipitée, de taille inférieure à 10 nm, a été observée à l'interface de soudure. Les cartes de diffraction par électron rétrodiffusé (EBSD) ont montré que la recristallisation discontinue se produisait dans la zone de soudure. La taille des zones affectées thermo-mécaniquement (TMAZ) et des zones de soudure a été estimée en utilisant des cartes EBSD, et confirmée par des mesures de microdureté.

Des mesures de mico-dureté sur des échantillons soudés ont révélé une diminution de la dureté dans les zones affectées thermo-mécaniquement due à la dissolution des particules γ' secondaires et une augmentation de la dureté dans la zone de soudure due au raffinement du grain.

L'examen de l'interface de soudure et de la matière extrudéà l'interface n'a révélé aucun phénomène de liquéfaction (formation de zones resolidifiées). Un nouveau modèle analytique a été développé ; celui-ci prédit les conditions de l'apparition ou de l'absence de la liquéfaction durant le soudage par LFW des superalliages base nickel. Une explication générale est proposée à l'aide de ce modèle qui est capable d'expliquer les données contradictoires rapportées dans la littérature.

Un traitement thermique post-soudage (PWHT), consistant en un traitement en solution sub-solvus γ' suivi d'un vieillissement, a été réalisé sur des éprouvettes soudées par la technique LFW. L'évolution de la microstructure à travers la soudure dans les conditions de soudure et de PWHT a été étudiée en utilisant la microscopie optique et électronique (MEB et EBSD). Les propriétés mécaniques des éprouvettes ont été évaluées en utilisant la microdureté, la traction à température ambiante et à 650°C, ainsi que des tests de fluage.

Des essais de traction 650°C sur des échantillons soudés ont révélé une rupture dans la zone affectée thermiquement (ZAT) en raison de la dissolution des précipités γ'. Les joints ayant subis un traitement thermique post-soudage présentaient une résistance à la traction et au fluage plus élevées que celles des échantillons soudés du fait de la re-précipitation des précipités γ' dans les zones TMAZ et ZAT ; ainsi qu'une croissance des grains dans la zone de soudure. Après le traitement thermique post-soudage (PWHT), les échantillons soudés par la technique LFW ont rompu dans le matériau de base lors des essais de traction. Les joints PWHT présentaient, d'une part une meilleure ductilité, que ceux du matériau de base, à 850°C et d'autre part, une durée de fluage légèrement inférieure à 700°C en comparaison avec le métal de base. L'examen de la microstructure a montré que des fissures étaient initiées à l'interface des particules oxydées à 700°C. La diminution de la résistance au fluage du superalliage AD730™ à 850°C était liée à la combinaison de la formation de zones exemptes de précipités (PFZ) au voisinage des joints de grains (GB) et de microfissuration assistée par oxydation. En outre, il a été trouvé que dans l'intervalle de température étudié, l'AD730™ PWHT avait des caractéristiques de fluage similaires à UdimetTM720 Li et Inconel 738LC pour des faibles valeurs des paramètres de Larson-Miller (LMP) et de meilleures propriétés de fluage que celles de l'alliage Inconel 617 pour des grandes valeurs de LMP.

Mots clés : Soudage friction linéaire ; Superalliage à base de Ni ; AD730^{TM} ; Cinétique de dissolution et de re-précipitation ; Température de liquéfaction ; Mécanismes de liquéfaction ; Propriétés mécaniques à hautes températures ; Mécanismes de fluage.

EVOLUTION OF MICROSTRUCTURE AND MECHANICAL PROPERTIES DURING LINEAR FRICTION WELDING OF AD730^{TM} NI-BASED SUPERALLOY

Fatemeh MASOUMI

ABSTRACT

Linear friction welding (LFW) is an emerging manufacturing technology for joining of blades to disks or repairing turbine disks in gas turbines and jet engines. LFW has already been applied to Ti alloys for compressor (i.e. low temperature) operation applications but not to high temperature components. Thus, many challenges need to be addressed before full industrial application. Some of these challenges will be considered in this research. The focus of this study is to develop a better understanding of the fundamental mechanisms governing the evolution of the microstructure and high temperature mechanical properties of LFWed Ni-based superalloys in the case of a newly introduced alloy, AD730^{TM}.

LFW experiments were carried out using different processing parameters. A methodology was developed for determining the optimum LFW parameters for the investigated alloy. The method can be extended and applied to other metallic alloys too. This consisted in estimation of the oscillation, frequency, friction and forge force using material plastic flow stresses, data reported in the literature and machine capability. Friction time was estimated based on an analytical thermal model. It was determined that the LFWed specimens with axial shortening of 3.5 mm were sound and free from oxide layers and microcracks.

The Ni-based superalloy, AD730^{TM}, was solution treated at different temperatures. Semi-analytical model was developed to describe the dissolution processes of γ′ particles, and quantify their volume fraction. This model was used to predict temperature or γ′ volume fraction in different zones of LFWed sample. Reprecipitation mechanisms and kinetics of γ′ particles during cooling from supersolvus and subsolvus temperatures were studied. Then, kinetic model was proposed to quantify and predict the volume fraction of reprecipitated γ′ particles for high and low cooling rates representing the post weld cooling at different distances from the weld interface.

Microstructure investigation using Scanning Electron Microscopy (SEM) revealed that γ′ volume fraction and size increased with the distance from the weld interface. These particles were totally dissolved at the weld interface, and only a monomodal re-precipitated γ′ distribution, less than 10 nm in size, was observed at the weld interface of the as-welded specimens. Electron Backscatter Diffraction (EBSD) maps showed that dynamic recrystallization occurred in the weld zone during LFW in as-welded samples. Thermo-mechanically Affected Zone (TMAZ) and weld zone sizes were estimated using EBSD maps, and were confirmed with microhardness measurements.

Micohardness measurements on as-welded samples revealed a decrease in hardness in TMAZ due to dissolution of secondary γ′ particles, and an increase in hardness in the weld zone due to grain refinement.

Examination of the weld interface and the flash did not reveal any occurrence of liquation (formation of resolidified zones). A new analytical model was developed that predicts the conditions for the occurrence or absence of liquation during LFW of Ni-based superalloys. Using this model, a general explanation is proposed that is able to explain the contradictory data reported in the literature.

Post Weld Heat Treatment (PWHT), consisting of γ′ sub-solvus solution treatment followed by aging, was conducted on LFWed specimens. Microstructure evolution across the weld in the as-weld and PWHT conditions were studied using optical microscopy, SEM and EBSD. Mechanical properties of the LFWed specimens were evaluated using microhardness, tensile at room temperature and 650°C, as well as creep tests.

Tensile tests on as-welded samples at 650°C revealed failure at Heat Affected Zone (HAZ) due to dissolution of γ′ precipitates. PWHTed joints showed higher tension and creep resistance than those of as-welded samples due to a combination of reprecipitation of γ′ precipitates at TMAZ and HAZ as well as grain growth at the weld zone. After PWHT, LFWed specimens failed in the base material under tensile tests. The PWHTed joints exhibited better ductility than those of base material at 850°C while they showed slightly lower creep life at 700°C in comparison to the base metal. Microstructure examination showed that cracks initiated at the interface of oxidized particles at 700°C. The decrease in creep resistance of AD730™ Ni-based superalloy at 850°C was related to a combination of the formation of Precipitate Free Zones (PFZ) in the vicinity of the grain boundaries (GBs) and microcracking assisted by oxidation. In addition, it was found that in the investigated temperature range, the PWHTed AD730™ had similar creep characteristics to Udimet™720 Li and Inconel 738LC at low values of Larson Miller Parameter (LMP) and better creep properties than those of Inconel 617 alloy at higher LMP values.

Key Words: Linear friction welding; Ni-based superalloy; AD730™; Dissolution and re-precipitation kinetics, Liquation temperature; Liquation mechanisms; Mechanical properties at elevated temperatures, Creep mechanisms

TABLE OF CONTENTS

LIST OF TABLES

LIST OF FIGURES

Page

LIST OF ABREVIATIONS

LFW	Linear Friction Welding
SEM	Scanning Electron Microscopy
EBSD	Electron Backscatter Diffraction
TMAZ	Thermo Mecanically Affected Zone
PWHT	Post Weld Heat Treatment
HAZ	Heat Affected Zone
PFZ	Precipitate Free Zones
LMP	Larson Miller Parameter
FSW	Friction Stir Welding
WZ	Weld Zone
DRX	Dynamic Recrystallization
FEG-SEM	Field Emission Gun Scanning Electron Microscopy
BSE	Back Scattered Electron
LAB	Low Angle Boundary
HAB	High Angle Boundary
DTA	Differential Thermal Analysis
EDS	Energy Dispersive Spectroscopy
JMA	Johnson Mehl Avrami
MAPE	Mean Absolute Percentage Error
MSE	Mean Squared Error

LIST OF SYMBOLS

Symbol	Unit	Description
k	MPa	Shear strength
μ	-	Friction coefficient
a and h	mm	Width and height of the specimen
$\bar{\sigma}$	MPa	Flow stress
ε	-	Strain
$\dot{\varepsilon}$	s^{-1}	Strain rate
T	K	Temperature
ρ	$Kg.m^{-3}$	Density
η	-	Thermal efficiency
C	$J.Kg^{-1}.K^{-1}$	Specific heat
v_r	$mm.s^{-1}$	Rubbing velocity
α	mm	Oscillation amplitude
f	HZ	Frequency
a	$W.m^{-1}.K^{-1}$	Thermal diffusivity
λ	$m^2.s^{-1}$	Thermal conductivity
$\dot{q}$	$W.m^{-2}$	Heat generation rate
x	mm	Distance from the weld interface
$P_{Fric.}$	MPa	Friction pressure
D	$m^2.s^{-1}$	Diffusion coefficient
r_0	mm	Initial precipitate radius
$k/2$		Supersaturation

C_0	-	Solute concentration in the matrix
C_{i}^{e}	-	Equilibrium solute concentrations at the precipitate
C_{p}^{e}	-	Equilibrium solute concentrations at solid solution
$F_{S\gamma'}$	-	γ′ area fraction
F_{Slim}	-	γ′ area fraction at thermodynamic equilibrium
F_l	-	Difference between the γ′ area fraction at t=0 seconds and F_{Slim}
t_1	min	Dissolution time
T_m	K	Holding temperature
Q	KJ.mol^{-1}	Activation energy for the dissolution of the γ′ phase
V_h	K(°).s^{-1}	Heating rate
V_c	K(°).s^{-1}	Cooling rate
t_m	s	Holding time
k_{LSW}	-	Coarsening rate constant
σ	J.m^{-2}	Interfacial free energy
Ω	m^3	Molar volume of the γ′ precipitates
R	J.mol^{-1}.k^{-1}	Gas constant
C_i^{γ}	-	Equilibrium concentration of the i th solute element in the γ matrix
K_i	-	Distribution coefficient of the i th solute element between the γ matrix and γ′ precipitates

INTRODUCTION

Ni-based superalloys have emerged as materials of choice for high temperature applications (above 800°C) in gas turbines in aerospace and power generation industries, when significant resistance to loading under static, fatigue and creep conditions is required (Reed, 2006b). Turbine discs and blades are two key components in gas turbines. Indeed, turbine blades are affected by high operation temperatures while high rotation speed imparts tensile stresses to both the turbine disc and blades. The development of new superalloys has therefore been motivated to increase efficiency by allowing higher operating temperatures. The cast and wrought (C&W) Ni-based superalloy, AD730™, has been recently developed by Aubert & Duval, and introduced especially for the first stages of the turbine discs with high properties up to 700°C (Devaux et al., 2012b). However, many of its fundamental properties are still unknown. For example, no quantitative data is available on dissolution and reprecipitation kinetics in AD730™.

In recent years, an emerging technology, LFW, has been developed for manufacturing and repair of aerospace components such as rotating gas turbine components. This technique has many advantages over traditional mechanical assembly process such as fir tree. For example, the weight is reduced, and the susceptibility to fatigue damages and initiation of fretting cracks from fir tree is decreased, and therefore, the service life is improved. In addition, it is economical to repair damaged blades tips by fusion welding rather than blade replacement. However, liquation and solidification which are often observed in fusion welded Ni-based superalloys has a deteriorating effect on mechanical properties of the welded components due to heat affected zone cracking. In this context, LFW can be an excellent alternative technique for the repair of damaged turbine disc and blades.

LFW is a solid state joining technique in which heat is generated by the reciprocal motion between a moving component and a stationary workpiece under compression loading. LFW is divided into three stages (Bhamji et al., 2011): I- conditioning stage: two parts to be joined are moving under specified frequency and amplitude, and brought together under small pressure; II- frictional stage: the friction pressure is increased. Thus, heat is increased due to

friction and sliding between the two parts. Plasticized material is expelled out of the weld interface due to applied friction pressure and high temperature, and axial shortening of the samples start to occur, and therefore, a flash is formed. III- forge stage: the amplitude is decreased to zero, and the workpieces are brought together while forge pressure is applied. The weld is consolidated and is strengthened at this stage.

This Ph.D. thesis begins with a comprehensive literature survey to review the state-of-the-art knowledge regarding linear friction welding of Ni-based superalloys. This chapter summarizes developments on manufacturing processes of gas turbine discs, and discusses different points of view about microstructure evolution of LFWed superlloys. Finally, an overview on the mechanical properties of LFWed samples is presented, the challenges are identified, and the objectives are defined. Based on these objectives, a methodology is proposed at the end of this section.

CHAPITRE 1

LITREATURE REVIEW AND RESEARCH METHODOLOGY

1.1 Superalloys

Superalloys were, and continue to be, developed for elevated temperature service. They are utilized at a higher proportion of their actual melting point than any other class of broadly commercial metallic material. They are divided into three classes, namely Ni-based superalloys, cobalt-based superalloys and iron-based superalloys (Sims, Stoloff et Hagel, 1987). Among them, the Ni-based superalloys are the most widely used for the hottest applications. In advanced aircraft engines, more than 50 percent of the weight comes from Ni-based superalloys. They are also used in power generation, chemical, and petroleum industries because of their superior mechanical properties and corrosion resistance at elevated temperature.

1.1.1. Composition–microstructure relationships in Ni-based superalloys

Most of the superalloys contain significant amounts of chromium, cobalt, aluminium and titanium. Small amounts of boron, zirconium and carbon are often included. Other elements that are added, but not to all alloys, include rhenium, tungsten, tantalum, hafnium, ruthenium, molybdenum, niobium and zirconium. Some superalloys, such as IN718 and IN706, contain significant proportions of iron, and should be referred to as nickel–iron superalloys. The first group of elements includes nickel, cobalt, iron, chromium, ruthenium, molybdenum, rhenium and tungsten; having atomic radii close to that of nickel, they prefer to partition to the austenitic γ and thereby stabilize it. A second group of elements, aluminum, titanium, niobium and tantalum, have greater atomic radii and promote the formation of ordered phases such as the compound Ni_3(Al, Ta, Ti), known as γ′. Boron, carbon and zirconium constitute a third class that tends to segregate to the grain boundaries of the γ phase, on account of their atomic sizes, which are very different from that of nickel. Carbide and boride phases can also be promoted. Chromium, molybdenum, tungsten, niobium, tantalum and titanium are

particularly strong carbide formers; chromium and molybdenum promote the formation of borides (Reed, 2006b).

The microstructure of a typical Ni-based superalloy consists therefore of different phases, drawn from the following list (Reed, 2006b):
(i) The gamma phase, denoted γ has a face centered cubic, FCC, structure, and in nearly all cases, it forms a continuous matrix phase in which the other phases reside. It contains significant concentrations of elements such as cobalt, chromium, molybdenum, ruthenium and rhenium.
(ii) The gamma prime phase, denoted γ′ forms as a precipitate phase, which is often coherent with the γ -matrix, and rich in elements such as aluminum, titanium and tantalum. In nickel–iron superalloys and those rich in niobium, a related ordered phase, γ″, is preferentially formed instead of γ′.
(iii) Carbides and borides. Carbon, often present at concentrations up to 0.2 wt%, combines with reactive elements such as titanium, tantalum and hafnium to form MC carbides. During processing or service, these can decompose to other species, such as $M_{23}C_6$ and M_6C (M=Cr, Mo, W), which prefer to reside at the γ - grain boundaries. Boron can combine with chromium or molybdenum to form borides which also reside at the γ - grain boundaries.

Other phases can be found in certain superalloys, particularly in the service-aged condition, for example, the topologically close-packed (TCP) phases μ, σ, Laves, etc. However, these phases are deleterious to mechanical properties, and the compositions and processing of superalloys are selected to avoid, rather than to promote, the formation of these compounds.

After the beneficial effects of the coherent phase γ′ in improving the strength properties of alloys at high temperatures were discovered (Durand-Charre, 1997; Reed, 2006b), more γ′ forming elements such as aluminium (Al), titanium (Ti), and tantalum (Ta) were added to the base composition to increase the proportions of γ′ in superalloys. The γ′ fraction of some single crystal superalloys can be as high as 70% (Murakumo et al., 2004). Some refractory metal additions, such as molybdenum, tungsten, and rhenium are also used in superalloys to provide additional strengthening through solid solution and carbide formation. In polycrystalline superalloys, boron and carbon are also added to form borides and carbides for

grain-boundary strengthening. In single-crystal superalloys, these elements are removed since there is no need for grain-boundary strengthening; instead, rhenium (Re) and ruthenium (Ru) gradually take greater roles in the development of new generations of single crystal superalloys.

1.2 Linear Friction Welding

Industrial and aircraft gas turbine engines are high technology products and their manufacturing processes involve various innovative techniques. Technological viability and manufacturing costs are the key factors in the successful development of new processes. In the turbine engines, ″blade″ and ″disk″ (BLISK) can be integrated by machining from a single forged part as a single piece for both compressor and turbine sections. However, this manufacturing technique is expensive for large BLISKs, and is not good for fabricating dissimilar blades and disk. Blades and disks can be attached mechanically (fir tree assembly); although damaged blades are easily replaceable, fatigue cracks initiate from the fir tree, and the weight of the part will increase due to the fir tree root. Figure 1.1 shows separated and integrated ″blade″ and ″disk″ in a typical gas turbine (Bhamji et al., 2011).

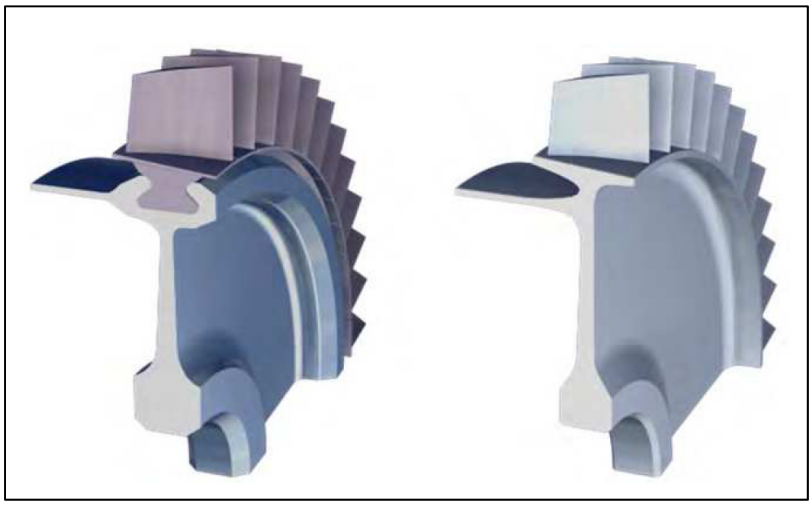

Figure 1.1 Two various attachments of blades and disk (Bhamji et al., 2011)

Recent developments have led to emerging LFW technology. The major commercial use of LFW is for the joining of aeroengine compressor blades to compressor discs to form blisks. As a result, much of the published literature on the subject has focused on the joining of materials for aeroengine applications. To this end, a range of titanium alloys and Ni-based superalloys have been studied for understanding the influence of LFW process parameters on the microstructural characteristics and mechanical performance. However, the process can be used to join other materials and interest in this aspect is growing. The application of LFW has greatly extended the commercial potential of conventional frictional welding techniques since non-round and round parts can be joined with precise angular alignment (Nicholas et Thomas, 1998).

Friction welding is classified as a solid state welding process, in which joining occurs at a temperature below the melting point of the work metal. If incipient melting does occur, there is no evidence in the finished weld, because the metal is worked during the welding stage (Bhamji et al., 2011).

In LFW, an imposed linear reversing motion of the two surfaces to be joined generates frictional heat and plasticizes the material at the weld interface (Figure 1.2). When adequate heat and metal flow has been reached, the moving part is brought into alignment with the stationary one while the axial load is maintained or increased to finalize the weld sequence. Material, including surface oxides, are expelled from the interface as “flash” and a Thermo-Mechanically Affected Zone (TMAZ) expands from the interface into the parent material (McAndrew et al., 2018). LFW has three main stages: Conditioning, Frictional and Forge (Bhamji et al., 2011; Vairis et Frost, 2000a).

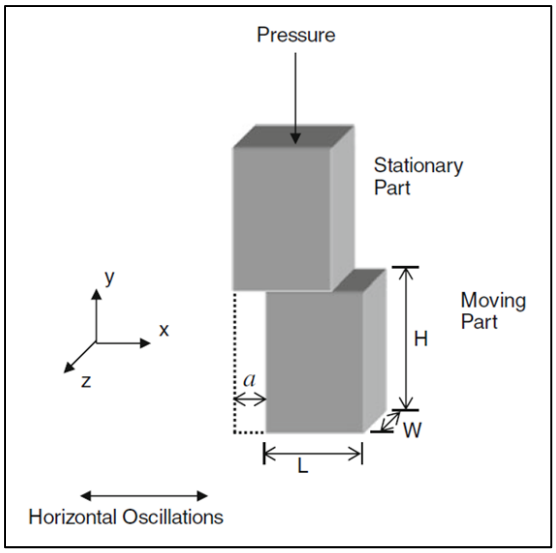

Figure 1.2 Sample geometry, LFW process principles

I) Conditioning Phase

Oscillation of one of the parts is increased and stabilized over a set period (usually very quickly) and the parts are brought together under a small force for a predetermined time (Figure 1.3).

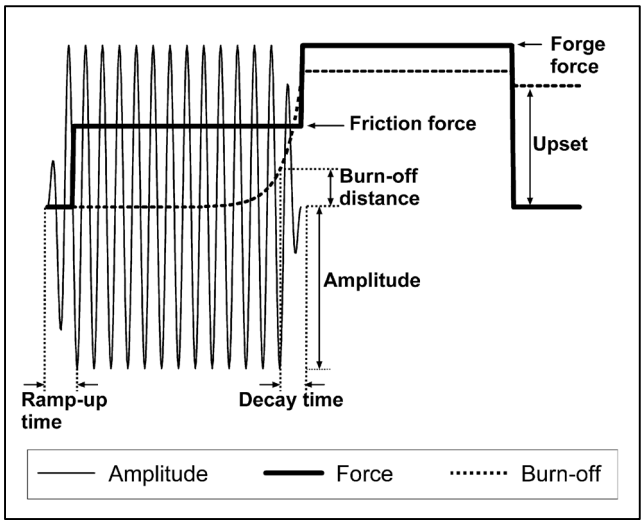

Figure 1.3 Schematic diagram of the parameter traces that are obtained during LFW process (Bhamji et al., 2011)

II) Frictional Phase

The compressive force (friction force) is increased to a set level and heat is generated at the interface. The material at the interface becomes plastic and flows out of the weld, as flash, because of the shearing motion between the two parts and the applied force. This loss of material from the weld causes the parts to shorten (or burn-off). This phase usually ends, and the next is triggered, when a predetermined loss of length, or burn-off distance, is reached. However, the next phase can also be triggered after the frictional phase has continued for a predetermined time (burn-off time) or a number of oscillation cycles (burn-off cycles). The LFW process is always carried out under load control, but other parameters also play a role in controlling the welding process. For example, when using a burn-off distance the load is controlled throughout the welding process, however, the burn-off is also monitored (although not controlled) and at a set burn-off distance, the next phase (forge phase) is triggered. Similarly with burn-off time or cycles the load is controlled throughout welding and the amount of time or cycles determines the transition to the next phase.

III) Forge Phase

The last phase is known as the deceleration or forge phase. The amplitude is decayed to zero over a predetermined time to ensure good alignment (usually very quickly). In other words, the materials are brought to rest after the desired shortening has been attained. Once the materials have been brought to rest and aligned, the axial pressure is increased and held for a set time until the weld is consolidated.

1.2.1 Thermomechanical Analysis of the LFW Process

As the solid surfaces rub against each other, heat is generated as a result of friction. The heat generated due to friction subsequently diffuses through the bulk of the contacting solid materials. Varis and Frost (1998; 1999b; 2000a) calculated the rate of heat generation during LFW by considering two solid objects with flat surfaces while pressed together with a friction pressure P and sliding against each other with a relative velocity of V:

$$\dot{Q} = \mu PV \tag{1.1}$$

where μ is the friction coefficient. If the contact area is A, the rate of thermal energy generation per unit area becomes:

$$q = \frac{\dot{Q}}{A} = \frac{\mu PV}{A} \tag{1.2}$$

Frictional heating along with the applied pressure increases temperature at the interface and plasticizes the material. The parent material cannot be melted by this frictional heat.
Varis and Frost (1998; 1999b; 2000a) proposed the following equation for the average friction heat rate:

$$q = \frac{2}{\pi}\mu\alpha\omega P \tag{1.3}$$

where α and ω are the amplitude and the oscillation angular velocity.
Thus, the main input parameters during LFW process are:

- Frequency (f): Number of oscillatory cycles per second,
- Amplitude (α): Maximum displacement of the oscillating sample from its equilibrium position,
- Friction Pressure ($P_{Fric.}$): Pressure applied during the friction stage,
- Forge Pressure ($P_{Forg.}$): Pressure applied during the forge stage.

By choosing appropriate LFW process parameters, a sufficient heat can be generated, oxides and other impurities could be expelled as flash, and a defect free joint with a narrow heat affected zone (HAZ) could be formed.

1.3 LFW of Superalloys

Very little has been published on LFW of Ni-based superalloys (Chamanfar et al., 2011a; 2012a; Dalgaard et al., 2012; Ola et al., 2011a; Ola et al., 2012). The few reported

publications have been focused on LFW of Ti alloys (Dalgaard et al., 2012; McAndrew et al., 2018). While fusion welding is an economical joining technique for the fabrication and repair of service-damaged Ni-based superalloy turbine parts; their poor weldability limits the application of welded components in critical structure locations. The alloys, particularly, those with high-volume fraction of the γ′ phase (>40%) are highly susceptible to intergranular microcracking during conventional welding processes. The fundamental cause of the weldability problem in these alloys is the liquation of grain boundary region, which weakens the material during joining (Rowe, Ishwar et Klarstrom, 2006). Developments in welding research have resulted in the use of solid-state friction joining processes (Henderson et al., 2004; Korsunsky et al., 2009). These include Friction Stir Welding (FSW), friction spot welding, inertia friction welding, continuous drive friction welding and LFW, which are state of- the-art in producing crack-free welds in difficult-to-weld structural alloys. Studies have shown that, in particular, LFW is potentially well-suited for joining highly crack-susceptible Ni-based superalloys (Karadge et al., 2008). Currently, there is active on-going research on effective and efficient industrial utilization of this technique in the manufacturing of aero-engine components like turbine discs and blades (Vairis et Frost, 1998).

1.3.1 Microstructure Evolution during LFW

Since the mechanical properties of superalloys strongly depend on their microstructure, and its widespread industrial applications, it is necessary to understand microstructural evolution with time, temperature and deformation during LFW to optimize the friction welding process.

Although the interface temperature during LFW is not expected to exceed the melting temperature of the materials being welded, the peak interface temperature is nevertheless very high, and could be close to the solidus temperature of the material (Mary et Jahazi, 2007a). In all reported cases, this high temperature, along with the applied pressure, cause significant microstructural variations at the weld interface and its neighboring region. These changes in microstructure are summarized in the following sections.

1.3.1.1 Microscopic Features of LFW

No widely accepted nomenclature exists for microstructural regions in linear friction welds. The following nomenclature that has received widespread acceptance for friction stir welds is also used for LFW (Threadgill, 2007). The weld is divided into four regions:

- Parent material (PM): This region corresponds to the base material, where no change in microstructure, mechanical properties or other properties can be detected.
- Heat-affected zone (HAZ): In this region, the microstructure and/or other properties have been changed by heat from the weld, but there is no optically visible plastic deformation. Changes could, for example, include one or more of grain growth, precipitate morphology, mechanical or physical properties.
- Thermo-mechanically affected zone (TMAZ): In this region, the material has been subjected to more heat than in the HAZ and shows clear evidence of plastic deformation. Phase transformation could also take place in some materials in this zone. Changes in this region would be expected to be more apparent than in HAZ.
- Weld zone (WZ): In many materials there will be a region close to the weld line where the microstructure is very different to that in other parts of the weld due to recrystallization, phase transformation, etc. As this area has been subjected to severe heat and plastic flow, it is a sub-group of the TMAZ.

I) Occurrence of Recrystallization

It is suggested that recrystallization occurs dynamically in linear friction welded poly-crystal to poly-crystal and single crystal to single crystal Ni-based superalloy, due to the thermomechanical conditions imposed during friction welding, namely, the combination of high strain and strain rates at elevated temperatures (Chamanfar et al., 2011a; Ola et al., 2012). The recrystallization behavior in the weld zone of linear friction welded CMSX-486 is notable, in that finer (smaller) grains are present at the weld centerline area (Figure 1.4) compared to other weld zone areas away from the centerline, where the grains are more than 5 times greater (Ola et al., 2012). LFW has many similarities with hot deformation processes, and can be compared with hot forging. Hot deformation of IN-718 induces competitive mechanisms of strain hardening, dynamic recovery and recrystallization. During

the first steps of hot deformation, the main phenomena are usually linked to energy storage and strain hardening. As strain increases, dislocations rearrange themselves into sub-boundaries that progressively divide them into finer grains. This phenomenon is called grain fragmentation and is followed by the nucleation of the first recrystallized grains. Through nucleation and grain boundary migration, the recrystallized microstructure progresses (Thomas, Montheillet et Dumont, 2003).

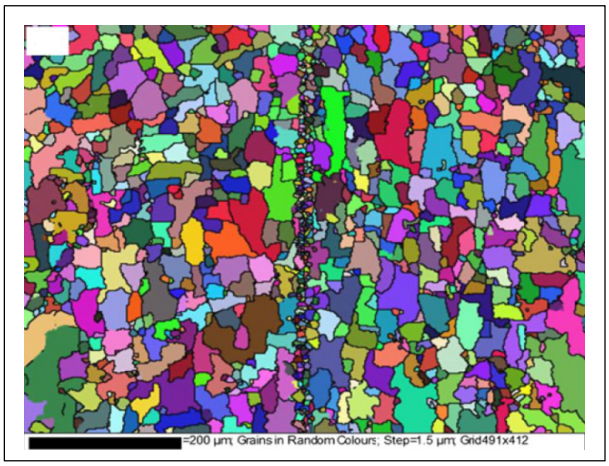

Figure 1.4 EBSD-based orientation maps showing the recrystallized grains of weld line in LFWed CMSX-486 (Ola et al., 2012).

II) γ′ Evolution

As the temperatures experienced during LFW are above the solvus temperatures of the strengthening precipitates, dissolution of the precipitates can occur in the weld zone and TMAZ/HAZ (Chamanfar et al., 2011a; Ola et al., 2012). Under equilibrium conditions, both coarse and fine γ′ precipitates start to dissolve as the temperature increases due to the diffusion of γ′ forming elements (Al and Ti) into the surrounding γ matrix. Therefore, above γ′ solvus temperature, full γ′ dissolution can occur. However, the rapid heating cycle experienced by the material during LFW is far from equilibrium conditions, and therefore, no significant diffusion of the γ′ forming elements occurs. Hence, probably only very fine γ′ particles dissolve and the coarse ones most likely remain intact. However, for linear but

mostly inertia friction welded Ni-based superalloys, during cooling from solvus temperatures, two types of γ′ evolution trends have been reported. (Chamanfar et al., 2011a; Damodaram, Raman et Rao, 2013; Huang et al., 2007a; Mary et Jahazi, 2007a; Preuss et al., 2002a; Preuss, Withers et Baxter, 2006a)

In alloys with low γ′ volume fraction, such as Inconel 718 or Waspaloy, γ′ completely dissolves in the vicinity of the weld line during friction welding and, does not reprecipitate during cooling (Figure 1.5) (Chamanfar et al., 2011a; Damodaram, Raman et Rao, 2013; Huang et al., 2007a; Mary et Jahazi, 2007a; Preuss et al., 2002a; Preuss, Withers et Baxter, 2006a). In these alloys, in the as-welded condition, the microhardness of the weld zone of the sample with prior solution treatment (ST) was found to be higher than that of its base material counterpart. The increase in hardness of the ST sample in the weld zone was attributed to grain refinement due to dynamic recrystallization. However, in the case of the sample with prior solution treatment followed by aging (STA) condition, the hardness of the weld zone was lower than that of the base material (Figure 1.6). This can be attributed to the dissolution of γ′ precipitates as the temperature reached in the weld zone was found to be above the γ′ solvus temperature (Damodaram, Raman et Rao, 2013).

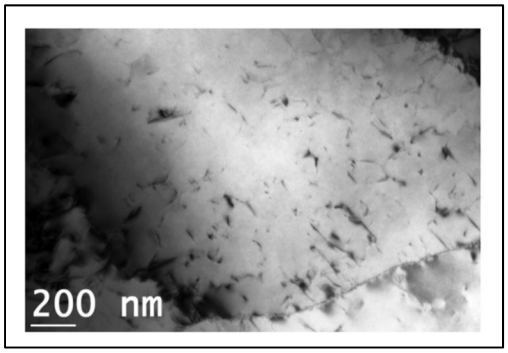

Figure 1.5 TEM microstructure of a friction weld interface of Inconel 718 (Damodaram, Raman et Rao, 2013).

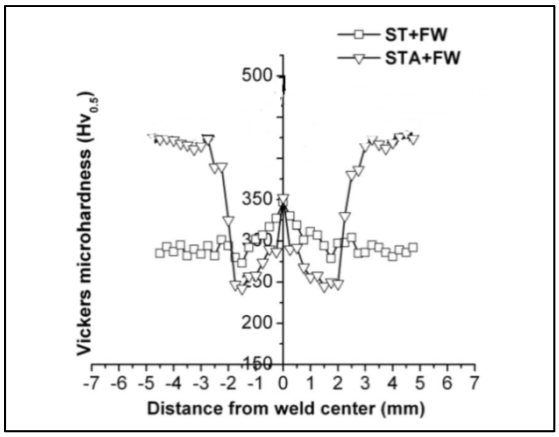

Figure 1.6 Microhardness profile obtained across the weld of Inconel 718 (Damodaram, Raman et Rao, 2013).

In contrast, in alloys with high γ′ volume fraction such as Astroloy and Udimet-720 Li and RR1000, close to the weld line, large amounts of dissolved γ′ reprecipitate during cooling. In these alloys, due to the high levels of Ti and Al, the driving force for reprecipitation during fast cooling is large. Preuss et al. (2002a) reported that at 1mm from the weld line only partial dissolution of γ′ has taken place during welding. Therefore, it can be assumed that the driving force for reprecipitation is larger at the weld line than 1mm from it. The high level of γ′ close to the weld line in these alloys is reflected in relatively high hardness values in this region (Figure 1.7) (Preuss, Withers et Baxter, 2006a).

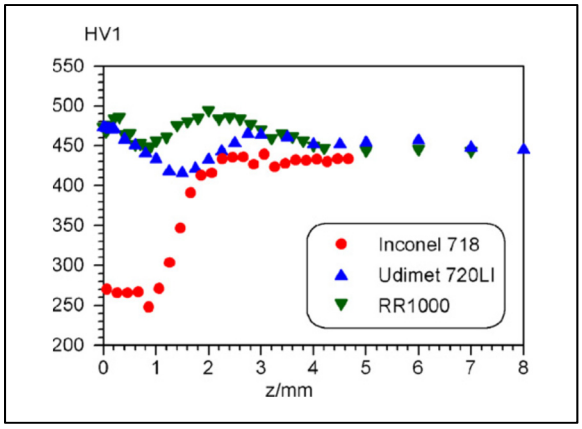

Figure 1.7 Vickers hardness profiles of Inconel 718, Alloy 720Li and RR1000 inertia friction welds in the as-welded condition as a function of axial distance from the weld line (z = 0) (Preuss, Withers et Baxter, 2006a).

1.3.1.2 Liquation and Microcracking during LFW

The necessary pre-conditions for the occurrence of liquation cracking include grain boundary liquation (a continuous film of liquid) and the existence of tensile stresses along the relatively weak wetted grain boundary. As a result, analysis of the microstructural changes during linear friction welding is really important. Ola et.al (2011a; 2011b; 2012) proposed a model to describe nonequilibrium dissolution behavior of the precipitates during rapid heating conditions. They showed that grain boundary liquation occurs during linear friction welding of IN 738 (Figure 1.8) as a result of nonequilibrium phase reaction between γ′ particles and the surrounding γ matrix. Using Gleeble testing, they observed interdendritic liquated areas at all temperatures above 1423 K (1150˚C). This newly formed fine eutectic product consisted of a major phase that chemically appeared to be based on Ni_5Hf intermetallic with a melting point around 1150˚C. A similar type of resolidified fine eutectic microconstituent was also observed in TMAZ interdendritic regions of a LFWed joint. Microscopic examinations showed that the morphology and chemical composition of the liquated phase was similar to the Ni_5Hf phase observed after Gleeble tests.

The main strengthening phase of the alloy, γ′ precipitates could also liquate through a phenomenon known as constitutional liquation. It generally occurs below equilibrium solidus temperature of the alloy by a eutectic-type reaction between a second-phase particle and the surrounding matrix, producing a metastable solute-rich liquid film at the particle/matrix interface. The basic requirement for the occurrence of constitutional liquation of an intermetallic compound A_xB_y in an alloy is the existence of A_xB_y particles at temperatures equal to or above the eutectic temperature of the matrix- A_xB_y system (Ola et al., 2011b). It is generally known that γ-γ′ eutectic reaction occurs during solidification of several γ′ precipitation- hardened Ni-based superalloys. The γ-γ′ eutectic reaction is often assumed to take place at the solidus temperature as the final solidification reaction during casting. Ola et.al. (2011a; 2011b; 2012) considered the possibility of compressive strains in aiding the dissolution kinetics of γ′ precipitates. An increase in dissolution of γ′ precipitates, which is typically known to be controlled by diffusion of γ′ forming elements away from the precipitate/matrix interface, is also observed to be significantly enhanced by externally induced compressive strains in nickel-base superalloys (Shahriari et al., 2009a). They explained that contrary to tensile stresses in fusion welds, compressive stresses are imposed on the work pieces during linear friction welding and may cause liquation cracks to close. They also attributed the cracking resistance of the joint to the rapid resolidification of intergranular and intragranular liquid aided by imposed compressive strain.

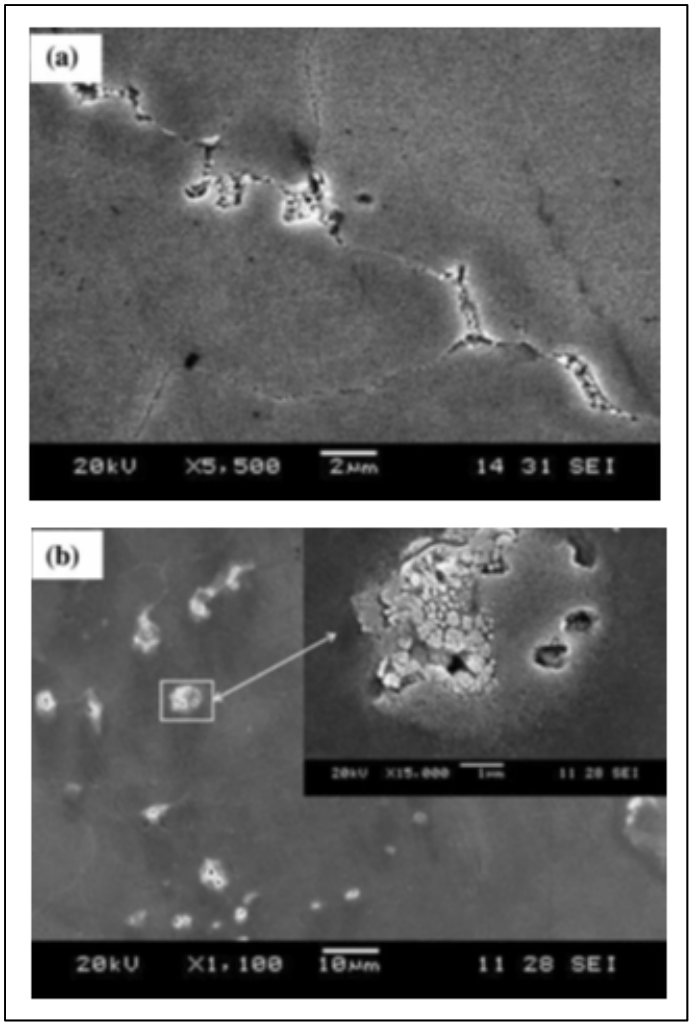

Figure 1.8 SEM micrographs of the TMAZ showing (a) intergranular and (b) intragranular liquation and the presence of resolidified fine γ- γ′ eutectic products that formed from residual liquid during weld cooling (Ola et al., 2011b).

In contrast, Chamanfar et.al. (2012b) did not observe γ′ liquation, and associated it with a lower peak temperature or γ′ sizes that do not reach the critical values. The incidence of Dynamic Recrystallization (DRX), lower peak temperature, lower level of welding stresses and high applied strains, which are specific to the LFW process, were identified as the main factors contributing to the suppressed microcracking of linear friction welded Waspaloy components (Chamanfar et al., 2012b). DRX in LFW leads to fast migration of grain boundaries during welding, leaving precipitates behind. Thus, the unity of the new grains is

preserved and no grain boundary liquation occurs. Furthermore, the rapid heating cycle experienced by the material during LFW is far from equilibrium conditions and therefore no significant diffusion of the γ′ forming elements occurs. Hence, probably only very fine γ′ particles dissolve and the coarse ones most likely less affected i.e. the peak temperature during welding is well below γ′ liquation temperature.

1.3.2 Mechanical Properties after LFW

Mechanical properties, especially tensile and creep strengths of the joints, are among the most important factors in mechanical design and performance in operation for gas turbine engine parts. The mechanical properties of LFWed samples significantly depend on process parameters which affect the microstructural zones that have been deformed in the region of the weld line during the process (Chamanfar et al., 2011a; Dalgaard et al., 2012). An appropriate post weld heat treatment (PWHT) may be needed to reduce residual stresses and recover the strengthening phases in the microstructure since γ′ precipitates could be dissolved at the weld interface during LFW process (Chamanfar et al., 2011a).

More heat input, and therefore higher axial shortening provides an oxide free joint with better mechanical properties. Accordingly, higher friction and forge pressure create localized severe deformation and result in more recrystallized structures and develop better tensile properties at room temperature (Amegadzie, 2012; Chamanfar et al., 2012a). Fine grains exhibit greater yield strength than the coarse ones at low temperature (Amegadzie, 2012) while at elevated temperature grain boundaries are weak and sliding occurs.

Recrystallization (i.e. grain refinement) is unfavorable for creep properties (Cormier et Cailletaud, 2010b; Cormier, Milhet et Mendez, 2007b; le Graverend et al., 2010b). Therefore, a grain coarsening solution annealing treatment can be performed on LFWed samples to improve the creep properties. The creep strength increases with increasing γ' content and thus, higher γ' fractions are often specified where creep strength is required (Cormier et Cailletaud, 2010b; Cormier, Milhet et Mendez, 2007b; le Graverend et al., 2010b). Optimum creep performance would require minimum coarsening rate of γ' precipitates.

1.4 LFW of Ni-based Superalloys: State-of-the-art

Based on the above mentioned literature, for joining "difficult to weld" materials like Ni-based superalloys, LFW is a very promising method because bulk melting does not occur during the process. However, many challenges need to be addressed before full industrial applications. Some of these challenges will be considered in this research as follows:

a) Determination of Optimum Linear Friction Welding Process Parameters for AD730^{TM} Alloy

The above literature review showed that there is ongoing research on LFW of superalloys. While extensive data is available on hot deformation of Ni-based superalloys, few data is available on microstructure evolution during LFW, and its role on mechanical properties of welded Ni-based superalloys. In addition, the effect of post weld heat treatment has been hardly studied on LFWed assemblies, especially Ni-based superalloys. Furthermore, no data is available in the literature on the methodology of designing LFW experiments to determine optimum process parameters. Moreover, the mechanical tests have been performed at room temperature, and the results cannot be directly applied to mechanical properties at high temperatures such as the one used in the present investigation. Hence, this study discusses the design of LFW experiments with the objective to determine the optimum process parameters, and fabricate sound LFWed joints. Finally, the integrity of the weld is evaluated by hot tensile tests.

b) Predicting Dissolved and re-Precipitated γ′ Volume Fraction after Various Heat Treatments

Literature review showed that significant microstructural changes, including dissolution and reprecipitation of γ′ particles, occur during thermomechanical processes such as LFW which play a key role in controlling the mechanical properties of the joints. However, no data is available on the kinetics of γ′ dissolution and reprecipitation during LFW of superalloys and particularly the investigated alloy.

c) Liquation and Microcracking during LFW

In the literature review, different ideas on one of the on-going debates in LFW about whether liquation and consequently cracks occur during this process were proposed. No quantitative data is available on the possibility of constitution liquation during LFW. Therefore, one quantitative study under non-equilibrium thermal cycles such as those encountered in LFW is conducted in this research to clarify the above mentioned debate.

d) Creep Properties after LFW

The components used in hot section of gas turbines are subjected to creep and/or fatigue damage during operation. Thus, improving their high temperature performance (e.g. creep behavior) is of paramount importance for industry. No data is available on creep properties of LFWed Ni-based superalloys in as-weld or post weld heat treated conditions. Hence, it is essential to systematically investigate creep performance of a defect free LFWed AD730^{TM} in as-weld and post weld conditions and compare the results with those of base material, and discuss the damage mechanisms governing the creep processes.

1.5 Objectives

During LFW, the interface material is exposed to severe deformation at high temperatures and high strain rates. Therefore, significant changes occur in microstructure and mechanical properties across the weld interface. So, the main objective of the present study is to understand and predict microstructural changes at the weld interface. This information is crucial for the mechanical behavior of the weld and quantifying the impact of LFW parameters. In this regard, it is also necessary to answer an ongoing debate in the scientific community about whether or not liquation of second phases and subsequent microcracking, often observed in fusion welded Ni-based superalloys occurs during LFW.

To reach the main objective, the sub-objectives are defined as follows:

1- To characterize the newly developed superalloy AD730^{TM}.

2- To determine the influence of LFW process parameters on microstructure and mechanical properties:
   a) To evaluate the effects of heat input on weld integrity and microstructure evolution,
   b) To evaluate the mechanical properties for optimal weld,
   c) To evaluate the liquation of second phases and cracking possibility.
3- To better understand the mechanisms of dissolution and reprecipitation of γ′ phase:
   a) To predict γ′ morphology and volume fraction,
   b) To predict γ′ characteristics in LFWed samples.

To tackle these objectives following methodology is developed.

1.6 Materials and Methods

1.6.1 Materials

The cast and wrought (C&W) Ni-based superalloy, AD730^{TM}, has been recently developed by Aubert & Duval and introduced especially for the first stages of the turbine discs with high properties up to 700°C (Devaux et al., 2012b). It was designed to provide a better combination between mechanical properties and cost compared to Rene88DT, N18, RR1000, and etc. This alloy has mechanical properties close to Udimet 720 and significantly higher than 718Plus, Waspaloy and Inconel 718. Table 1-1 shows a comparison between chemical composition and γ' volume fraction of these alloys. AD730^{TM} is also strengthened by γ′ precipitates and presents a good ability for C&W manufacturing process with desired strength, creep and fatigue properties. The equilibrium volume fraction of γ′ (V_f) is around 37-40% for this alloy. Primary γ' particles exist at the grain boundary while secondary and tertiary γ' are within the grains. The first type of γ' particles are formed during forging stages while the secondary and tertiary precipitates form during the cooling process. Thus, size and distribution of the precipitates in this alloy are determined by the cooling rate after solution heat treatment and can be adjusted with the aging process.

Table 1-1 Chemical composition and γ' volume fraction of AD730^{TM} compared to some other Ni-based superalloys (wt%)

	Ni	Fe	Co	Cr	Mo	W	Al	Ti	Nb	B	C	Zr	V_f
718	Bal.	18	-	18	3	-	0.5	1	5.4	0.004	0.03	-	17
718Plus	Bal.	10	9	18	2.75	1	1.5	0.7	5.5	0.004	0.02	-	24
Waspaloy	Bal.	-	13.5	19.5	4.25	-	1.5	3	-	0.006	0.05	0.03	32
U720Li	Bal.	-	15	16	3	1.3	2.5	5	-	0.015	0.02	0.03	44
AD730^{TM}	Bal.	4	8.5	15.7	3.1	2.7	2.25	3.4	1.1	0.01	0.015	0.03	37

1.6.2 Methods

The literature review extracted the knowledge useful for the purpose of this study and introduced the shortcomings of the literature in dealing with LFW of superalloys. This information allowed defining the methodology to accomplish the objectives introduced in introduction.

Regarding objective 2, to develop defect free LFWed specimens, the ranges of friction and forge pressures and time were designed based on the proposed analytical method, and several samples were welded with various process parameters and heat inputs. Optimum welding parameters were determined performing microhardness, room and hot tensile and creep tests. The size of weld zone and TMAZ, and grain size evolution at the weld interface were determined using EBSD maps. Creep and tensile damage mechanisms were investigated using SEM.

With regard to objectives 1 and 3, understanding microstructure evolution during LFW, conventional heat treatments were designed, and performed. To predict dissolved γ′ volume fraction or temperature in different zones of a LFW joint, various solution treatments with two different heating rates, were carried out. To predict re-precipitated γ′ volume fraction at weld interface of LFW, heat treatments with various cooling rates were performed. For microstructural studies, Field Emission Gun Scanning Electron Microscopy (FEG-SEM) was used. Then, γ′ size and volume fraction changes during solution and cooling treatments were

determined. Semi-analytical models were developed to describe the dissolution and re-precipitation processes during heating and cooling steps of heat treatments.

To evaluate grain boundary and second phase liquation and cracking possibility, liquation temperature of AD730^{TM} was determined using Gleeble™ 3800 physical simulator and SEM. Then, temperature distribution in LFWed specimen was obtained using analytical models based on primary and secondary γ′ dissolution temperatures (obtained by Gleeble) as boundary conditions. The determined weld temperature was compared to liquation temperature of AD730^{TM} to justify whether or not liquation occurs during LFW. Finally, microscopic analysis of the weld was performed by SEM to evaluate if liquated and solidified products are observed in weld zone or TMAZ.

The objectives are addressed in chapters 2 to 7 in this Ph.D. thesis.

Chapter 2 proposes an analytical method, validated by experiments, for the determination of the optimum LFW process parameters. Then, it focuses on performing LFW experiments using different processing parameters. Appropriate LFW process parameters are chosen to generate sufficient heat for obtaining sound welds, and removing oxides and other impurities as flash, and to form a defect free joint with a narrow TMAZ. Subsequently, microstructure and mechanical properties including hardness, room and high temperature tensile properties are investigated. This chapter responds to the first and second part of the second objective which is discussing about the interaction of process parameters to maximize the integrity of LFWed AD730^{TM}. A paper on this chapter is being prepared for publication.

Chapter 3 presents the first published article in *Journal of Alloys and Compounds*. During second stage of LFW (heating stage), the alloy is heated to the temperatures at which the γ′ precipitates are dissolved. Therefore, size distribution and morphology evolution of γ′ particles are quantified and analyzed during dissolution process in this article. Finally, a semi-analytical model for dissolution and coarsening kinetics is proposed, and a better understanding of fundamental mechanisms governing γ′ dissolution in Ni-based superalloys is developed. This chapter responds to the first and third objective which is to propose a model for predicting γ′ volume fraction at high temperatures.

Chapter 4 is the second published article in *Scientific Reports*. Depending on the portions of Al and Ti elements, γ′ particles re-precipitate during the third stage of LFW (cooling stage). Thus, this article addresses fundamental mechanisms of re-precipitation during cooling stage of heat treatments. In addition, volume fractions of re-precipitated γ′ with temperature and time and γ′ re-precipitated kinetics are predicted. This chapter responds to the third objective of the thesis.

Chapter 5, published in *Metallurgical and Materials Transactions A*, aims to investigate the possibility of second phase liquation and microcracking during LFW of AD730^{TM}. Then, the conditions under which liquation can take place during LFW were determined using Gleeble™ 3800 machine, and possible governing mechanisms are discussed. This chapter responds to the third objective and the first and third part of the second objective which tries to answer an ongoing debate in the scientific community about the possibility of liquation during LFW.

In Chapter 6, published in *Material Science and Engineering A*, the high temperature creep performance of LFWed AD730^{TM} is investigated in as weld and post welded conditions, and the results are compared to the creep properties of the base material. Furthermore, creep life of the joint is predicted by Larson-Miller plot, and then, the creep properties are compared with those of several other Ni-based superalloys. Finally, the governing damage mechanisms are discussed. This chapter responds to the second part of the second objective

Conclusions section constitutes a summary of the research work presented in chapters 2 to 6. Recommended future works are presented subsequently after this section.

In summary, in the current work, a procedure for determining process parameters to reach a defect free LFWed joint is proposed. Also, microstructure of LFWed AD730^{TM} was studied. Models for γ′ evolution during various heating and cooling cycles are proposed. In addition, second phase and grain boundary liquation and cracking possibility during joining were evaluated. Finally, the mechanical properties, including room and hot tensile and creep properties of LFWed AD730^{TM} were studied.

CHAPITRE 2

DETERMINATION OF OPTIMUM LINEAR FRICTION WELDING PROCESS PARAMETERS FOR AD730^{TM} ALLOY

2.1 Introduction

LFW is fundamentally a hot deformation process. During LFW of Ni-based superalloys, microstructural changes such as dissolution and subsequent re-precipitation of γ′ precipitates have substantial impact on mechanical properties of welded joint. In addition, dynamic and post-dynamic recrystallization as well as dissolution of tensile resisting phases occur during welding which are expected to impact on mechanical properties of the joint (Cormier et Cailletaud, 2010b; Cormier, Milhet et Mendez, 2007b; le Graverend et al., 2010b). While extensive data is available on hot deformation of Ni-based superalloys (Ola, Ojo et Chaturvedi, 2013b; Shahriari et al., 2009a; Viswanathan et al., 2015; Wang et al., 2011b), few data is available on microstructure evolution during LFW, and its role on mechanical properties of welded Ni-based superalloys. In addition, the effect of post weld heat treatment has been hardly studied on LFWed assemblies, especially Ni-based superalloys (Chamanfar et al., 2011a; Damodaram, Ganesh Sundara Raman et Prasad Rao, 2014a). Damodaram et al. (2014a) studied tensile properties of as weld and post weld heat treated (PWHT) conditions on continuous drive friction welded Inconel 718 specimens. Post weld heat treated samples exhibited better room temperature tensile properties than those of as-welded samples. Reduction in average size and volume fraction of γ′ precipitates results in reduction in mechanical properties of as-welded specimens (Damodaram, Ganesh Sundara Raman et Prasad Rao, 2014a). Chamanfar et al. (2012a) reported that post weld heat treatment of LFWed Waspaloy leads to superior hardness properties compared to as-weld condition. However, the tests have been performed at room temperature, and the results cannot be directly applied to tensile properties at high temperatures such as the one used in the present investigation. Furthermore, no data is available in the literature on the methodology of designing LFW experiments to determine optimum process parameters.

Hence, this chapter discusses the design of LFW experiments with the objective to determine the optimum process parameters, and fabricate sound LFWed joints. In this regard, the roles of frequency, amplitude, and pressure on weld integrity are discussed in details. In addition, evolution of the microstructure, especially γ′ precipitates and γ grain size is quantified, and its impact on microhardness changes, room and hot tensile properties are discussed.

2.2 Selection of the LFW Process Parameters

2.2.1 Selection of Friction and Forge Pressures

The friction and forging phases in LFW can be considered as an upsetting process, consisting in deforming a metal between two flat dies. In this case, a plane-strain hot compression with sticking friction condition could be used to analyze these two stages. Using the slab analysis method for plane strain compression, average pressure due to friction and forge pressures can be estimated by (Altan, Ngaile et Shen, 2005; Dieter, Kuhn et Semiatin, 2003; Hosford et Caddell, 2014):

$$P_{ave.} = 2k(1 + \frac{\mu a}{h}) \tag{2.1}$$

where k is the shear strength, μ is the constant coefficient of friction, a and h are width and height of the specimen, respectively.

By considering plane strain compression, k can be expressed as:

$$k = \frac{\bar{\sigma}}{\sqrt{3}} \tag{2.2}$$

where $\bar{\sigma}$ is the flow stress.

By substituting k into Eq.(2.1), the minimum pressure at the onset of plastic flow during LFW process will become:

$$P_{ave.} \geq \frac{2\bar{\sigma}}{\sqrt{3}} \tag{2.3}$$

Therefore, accurate estimation of material flow stress is a necessary condition to determine the pressure that allows plasticizing the material. In its most general form, the flow behavior of a material is a function of strain (ε), strain rate ($\dot{\varepsilon}$) and temperature (T) (Dixit, Joshi et Davim, 2011; Lin et Chen, 2011; Turner et al., 2014). In the present investigation, a combination of published data on hot deformation and LFW of Ni-based superalloys and analytical calculations were used to estimate the flow stress and its relation as a function of the above variables, as described in the following:

2.2.1.1 Strain during LFW

The equivalent plastic strain distributions were estimated during friction welding process of a typical Ni-based superalloy using Finite Element Modelling (FEM) simulation (Yang et al., 2015). Based on the authors' results, the plastic strain at the center of interface reached about 12. However, no experimental support was provided. Similarly, the strains at 1mm and 8mm far from the weld line were estimated to be approximately 0.8 and 0.01, respectively. In order to analyze and implement flow stress curves under isothermal compression, the reliable strain is approximately 1 (Yang et al., 2016). Therefore, the flow behaviour of the investigated material was estimated at a strain of 0.8 at various temperatures and strain rates to simulate deformation during LFW.

2.2.1.2 Strain Rate during LFW

A wide range of strain rate values (between 0.1 to 2000 s^{-1}) has been proposed for LFW (Buffa et Fratini, 2017; Chamanfar, Jahazi et Cormier, 2015b; Li et al., 2016; Turner et al., 2011b). However, most of the authors have reported strain rates between 0.1 $s^{-1}$and 20 s^{-1} for LFW. The case of 2000 s^{-1} has been based on simulation results with no experimental support (Turner et al., 2011b). Varis et al. (2016) reported that strain rate has the minimum value at the friction stage of LFW and reaches the highest value during the forge phase. Thus, in the present work, the friction pressure was estimated at a strain rate of about 0.1s^{-1} while the forge pressure was calculated based on the available data on high strain rate values.

2.2.1.3 Deformation Temperature Estimation

Temperature should be high enough to allow easy plasticization of the metal during LFW. Considering that the strength of the Ni-based superalloys is strongly dependent on the presence of γ′ particles, the minimum temperature to start deformation is the temperature at which these particles are dissolved. However, the dissolution temperature of the primary γ′ particles varies with the heating rate and since the heating rate varies at different locations from the joint interface, the dissolution kinetics of the γ′ particles is expected to change with the distance from the weld interface. In the present investigation, Differential Thermal Analysis (DTA) and Gleeble®3800 physical simulator were used to determine the dissolution temperatures of primary γ′ at low (up to $2^{\circ}C.s^{-1}$) and high heating rates (up to $400^{\circ}C.s^{-1}$), respectively. Figure 2.1 shows the influence of heating rate on primary γ′ dissolution temperature for the AD730^{TM} alloy. It can be seen that the lowest temperature for γ′ dissolution is around 1060°C. Thus, the minimum temperature that needs to be reached before the application of deformation in the initial stage of the LFW process is considered to be 1060°C.

Temperature measurements using an infrared thermal imaging instrument indicated that the temperature at the joint interface was about 1100°C during friction stage of LFW of a Ni-based superalloy (Yang et al., 2015). Li et al. (2016) reported that the weld interface temperature in the steady state zone was between 0.75 and 0.95 of the melting temperature T_M. In this study, $0.85T_M$ was considered as the upper limit which corresponds to 1150°C (the melting temperature of AD730^{TM} alloy was taken as 1350°C based on the literature (Devaux et al., 2012b).

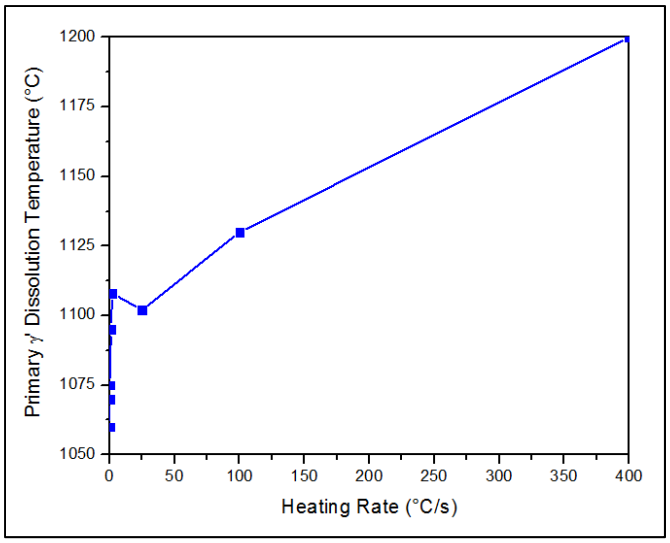

Figure 2.1 Primary γ′ dissolution temperature of the AD730^{TM} at different heating rates.

2.2.1.4 Influence of Adiabatic Heating

For accurate calculation of the forge pressure, temperature increase due to straining, and consequently adiabatic heating, needs to be considered. Since adiabatic heating is only present during friction stage, it is only estimated for a strain rate of 0.1s^{-1} (corresponding to the friction phase of LFW) and 1s^{-1} (corresponding to the end of friction phase of the LFW process). The effect of adiabatic heating can be estimated by $\Delta T = \frac{0.95\eta}{\rho C}\int_0^{\varepsilon}\sigma d\varepsilon$ (Altan, Ngaile et Shen, 2005). In this equation, η is the thermal efficiency (63.5% for strain rate of 0.1s^{-1} and 95% for strain rate of 1s^{-1}), ρ the density of the alloy (8155.33 Kg.m^{-3} at 1150°C), C the specific heat (792.68 J.Kg^{-1}.K^{-1} at 1150°C), ε the maximum strain (0.8) and σ maximum flow stress (peak stress) during hot deformation. The peak stress values for AD730^{TM} and some other Ni-based superalloys (Jiang et al., 2015; Wang et al., 2013) which are similar to AD730^{TM} at strain rates of 0.1s^{-1} and 1s^{-1} in the temperature range of 1000-1250°C are shown in Figure 2.2 andFigure 2.3. In these curves, only the one for AD730^{TM} was adjusted for adiabatic heating calculation. From Figure 2.2 and Figure 2.3, it can be found that the 'adjusted' peak stress at 1150°C is approximately 120 MPa at strain rate of 0.1s^{-1} while it is around 290 MPa at strain rate of 1s^{-1}. Using the above data, ΔT was calculated to be ~10°C for a strain rate of 0.1s^{-1} and ~30°C for a strain rate of 1s^{-1}. Therefore,

the maximum weld interface temperature or the upper limit of deformation temperature at the end of friction stage is estimated to be approximately 1200°C.

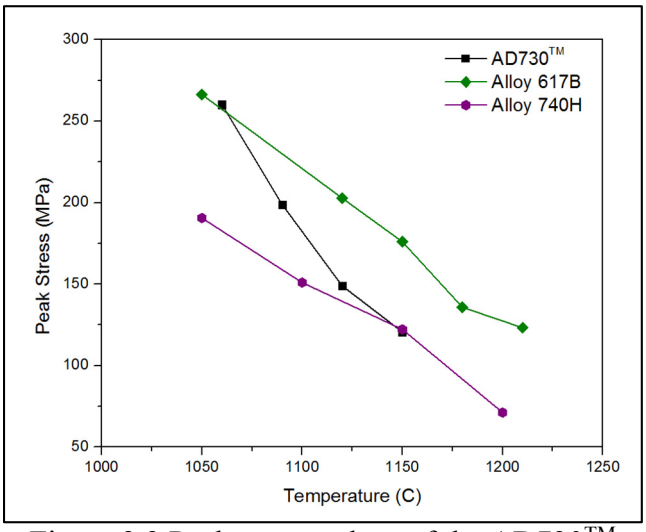

Figure 2.2 Peak stress values of the AD730™ and the other Ni-based superalloys at strain rate $0.1s^{-1}$.

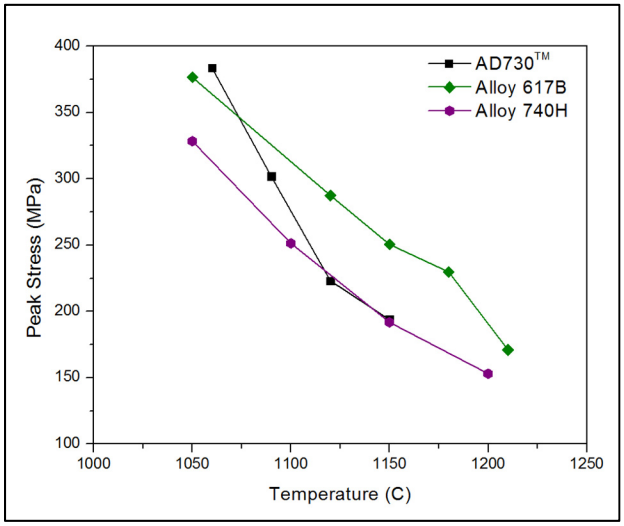

Figure 2.3 Peak stress values of the AD730™ and the other Ni-based superalloys at strain rate $1s^{-1}$.

In order to estimate forge pressure, the available data on highest strain rate values (10 and $20s^{-1}$) for Ni-based superalloys were used. Temperature dependence of the peak stress at strain rates of 10 and $20s^{-1}$are shown in Figure 2.4. The experimental peak stress data at these strain rates is not available for AD730^{TM}, and is only available for 617B and 740H superalloys. In addition, these alloys have similar behavior in deformation temperature of 1060˚C to 1150˚C as γ′ precipitates are dissolved at these temperatures. Furthermore, at low and medium strain rates (0.1 and $1s^{-1}$), AD730^{TM} has almost similar behavior to 617B and 740H superalloys (Figure 2.2and Figure 2.3). Therefore, the measured peak stresses for these alloys were used for the calculations of forge pressure at strain rates of 10 and $20s^{-1}$ (Figure 2.4).

Based on the above analysis, to estimate friction pressure, the peak stress at strain rate of $0.1s^{-1}$ and deformation temperature of 1060°C to 1150°C were used while the flow stress at strain rate of 20 s^{-1} and deformation temperature of 1060°C to 1200°C were used to calculate forge pressure. From Figure 2.2, it can be found that the corresponding peak stress at about 1060˚C is 260MPa while it is around 120MPa at 1150°C. Then, according to Eq.(2.3), friction pressure for AD730^{TM} was calculated to be ranging from 133 to 285MPa.

From Figure 2.4, it can be seen that the peak stress for the weld joint temperature interval of 1060-1200°C varies between 530MPa and 240 MPa, respectively. On the basis of the above analysis and using Eq.(2.3), the forge pressures during the LFW process of AD730^{TM} alloy were calculated to be between 265 and 580MPa.

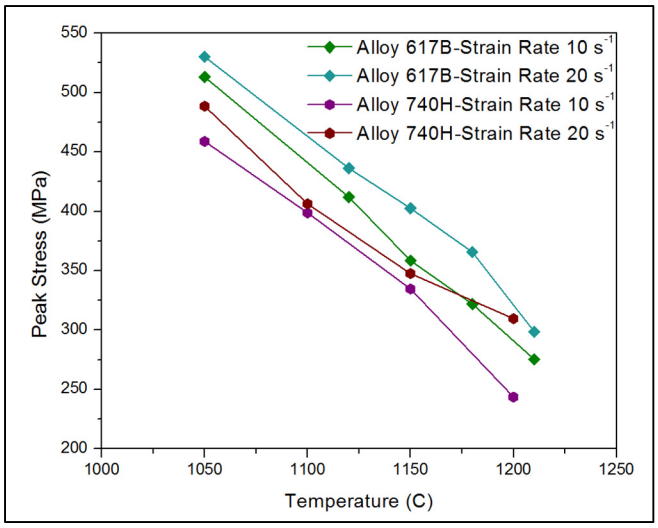

Figure 2.4 Peak stress values of the various Ni-based superalloys at strain rates 10 and 20s^{-1}.

2.2.2 Oscillation Frequency and Amplitude

The oscillation frequency and amplitude also influence the maximum weld line temperature. By increasing these two parameters, the weld interface temperature increases rapidly at the early stage of LFW process and then reaches an almost stable state. In order to quantify the impact of these two parameters, Addison's equation (2010) was used:

$$v_r = 4.\alpha.f \tag{2.4}$$

where v_r is the rubbing velocity, α and f are the oscillation amplitude and frequency.

A sound LFW joint can be formed by increasing the rubbing velocity which may cause a slight increase of the heat input, and consequently, higher temperature and removal rate of oxide layers. Therefore, the rubbing velocity has to be kept as a maximum value. The maximum values were selected for oscillation amplitude and frequency within the operating window of the LFW machine. Figure 2.5 illustrates the recommended amplitude and frequency parameters for the LFW machine at TWI, Cambridge, UK, used in this study. As shown in Figure 2.5, the highest oscillation amplitude was about 2.7 mm, and the highest allowable amplitude was 2.5 mm which was selected for the welding trials. Similarly, the highest allowable oscillation frequency was 40 HZ, which was used for the tests. On this

basis, the maximum rubbing velocity from Eq. (2.4) was calculated to be 400 $mm.s^{-1}$.

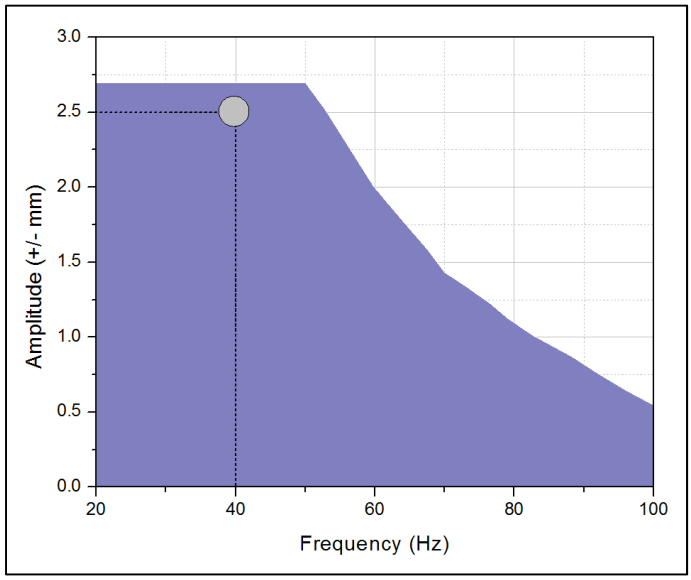

Figure 2.5 Operating window for LFW machine (FW34 at TWI, Cambridge, UK).

According to the above analysis, using analytical calculation, machine capability, and data in the literature, and with the view to reaching a defect free joint with optimum mechanical properties, an experimental plan was therefore conducted using the welding conditions provided in Table 2-1. Among the four variables of the LFW process, i.e. oscillation frequency, amplitude, friction and forge pressure, the first three provide heat at the interface while the fourth one controls the joint integrity. As discussed, the highest allowable values were considered for oscillation frequency and amplitude in the four trials. Then, trials 1 and 4 were conducted at the lowest and highest limits of calculated friction and forge pressures, respectively. Intermediate values of friction and forge pressures were selected between the minimum and maximum of the calculated values for trials 2 and 3.

Table 2-1 Linear friction welding parameters determined and used for AD730^{TM} a Ni- based superalloy

Test Condition	Oscillation Amplitude (mm)	Oscillation Frequency (Hz)	Friction Pressure (MPa)	Forging Pressure (MPa)	Heat Input ($W.m^{-2}$)
#1	2.5	40	133	330	3.192×10^{7}
#2			150	265	3.600×10^{7}
#3			187.5	265	4.500×10^{7}
#4			285	580	6.840×10^{7}

2.2.3 Estimating the Heat Input

In order to estimate the heat input (HI) in the friction phase for the selected LFW process parameters reported in Table 2-1, the following equation was used (Li et al., 2016; Vairis et Frost, 1999b):

$$HI = \dot{q} = \mu . v_r . P_{Fric.} \tag{2.5}$$

where μ is the friction coefficient, v_r and $P_{Fric.}$ are the rubbing velocity and friction pressure. For the calculation purposes, a fixed rubbing velocity of 400 $mm.s^{-1}$ was considered, and the friction coefficient was taken equal to 0.6, as reported in the literature (Li et al., 2014; Maalekian, 2007; Yang et al., 2015). As presented in Table 2-1, the higher friction pressure will generate more heat at the weld interface which will lead to higher deformation rate and hence higher axial shortening, if the appropriate forging pressure is applied.

Based on Eq. (2.5), test conditions #1 and #4 have the lowest and the highest heat input, respectively.

2.2.4 LFW Process Time

To determine the optimum linear friction welding time, an analytical procedure based on one dimensional (1D) thermal model was used. During the LFW process, heat losses by radiation and convection are usually negligible (Maalekian, 2007). Therefore, the temperature distribution in each solid part can be determined by solving the 1D heat conduction equation

(Bergman et Incropera, 2011; Grong, 1997; Lindgren, 2006; Yilbas et Sahin, 2014). Heat equation for three-dimensional without energy generation is given by:

$$\frac{\partial T}{\partial t} = a\left(\frac{\partial^2 T}{\partial x^2} + \frac{\partial^2 T}{\partial y^2} + \frac{\partial^2 T}{\partial z^2}\right) \tag{2.6}$$

where T is the temperature, t is the time, x, y, z are the heat flow directions, and a is the thermal diffusivity. The thermal diffusivity is related to thermal conductivity λ, densityρ and specific heat C_p through the following equation (Bergman et Incropera, 2011):

$$a = \frac{\lambda}{\rho C_P} \tag{2.7}$$

The concept of instantaneous heat source in an infinite medium was used to solve the heat conduction Equation (2.6) in relation to the LFW process (Grong, 1997; Yilbas et Sahin, 2014). The analytical solution for the 1D transient temperature distribution with time, in the case of frictional heat generation at a rate of $\dot{q}$ ($^{W}/_{m^2}$) diffusing along the x distance from the weld interface, is given by (Grong, 1997):

$$T(x,t) = T_i + \frac{\dot{q}}{2\lambda}\left[\sqrt{\frac{4at}{\pi}}\,exp\left(-\frac{x^2}{4at}\right) - xerfc\left(\frac{x}{2\sqrt{at}}\right)\right] \tag{2.8}$$

where T_i is the ambient temperature.

According to Eq. (2.8) for $x = 0$, the temperature distribution is given by:

$$T(0,t) = T_i + \frac{\dot{q}}{\lambda}\sqrt{\frac{at}{\pi}} \tag{2.9}$$

Using Eq. (2.9) and the analysis made in section 2.2.1.3, the maximum temperature of the weld interface was estimated to be about 1250°C at the end of the process. The thermal diffusivity and thermal conductivity of the investigated alloy are 11.15 $W.m^{-1}.K^{-1}$ and 2.79×10^{-6} $m^2.s^{-1}$, respectively (Devaux et al., 2012b).

Using the LFW process parameters given in Table 2-1, Eq. (2.5) and Eq. (2.9), the estimated temperature profiles were calculated for different test conditions and are presented in Figure 2.6. Test condition #1 has minimum heat input with the interface reaching approximately the estimated maximum weld line temperature after about 10 s. In contrast, for the test condition #4, in which frictional heat input is the highest, the estimated maximum weld line temperature is obtained after 2.5 s. Considering the research nature of the work, it was decided to use a constant processing time of 10 s to allow better weld integrity and bonding for all test conditions. The selected processing time will be sufficient for reaching the maximum temperature of 1250°C at the weld interface which is sufficient for inducing plastic deformation over the entire weld interface.

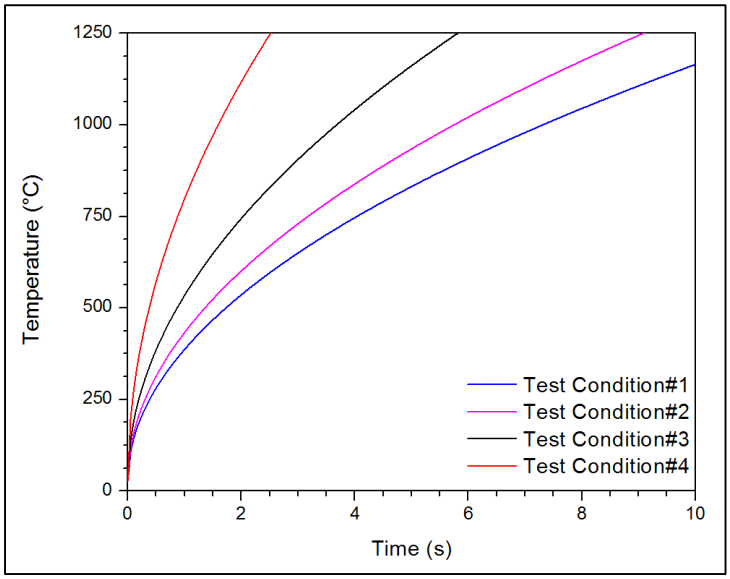

Figure 2.6 Temperature variation with time for different LFW process parameters.

2.2.5 Estimating the Axial Shortening

Based on Eq. (2.5), test conditions #1 and #4 have the lowest and the highest heat input, respectively. Then, temperature distribution in the stationary part for these two test conditions was calculated according to Eq. (2.8), and the results are shown in Figure 2.7 (a, b). The evolution of temperature with position from the weld interface and heating period

times can be clearly observed in these figures. For both conditions, the temperature in the bulk of the material increases with increasing welding process time. It is a reasonable approximation to assume that when the material flow starts at $0.85T_M$, a significant volume fraction of the secondary and primary γ′ precipitates have already been dissolved. Therefore, locations at 0.3mm and 0.4mm away from the weld interface are expected to be easily deformed under test conditions #1 (after 10 s) and #4 (after 2.5 s), respectively. As shown in Figure 2.7 (a), the minimum heat input results in 0.6 mm plastic deformation in 10s, while the maximum heat input provides an overall deformation of 0.8 mm after 2.5 s (Figure 2.7 (b)). Hence, the corresponding axial shortening values predicted from the temperature profiles are around 0.6 mm and 3.2 mm for low and high frictional heating inputs. In the next section, the metallography (macro and micro) examination of the samples for 4 testing conditions will be presented and the obtained results will be compared and validated with the above predictions.

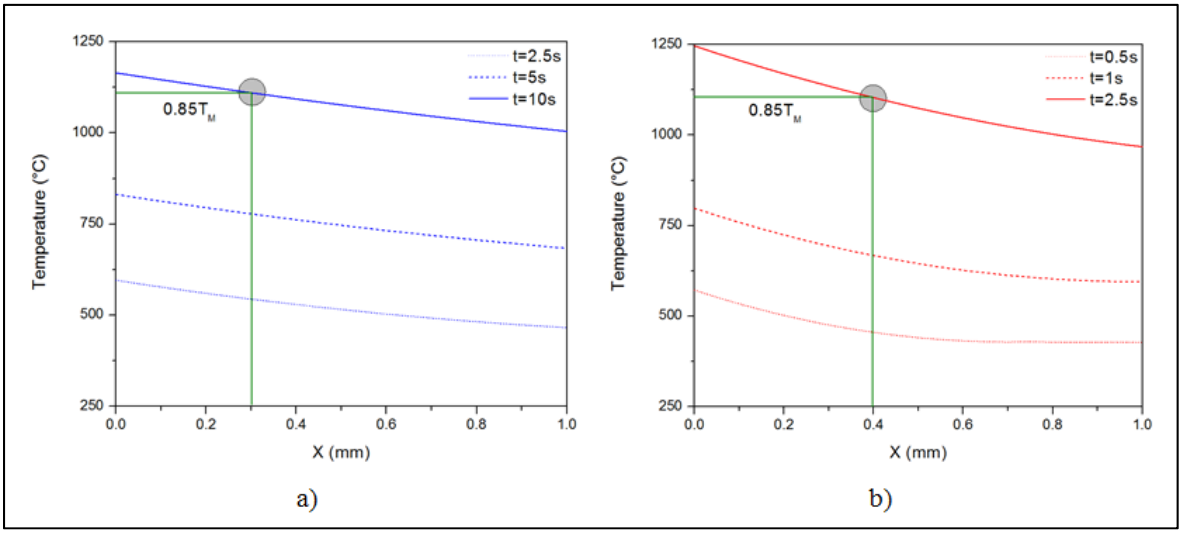

Figure 2.7 Temperature distribution with various times along the x-axis with (a) the lowest and (b) the highest heat input.

2.3 Macrostructure

2.3.1 Macroscopic Evaluation of the Joint after LFW

Figure 2.8 shows the LFWed samples for the four selected conditions. It can be seen that while a very little flash is formed under conditions 1 and 2, a well-formed flash, and consequently better joint integrity, is generated with test conditions #3 and #4. The amounts of measured axial shortening were 0.5mm, 0.58 mm, 1.7 mm and 4mm for test conditions 1 to 4, respectively. The flash material was cut from the samples for further examination, as it will be documented in the upcoming chapters.

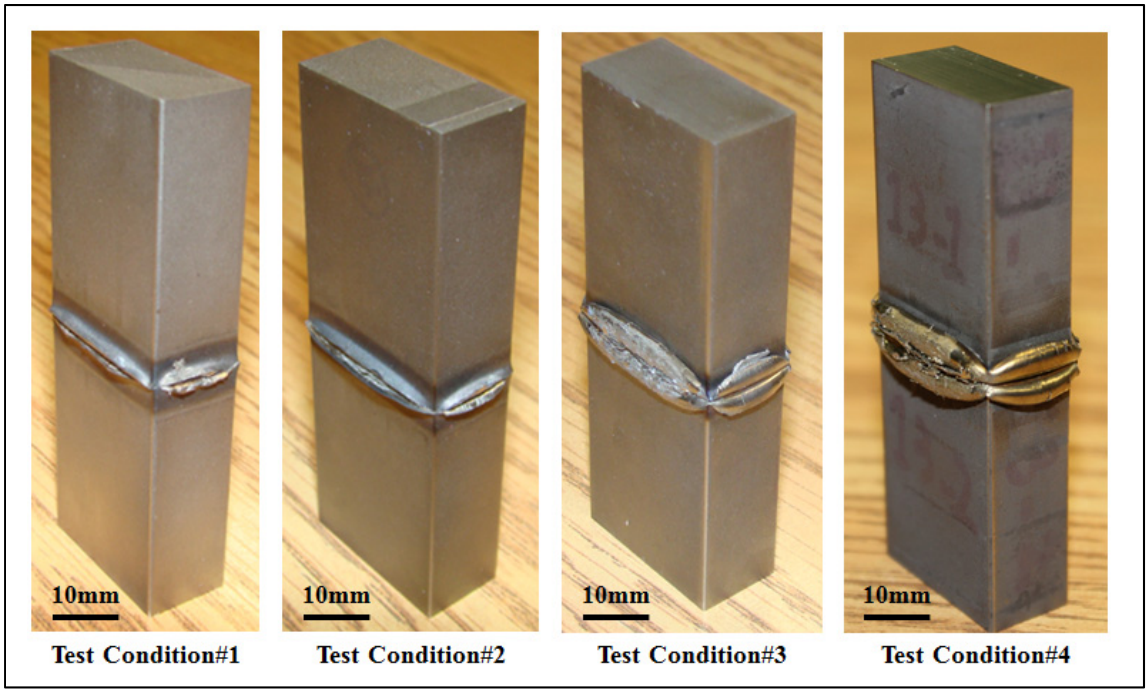

Figure 2.8 Photographs of side views of the LFWed AD730^{TM} joints. Minimum flash is observed in the test condition #1 while test conditions #3 and #4 present well-formed flash.

Only macroscopic features of the LFWed joints #1 and #4, which have respectively the minimum and maximum flash, are illustrated in Figure 2.9 (a, b) for comparison. Impurities like oxide layers appeared at the weld interface of sample #1 while under welding condition #4 it appeared that a defect-free joint was produced. The oxide inclusions present in weld #1

had a wavy shape. Similar observation has also been reported on other LFWed joints, and related to the reciprocating motion of the parts during the welding process (Senkov et al., 2014). Appropriate selection of the process parameters in test condition #4 allowed obtaining a good bonding structure and a sound joint. Visual inspection of the weld interfaces showed that bifurcated flash was formed during LFW. In sample #4, the flash was connected around the corners of the specimen which is indicative of its high integrity. Further examination of the weld line at higher magnifications (Figure 2.9 (c)) did not reveal oxide particles, voids or microcracks at the corner of the LFWed sample, indicating that all the oxides were removed from the weld line due to sufficient extrusion of the interface material. Thus, further macroscopic and microscopic evaluations as well as evaluation of mechanical properties were performed on the sample#4.

Figure 2.10 shows the heat input calculated based on Eq. (2.5) versus the measured and the predicted axial shortening (calculated based on Eq.(2.8)) for the four test conditions. A good agreement is observed between the analytical methodology and experiments. A better conformance can be observed for lower axial shortenings than that of the higher one. Therefore, 2D or 3D numerical simulations are recommended to be employed to predict more accurate axial shortenings.

No oxide particles were observed at the weld interface of AD730^{TM} with an axial shortening larger than 1.7 mm. This finding is confirmed by reports in which an axial shortening of more than 2 mm could provide a weld interface without any defects as well as adequate room temperature tensile properties for Ti6Al4V and Waspaloy (Chamanfar et al., 2012a; Wanjara et Jahazi, 2005). It can be concluded that the axial shortening should be in the range of ~2-4mm in order to produce a high quality joint for AD730^{TM} Ni-based superlloy. Therefore, the proposed analytical approach appears to be very efficient in identifying LFW process parameters without employing a large number of welding experiments.

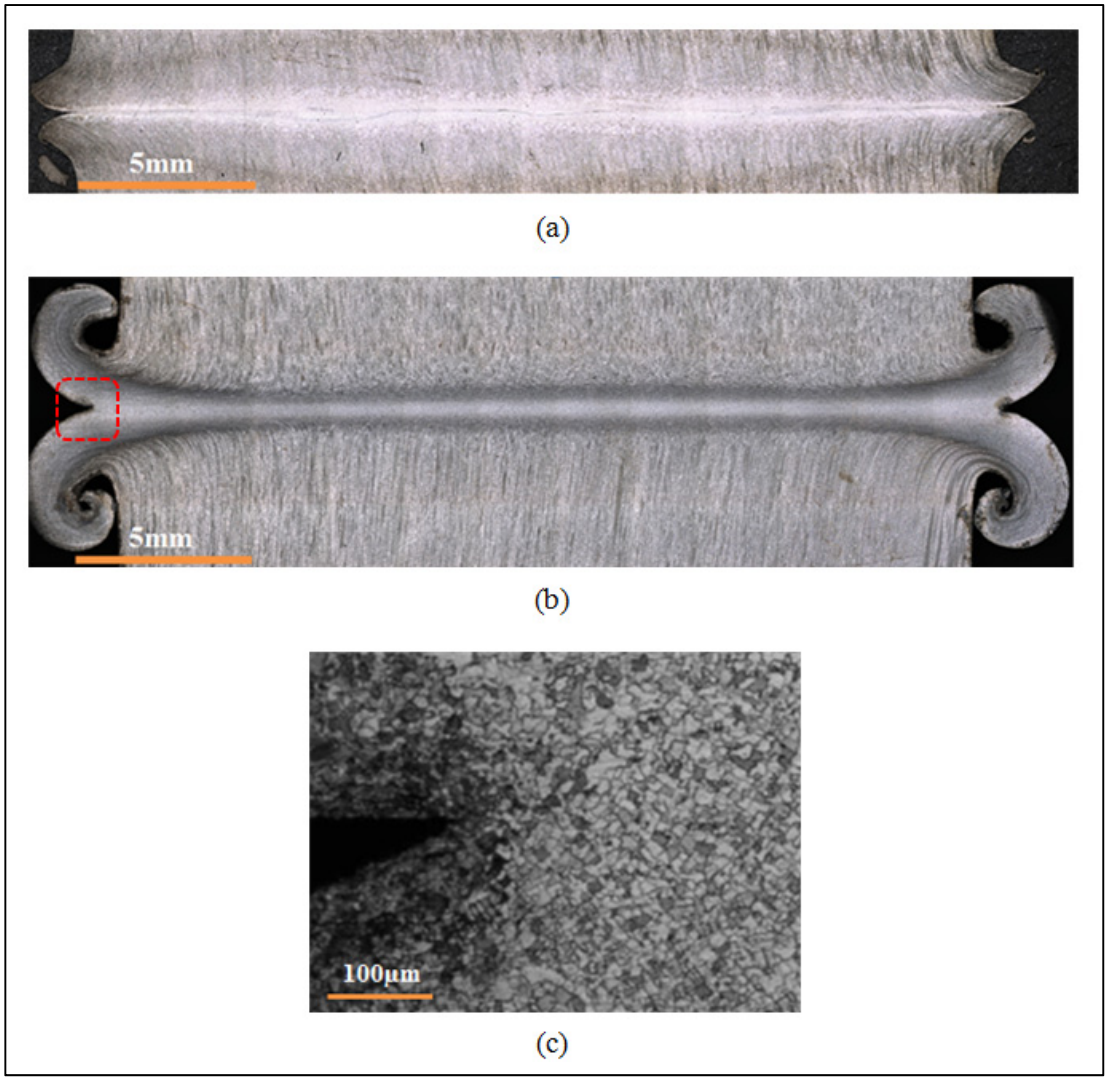

Figure 2.9 Macrograph of the LFWed joints#1 and #4. Oxides are forming similar to sinusoid or wavy shape at the weld interface in test condition #1(a) while uniform deformation is attained in test condtion#4(b). Higher magnification of red box is revealed in (c) where no voids or oxides are observed.

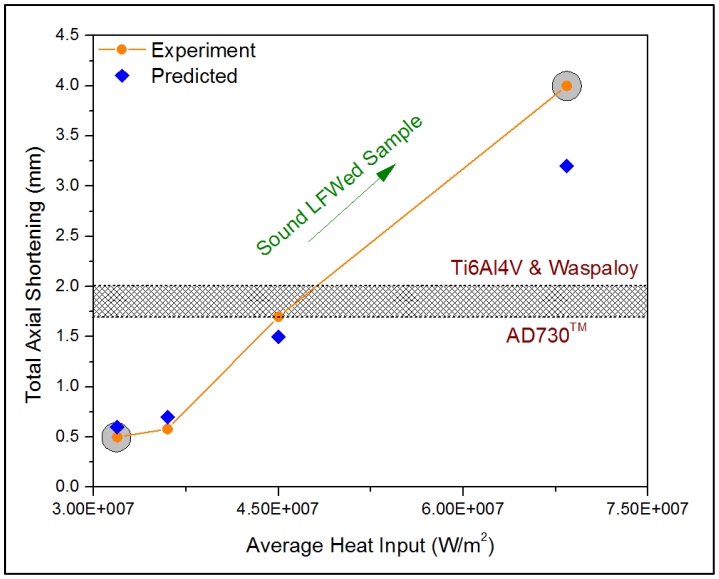

Figure 2.10 Variation of axial shortening with the expected heat input.

2.4 Microstructure

2.4.1 Grain Refinement at the Weld Interface

The EBSD map of the base material is provided in Figure 2.11 (a) and the distribution of grain misorientation in Figure 2.11 (b). An average grain size of approximately 40 µm was calculated based on ASTM E112 standard and image J analysis software. About 57% of the grain boundaries were high angle in character (HAB) with misorientation ranging from 15 to 55°. Low angle grain boundaries (LABs defined in the misorientation range of 1 to 15°) fraction was as low as 9 % with most of them clustered within some grains as shown by black dots in Figure 2.11 (a). Finally, about 34% of the microstructure was composed of twins, shown by yellow lines in Figure 2.11 (a) (Figure 2.11 (b)).

Table 2-2 summarizes the distribution of grain orientations in the base metal and its evolution from the base metal to the weld interface.

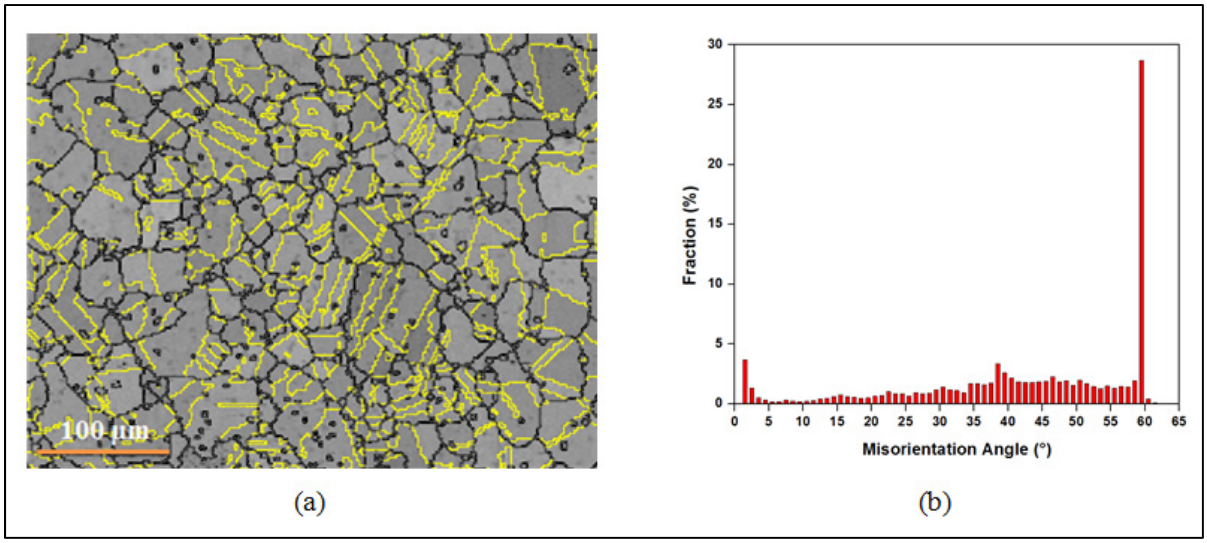

Figure 2.11 (a) EBSD map of the base material, (b) misorientation distribution in the parent material.

Table 2-2 Distribution of grain orientations from the base material to the weld region of sample #4

Microstructural Region (mm)	HAB % (between 15-55 misorientation)	LAB %	Twin %
Base Material	57	9	34
1.8-2	43	27	30
0.8-1	17	61	21
0.6-0.8	20	65	15
0.4-0.6	27	60	12
0-0.4	40	56.1	3.9

Figure 2.12 shows an EBSD map of sample#4 over a large distance covering both sides of the weld line. Since the measured distance was very large, the width of the recording window was small; however, this does not affect the interpretation of the obtained results. In Figure 2.12, the area with concentrated red zones, with a width of approximately 4mm corresponds to the TMAZ, and shows a heavily deformed region.

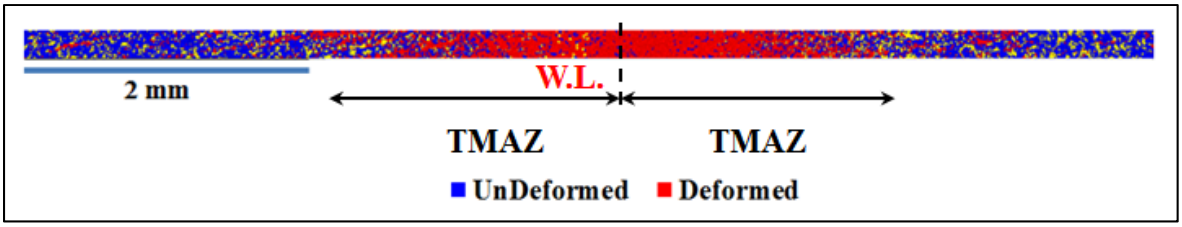

Figure 2.12 Low magnification EBSD map of the transversal cross section of the LFWed sample#4. Red zones depict deformed areas and blue areas are undeformed zones.

In Figure 2.13, the evolution of the microstructure at different locations from the weld line is presented. The LABs, HABs and Σ3 twin boundaries (within 5° tolerance) are depicted as green, black and yellow lines, respectively. At approximately 2 mm far from the weld line, LABs start to develop within parent grains or near parent grain boundaries (Figure 2.13 (a)). Therefore, this zone could be considered as the outer edge of the TMAZ. The LABs have very low misorientations, and the HAB fraction in this region is close to that of the base material. Furthermore, twin boundaries are transformed into random boundaries and their fraction is reduced from 34% to 30% and gradually disappeared from the microstructure (Figure 2.13 (b)-(f) and Table 2-2). This phenomenon is attributed to strain-induced crystallographic rotations of the twins and their surrounding matrix from their initial orientations [5].

Closer to the weld zone, LABs are observed within most of the original grains, and mostly concentrated close to the original grain boundaries. As shown in Table 2-2, the LABs fraction is significantly increased from 9% in the base material to 60% at 0.6 mm from the weld line while the twin fraction is substantially reduced from 34% in the base material to 12%. Grain boundary bulging was clearly visible in the microstructure located at 0.4-0.6 mm from the weld line, as shown in Figure 2.13 and Figure 2.14. Some of these serrated boundaries transform into fine grains indicating the occurrence of Dynamic Recrystallization (DRX) (Mironov et al., 2008). This process probably starts from L=0.8 mm, as HAB fraction in the misorientation range of 15-55° gradually increases from 17% at L=1 mm to 20% at L=0.8 mm (Table 2-2 and Figure 2.13). The average grain size at L=1 mm zone was determined to be about 25 μm.

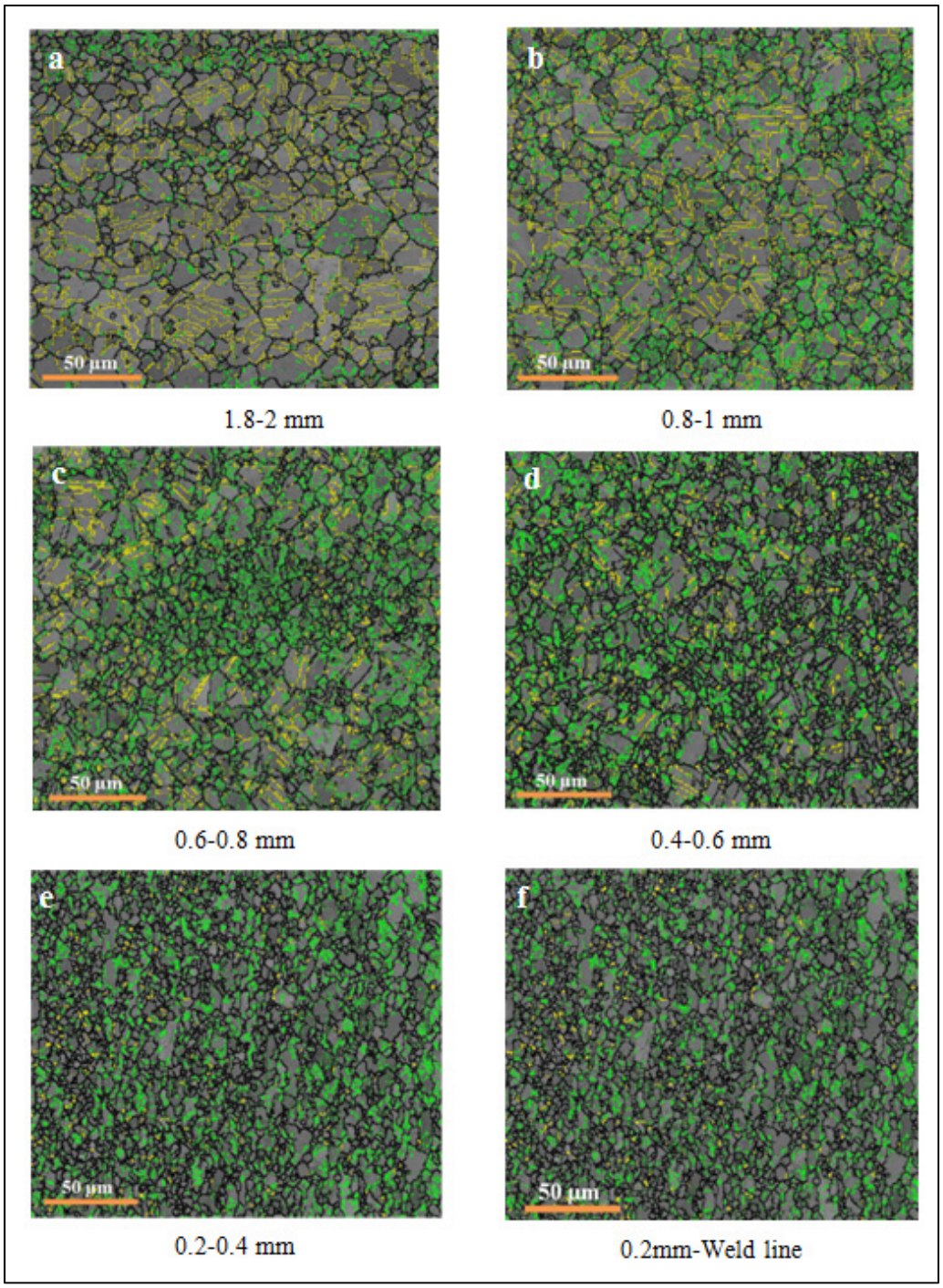

Figure 2.13 EBSD grain boundary maps showing microstructural changes of the LFWed sample#4. (a) 1.8-2mm, (b) 0.8-1mm, (c) 0.6-0.8mm, (d) 0.4-0.6mm, (e) 0.2-0.4mm from the weld interface and (f) 0.2mm to weld line. In the maps, LABs, HABs and twin boundaries are depicted as green, black and yellow lines, respectively.

Figure 2.14 EBSD grain boundary map of the LFWed sample#4; (a) 0.6 mm and (b) 0.2 mm from the weld interface showing grain boundary bulging.

HAB fraction drastically increased to 40% at L=0.4 mm and until the weld line indicating a substantial increase in the recrystallization process. Therefore, this zone was identified as the weld zone. In this zone, bulging of the grain boundaries and formation of fine grains around the original grains led to the formation of a necklace structure (Figure 2.14 (b)). The average grain size was reduced from 40 µm in the base material to about 4 µm in this zone. These fine grains are characterized by a very low dispersion in misorientation. Furthermore, twin boundaries, which made 34% of the grain boundaries of the base material were nearly absent in this zone with their fraction reducing to only 3.9% in the weld zone.

Finally, it must be noted that the observed recrystallization process was not the result of progressive movement of LAB peak toward HAB misorientations but mostly due to the building up of a wide peak near 45°, as illustrated in Figure 2.15. The above observed microstructural changes correspond very well with the main characteristics of the dynamic recrystallization phenomenon as reported by Mironov et al. (2008).

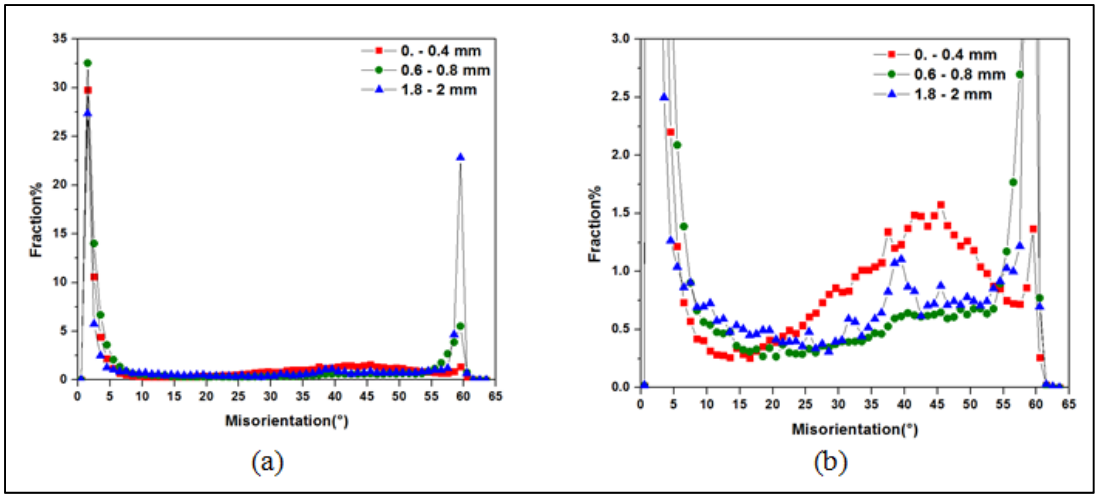

Figure 2.15 (a) Misorientation distribution in weld zone(0-0.4mm), TMAZ (0.6-0.8mm) and base metal (1.8-2mm) of the LFWed sample#4. (b) Higher magnification of (a).

2.4.2 γ′ Size and Volume Fraction Variation across the Weld

In addition to changes in grain size and misorientations in different zones of the LFW joint, significant changes were also observed and quantified in volume fraction, morphology and distribution of the γ′ phase. Figure 2.16 shows variation of γ′ size and volume fraction at different distances from the weld interface. FEG-SEM examination of the as-received AD730^{TM} alloy revealed that the material consisted of 8% primary, 26% secondary and 3% tertiary γ′ precipitates. With a decrease in distance from the weld interface, γ′ precipitates volume fraction and size decrease, as shown in Figure 2.16 (e) and (f). Secondary and tertiary γ′ precipitates began to dissolve at 2.2 mm from the interface while primary γ′ particles started to dissolve from 1 mm. The total γ′ volume fraction at 2.2 mm from the weld interface was similar to that of the parent material. This finding indicates that TMAZ width is around 4 to 4.4 mm which confirms the EBSD results shown in Figure 2.12 and Figure 2.13as well as in Table 2-2.

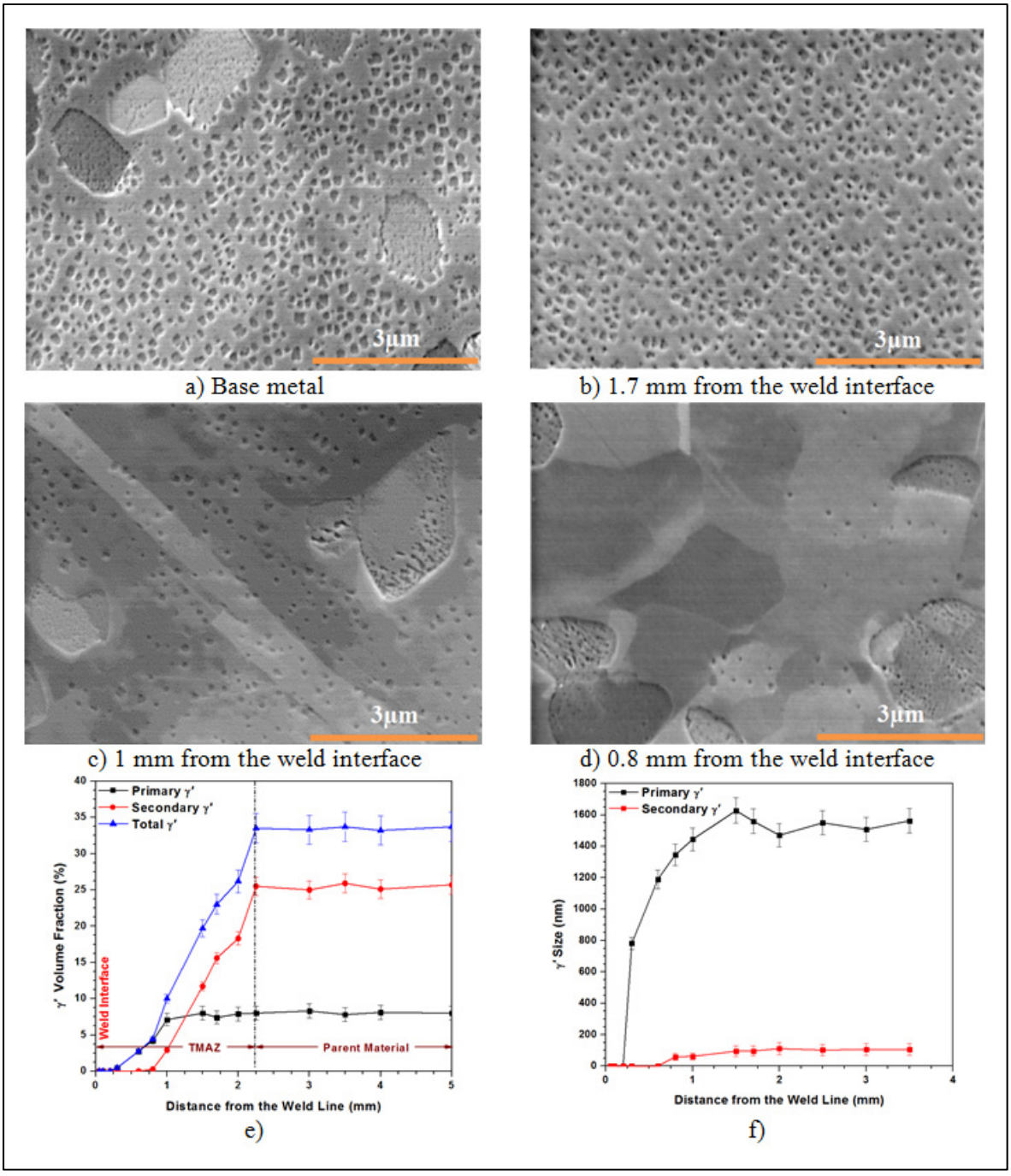

Figure 2.16 FEG-SEM images of γ′ precipitates in sample#4 (a) in the parent material, (b) to (d) respectively at 1.7, 1, and 0.8mm from the weld interface. (e) Variation of γ′ volume fraction as a function of the distance from the weld interface. (f) Average γ′ size at various distances from the weld line. The standard deviations of the γ′ volume fraction and size measurements are shown by error bars.

Secondary and primary γ′ particles were mostly dissolved at respectively 0.8 mm, and 0.2 mm from the weld interface, as shown in Figure 2.16. At the weld interface and until 100 μm from that, all γ′ precipitates were dissolved, and only a monomodal re-precipitated γ′ distribution, less than 10 nm in size, was observed in the microstructure of the as-welded specimens. The absence of primary or secondary γ′ particles at the weld line indicates that the temperature in this zone was above the γ′ solvus. Figure 2.1 shows that primary γ′ solvus is around 1200˚C at a heating rate of 400˚C/s (physically simulated heating rate at the weld interface). Therefore, weld line and until 100 μm from that (i.e. very close to the weld interface) experienced temperatures higher than 1200˚C which confirms the analytical results obtained from Eq. (2.9) for weld interface temperature.

2.5 Mechanical Properties

2.5.1 Microhardness Variation across the Weld

Microhardness profiles were obtained for LFWed samples with different heat inputs to evaluate weld strength. Figure 2.17 depicts the results of the microhardness measurements across the weld. The microhardness profiles for test condition #1 with low heat input and LFWed joint#4 with high heat input are shown in Figure 2.17 (a) and (b), respectively.

Figure 2.17 (a) (sample #1) shows that LFW with lower heat input, friction and forge pressure results in lower hardness in the weld line (425 HV) and a wider TMAZ (8.2 mm) than those of sample#4 (Hardness of 470 HV and TMAZ of around 4.3 mm). Figure 2.18 shows that grain size (20 μm) in the weld line of sample#1 is bigger than that of sample #4 (4 μm).

Based on Zener-Hollomon equations (Medeiros et al., 2000), dynamic recrystallization (DRX) grain size (d) can be correlated to process parameters of strain rate ($\dot{\varepsilon}$) and temperature (T): $Z = \dot{\varepsilon}\cdot\exp(\frac{Q}{RT})$ and $d_{DRX} = Az^{-\beta}$ where Z is the Zener-Hollomon parameter, Q activation energy and A and β are material constants. According to this equation, recrystallization is accelerated at higher temperatures. As shown in Figure 2.10, heat input (and consequently weld interface temperature) of sample #4 (6.84×10^7 W/m^2) is

higher than that of sample #1(3.192×10^7 W/m^2). In addition, forge pressure during LFW of sample #4 (580 MPa) is higher than that of sample#1 (330 MPa). It has been reported that when the forge pressure increased from P to 2.5P or 4P, DRX grain size of Waspaloy and INCONEL 738 decreased from 13.1 µm to 4 µm and from 17 µm to 5 µm, respectively (Amegadzie, 2012; Chamanfar et al., 2013). Thus, lower temperature and pressure lead to lower driving force for recrystallization and consequently, bigger grain size (20 µm) in the weld line for sample#1, as shown in Figure 2.18, compared to that of sample#4 (4 µm). Therefore, hardness of the weld line for sample#1 is lower than that of sample#4. As shown in Figure 2.17 (b), the width of TMAZ is around 4.3 mm for sample #4 (2 to 2.2 mm on either side of the weld interface), and the size of the weld zone is 0.3-0.4 mm. These findings further confirm the EBSD and microstructure analysis results shown in Figure 2.12 and Figure 2.13 and Table 2-2 for determining the size of TMAZ and weld zone.

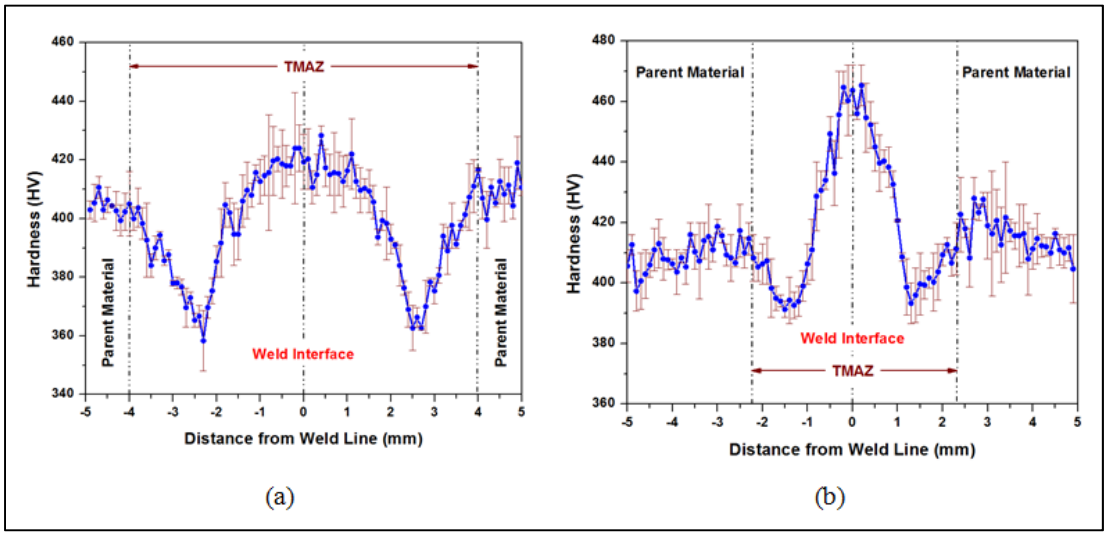

Figure 2.17 Variation in microhardness with distance from the weld line of LFWed samples produced at (a) low heat input with test condition #1 and (b) high heat input with test condition #4. The standard deviation of the microhardness measurement is shown by error bars.

Two symmetrically hardness zones are observed on either side of the TMAZ. At 1 mm from the weld interface, the hardness decreased from 470 to 387 HV (Figure 2.17(b). This drop in hardness can be correlated to the evolution of γ′ volume fraction across

the weld (Figure 2.16). As shown in Figure 2.16, secondary γ′ volume fraction which is most effective in increasing the hardness (Monajati et al., 2004b) decreases from 26% in the base material to 2.9% at 1 mm from the weld interface, and lower portion of γ′ particles reprecipitates compared to those of weld metal. This abrupt change is probably the root cause for the observed decrease in the microhardness level. On the other hand, Figure 2.17 (b) shows that with a decrease in the distance from the LFW interface, the microhardness increases gradually. This is probably due to γ′ reprecipitation (see chapter 6) and the partially refined grain structure, as shown in Figure 2.13. Figure 2.17 (b) shows that LFW leads to significant increase in the weld hardness as the hardness of the parent material at 1 mm from the LFW interface increases from 387 to 470 HV at the weld interface. Based on Figure 2.13, this increase can be attributed to grain refinement of the material decreasing from 25 μm to 4 μm at the weld interface during LFW and γ′ reprecipitation.

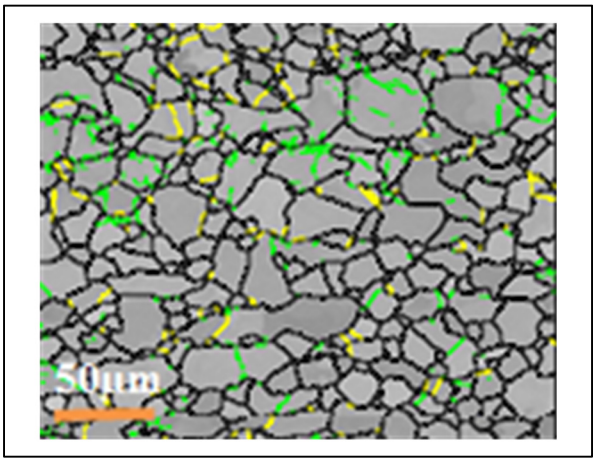

Figure 2.18 EBSD grain boundary map of the LFWed sample#1 at the weld interface.

Furthermore, it is important to note that the TMAZ width in sample#4 is smaller than that of sample#1. This finding could be explained in terms of the processing conditions of sample#4. The higher heat input results in more heating and therefore more softening to occur in sample#4 compared to sample#1. In addition, the higher forge pressure of 580 MPa in this sample provides more extrusion of the softened material as flash from the weld interface. The combination of these two phenomena results in smaller TMAZ width in sample#4. Similar

trend in TMAZ reduction due to increasing forge pressure has been observed for Waspaloy and INCONEL 738 (Amegadzie, 2012; Chamanfar et al., 2012a).

2.5.2 Mechanical Properties of as-welded and Post Weld Heat Treated (PWHTed) Samples

As a criterion, it was considered that a defect-free and sound LFW joint was produced when its tensile strength at room and high temperatures was higher than the ultimate tensile strength of the base material. In this case, fracture of the welded joint should appear far from the weld zone. Accordingly, the quality of the LFWed sample was evaluated by performing tensile tests at room and elevated temperatures.

It has been reported that by increasing axial shortening, the yield and ultimate tensile strengths at room temperature increase (Chamanfar et al., 2012a; Wanjara et Jahazi, 2005). Therefore, in the present investigation, the weld joint with the maximum axial shortening corresponding to the highest amount of heat input (i.e. sample#4) was studied.

The as-welded samples were subjected to solution treatment and aging before tensile testing. Solutionizing was carried out in two steps: initially the samples were heated to 900˚C and held for 2 hours. Then, they were heated at 0.15˚C/s to 1080˚C, held at this temperature for 4 hours followed by air cooling. The aging treatment was conducted at 730˚C for 8 hours followed by air cooling. The average grain size in the weld interface was about 8 μm after PWHT, as shown in Figure 2.19. This grain size is nearly twice the size of the grains in as welded samples. This increase could be associated with the dissolution of the primary γ′ particles at the weld line, thereby facilitating the grain growth during PWHT in this zone, as demonstrated in Figure 2.19.

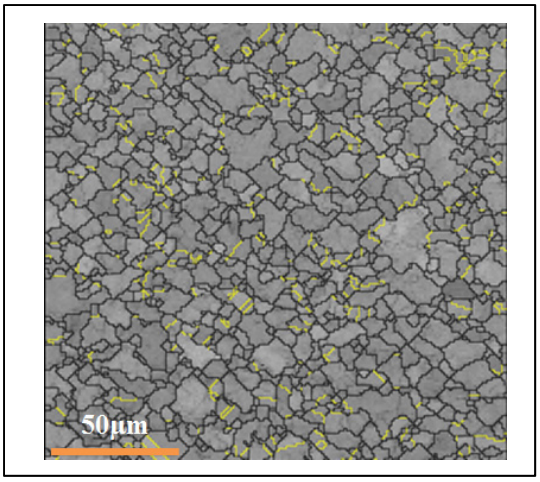

Figure 2.19 EBSD grain boundary map
of the LFWed sample#4 after PWHT.

The configuration of tensile test specimens inside LFWed sample and its geometry are reported in Figure 2.20. The specimens were machined in such a way that the LFWed joint interface was located in the middle of the gauge length and perpendicular to the tension axis. Tensile tests were carried out at 20°C and 650°C using a constant strain rate of $10^{-3}s^{-1}$ on an electromechanical "Insrton8562" machine. Sample temperature was controlled using S-type thermocouples and the gauge of the specimen was measured. During hot tensile tests, the temperature difference between the programmed and the actual sample was within ±1°C.

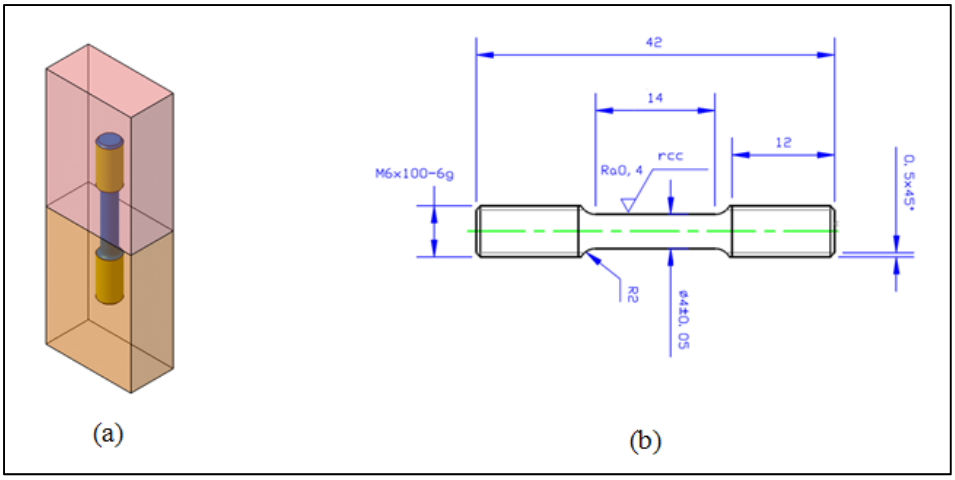

Figure 2.20 Configuration of (a) tensile specimen inside LFWed sample and (b) specimen geometry for tensile tests according to ASTM A370 standard (all dimensions are in mm).

Fractured samples after room and hot tensile tests on the PWHT joint#4 are shown in Figure 2.21. Macroscopic examination revealed that both specimens were failed out of the weld zone.

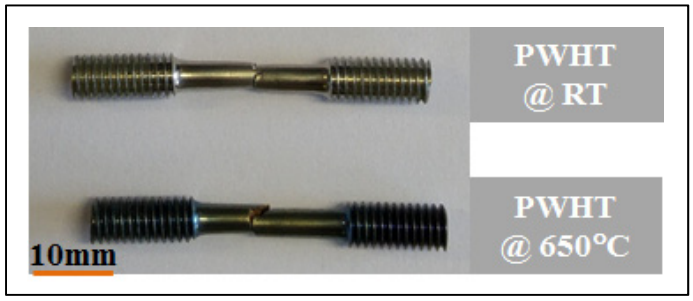

Figure 2.21 Fractured PWHT tensile samples of jonit#4 at room temperature (RT) and 650 °C.

Tensile properties at room and elevated temperatures of the base material as well as PWHT joint are given in Table 2-3. These data are the mean value of three tensile experiments.

Table 2-3 Room and elevated tensile properties

Specimen	Test Temperature(ºC)	Yield Strength(MPa)	Ultimate Tensile Strength(MPa)	Elongation (%)
Base Material	20	1247±20	1587±18	20.0±3
	650	1116±15	1362±16	22.0±3
PWHTed Sample#4	20	1264±19	1911±8	22.1±2
	650	1162±17	1647±6	24.7±2
As-LFWed Sample#4	20	961±5	1781±12	22.3±3
	650	936±7	1447±10	23.2±3

Figure 2.22 displays tensile stress-strain curves for LFWed samples before and after post weld heat treatment at room temperature and 650°C. As shown in Figure 2.22 and Table 2-3, tensile properties improved after subjecting welded specimens to post weld heat treatment. Table 2-3 shows that the as-welded joints have lower yield strength but higher ultimate tensile strength than those of the base material. Microstructural examination results reported in Figure 2.16 showed that secondary γ′ precipitates started to dissolve at 2 mm from the weld line until the weld interface, due to high temperatures experienced by this zone during LFW. On the other hand, it was found (see chapter 6) that γ′ particles (in the range of a few nanometers) reprecipitated in the weld interface after LFW during cooling in higher portion than those of TMAZ. Therefore, the observed higher strength of the weld zone compared to TMAZ in the present work, is probably due to higher portion of γ′ reprecipitates and the fine grain microstructure, as shown in Figure 2.13 and Figure 2.17 (b). Thus, TMAZ should be the region which experiences cracking and failure during tensile tests at 650°C of the as-welded specimens due to dissolution of strengthening precipitates and lower level of reprecipitated γ′ particles.

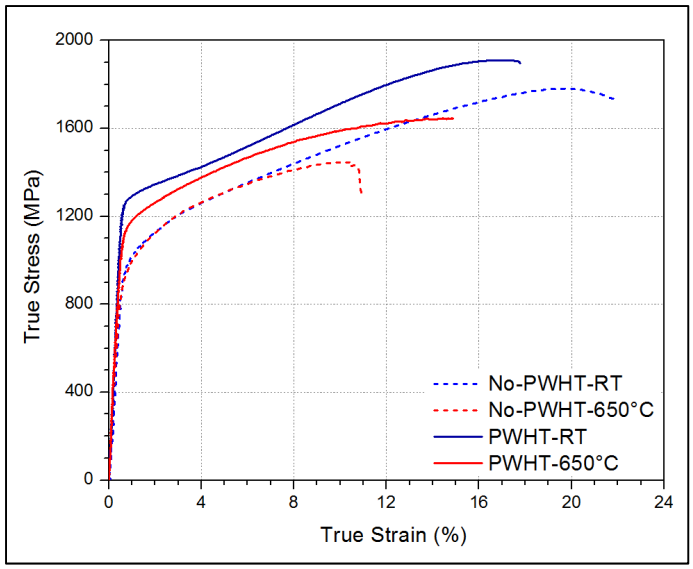

Figure 2.22 Stress-strain curves of the LFWed sample #4 before and after heat treatment.

Yield and ultimate tensile strengths of the PWHTed sample at room temperature and 650°C show higher values than those of the base material. For example, the yield strength of the PWHTed sample tested at 650°C is about 46MPa higher than that of the base material. In addition, fracture strength of PWHTed sample is approximately 285MPa more than the ultimate strength of the base material tested at 650°C. Such behavior is indicative of forming a good joint in this sample.

The grain size in the weld region of the sample is 8μm after PWHT which is 5 times finer than that of the base metal (40 μm). Therefore, the defect-free joint with dynamically recrystallized grains in the weld zone in this sample subjected to PWHT led to higher ultimate tensile strength. In addition, as shown in Figure 2.23, PWHT leads to reprecipitation of γ′ particles in the TMAZ and restores tensile properties of the LFWed joints. Thus, after PWHT, all LFWed specimens failed in the base material.

The fracture surfaces of the samples in PWHT condition were examined, and the findings are discussed in details as follows.

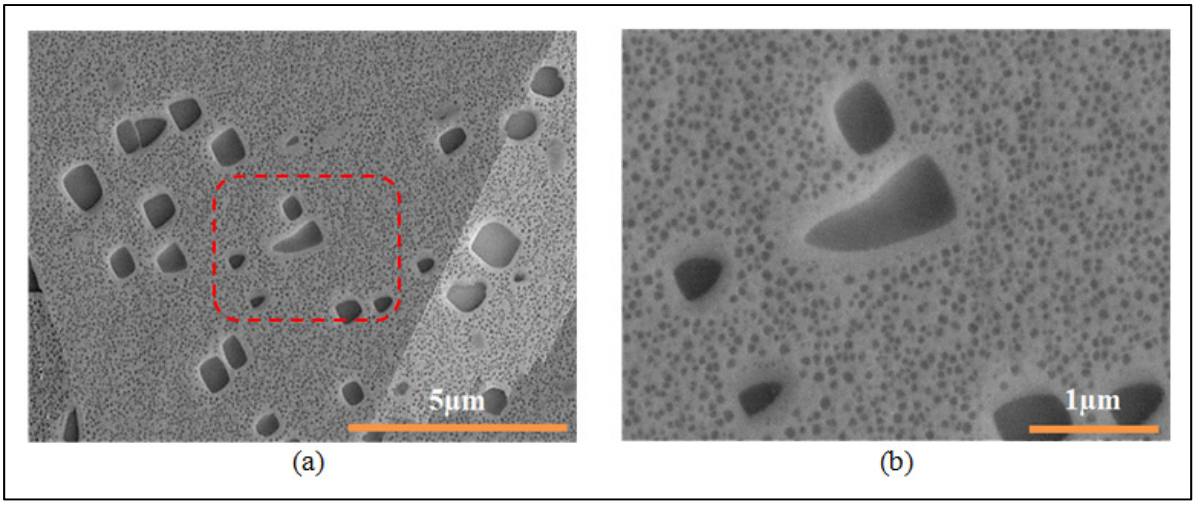

Figure 2.23 FEG-SEM images γ' particles of the LFWed sample #4 after PWHT
(a) at 1mm from the weld interface, (b) higher magnification of the inset(red box) in (a).

2.5.2.1 Fracture Surface of Tested Samples in PWHT Condition

The fractograhic features of the tensile tested specimens at room temperature and 650˚C are shown in Figure 2.24 and Figure 2.25, respectively. Figure 2.24 shows that the fracture surface is almost flat and dark at the center of the sample while it is bright and orientated at ±45˚ to the fracture surface at the edges. Higher magnification of the flat surface (Figure 2.24 (a)) shows dimples on fractured area, indicative of a ductile type fracture.

More detailed analysis of the fractured specimen and fracture surface (Figure 2.21 andFigure 2.24) revealed that failure initiated in the base material during tensile testing at room temperature. Final fracture occurred in zones adjacent to the TMAZ, by shearing at ±45˚ to the tensile axis.

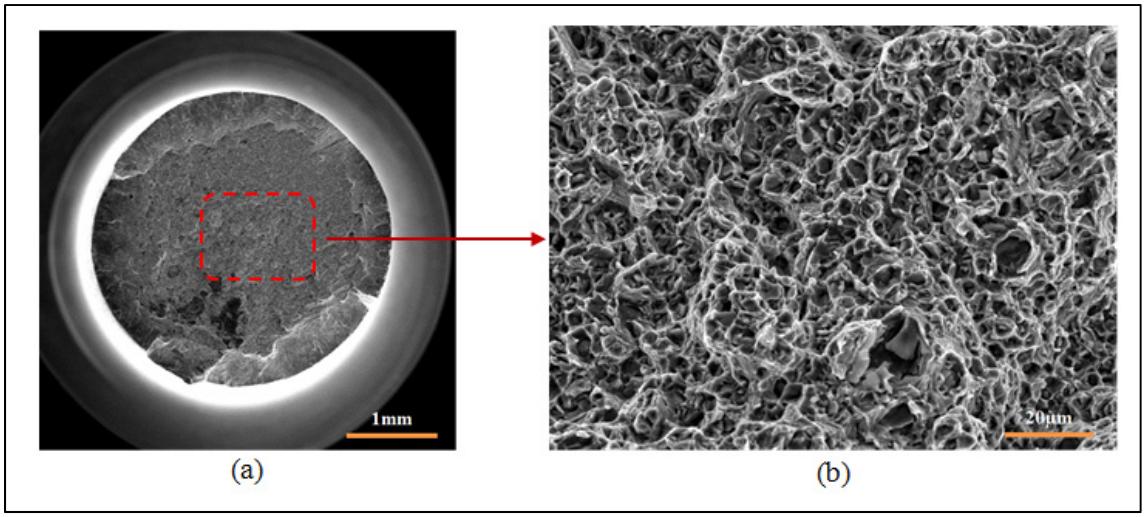

Figure 2.24 (a) Macrofractograph of the fractured surface at room temperature. The central portion of the fracture is slightly flat and 45° shear lips surround this region. (b) Higher-magnification view of the selected area (red box) at the center of the specimen which consists of equiaxed dimples formed during ductile rupture.

Figure 2.25 shows the fracture surface of the sample tested under tensile stress at 650°C. The surface is characterized by flat regions of shallow dimples (Figure 2.25 (b)), indicative of ductile fracture. The crack propagation is transgranular, and occurs in the parent material, as shown in Figure 2.25 (c). The presence of primary γ′ precipitates, as marked by orange arrows in Figure 2.25 (c), and topography of the fracture surface is consistent with a transgranular fracture. Two portions of the fracture surface next to the edge of the sample, shown by black arrows, are slanted suggesting a shear lip (Figure 2.25 (a)). Therefore, the final fracture occurs by shear, one side in the parent material and the other side in the weld zone.

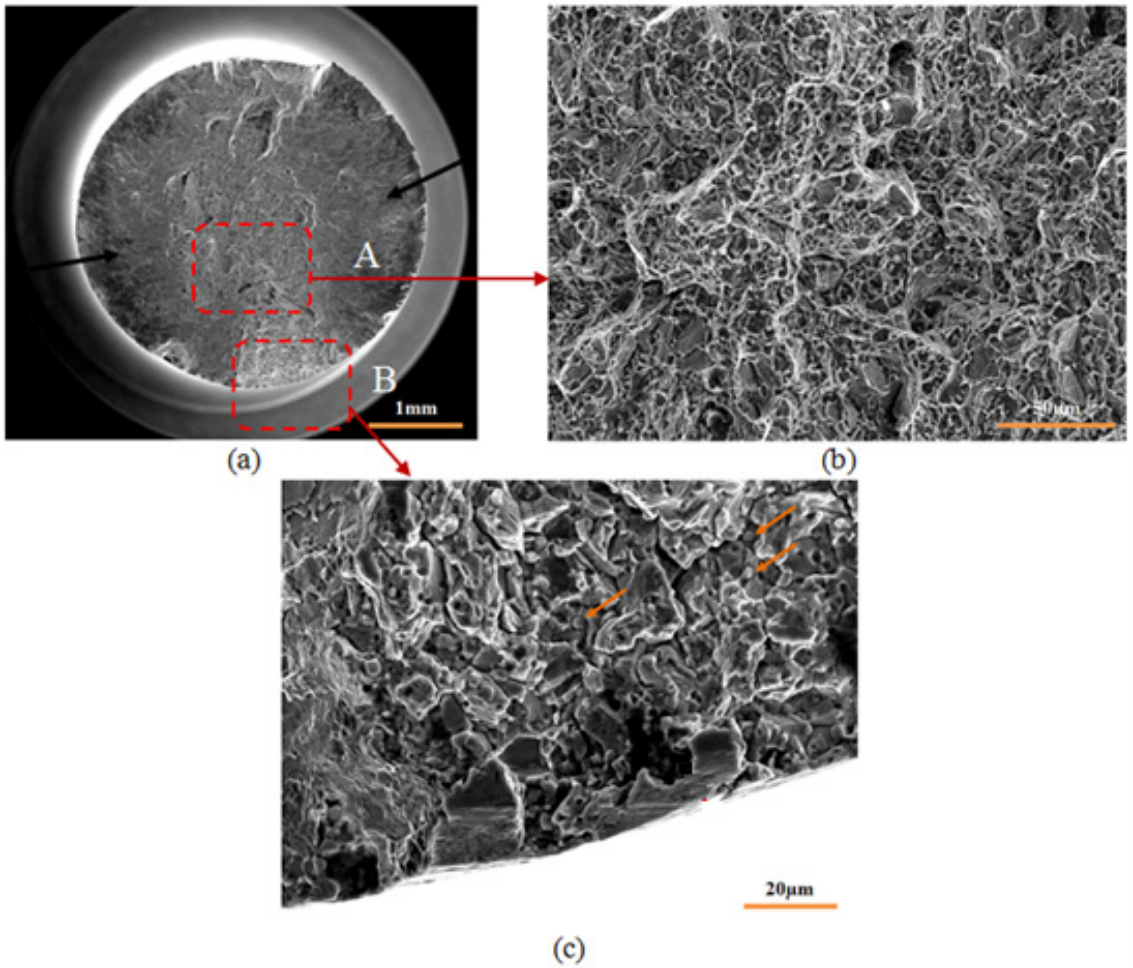

Figure 2.25 (a) Macrofractograph of the fractured surface at 650°C. Shear lips observed at 45° to the stress axis are indicated by black arrows. (b) Magnified view of a flat area from region A (inset in (a)). Ductile dimple rupture is the fracture mode. (c) Typical features of region B (inset in (a)) which consists of γ′ particles (orange arrows) in the fracture surface.

2.5.3 Conclusions

1- The proposed analytical method was validated by experiments, and a good agreement was obtained between the predicted axial shortening and the experiments. Therefore, the simplified robust and reliable analytical approach can allow for rapid determination of the optimum LFW process parameters for AD730^{TM} alloy. The proposed methodology can be applied to other materials.

2- The different zones of LFWed joints were determined and the evolution of their microstructure and microhardness as a function of processing parameters was related to fundamental metallurgical processes.

3- Yield and ultimate tensile strengths of the PWHTed samples at room temperature and 650°C showed values higher than those of the as-welded samples indicating that a PWHT is necessary after LFW of AD730™ superalloy.

4- Macroscopic examination of room and high temperature PWHTed tensile samples showed that both specimens failed out of the weld zone. Tensile strengths of the PWHTed samples showed higher values than those of the base material at room temperature and 650°C, further demonstrating the appropriate selection of processing parameters for obtaining a sound LFW joint, proposed in the present investigation.

References

Addison, A. C. 2010. *Linear Friction Welding Information for Production Engineering*. Cambridge, U.K.: TWI industrial members report — 961/2010.

Altan, T., G. Ngaile et G. Shen. 2005. *Cold and Hot Forging: Fundamentals and Applications*. ASM International, 342 p.

Amegadzie, M. Y. 2012. « Effect of Forging Pressure on the Microstructure of Linear Friction Welded Inconel 738 Superalloy ». Canada, University of Manitoba.

Bergman, T. L., et F. P. Incropera. 2011. *Fundamentals of Heat and Mass Transfer*. John Wiley & Sons.

Buffa, G., et L. Fratini. 2017. « Strategies for Numerical Simulation of Linear Friction Welding of Metals: A Review ». *Production Engineering,* vol. 11, nº 3, p. 221-235.

Chamanfar, A., M. Jahazi et J. Cormier. 2015b. « A Review on Inertia and Linear Friction Welding of Ni-Based Superalloys ». *Metallurgical and Materials Transactions A,* vol. 46, nº 4, p. 1639-1669.

Chamanfar, A., M. Jahazi, J. Gholipour, P. Wanjara et S. Yue. 2011a. « Mechanical Property and Microstructure of Linear Friction Welded Waspaloy ». *Metallurgical and Materials Transactions A,* vol. 42, nº 3, p. 729-744.

Chamanfar, A., M. Jahazi, J. Gholipour, P. Wanjara et S. Yue. 2012a. « Maximizing the Integrity of Linear Friction Welded Waspaloy ». *Materials Science and Engineering: A,* vol. 555, p. 117-130.

Chamanfar, A., M. Jahazi, J. Gholipour, P. Wanjara et S. Yue. 2013. « Modeling Grain Size and Strain Rate in Linear Friction Welded Waspaloy ». *Metallurgical and Materials Transactions A,* vol. 44, nº 9, p. 4230-4238.

Cormier, J., et G. Cailletaud. 2010b. « Constitutive Modeling of the Creep Behavior of Single Crystal Superalloys under Non-Isothermal Conditions Inducing Phase Transformations ». *Materials Science and Engineering: A,* vol. 527, nº 23, p. 6300-6312.

Cormier, J., X. Milhet et J. Mendez. 2007b. « Non-Isothermal Creep at Very High Temperature of the Nickel-Based Single Crystal Superalloy MC2 ». *Acta Materialia,* vol. 55, nº 18, p. 6250-6259.

Damodaram, R., S. Ganesh Sundara Raman et K. Prasad Rao. 2014a. « Effect of Post-Weld Heat Treatments on Microstructure and Mechanical Properties of Friction Welded Alloy 718 Joints ». *Materials & Design,* vol. 53, p. 954-961.

Devaux, A., B. Picque, M. F. Gervais, E. Georges, T. Poulain et P. Heritier. 2012b. « AD730™ -A New Nickel-Based Superalloy for High Temperature Engine Rotative Parts ». In *12th International Symposium on Superalloys, Superalloys 2012, September 9, 2012 - September 13, 2012*. (Seven Springs, PA, United states), p. 911-919. Coll. « Proceedings of the International Symposium on Superalloys »: Minerals, Metals and Materials Society.

Dieter, G. E., H. A. Kuhn et S. L. Semiatin. 2003. *Handbook of Workability and Process Design*. ASM International, Materials Park, Ohio, USA.

Dixit, U. S., S. N. Joshi et J. P. Davim. 2011. « Incorporation of Material Behavior in Modeling of Metal Forming and Machining Processes: A Review ». *Materials & Design,* vol. 32, n° 7, p. 3655-3670.

Grong, O. 1997. *Metallurgical Modelling of Welding*, Second Edition. Institute of Materials, 605 p.

Hosford, W. F., et R. M. Caddell. 2014. *Metal Forming: Mechanics and Metallurgy*. Cambridge University Press, 344 p.

Jiang, H., J. Dong, M. Zhang, L. Zheng et Z. Yao. 2015. « Hot deformation Characteristics of Alloy 617B Nickel-Based Superalloy: A study Using Processing Map ». *Journal of Alloys and Compounds,* vol. 647, n° Supplement C, p. 338-350.

le Graverend, J. B., J. Cormier, M. Jouiad, F. Gallerneau, P. Paulmier et F. Hamon. 2010b. « Effect of Fine γ′ Precipitation on Non-Isothermal Ceep and Creep-Fatigue Behaviour of Nickel Base Superalloy MC2 ». *Materials Science and Engineering: A,* vol. 527, n° 20, p. 5295-5302.

Li, W., A. Vairis, M. Preuss et T. Ma. 2016. « Linear and Rotary Friction Welding Review ». *International Materials Reviews,* vol. 61, n° 2, p. 71-100.

Li, W., F. Wang, S. Shi et T. Ma. 2014. « Numerical Simulation of Linear Friction Welding Based on ABAQUS Environment: Challenges and Perspectives ». *Journal of Materials Engineering and Performance,* vol. 23, n° 2, p. 384-390.

Lin, Y. C., et X. M. Chen. 2011. « A Critical Review of Experimental Results and Constitutive Descriptions for Metals and Alloys in Hot Working ». *Materials & Design,* vol. 32, n° 4, p. 1733-1759.

Lindgren, L. E. 2006. « Numerical Modelling of Welding ». *Computer Methods in Applied Mechanics and Engineering,* vol. 195, nº 48, p. 6710-6736.

Maalekian, M. 2007. « Friction Welding – Critical Assessment of Literature ». *Science and Technology of Welding and Joining,* vol. 12, nº 8, p. 738-759.

Medeiros, S. C., Y. V. R. K. Prasad, W. G. Frazier et R. Srinivasan. 2000. « Microstructural Modeling of Metadynamic Recrystallization in Hot Working of IN 718 Superalloy ». *Materials Science and Engineering: A,* vol. 293, nº 1, p. 198-207.

Mironov, S., Y. Zhang, Y. S. Sato et H. Kokawa. 2008. « Development of Grain Structure in β-Phase Field during Friction Stir Welding of Ti–6Al–4V Alloy ». *Scripta Materialia,* vol. 59, nº 1, p. 27-30.

Monajati, H., M. Jahazi, R. Bahrami et S. Yue. 2004b. « The Influence of Heat Treatment Conditions on γ′ Characteristics in Udimet® 720 ». *Materials Science and Engineering: A,* vol. 373, nº 1, p. 286-293.

Ola, O. T., O. A. Ojo et M. C. Chaturvedi. 2013b. « Effect of Deformation Mode on Hot Ductility of a γ′ Precipitation Strengthened Nickel-Base Superalloy ». *Materials Science and Engineering: A,* vol. 585, p. 319-325.

Senkov, Oleg N., David W. Mahaffey, S. Lee Semiatin et Christopher Woodward. 2014. « Inertia Friction Welding of Dissimilar Superalloys Mar-M247 and LSHR ». *Metallurgical and Materials Transactions A,* vol. 45, nº 12, p. 5545-5561.

Shahriari, D., M. H. Sadeghi, A. Akbarzadeh et M. Cheraghzadeh. 2009a. « The Influence of Heat Treatment and Hot Deformation Conditions on γ′ Precipitate Dissolution of Nimonic 115 Superalloy ». *The International Journal of Advanced Manufacturing Technology,* vol. 45, nº 9, p. 841.

Turner, R., J. C. Gebelin, R. M. Ward et R. C. Reed. 2011b. « Linear Friction Welding of Ti–6Al–4V: Modelling and Validation ». *Acta Materialia,* vol. 59, nº 10, p. 3792-3803.

Turner, R., F. Schroeder, R. M. Ward et J. W. Brooks. 2014. « The Importance of Materials Data and Modelling Parameters in an FE Simulation of Linear Friction Welding ». *Advances in Materials Science and Engineering,* vol. 2014, p. 8.

Vairis, A., et M. Frost. 1999b. « On the Extrusion Stage of Linear Friction Welding of Ti 6Al 4V ». *Materials Science and Engineering: A,* vol. 271, nº 1, p. 477-484.

Vairis, A., G. Papazafeiropoulos et A. M. Tsainis. 2016. « A Comparison between Friction Stir Welding, Linear Friction Welding and Rotary Friction Welding ». *Advances in Manufacturing,* vol. 4, nº 4, p. 296-304.

Viswanathan, G. B., R. Shi, A. Genc, V. A. Vorontsov, L. Kovarik, C. M. F. Rae et M. J. Mills. 2015. « Segregation at Stacking Faults within the γ′ Phase of two Ni-Base Superalloys Following Intermediate Temperature Creep ». *Scripta Materialia,* vol. 94, p. 5-8.

Wang, J., J. Dong, M. Zhang et X. Xie. 2013. « Hot Working Characteristics of Nickel-Base Superalloy 740H during Compression ». *Materials Science and Engineering: A,* vol. 566, nº Supplement C, p. 61-70.

Wang, Y., W. Z. Shao, L. Zhen et B. Y. Zhang. 2011b. « Hot Deformation Behavior of Delta-Processed Superalloy 718 ». *Materials Science and Engineering: A,* vol. 528, nº 7, p. 3218-3227.

Wanjara, P., et M. Jahazi. 2005. « Linear Friction Welding of Ti-6Al-4V: Processing, Microstructure, and Mechanical-Property Inter-Relationships ». *Metallurgical and Materials Transactions A,* vol. 36, nº 8, p. 2149-2164.

Yang, X., W. Li, J. L. Li, B. Xiao, T. Ma, Z. Huang et J. Guo. 2015. « Finite Element Modeling of the Linear Friction Welding of GH4169 Superalloy ». *Materials & Design,* vol. 87, nº Supplement C, p. 215-230.

Yang, X., W. Li, J. Ma, S. Hu, Y. He, L. Li et B. Xiao. 2016. « Thermo-Physical Simulation of the Compression Testing for Constitutive Modeling of GH4169 Superalloy during Linear Friction Welding ». *Journal of Alloys and Compounds,* vol. 656, p. 395-407.

Yilbas, B. S., et A. Z. Sahin. 2014. *Friction Welding: Thermal and Metallurgical Characteristics*. Springer Science & Business Media.

CHAPITRE 3

ARTICLE 1: COARSENING AND DISSOLUTION OF γ′ PRECIPITATES DURING SOLUTION TREATMENT OF AD730™ NI-BASED SUPERALLOY: MECHANISMS AND KINETICS MODELS

F. Masoumi[a] , M. Jahazi[a], D. Shahriari[a], J. Cormier[b]

[a] Department of Mechanical Engineering, École de Technologie Supérieure (ETS), H3C 1K3, Montreal, QC, Canada
[b] Institute Pprime, UPR CNRS 3346, Physics and Mechanics of Materials Department, ISAE- ENSMA, BP 40109, Futuroscope- Chasseneuil Cedex 86961, France

This article has been published in the Journal of Alloys and Compounds in November, 2015

3.1 Abstract

The kinetics of γ′ size and volume fraction changes during solution treatment of the advanced Ni-based superalloy, AD730™ are determined and the underlying mechanisms are investigated. High resolution Differential Thermal Analysis (DTA) and thermodynamic modeling were used to design and perform solution heat treatment experiments. Semi-analytical models are developed to describe the dissolution and coarsening processes. The results from the proposed models, supported by electron microscopy observations, indicate that coarsening occurs before complete dissolution takes place. Agglomeration is shown to be the governing coarsening mechanism for this alloy after calculation of the coefficients for both the Ostwald ripening and agglomeration mechanisms. Electron microscopy observations revealed that the early stages of agglomeration occur by neck formation between two neighboring particles. The splitting of γ′ particles was identified as one of the main dissolution mechanisms. Based on the obtained results, a dissolution kinetics model is proposed to quantify the volume fraction of dissolved γ′ particles and estimate the activation energy of this process for AD730™. A coarsening model based on the time-temperature dependence of the γ′ coarsening rate coefficient is also proposed taking the concentration of elements, γ′ volume fraction and the temperature into consideration. Based on this model, a method is developed to predict γ′ size evolution during aging heat treatment process and an optimum heat treatment to reach the desired γ′ distribution is proposed. The validity and

accuracy of the proposed models were verified by carrying out different heat treatment experiments.

Keywords: Ni-based Superalloys; AD730^{TM}; γ′ Phase Dissolution; γ′ Phase Coarsening; Semi-Analytical Modeling; Activation energy

3.2 Introduction

Thermomechanical processes such as rolling, forging, machining and friction welding involve substantial microstructural changes including dissolution and subsequent re-precipitation of γ′ precipitates in Ni-based superalloys. These changes play a key role in controlling the mechanical properties of these alloys. The thermal cycle (heating rate, temperature, and holding time) in addition to accumulated plastic strain and applied stress were found to enhance γ′ dissolution rate in Ni-based superalloys (Cormier, Milhet et Mendez, 2007a; Giraud et al., 2013; Shahriari, Sadeghi et Akbarzadeh, 2009; Shahriari et al., 2009b). Out of the parameters listed above, the heating stage plays a major role in determining optimum processing parameters. In addition, in thermal processes such as aging and creep, dissolution and coarsening of γ′ have a determining effect in property evolution. Therefore, γ′ size and volume fraction are critical inputs for models of mechanical behavior and microstructure evolution (Cormier et Cailletaud, 2010a; Le Graverend et al., 2014; Payton, 2008). For reliable and accurate kinetics models to be developed, it is necessary to better understand the underlying mechanisms governing γ′ phase evolution during solution heat treatment (SHT).

After solutionizing, aging is carried out to achieve a controlled γ′ phase re-precipitation (Fuchs, 2001). Although γ′ reprecipitation during isothermal aging or continuous cooling in Ni-based superalloys has been the subject of extensive research works (Monajati et al., 2004a; Radis et al., 2009; Singh et al., 2013; Wen et al., 2006), much less attention has been paid to the dissolution kinetics during the heating stage (Cormier, Milhet et Mendez, 2007a; Wang et al., 2009). Hence, the main objective of this research is to accomplish a time and temperature dependent study concerning the evolution of the γ′ phase during the heating stage of the solution heat treatment process.

Theoretically, as suggested by Semiatin et al. (2004), the homogenizing should be performed between γ′ solvus and the solidus temperature of the alloy in order to entirely dissolve γ′ and other phases. This approach also removes chemical non-uniformity formed during previous preparation processes. However, solution heat treatments at temperatures high enough to dissolve all the primary γ′ particles have been seriously limited in various superalloys due to the occurrence of incipient melting (Ojo, Richards et Chaturvedi, 2004b). To elucidate the influence of the solutionizing temperature on γ′ dissolution kinetics and eliminate possible microstructural damage, both subsolvus and near solvus heat treatments are used in the present investigation.

Thomas et al. (1961) presented a theory on the dissolution kinetics of a single precipitate in which dissolution was considered to be approximately the reverse of growth. However, Whelan mentioned that this assumption was not fully accurate (Whelan, 1969). Lifshitz, Slyozov, and Wagner (LSW) (1961) proposed an analytical theory describing diffusion-limited coarsening (or Ostwald ripening) of isolated precipitates. The LSW theory is based on the Gibbs-Thomson equation, which describes that solubility in the small precipitates with a large surface area-to-volume ratio is higher than that for larger precipitates. The larger precipitates, therefore, tend to grow at the expense of the smaller ones to decrease the total interfacial free energy of the alloy. Umantsev, Olson (1993) and Philippe et al. (2013) expanded the LSW theory to multicomponent systems.

Coarsening and coalescence of γ′ precipitates, through application of the LSW theory and particle agglomeration mechanism have been studied in several research works (Mao et al., 2007; Wang et al., 2008). However, the contributions of these two mechanisms to the dissolution process have not yet been identified nor quantified. Whelan et al. (1969) developed an analytical solution for the dissolution of a *single precipitate* under assumptions of stationary interface. This solution can be considered as one of the most accurate analytical solutions to date. However, in real systems, precipitates are often close to each other making it reasonable to assume that some impingement of diffusion fields of neighboring precipitates takes place (Ferro, 2013). This assumption was not taken into account in the Whelan model.

In the present study, this aspect is addressed and a model which considers multiple precipitates is presented for dissolution kinetics and validated after a series of experiments.

Wang et al. (2009) developed a model to study the influence of initial particle size distribution (PSD) on the dissolution rate of Ni-Al alloys (above the solvus) by using 3D phase field simulations. A critical review of this work indicates that during dissolution the volume fraction of particles decays exponentially with time and while the initial PSD does not affect this trend, the dissolution rate is strongly dependent on PSD. However, computer based simulation methods are generally associated with long computation times and large and expensive infrastructures, particularly when it comes to simulating the behavior of industrial size components. Many physical constants such as element diffusion coefficients, surface energies, interface kinetic coefficients and driving forces for phase transformations are needed for obtaining reliable results. However, this data is not always readily available for alloys with complex compositions (Kovačević et Šarler, 2005). The situation becomes even more complicated when a new alloy, such as the one used in the present investigation, is considered.

Semi-analytical models calibrated by experiments were proposed to address this problem. These models are widely used for characterizing phase precipitation under isothermal and non-isothermal conditions (Ferro et Bonollo, 2012; Lee et Kim, 1990) but to the knowledge of the authors, no such models exist for the identification and quantification of the dissolution mechanisms during the solution heat treatment process of Ni-based superalloys. In addition, AD730^{TM} is a newly developed Ni-based superalloy for turbine disk applications with reported superior service properties at 700°C (Bellot et Lamesle, 2013; Devaux et al., 2012a; Masoumi et al., 2014). However, many of its properties are unknown for advanced manufacturing applications and especially no quantitative data is available on γ′ dissolution kinetics in AD730^{TM}.

On the basis of the previous analysis, the objectives of this study are three fold:
1- To identify the dissolution temperatures for different populations of γ′ by DTA, Thermo-calc® and heat treatment for AD730^{TM} alloy.

2- To quantify and analyze size distribution and morphology evolution of γ′ precipitates during dissolution process using electron microscopy and image analysis.
3- To propose and validate semi-analytical models for dissolution and coarsening kinetics and calculate the partitioning contribution of various coarsening mechanisms during γ′ dissolution process.

Research results will help to develop a better understanding of fundamental mechanisms governing γ′ dissolution in Ni-based superalloys.

3.3 Coarsening by agglomeration

Smoluchowski (1916) proposed that the agglomeration process can be modeled as an infinite set of second-order reactions. Smaller particles combine to form larger particles, and dissociation is not considered. The rate of change in number density of particle size distribution is given by:

$$\frac{\partial f}{\partial t} = \frac{1}{2}\int_0^v W(v', v-v')f(v',t)f(v-v',t)dv' - f(v,t)\int_0^\infty W(v',v)f(v',t)dv' \quad (3.1)$$

where $f(v,t)dv$ is the number density of precipitates per unit volume with particles volumes in the range of v, $v+dv$ and where $W(v',v)$ is the volume of the agglomerated particle.
The first term describes the coalescence of precipitates whose volumes are respectively $v-v'$ and v'. Merging upon contact, the two particles become one, the resulting volume equal to v. The second term describes the annihilation of the precipitates with volume of v through diffusion. After some manipulation Eq. (3.1) gives (Thompson, 1968):

$$\frac{dn}{\partial t} = -\frac{1}{2}\int_0^\infty \int_0^\infty W(v',v)\, f(v',t)f(v,t)dv'dv \quad (3.2)$$

where $n(t)$ is the number density of the particles and $n(t) = \int f(v,t)\ dv$.

To obtain the growth law for a particle with an average radius r_0, Eq. (3.2) can be simplified by considering $W(v', v) \approx \bar{W}$ that is the average volume of an agglomerated particle (Ratke, 1987; 1995):

$$\frac{dn}{dt} = -\frac{1}{2}\bar{W}n(t)^2 \tag{3.3}$$

Eq. (3.3) shows that particle density in the agglomeration reaction decays with time. The solution to this equation is:

$$n(t) = \frac{n_0}{1 + \frac{1}{2}n_0\bar{W}\,t} \tag{3.4}$$

where n_0 is the initial density of particles. Since agglomeration does not change the volume concentration of precipitates, $n_0\bar{v}_0 = n(t)\bar{v}$ (t) or:

$$\frac{4}{3}\pi\bar{r}_0^3 n_0 = \frac{4}{3}\pi\overline{r(t)}^3 n(t) \tag{3.5}$$

So, the change in the average particle radius is:

$$\overline{r(t)}^3 - \bar{r}_0^3 = \frac{1}{2}n_0\bar{r}_0^3\bar{W}\,t = K_{agg}t \tag{3.6}$$

Since the growth law is similar to that of the Ostwald ripening mechanism, it is possible to combine them, resulting in Eq. (3.7):

$$\overline{r(t)}^3 - \bar{r}_0^3 = (K_{LSW} + K_{agg})t \tag{3.7}$$

3.4 Experimental Procedure

The material used in this study, AD730^{TM}, was supplied by Aubert & Duval Co. in the form of a forged square bar. A post forge heat treatment consisting in solutionizing at 1080°C for four hours followed by air cooling had also been conducted on the material. The chemical composition of the AD730^{TM} alloy used in this study is provided in Table 3-1. Three different solution treatment temperatures (1,080°C, 1,100°C and 1,110°C) were used in the investigation. These solutionizing temperatures were selected based on calculations using Thermo-calc® with the TCNI5 database and DTA results. The DTA was carried out using Diamond TG/DTA PerkinElmer with Pt crucible and a flowing Ar atmosphere. DTA samples were heated at the rate of 1°Cs^{-1} in order to replicate as close as possible the heating rate applied during the solutionizing process of γ′ particles.

Table 3-1 Chemical composition of AD730^{TM} (wt%)
(Devaux et al., 2012a)

Ni	Fe	Co	Cr	Mo	W	Al	Ti	Nb	B	C	Zr
Base	4	8.5	15.7	3.1	2.7	2.25	3.4	1.1	0.01	0.015	0.03

Sample size for solution treatment trials was 5×5×5mm^3. Holes of 1.5mm in diameter were drilled in the center of one face to a depth of 2.5mm before inserting a K-type thermocouple. All the tests were carried out on samples with thermocouples. Since thermal and thermomechanical processes are performed at various heating rates, two different heating rate ranges (low and high) were selected. The higher range used to simulate the dissolution process, the lower implemented to validate the model. For the high heating rate experiments, samples were heated from room temperature to 900°C at a constant rate of 20°Cs^{-1} and then from 900°C to the target temperature at 1°Cs^{-1}. The heating cycle for the low heating rate experiments consisted of heating to 900°C at 2°Cs^{-1} and then from 900°C to target temperature at 0.4°Cs^{-1}. The specimens were held for 1.5, 5, 15, 30, and 60 minutes, at the corresponding temperature followed by quenching in iced salt water at a rate of over 100°Cs^{-1} in order to conserve the microstructure developed at high temperatures. For each test, the heating and

cooling profiles were recorded by a computer aided electronic device using the attached thermocouple.

For microstructural studies, the samples were mounted and polished using standard metallographic techniques and etched using two different etchants. The first was composed of 170cc H_3PO_4, 10cc H_2SO_4 and 15gr Cro_3, the second a mixture of Regia water (2/3) and distilled water (1/3). After etching, the specimens' microstructures were observed using optical and Field Emission Gun Scanning Electron Microscopy (FEG-SEM). Characterization of the nanometric size particles and morphology of the precipitates were conducted using Hitachi SU70 SEM in the secondary electron (SE) mode. The back-scattered electron (BSE) images were recorded from polished cross sections by use of a backscattered electron detector attached to the SEM. Furthermore, distribution mappings of the different chemical elements constituting the specimen were obtained by Energy Dispersive Spectroscopy (EDS). Analyses were carried out at a microscopic scale using small and high magnification SEM images such as 2000, 50,000 and 100,000 magnifications to investigate γ′ morphology. The average dimensions and volume fractions of the γ′ precipitates were quantified using digitized images and ImageJ analysis software. The area of each particle was measured using the ImageJ software in view to measure γ′ phase size. The particle radius was then calculated as the radius of a circle whose surface area equaled that of the corresponding particle.

3.5 Results

3.5.1 Characteristics of the As-Received Material

FEG-SEM examination of the as-received AD730^{TM} material revealed that its microstructure consisted of γ matrix, primary γ′ precipitates, most of them present at the grain boundaries, intragranular secondary and tertiary γ′ particles, borides and two types of carbides (Figure 3.1 and Figure 3.2). The average size of the primary, secondary and tertiary γ′ were found to be 1.4 μm, 30 nm and 8 nm, respectively. Primary γ′ precipitates were oval and had irregular shapes while secondary and tertiary ones were either spherical or cuboidal. The average

volume fractions of the primary, secondary and tertiary γ′ were measured and are 8%, 26%, and 3%, respectively.

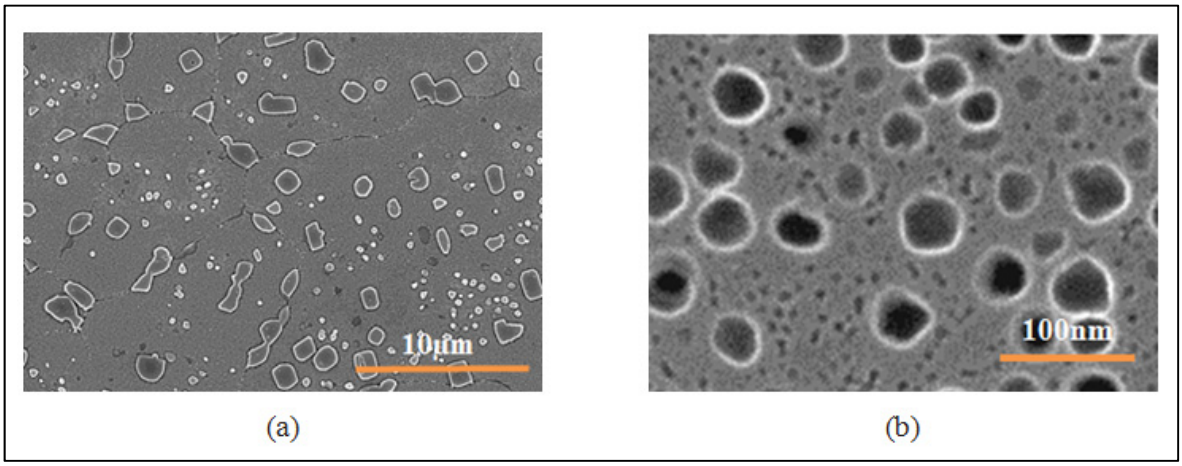

Figure 3.1 SEM microstructure of the as-received AD730^{TM} superalloy showing a) primary γ′ b) secondary and tertiary γ′.

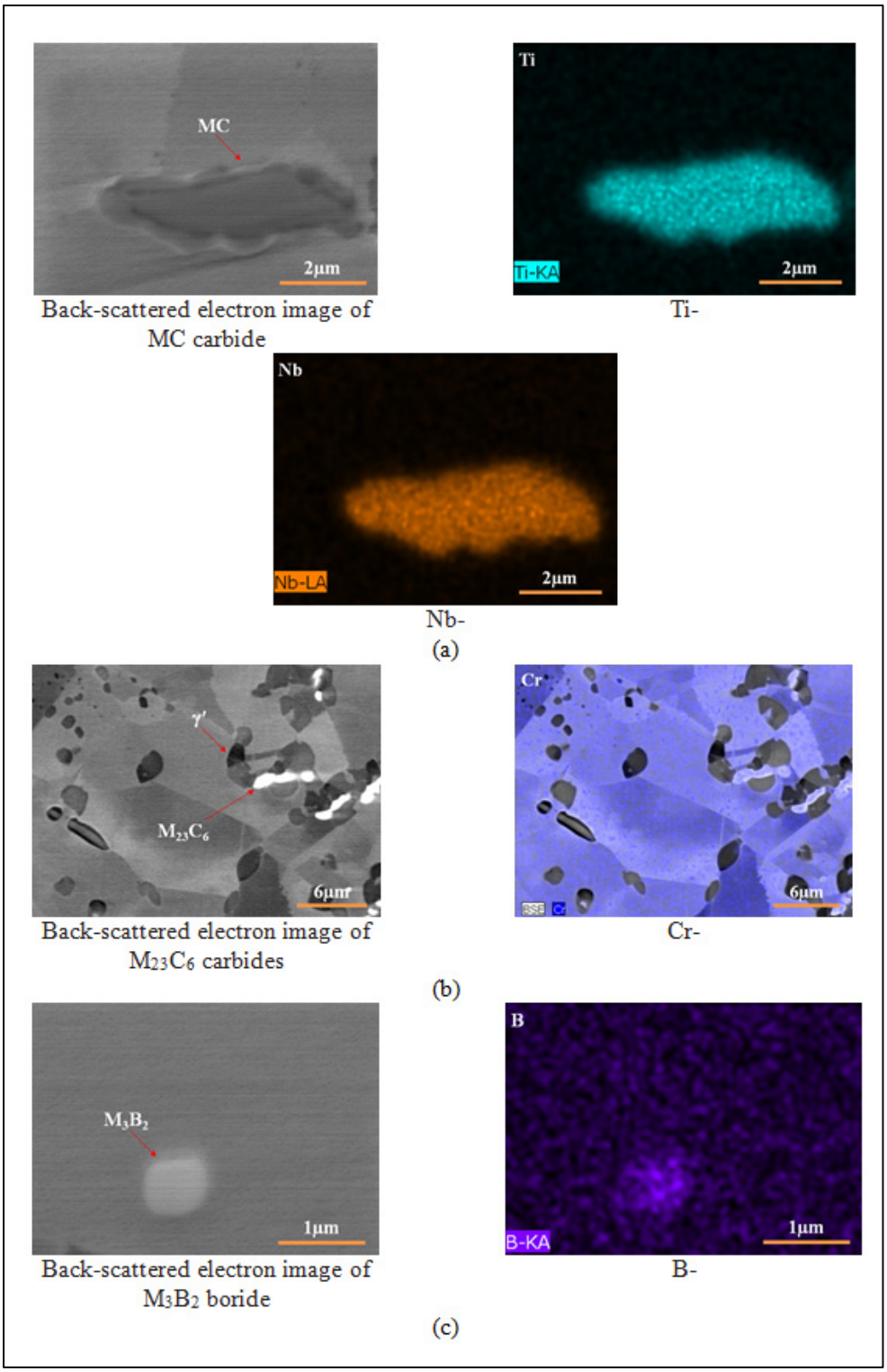

Figure 3.2 BSE/EDS X- ray maps of the (a) MC carbide mainly consisting of Ti, Nb (b) $M_{23}C_6$ carbides mainly consisting of Cr (c) M_3B_2 boride.

MC carbides formed during solidification generally exhibit coarse, random, globular or blocky, and script morphologies and are located inside the γ matrix as well as at grain boundaries. The second type of carbides, $M_{23}C_6$, are observed mostly at grain boundaries in the form of films, globules, platelets, lamellae and cells. Borides are hard particles, blocky to half-moon appearance, that are observed at grain boundaries (Safari et Nategh, 2006; Sajjadi et al., 2006; Shahriari, Sadeghi et Akbarzadeh, 2009; Shahriari et al., 2009b; Siddall et Eggar, 1986). Figure 3.2 presents an X-ray map of boron as well as the two former carbides. MC carbide and M_3B_2 boride phases mainly consist of Ti, Nb and Mo whilst the $M_{23}C_6$ phases contain significant amounts of Cr, Mo, and W. Out of all these elements, only Ti, Nb and Cr maps are shown in Figure 3.2.

3.5.2 Thermo-calc ® Simulations

The Thermo-calc® software is widely used for simulating phase transformations processes under equilibrium conditions. Figure 3.3 shows a simulation of the amounts of phases, in moles, between 400 and 1400°C for the AD730™ superalloy under equilibrium conditions on two different scales. On the first scale, phases like γ′, γ, liquid and σ are shown. The simulation results predict that the γ′ solvus, solidus, and liquidus temperatures are respectively 1090, 1220 and 1350°C. The secondary scale displays MC and $M_{23}C_6$ carbides, M_3B_2 borides and τ phases. The MC carbide is stable and does not dissolve until 1300°C.

It is well-known that, in Ni-based superalloys, the principal purpose of the homogenization process is to dissolve the irregular-shaped primary γ′ precipitates that are formed during the casting process in view of fine particles re-precipitation during cooling (Semiatin et al., 2004). Thus, from a theoretical point of view, the ideal temperature region for conducting the homogenizing of the investigated alloy would be between its γ′ solvus and solidus temperatures. This corresponds to a three- phase region composed of γ, MC carbide and M_3B_2 boride phases and in the temperature range of 1090-1220°C. Subsequently, the simulation results indicate that under equilibrium conditions, the percentage of γ′ phases, in moles, is 3% at 1080°C and no γ′ is present at 1100 and 1110°C.

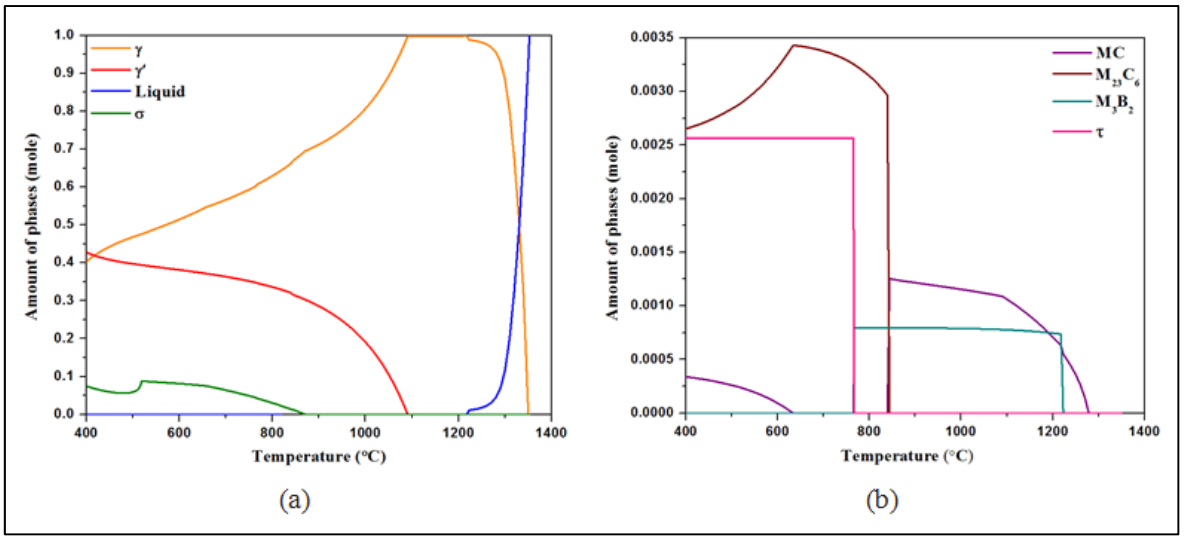

Figure 3.3 (a) and (b) Calculated equilibrium phase diagram of AD730^{TM} superalloy representing the amounts of all phases between 400 and 1400°C.

3.5.3 DTA Experiments

Figure 3.4 displays a DTA diagram obtained using a heating rate of 1°Cs^{-1}. Various endothermic peaks indicating the dissolution of γ′ at specific temperatures are revealed. Three peaks can be clearly distinguished from the heating curve: The first peak, Peak A, occurs around 615°C and shows that for a given phase volume fraction, some energy depicted by the area under the peak, is required for the transformation to be completed. This peak can correspond to the dissolution of tertiary (i.e. the finest) γ′ particles because equilibrium phase diagram calculated by Thermo-calc® software does not show any other phases with transformation temperature around 600°C. The second peak (Peak B), occurring around 800°C represents the dissolution of secondary γ′ particles, and the third peak is linked to primary γ′ dissolution and is around 1107°C (Peak C).

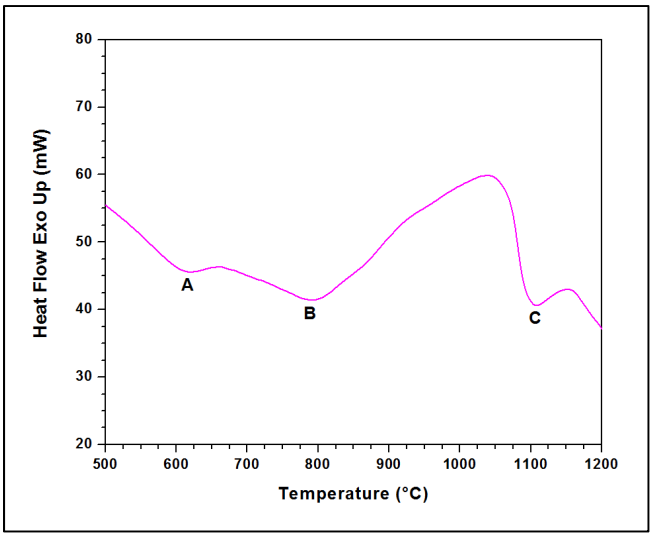

Figure 3.4 DTA curve at the 1°Cs^{-1} heating rate, showing three endothermic reactions that occur during heating indicating tertiary (Peak A), secondary (Peak B) and primary γ′ (Peak C) dissolution temperatures.

The above findings are in agreement with those of other researchers (Singh et al., 2013) who reported the temperature ranges of 600-650°C and 800-850°C for respective transformations of tertiary and secondary γ′ particles in Rene 88 DT superalloy, which contains almost the same volume fraction of γ′ as AD730^{TM}.

3.5.4 Dissolution Kinetics

Figure 3.5 and Figure 3.6 show the evolution of γ′ particles morphology and size after solution treatments at temperatures between 1080 and 1110°C. Heat treatment at 1080°C using a heating rate of 20°Cs^{-1} results in the dissolution of all tertiary and secondary γ′ particles (Figure 3.7 (b)) and the coarsening of primary γ′ (Figure 3.5 (a),Figure 3.6 and Figure 3.7). As the temperature increases to 1100°C, tertiary, secondary and small primary γ′ precipitates are dissolved.

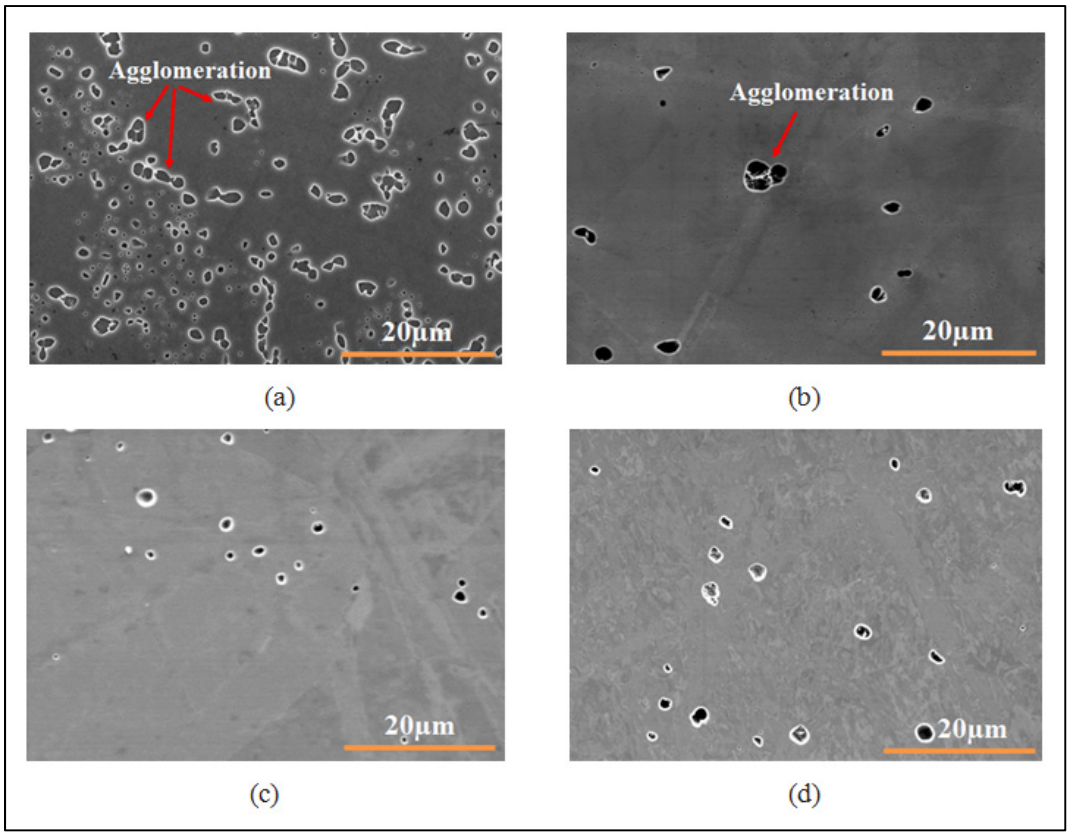

Figure 3.5 Microstructure of solution treated samples at (a) 1080°C for 15min and (b) 1100°C for 15min, showing the occurrence of γ′ particles agglomeration (c) 1110°C for 15min and (d) 1110°C for 1.5min, showing γ′ particles' dissolution.

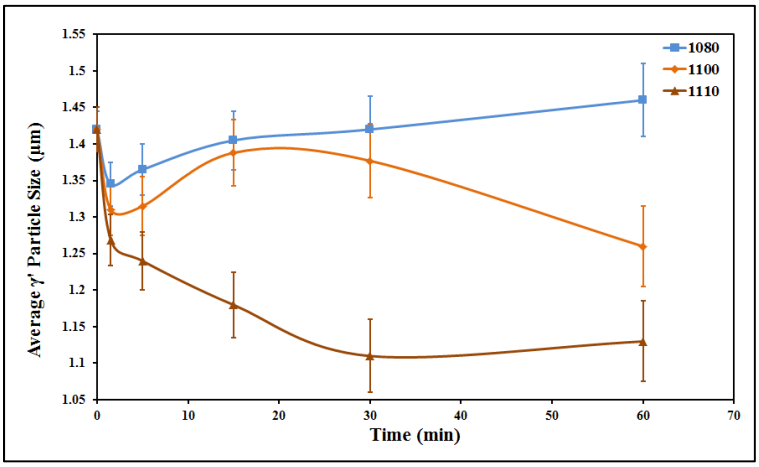

Figure 3.6 Evolution of average γ′ particle size as a function of time at 1080, 1100 and1110°C.

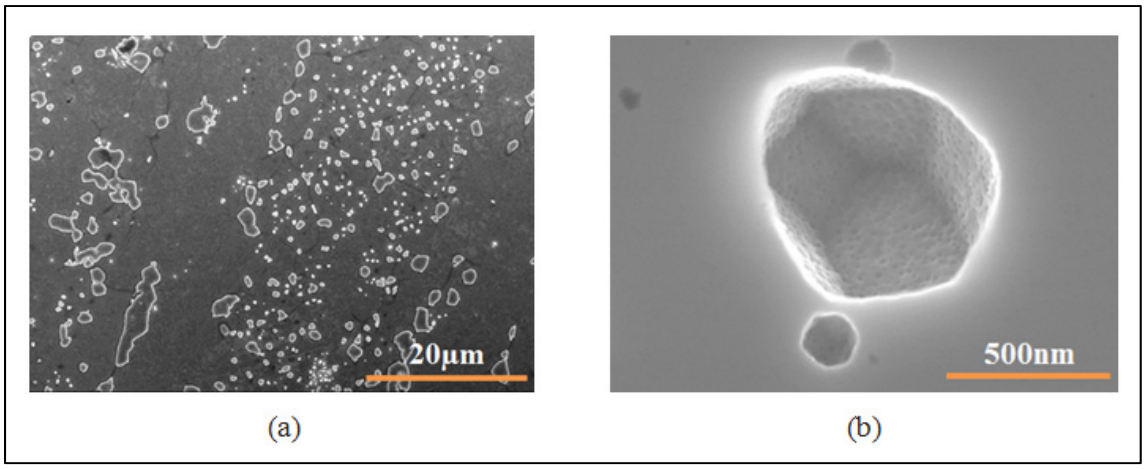

Figure 3.7 Denuded zones from the small precipitates around primary γ′ particles at 1080˚C for 5 minutes at (a) lower magnification (b) higher magnification.

However, measurements of γ′ average size, shown in Figure 3.6, indicate that the size of larger precipitates increases before final dissolution. These increases in particle sizes appear to be the result of two complementary processes: particles agglomeration (Figure 3.5 (a) and Figure 3.5(b)) and Ostwald ripening (Figure 3.7). Measurements of γ′ size and volume fraction indicate that only particle dissolution is observed when increasing the solution temperature from 1080 to 1110˚C. For instance, heat treatment at 1110˚C for 15min leads to the complete dissolution of all the tertiary and secondary γ′ precipitates, forming initially 83% of the total γ′ content in the matrix. In addition, the primary γ′ average size is decreased from 1420 nm to 1150 nm and its volume fraction from 8% to 1%. It is also worth noting that the average volume fraction of γ′ reduces from 37% in the as received material to about 1% after solutionizing at 1110˚C for 15 minutes.

Microstructural examinations of the samples heat treated at 1110˚C revealed that 90% of γ′ particles are dissolved after a short holding time of 1.5 minutes (Figure 3.5 (d)). After one hour, only 0.3% of initial γ′ remains. On the contrary, MC carbides average size and volume fraction show no change during heat treatment at 1110˚C while $M_{23}C_6$ carbides are totally dissolved. Based on the above analyses, the γ′ solvus can be estimated to be about 1110˚C for AD730^{TM} with the high heating rate.

3.5.4.1 Dissolution Kinetics Model for a Single Precipitate

The dissolution of γ′ in Ni-based superalloys is a diffusion controlled process (Fuchs, 2001). The following analytical model, based on the work of Whelan et al. (1969), was applied to analyze this process in the AD730^{TM} alloy.

The dissolution of a spherical precipitate under diffusion controlled conditions can be formulated as:

$$\frac{dr}{dt} = -\frac{kD}{2}\left[\frac{1}{r} + \frac{1}{\sqrt{\pi Dt}}\right] \tag{3.8}$$

The solution to Eq. (8) is:

$$r = r_0 - \frac{kDt}{2r_0} - \frac{k\sqrt{Dt}}{\sqrt{\pi}} \tag{3.9}$$

where r is the particle radius after 't' seconds, r_0 the initial precipitate radius, $k/2$ the supersaturation and D the solute interdiffusion coefficient in the matrix at temperature T. k is given by:

$$k = \frac{2(C_0 - C_i^e)}{C_p^e - C_i^e} \tag{3.10}$$

where C_0 is the solute concentration in the matrix, C_{i}^e and C_{p}^e are equilibrium solute concentrations respectively at the precipitate/solid solution interface and in the precipitate. Using the Thermo-calc® software, C_i and C_p values were calculated in the present investigation to estimate the coefficient k in Eq. (3.10). This value was determined to be 0.35 with Al and Ti considered as solutes.

The solute interdiffusion coefficient follows an Arrhenius type equation and is given by:

$$D = D_0 exp(\frac{-Q}{RT}) \tag{3.11}$$

where D_0 is the frequency factor, Q the activation energy, R the gas constant and T the absolute temperature.

Table 3-2 shows the calculated values of D for Al, Ti and Cr in a nickel matrix. As illustrated, D increases with the solutionizing temperature and therefore, according to Eq. (3.8), the dissolution rate should increase by 43% with a 30°C temperature increment starting from 1080°C.

The variation of precipitate radii versus dissolution time at 1110°C is plotted in Figure 3.8 for three different particle sizes. The two biggest radii (1.4 and 0.5 μm) are representative of primary γ′, the smallest (0.2 μm) corresponds to secondary γ′. The dissolution rate is shown to increase from 1.46×10^{-3} μm $.s^{-1}$ for primary γ′ to 5.02×10^{-3} μm $.s^{-1}$ for secondary γ′, mainly due to their smaller sizes.

Table 3-2 Activation energies Q , frequency factors D_o (Campbell, Boettinger et Kattner, 2002) and calculated D for the diffusion of aluminium, titanium and chromium in nickel

Element	D_0 (m^2s^{-1})	Q (KJ $mole^{-1}$)	T(°K)	*Calculated D (m^2s^{-1})
Al	2.94×10^{-4}	269	1353	1.2×10^{-14}
			1373	1.7×10^{-14}
			1383	2.1×10^{-14}
Ti	4.1×10^{-4}	275	1353	9.9×10^{-15}
			1373	1×10^{-14}
			1383	2×10^{-14}
Cr	5.2×10^{-4}	289	1353	3.6×10^{-15}
			1373	5.2×10^{-15}
			1383	6.3×10^{-15}

*This work

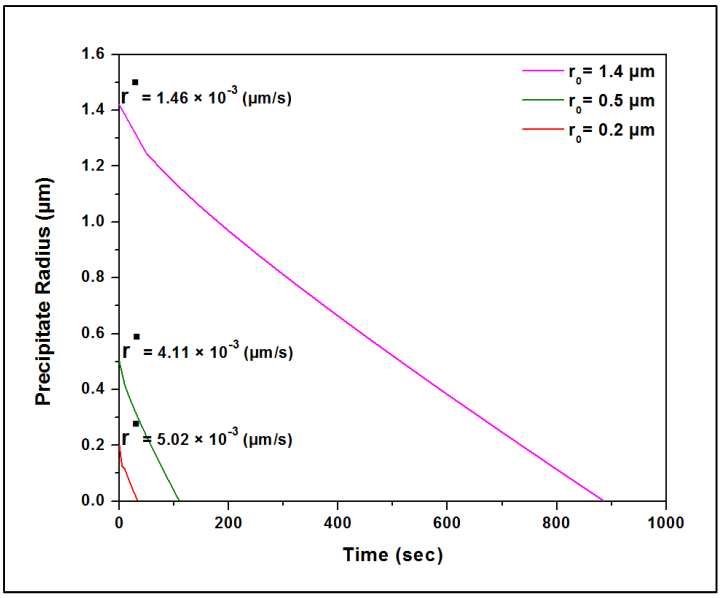

Figure 3.8 Comparison of the single γ′ precipitate dissolution kinetics at different sizes at 1110°C indicating the influence of particle size on dissolution rate.

3.5.4.2 Dissolution Kinetics Model for Multiple Precipitates

A dissolution model based on Johnson-Mehl-Avrami-Kolmogorov (JMAK) (1941) is proposed to study the precipitation evolution in AD730™. More specifically, the γ′ area fraction on various samples from different solution heat treatments is measured and used as a basis to estimate dissolution kinetics.

The γ′ area fraction ($F_{S\gamma\prime}$) can be written as a function of heat treatment time:

$$F_{S\gamma\prime} = F_{Slim} + F_1\, exp(\frac{-t}{t_1}) \tag{3.12}$$

where F_{Slim} is the γ′ area fraction at thermodynamic equilibrium, F_1 the difference between the γ′ area fraction at t=0 seconds and F_{Slim}, t_1 a constant dissolution time and F_{Slim} a material parameter. An optimization procedure was developed, using Origin and Matlab 2013, in order to find the values for the preceding factors for each solution heat treatment temperature. The procedure is based on nonlinear least-squares method and uses the

Levenberg-Marquardt algorithm which was implemented in the optimization module. The routine searches for optimized parameter values.

The evolution of the γ′ area fraction as a function of the holding time for three different dissolution temperatures and the heating rate of 20°Cs^{-1} is presented in Figure 3.9 (a). A decrease in area fraction of γ′ precipitates is observed as temperature or holding time increases. The different parameters of Eq. (3.12) were identified for each experimental condition allowing quantification of the dissolution kinetics.

The dissolution equations for each heat treatment temperature are given as follows:

$$F_{S\gamma'} = 5.83 + 31.16\ exp(\frac{-t}{0.69}) \quad \text{(For heat treatment at 1080°C)} \quad (3.13)$$

$$F_{S\gamma'} = 2.47 + 34.53\ exp(\frac{-t}{0.57}) \quad \text{(For heat treatment at 1100°C)} \quad (3.14)$$

$$F_{S\gamma'} = 1.08 + 35.92\ exp(\frac{-t}{0.54}) \quad \text{(For heat treatment at 1110°C)} \quad (3.15)$$

In order to quantify the differences in γ′ dissolution kinetics, a criterion, known as “settling time”, or the time required to reach a given percentage of the equilibrium value, was used (Giraud et al., 2013). This criterion is also used in the analysis of electronic systems and is shown schematically in Figure 3.9 (b).

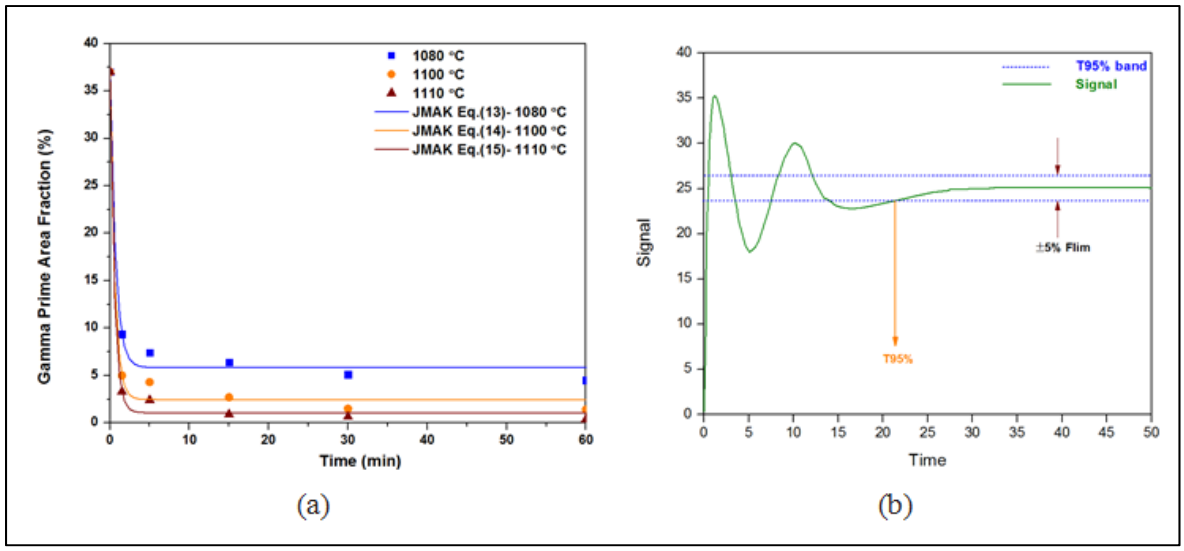

Figure 3.9 (a) Comparison of the multiple γ′ precipitate dissolution kinetics at 1080, 1100 and1110°C (b) Schematic of the T95%.

In this research, a settling time of 95% was selected. As illustrated in Figure 3.9 (b), T95% is the time needed for the γ′ volume fraction to satisfy the following condition:

$$0.95F_{S\gamma'}(at\ 60\,min) \leq F_{S\gamma'}(at\ T95\%) \leq 1.05F_{S\gamma'}(at\ 60\,min) \tag{3.16}$$

From the calculated $F_{S\gamma'}$ values and Arrhenius law, the activation energy (Q) for the dissolution of γ′ was calculated using the following equations:

$$k = \frac{dF_{S\gamma'}}{dt} = \frac{F_1}{t_1} exp(\frac{-t}{t_1}) \tag{3.17}$$

$$k = A\, exp(\frac{-Q}{RT_k}) \tag{3.18}$$

Table 3-3 shows the results for the kinetics of dissolution, k, and Q for different heat treatment temperatures at various holding times. As shown in Figure 3.9 (a), although solutionizing starts with very high kinetics at the beginning due to the dissolution of large proportions of secondary γ′, it slows with time. After only 1.5 minutes, all ultra-fine γ′

precipitates, which make 83% of initial γ′ particles, are dissolved (see Figure 3.7 (b)). The γ′ area fraction will reach 8%, 5%, and 3.3% respectively for 1080°C, 1100°C, and 1110°C, in comparison to 37% at room temperature.

Table 3-3 Dissolution kinetics and activation energies for various solution treatments

t (min)	T (°K)	K (%.min^{-1})	Q (kJ.mol^{-1})
0-1.5	1353	-0.45159	204
	1373	-0.60042	
	1383	-0.66565	
1.5-5	1353	-0.0247	273
	1373	-0.03912	
	1383	-0.04066	

The above findings are consistent with DTA results which showed that the dissolution temperature for ultrafine γ′ was lower than that of primary γ′ particles (Figure 3.4). On the other hand, since primary γ′ particles are coarse and difficult to dissolve (Figure 3.8), the activation energy increases from 204 kJ.mol^{-1} to 273 kJ.mol^{-1} demonstrating the impact of particle size on dissolution kinetics. Therefore, when holding times are longer than 1.5 minutes, dissolution becomes slower (Table 3-3, Figure 3.9 (a)). These results have revealed that the activation energy needed to dissolve γ′ varies during the dissolution process and that particle size evolution is an important consideration for accurate calculation of γ′ dissolution kinetics.

Bellot et al. (2013) reported that γ′ particles in the AD730^{TM} alloy contain fractions of Al, Ti and Nb. So, the presence of Nb in secondary γ′ particles, which is not possible to be verified by EDS, has been proved using extraction replicas in the AD730^{TM} alloy (Bellot et Lamesle, 2013) . Furthermore, Figure 3.10 reveals schematically that primary γ′ precipitates contain higher contents of Al and Ti whilst secondary γ′ have lower Al and Ti and higher Co and Cr. Thus, in addition to particle size, chemical composition can also affect the dissolution rate in the multi precipitate model. Indeed, since the secondary γ′ particles in the as-received alloy were found to be small in size, their sizes increased using slower cooling rates (10°C/min)

from 1110°C. In this way, as shown in Figure 3.10, it was possible to obtain a qualitative estimate of the difference in the chemical composition between primary and secondary γ′ precipitates using EDS line map analysis. Therefore, it can be said that for primary γ′ particles, activation energy should be correlated mainly with those of Al and Ti while for secondary γ′, Al and Ti play a less important role in diffusion.

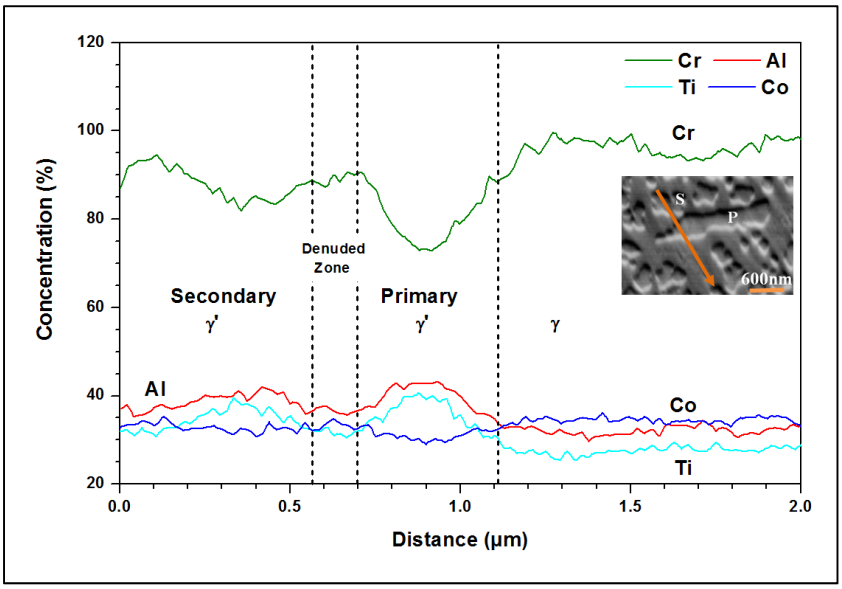

Figure 3.10 Comparison of the Al, Ti, Co and Cr concentration profiles for large or primary (P) and small or secondary (S) γ′ particles using EDS line map analysis.

The activation energy values determined in the present investigation are in accordance with the reported activation energies for the dissolution of Al (269 kJ.mol^{-1}), Ti (272 kJ.mol^{-1}) (Baldan, 2002; Campbell, Boettinger et Kattner, 2002) and Nb (203 kJ.mol^{-1}) (Patil et Kale, 1996) elements in a nickel matrix. In other words, since Nb atoms have lower activation energy than the other elements, their dissolution rate is higher and they dissolve first. By contrast, longer holding times increase the diffusion of Al and Ti atoms. The above results prove that the dissolution of γ′ precipitates is controlled mostly by the diffusion of Al, Ti and Nb in γ matrix. On the basis of the above calculations, average dissolution kinetics of -0.3 %.min^{-1} which shows decrease in volume fraction of γ′ precipitates as a function of time is obtained.

In addition to the well-known effects of temperature and holding time, heating and cooling rates also have significant effects on γ′ evolution in superalloys (Soucail et Bienvenu, 1996). To address this aspect, a time-temperature dependent analytical method, proposed by Soucail and Bienvenu (1996), was used in the present investigation to analyze the effect of a thermal cycle on γ′ evolution. In this model, equivalent holding time (t_e) is represented by the following equation:

$$t_e = \frac{RT_m^2}{Q}\left(\frac{1}{V_h} + \frac{1}{V_c}\right) + t_m \tag{3.19}$$

where T_m is the holding temperature, Q the activation energy for the dissolution of the γ′ phase, V_h and V_c respectively the heating and cooling rates, and t_m the holding time. t_e was calculated to be about (32 (sec) + t_m) at 1080 and 1100°C for low heating rates. Then, the γ′ surface fraction, $F_{S\gamma'}$ was calculated by substituting the obtained value into Eqs. (For heat treatment at 1080°C) (3.13) and(For heat treatment at 1100°C) (3.14). The calculated values of $F_{S\gamma'}$ for each temperature were validated through experimental data for low heating rate testing conditions. These values are presented in Figure 3.11.

The results indicate a good correlation between the calculated and measured data thereby confirming the validity of the proposed approach (Eqs. (For heat treatment at 1080°C) (3.13)-(For heat treatment at 1110°C) (3.15)).

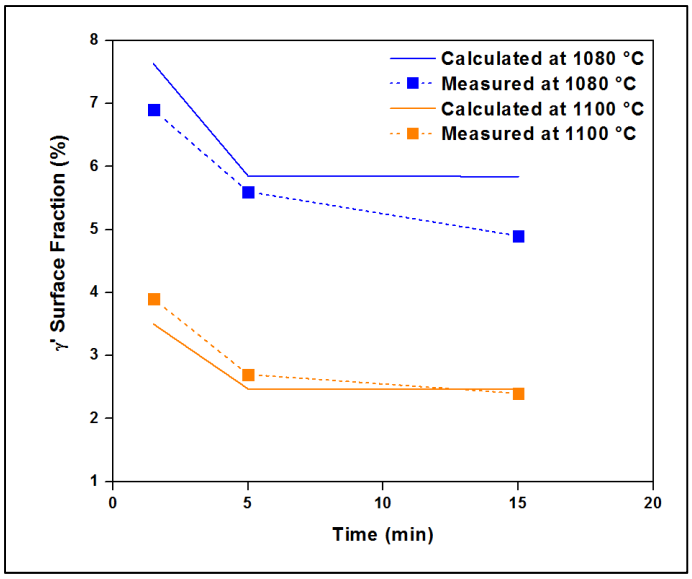

Figure 3.11 Comparison of experimental data and theoretical prediction of γ′ surface fraction as a function of time at 1080 and 1100°C for low heating rate heat treatments.

3.5.5 Coarsening Kinetics Model

The experimental results reported in Figure 3.5 indicated that γ′ coarsening takes place during the dissolution process. In order to determine the coarsening rate during this process, the Lifshitz, Slyozov, and Wagner (LSW) analytical model is modified to account for both Ostwald ripening and the agglomeration that occurs during the dissolution process. A linear relationship between heat treatment time and the cube of average precipitate size exists in the LSW model (Lifshitz et Slyozov, 1961; Wagner, 1961):

$$\bar{r}_t^3 - \bar{r}_0^3 = k_{LSW} t \tag{3.20}$$

where $\bar{r}_t$ is the average precipitate radius at time t, $\bar{r}_0$ the average precipitate radius at the beginning of coarsening, and k_{LSW} the coarsening rate constant. Umantsev, Olson and Philippe expanded the LSW theory to a multicomponent system (UO theory) (Philippe et Voorhees, 2013; Umantsev et Olson, 1993). Since low mobility elements in a multicomponent alloy limit the kinetics of coarsening, for simplicity purposes, only Ti and

Cr, which have the lowest mobilities, were considered for coarsening rate calculations. On this basis, the coarsening rate constant of γ′ precipitates, k_{UO}, is expressed as:

$$K_{UO} = \frac{8\sigma\Omega}{9RT[\frac{C_{Ti}^{\gamma}(1-K_{Ti})^2}{D_{Ti}} + \frac{C_{Cr}^{\gamma}(1-K_{Cr})^2}{D_{Cr}}]} \tag{3.21}$$

where σ is the interfacial free energy, Ω the molar volume of the γ′ precipitates, R the gas constant, T the heat treatment temperature, $D_i = D_0 \exp(\frac{-Q}{RT})$ the diffusion coefficient, C_i^{γ} the equilibrium concentration of the i th solute element in the γ matrix, and $K_i = \frac{C_i^{\gamma\prime}}{C_i^{\gamma}}$ the distribution coefficient of the i th solute element between the γ matrix and γ′ precipitates.

In the present investigation, the coarsening rate constant was determined and Eq. (3.20) was modified so that the contributions of both agglomeration and the Ostwald ripening processes were quantified. Furthermore, the flux from small to large particles is larger than expected with increasing volume fraction indicating that when the volume fraction of particles is not negligible, coarsening rate will increase (Laughlin et Hono, 2014). The coarsening rate constant in Eq. (3.20) is therefore modified by $k(f_v)$, a precipitate volume fraction function (Laughlin et Hono, 2014; Voorhees et Glicksman, 1984).

The results of FEG-SEM microscopy experiments (Figure 3.5 (a) and (b)) and reported simulations (Mao et al., 2007), however, demonstrate that the agglomeration mechanism cannot be excluded in the coarsening of Ni-based superalloys. It is reasonable to assume that particle growth follows a pattern similar to that of LSW during the agglomeration process as demonstrated in Eqs. (3.1) to (3.6). This assumption has also been used by Ratke for modeling particle coarsening through coagulation (Ratke, 1987; 1995).

Combining Eq. (3.6) and Eq. (3.20), and considering that $k_{Coarsening}$ is dependent on the γ′ volume fraction, the following equation is obtained:

$$r_t^3 - r_0^3 = k(f_v)(k_{UO} + k_{agg.})t \tag{3.22}$$

Therefore, agglomeration and Ostwald ripening coarsening follow the same growth law for average γ′ particle size with different rate constants.

The coarsening rate can be written as Eq. (3.23) considering that C'^{γ}_{i} is a temperature dependent, and being different of $k(f_v)$ values for various γ′ volume fractions:

$$k_{Coarsening} = \frac{A_0 k(f_v)}{(D_{0Ti} C'^{\gamma}_{Cr} + D_{0Cr} C'^{\gamma}_{Ti})T} \times exp(\frac{-Q}{RT}) \qquad (3.23)$$

where $C'^{\gamma}_{Cr} = C^{\gamma}_{Cr}(1 - k_{Cr})^2$ and $C'^{\gamma}_{Ti} = C^{\gamma}_{Ti}(1 - k_{Ti})^2$.

The value of $k(f_v)$ was found by Ardell (Laughlin et Hono, 2014), Voorhees and Enomoto (1984) for different volume fractions of precipitates. Voorhees and Enomoto reanalyzed the model both analytically and numerically showing coarsening rate increases with the volume fraction but at a slower rate than first suggested by Ardell (Laughlin et Hono, 2014). Using the above analysis, the value of $k(f_v)$ for the present investigation is considered to be 1.2 and 1.3 for 1100°C and 1080°C heat treatment temperatures, respectively.

The activation energy Q for γ′ dissolution in AD730™ was calculated to be 273 kJ.mol^{-1} from the slope of the plot of Lnk versus $1/T$, with k representing dissolution kinetics. The calculated value is close to reported activation energies for the diffusion of either Ti (272 kJ.mol^{-1}) or that of Cr in a Ni matrix (286 kJ.mol^{-1}) (Campbell, Boettinger et Kattner, 2002). Values for D_{0i} are given in Table 3-2. C'^{γ}_{i} values were determined for different elements of solute in a γ matrix at various heat treatment temperatures by Thermo-calc® software. Figure 3.12 shows the composition of solute elements in the γ matrix and γ′ precipitates at different temperatures.

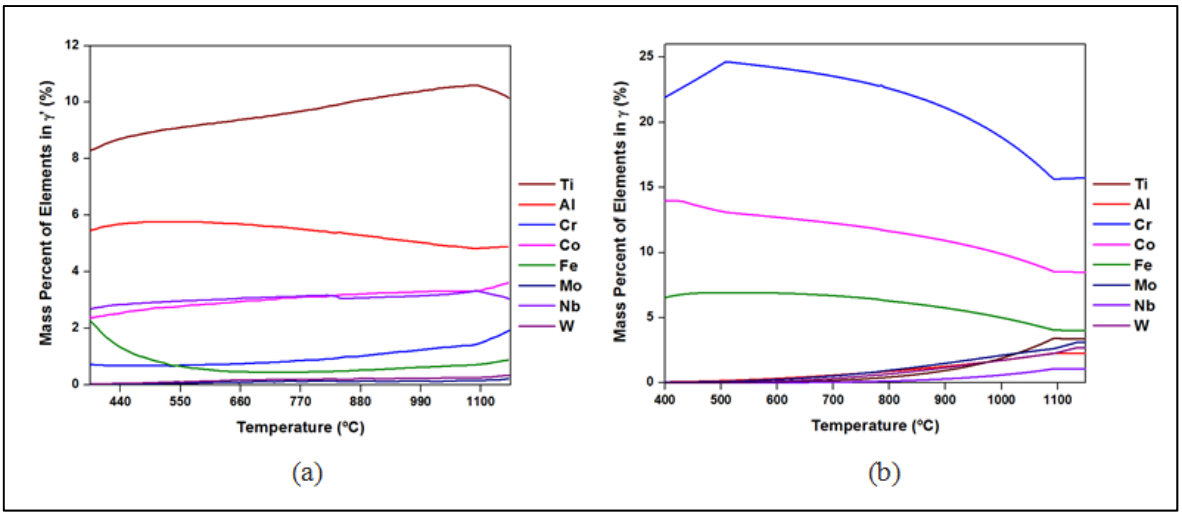

Figure 3.12 Calculated equilibrium composition of (a) γ′ phase
(b) γ phase, as a function of temperature.

The coarsening kinetics of γ′ particles in AD730^{TM} can be predicted using Eqs. (3.20), (3.21) and (3.23):

$$r_t^3 - r_0^3 = \frac{2.23 \times 10^{-13}\, k(f_v)}{(D_{0Ti} C'^{\gamma}_{Cr} + D_{0Cr} C'^{\gamma}_{Ti}) T} exp(\frac{-273000}{RT})t \tag{3.24}$$

According to the data presented in Figure 3.12, the mass percentages of Ti and Cr in the γ matrix were determined to be 3.2% and 16.1% respectively. Furthermore, k_{Ti} and k_{Cr} were calculated to be 3.34 and 0.09 respectively. Since the fluctuation of C'^{γ}_i is negligible for temperatures around 1080°C and 1100°C, using previous data and Eq. (3.24), kinetics of γ′ coarsening for this alloy at these temperatures can be summarized by:

$$r_t^3 - r_0^3 = \frac{1.53 \times 10^{-11}\, k(f_v)}{T} exp(\frac{-273000}{RT})t \tag{3.25}$$

3.6 Discussion

3.6.1 γ′ Precipitate Size Evolution after Short Exposure Time

As shown in Figure 3.6, γ′ size decreases continuously for the first 1.5 minutes for all heat treatment temperatures (i.e. the dissolution process is dominant). However, the dissolution rate is higher at 1100 and 1110°C than that observed at 1080°C. These findings are in agreement with the calculated values based on the diffusion coefficients (Table 3-2) and Eq. (3.8).

Figure 3.13 regroups the evolution of the primary γ′ size distribution during dissolution for three different temperatures below and around the AD730™ γ′ solvus. In all cases, the peak was observed to shift to smaller precipitate size after 1.5 minutes. In the case of 1080°C, only size reduction of γ′ occurs and particle disappearance is not observed while for the other temperatures, only few γ′ disappear. The previous analysis confirms that for the investigated conditions average particle size reduces with time and is mostly controlled by γ′ size reduction up to 1.5 minutes (Figure 3.6). Moreover, as shown in Figure 3.8, the dissolution rate of the large precipitates is slower compared to that of fine particles.

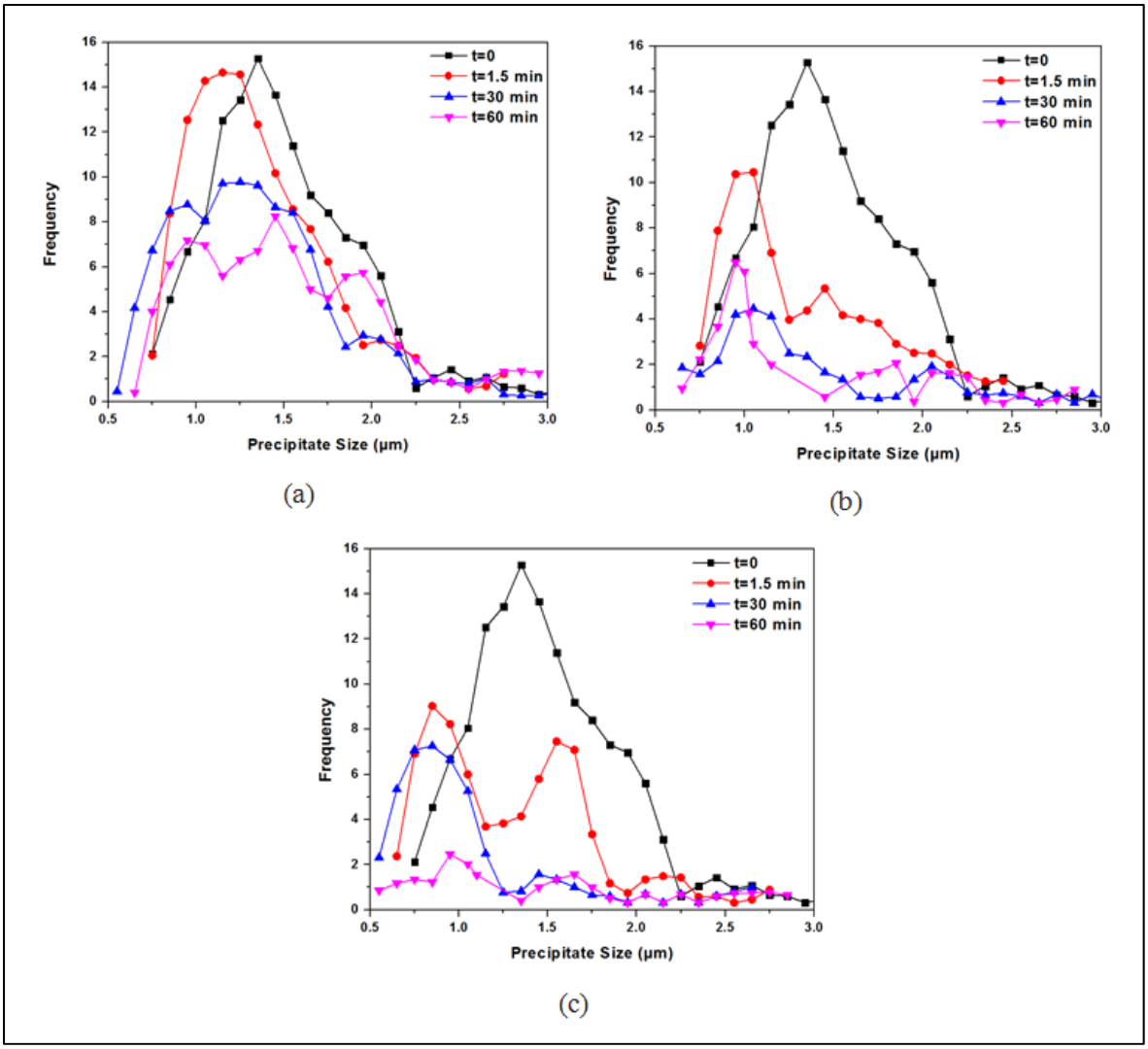

Figure 3.13 Evolution of γ′ particle size distribution as a function of time at (a) 1080°C (b) 1100°C (c) 1110°C. The plot indicates that dissolution occurs for the first 1.5 minutes and coarsening takes place after 30 minutes holding time at 1080 and 1100°C. For heat treatment at 1110°C, only dissolution occurs at all holding times.

So, it is predicted that primary (large) γ′ particles also dissolve slower than secondary (fine) γ′ in multiple particles dissolution process because more solutes are required to diffuse from large particles toward the matrix. Consequently, soft impingement may take place. In addition, when small particles dissolve, large precipitates grow due to the Ostwald ripening effect. Moreover, primary γ′ particles have higher amounts of Al and Ti and lower contents of Co and Cr than those of secondary γ′ (Figure 3.10) which slows down further the

dissolution process. Thus, the combination of the soft impingement process, the coarsening processes and chemical composition can probably lead to a deceleration of the dissolution of the large γ′ particles.

3.6.2 γ′ Precipitate Size Evolution after Longer Holding Times

As shown in Figure 3.6, γ′ coarsening is observed for 1080°C and 1100°C solution heat treated samples and for holding times superior to 1.5 minutes whereas dissolution dominates for the 1110°C heat treated samples. It was shown that after solution heat treatments at 1080°C and 1100°C, *agglomeration* of the primary γ′ particles (Figure 3.5(a) and Figure 3.5(b)), and their *coarsening* at the expense of secondary or tertiary γ′ (Figure 3.7) take place. Figure 3.14 shows an illustrative example of the coalescence of two γ′ particles through a diffuse necking process.

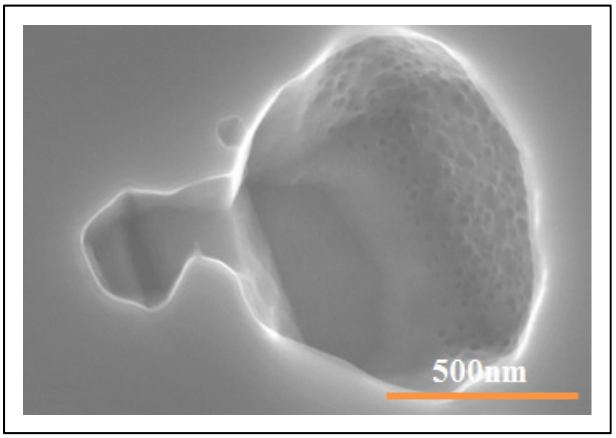

Figure 3.14 Early stage of coalescence of two γ′ particles through diffuse neck at 1100°C for 5 minutes.

Agglomeration is seen to start by neck formation between two neighboring particles which is consistent with the predictions for multicomponent Ni (Al, Cr) alloys (Mao et al., 2007). It must be noted that the coalescence process includes the overlapping of precipitates diffusion fields followed by neck formation. Finally, fast diffusion along the precipitate-matrix interface leads to its migration and precipitates coalescence (Mao et al., 2007).

In addition to neck formation, solute absorption from the matrix could be an additional factor influencing γ′ coarsening during solution heat treatment. The solute absorption process is characterized by the formation of denuded zones around primary γ′ particles (Philippe et Voorhees, 2013). The results obtained in the present investigation confirm the occurrence of a solute absorption process in the AD730^{TM} alloy. An illustrative example is shown in Figure 3.7 (b) where denuded zones from secondary and tertiary γ′ can be observed around primary γ′ in 1080°C solution treated samples for 5 minutes. As reported in the section above, all tertiary γ′ precipitates were dissolved after a 1.5 minute holding time for any of the three selected SHT temperatures. The dissolved fine particles could provide the necessary solutes which could migrate to the larger particles, thus increase the size of the larger particles.

Coarsening continues up to 15 minutes holding time for SHT at 1100˚C and 60 minutes for 1080˚C. As particle size measurements did not indicate significant changes between 15 and 30 minute holding times at 1080 and 1100˚C (Figure 3.6), comparisons were made for the 30 minute holding time condition only. Figure 3.13 shows that for 1080˚C SHT, precipitate size distribution peak after a 30 minute holding time shifts to the larger particle size of 1.24 μm in comparison to 1.15 μm for the 1.5 minute holding time. For 1100°C SHT, the peak at the 30 minute holding time also shifts to 1.05 μm compared to 950 nm for 1.5 minute holding time. However, the number of particles decreases from 15 to 10 for 1080˚C and from 10 to 4 for 1100˚C SHT. These findings confirm the occurrence of coarsening for holding times superior to 1.5 minutes due to the coalescence and agglomeration of γ′ particles (Figure 3.5 and Figure 3.7). Average γ′ size is therefore controlled by particle disappearance and solute diffusion between adjacent particles.

3.6.2.1 Determination of the Coarsening Rate

Using Eq. (3.22) and the experimental data provided in Figure 3.6, the total coarsening rate constant (i.e. $k(f_v)(k_{UO} + k_{agg.})$) was calculated to be 3.24×10^{-23} m^3s^{-1} for SHT at 1080˚C and 6.31×10^{-23} m^3s^{-1} for SHT at 1100˚C. The determined values indicate that γ′ precipitates coarsen about two times faster for a solution temperature at 1100˚C in comparison to 1080˚C. The value of the agglomeration coefficient $k_{agg.}$ was also determined to be 3.15×10^{-23} m^3s^{-1}

and 6.13×10^{-23} m^3s^{-1} respectively, for heat treatments at 1080˚C and 1100˚C. The results indicate that agglomeration has the most important contribution (97%) to the coarsening process for SHT temperatures of 1080 and 1100˚C; while the contribution of the Ostwald ripening process is only very minor (3%).

The fraction of agglomerated γ′ particles (ξ) is obtained by:

$$\xi = \frac{N_{ppt.}^{Agg.}}{N_{ppt.}^{Tot.}} \tag{3.26}$$

where $N_{ppt.}^{Agg.}$ is the number of agglomerated γ′ particles and $N_{ppt.}^{Tot.}$ the total number of γ′ particles in the analyzed surface. The values of ξ for heat treatments at 1100˚C shown in Figure 3.15 indicate that the amount of agglomeration first increases for longer heat treatment times before reaching a peak value for 15 minutes holding time and then decreases as the time increases.

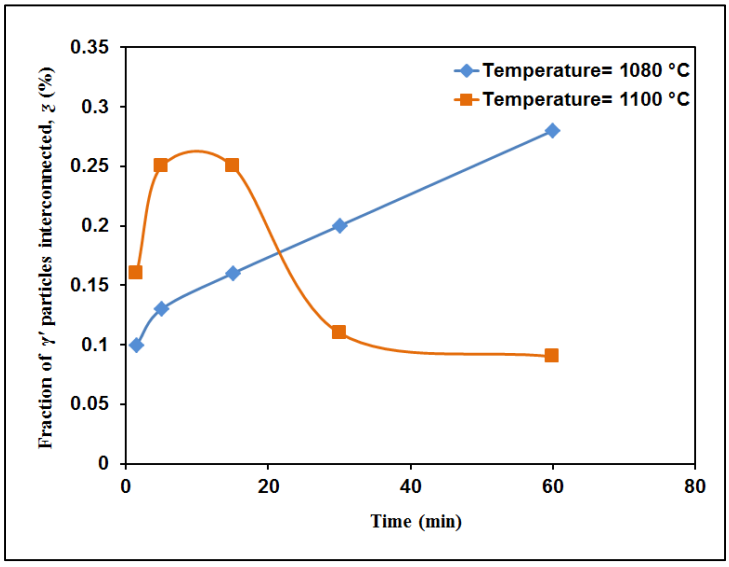

Figure 3.15 The fraction of γ′ particles interconnected by neck as a function of holding time at 1080 and 1100˚C.

On the other hand, agglomeration monotonically increases as the heat treatment time at 1080°C increases. These trends are similar to the ones observed for the evolution of average γ′ particle size with time, as previously reported in Figure 3.6, indicating that coarsening is mainly dominated by the agglomeration of the precipitates. Furthermore, Figure 3.15 reveals that the coarsening rate for 1100°C is higher than that of 1080°C, correlating with the previous finding of a higher value (almost twice) for $k_{agg.}$ at 1100°C in comparison to 1080°C.

As a result, it is concluded that both mechanisms, agglomeration and Ostwald ripening, govern γ′ size evolution during the heat treatment process of the AD730™ Ni-based superalloy. However, it appears that the Ostwald ripening contribution is negligible, affirming agglomeration is the dominant coarsening mechanism for short heat treatments at subsolvus or around solvus temperatures.

The evolution of the cubed of the precipitate radius, $\bar{r}^3$, as a function of holding time, t, is plotted in Figure 3.16 for heating conditions of 1080 and 1100°C. A linear relationship was identified (R^2 >0.93), suggesting that particles growth kinetics follow a cube power law and are consequently diffusion controlled. In addition, the slope of the linear regression increases for higher solution temperatures indicating faster coarsening rates.

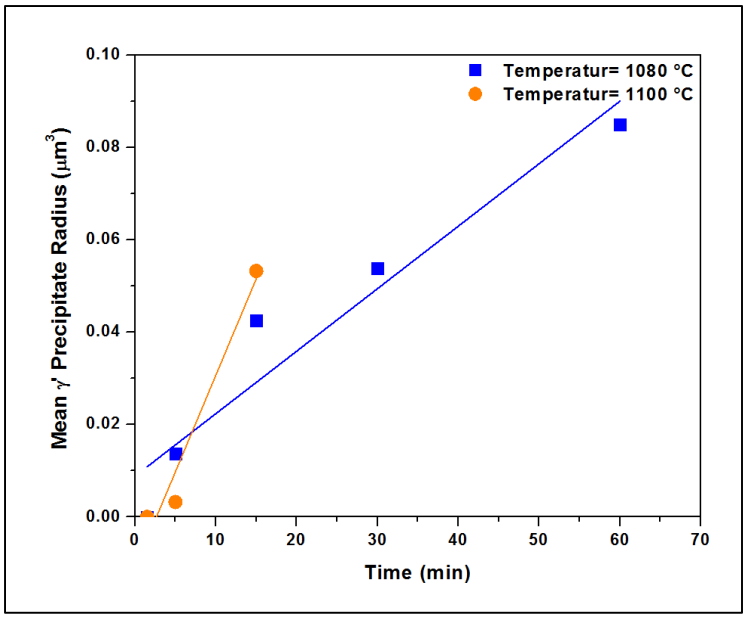

Figure 3.16 Mean precipitate radius cubed, $\bar{r}^3$, as a function of holding time at 1080 and 1100°C. Points represent experimental values and the regression line shows there is a reasonable linear relationship (R^2 >0.93) between $\bar{r}^3$ and t.

This further confirms the obtained values of $k(f_v)(k_{UO} + k_{agg.})$ for 1080 and 1100°C and the results obtained from Figure 3.15 in which the coarsening rate is higher for heat treatments at 1100°C.

3.6.2.2 Application to Aging Heat Treatments

Using Eq. (3.24), the evolution of γ′ average size after various aging times for different heat treatment temperatures can be predicted. Figure 3.17 illustrates this evolution for aging heat treatments at 700°C, 750°C and 800°C. Monajati et al. reported that γ′ particles above 200nm in size play a smaller role in the hardness increment for Udimet 720 (Monajati et al., 2004a). It has also been reported that in Ni-based superalloys, the achievable optimum hardening is directly related to an optimal γ′ particle size. For example, for PE16 and Nimonic 105, the optimum diameter was respectively found to be in the range of 26-30 nm and 55-85 nm (Reed, 2006a). Hence, the data in Figure 3.17 can be practically used to design aging heat treatment schedules for the AD730™ superalloy in order to reach the desired γ′ particle size.

This was applied in the current investigation for average secondary γ′ particle size of the as-received material which was 30nm.

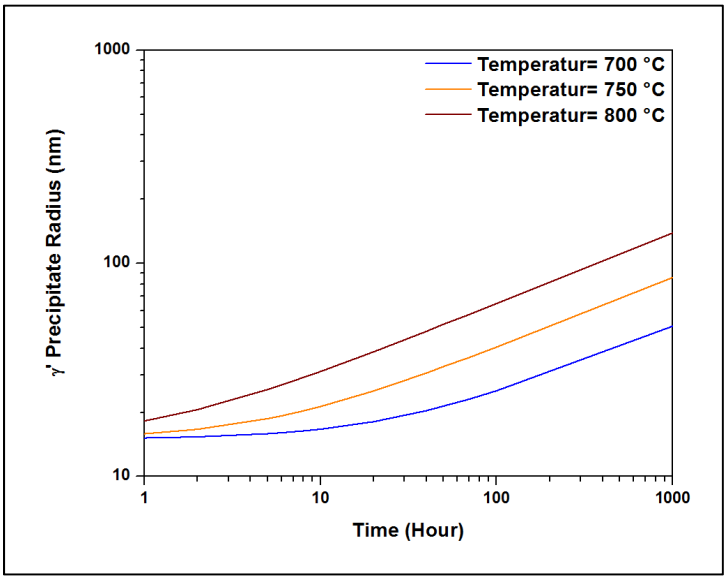

Figure 3.17 Model predictions of γ′ precipitate radius as a function of aging time at 700, 750 and 800°C based on Eq. (3.24).

On the basis of the above findings, Eq. (3.24) and Figure 3.17, an aging heat treatment at 750°C for 8 hours would be necessary to reach a mean diameter of 40nm. In order to achieve precipitate sizes of 60 nm, an 8 hour holding at 800°C would be required. Devaux et al. (2014) carried out aging heat treatment at 750°C for 8 hours and reached an average particle size of 37nm. This value is very close (about 7% difference) to the predicted value by the model proposed in this investigation.

The proposed treatment is also very close to the one reported by the former authors who used 730°C for 8 hours in order to achieve the best compromise between creep and tensile properties (Devaux et al., 2014). Therefore, Eq. (3.24) and Figure 3.17 can be used as a very efficient tool for determining desired γ′ size for specific applications such as aging.

3.6.3 γ′ Precipitate Dissolution Mechanisms

As Figure 3.5 and Figure 3.6 show, only dissolution is observed for heat treatments at 1110˚C. Under these conditions, fine precipitates are completely dissolved during the early stages of heat treatment. Average particle size is therefore totally controlled by primary γ′ size reduction for the entire holding time. Figure 3.13 shows a shift of particle size peaks to lower values and a reduction in the number of particles for all holding times. γ′ size peak reaches 800nm, from a starting value of 1.35 μm in as-received condition, after a 30 minute holding time at 1110˚C. The number of particles decreases by 53%. Complete dissolution of primary γ′ particles occurs at 1110˚C for a holding time of 60 minutes and with the high heating rate.

Interestingly, the number of particles is increased by 50% for 1100˚C SHT and a holding time of 60 minutes, although γ′ size peak shifts to smaller values of 950 nm from a starting value of 1.05 μm in comparison with a 30 minute holding time at1100˚C. This confirms that primary γ′ particles break into small pieces or split until their complete dissolution occurs (Figure 3.18).

Several dissolution patterns were observed depending on the SHT temperature. As shown in Figure 3.18, splitting of the γ′ particles in which two or more particles with parallel interfaces are created and dissolving from the center, corner and in the form of layers of γ and γ′ are observed. Similar behavior was also reported for other Ni-based superalloys (Reed, 2006a). The results of the present investigation are in agreement with the theoretical model of Doi (1992) and finite element model of Hazotte (1996) in which they stated that above a certain lattice misfit value and consequently certain strain energy, particles split to create precipitates with parallel interfaces.

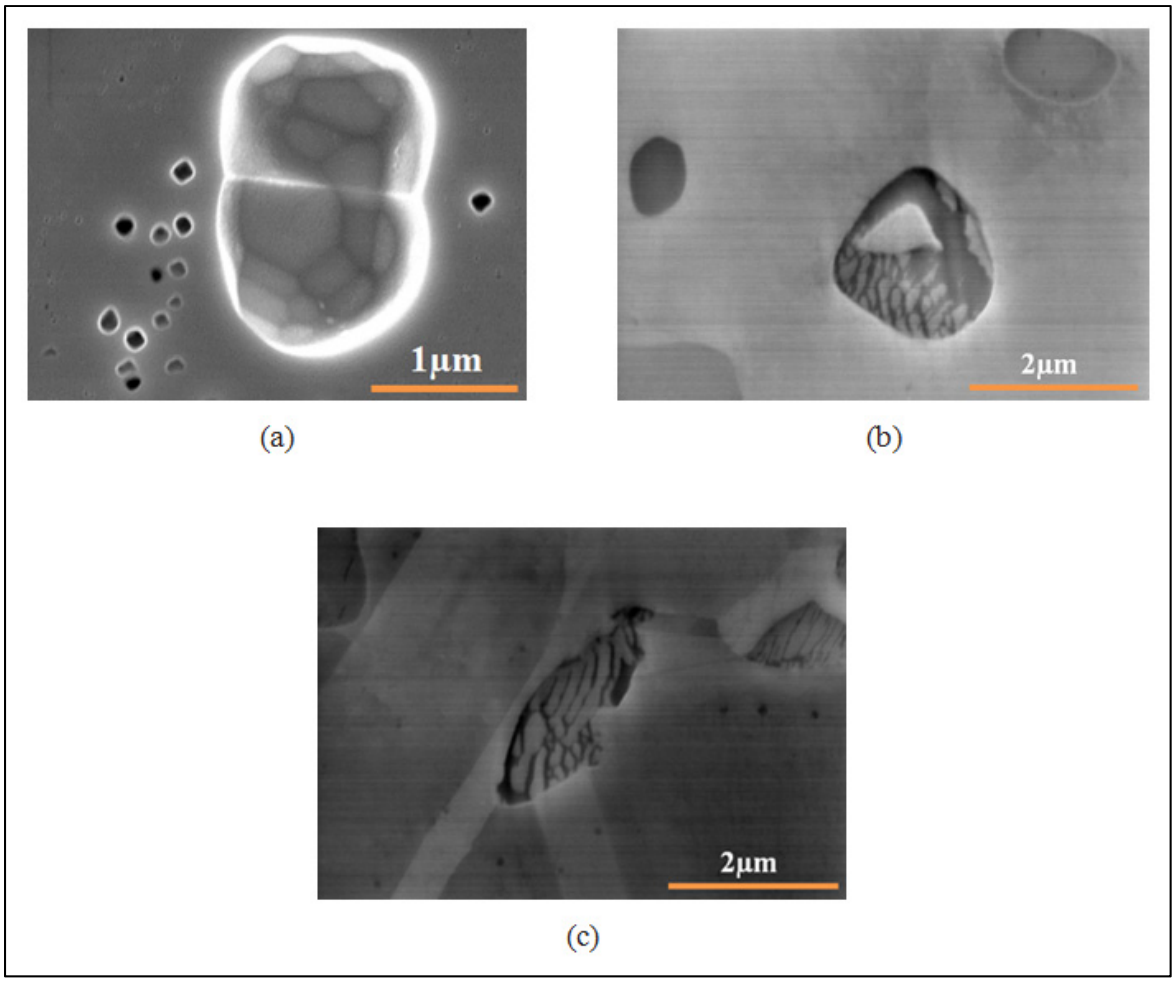

Figure 3.18 Various dissolution mechanisms a) Splitting (b) Dissolution from center and corner (c) Dissolution in the form of layers of γ and γ′.

The results obtained based on the analytical model for single particle dissolution illustrate that secondary and primary γ′ with diameters of 200 nm and 1.4 µm dissolve completely after respectively 12 seconds and 6 minutes. However, experimental results indicated that, a 15 minute holding at 1110˚C is required to reach a 1% γ′ volume fraction and 60 minutes in order to reach 0.3 % γ′. As the analytical solution is limited to single precipitate dissolution in a matrix, it does not consider the impingement of diffusion fields of neighboring particles nor precipitate size distribution during the dissolution process. This probably explains the underestimated dissolution times obtained by using the single particle model. The proposed multi-particle model however, has a relatively better prediction of γ′ dissolution kinetics as

illustrated in Figure 3.9 (a) and Eqs. (For heat treatment at 1080°C) (3.13)-(For heat treatment at 1110°C) (3.15).

Figure 3.19 (a) and Figure 3.19 (b) compare precipitate size distribution for the three selected SHT temperatures for holding times of 30 and 60 minutes, respectively. It can be seen that the peak shifts to smaller particle sizes for higher temperatures and time values suggesting particle dissolution is dominant during heat treatments at 1100 and 1110°C for the above holding times. Furthermore, the number of particles for a heat treatment at 1110°C is superior by 75% in comparison to that of 1100°C for 30 minutes holding times. This indicates the breaking and splitting of larger particles into smaller ones (Figure 3.19).

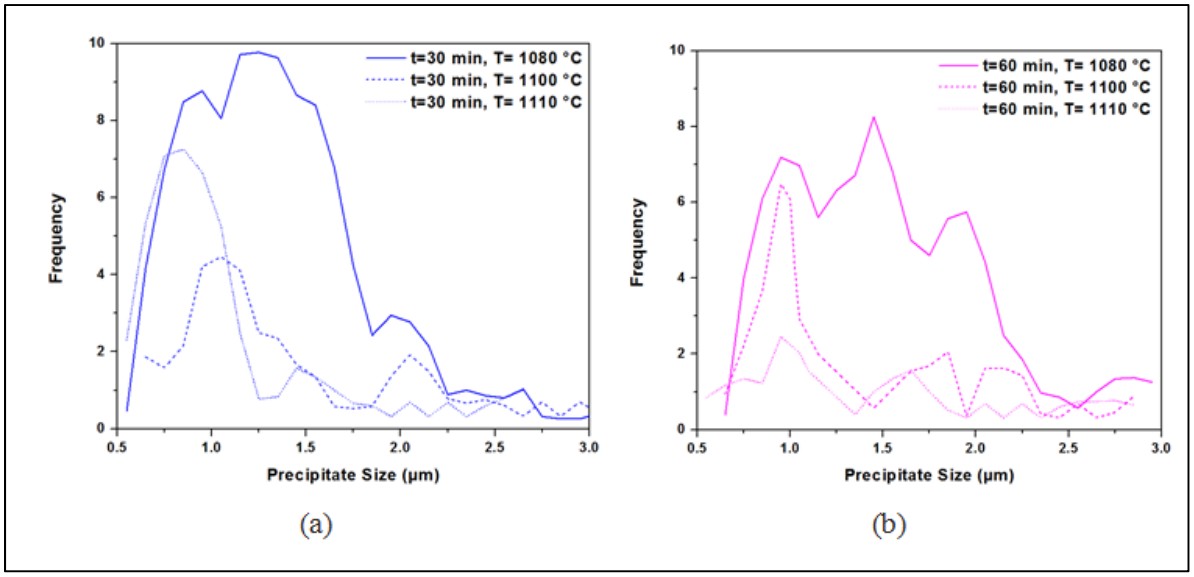

Figure 3.19 Comparison of γ′ particle size distribution at 1080, 1100 and 1110°C for (a) 30 minutes holding time (b) 60 minutes holding time. The plot indicates that breaking and splitting of larger particles into smaller ones occurs during heat treatment at 1110°C for 30 minutes holding time.

The observations are in agreement with phase field simulations reported previously by Wang et al. (2009) and confirm the simulation results concerning the occurrence of coarsening before final dissolution. It is important to note that the results obtained in this research can be directly applied to thermal or thermomechanical processes characterized by very short or long processing times. For example, the findings can be applied to analyze the Linear

Friction Welding (LFW), an emerging joining process in aerospace industry (Mary et Jahazi, 2007a) in which the joining cycle is completed in less than 30 seconds. Based on the data presented in Figure 3.6, only dissolution is dominant in heating cycles less than 1.5 minutes. γ′ evolution and dissolution kinetics can therefore be modeled from the dissolution equations allowing for rapid optimization of the LFW process parameters. Similarly, for some thermal processes such as aging, post weld heat treatments and creep in which the process time is long, coarsening equations can be applied.

3.7 Summary and Conclusions

This study represents a detailed investigation of the dissolution and coarsening mechanisms and kinetics of γ′ precipitates during solution treatment in the newly developed AD730^{TM} Ni-based superalloy. The findings are summarized as follows:

1-Evidence of various dissolution temperatures for different size distributions of γ′ were observed by DTA investigation. Three methods including DTA, Thermo-calc®, and heat treatments via microstructure observations were used to determine the dissolution temperature of the primary γ′ particles. The solvus temperatures of primary, secondary and tertiary γ′ were determined to be 1110°C, 800°C, and 615°C respectively.

2- Dissolution kinetics and coarsening models are proposed to predict γ′ volume fraction and its average size at various heat treatment temperatures. The results from the proposed models and FEG-SEM observations indicate that before complete dissolution, coarsening through agglomeration and Ostwald ripening occurs when short holding times at subsolvus temperatures are used. It was also found that not just the average size, but the size distribution of the γ′ phase plays a critical role in microstructural evolution in the dissolution and coarsening processes.

3- The activation energy during the dissolution process of the AD730^{TM} alloy was determined during this investigation. This value varies throughout the heat treatment cycle; 204 kJ.mol^{-1} up until 1.5minutes, increasing to 273 kJ.mol^{-1}after that. The dissolution of γ′

precipitates is concluded to be mostly controlled by the diffusion of Al, Ti and Nb in the γ matrix.

4- The contribution to coarsening from agglomeration and Ostwald ripening were quantified for temperature ranges from 1080˚C to 1100˚C. In the case of the AD730^{TM} superalloy, agglomeration contributes for 97% compared to only 3% for the Ostwald ripening mechanism.

5- It is demonstrated that the early stage of agglomeration is created by neck formation between two neighboring particles. Splitting and breaking of the larger γ′ particles into smaller ones and dissolution from the center of the particles can be identified as mechanisms of γ′ dissolution.

6- A single particle analytical model was used to determine dissolution kinetics and a multi-particle semi-analytical dissolution model was proposed to quantify and predict dissolution kinetics. The models were validated by experiments. The comparison of single and multi-particle models indicated that the proposed multi-particle model has a relatively better prediction of γ′ dissolution kinetics.

3.8 Acknowledgements

The financial support from the Natural Sciences and Engineering Research Council (NSERC) of Canada in the form of a Discovery Grant is gratefully acknowledged. The authors express appreciation to Aubert & Duval Co. and to Dr. Alexandre Devaux for providing AD730^{TM} samples and for invaluable discussions.

Appendix A: Analytical Solution to the Non-Linear Differential Equation: Eq. (3.8) is used for dissolution of a spherical precipitate:

$$\frac{dr}{dt} = -\frac{kD}{2}\left[\frac{1}{r} + \frac{1}{\sqrt{\pi Dt}}\right]$$

To integrate Eq. (3.8) assuming:

$$a = \frac{2D(C_0 - C_\gamma^e)}{C_{\gamma\prime}^e - C_\gamma^e};\ b = \frac{\sqrt{\frac{D}{\pi}}(C_0 - C_\gamma^e)}{C_{\gamma\prime}^e - C_\gamma^e};\ p = \frac{b}{a};\ y = \frac{R}{R_0};\ \tau = \frac{a^2 t}{{R_0}^2} \tag{A1}$$

Eq. (3.8) then becomes:

$$\frac{dy}{d\tau} = -\frac{1}{2y} - \frac{p}{\sqrt{\tau}} \tag{A2}$$

Eq. (A2) can be integrated by substitution $y^2 = w^2\tau$. Therefore, the following implicit relation for y as a function of τ is obtained.

$$ln\left(y^2 + 2p\sqrt{\tau}y + \tau\right) = -\frac{2p}{\sqrt{1-p^2}}\ tan^{-1}\left(\frac{\sqrt{1-p^2}}{\left({}^{y}/_{\sqrt{\tau}}\right) + p}\right) \tag{A3}$$

Thus, Eq. (3.8) at short times is integrated approximately to give an analytical solution. Hence the answer for this assumption is:

$$y = 1 - \frac{1}{2}\tau - 2p\sqrt{\tau} \tag{A4}$$

This gives the solution of:

$$r = r_0 - \frac{kDt}{2r_0} - \frac{k\sqrt{Dt}}{\sqrt{\pi}}$$

References

Avrami, M. 1941. « Granulation, Phase Change, and Microstructure Kinetics of Phase Change. III ». *The Journal of Chemical Physics,* vol. 9, nº 2, p. 177-184.

Baldan, A. 2002. « Progress in Ostwald Ripening Theories and their Applications to the γ′-Precipitates in Nickel-Base Superalloys Part II: Nickel-Base Superalloys ». *Journal of Materials Science,* vol. 37, nº 12, p. 2379-2405.

Bellot, C., et P. Lamesle. 2013. « Quantitative Measurement of Gamma Prime Precipitates in Two Industrial Nickel-Based Superalloys Using Extraction and High Resolution SEM Imaging ». *Journal of Alloys and Compounds,* vol. 570, p. 100-103.

Campbell, C. E., W. J. Boettinger et U. R. Kattner. 2002. « Development of a Diffusion Mobility Database for Ni-Base Superalloys ». *Acta Materialia,* vol. 50, nº 4, p. 775-792.

Cormier, J., et G. Cailletaud. 2010a. « Constitutive Modeling of the Creep Behavior of Single Crystal Superalloys Under Non-Isothermal Conditions Inducing Phase Transformations ». *Materials Science and Engineering A,* vol. 527, nº 23, p. 6300-6312.

Cormier, J., X. Milhet et J. Mendez. 2007a. « Effect of Very High Temperature Short Exposures on the Dissolution of the γ′ Phase in Single Crystal MC2 Superalloy ». *Journal of Materials Science,* vol. 42, nº 18, p. 7780-7786.

Devaux, A., A. Helstroffer, J. Cormier, P. Villechaise, J. Douin, M. Hantcherli et F. Pettinari-Sturmel. 2014. « Effect of Aging Heat-Treatment on Mechanical Properties of AD730™ Superalloy ». In *8th International Symposium on Superalloy 718 and Derivatives 2014, September 28, 2014 - October 1, 2014*. (Pittsburgh, PA, United states), p. 521-535. Coll. « 8th International Symposium on Superalloy 718 and Derivatives 2014 »: John Wiley and Sons Inc.

Devaux, A., B. Picque, M. F. Gervais, E. Georges, T. Poulain et P. Heritier. 2012a. « AD730™-A New Nickel-Based Superalloy for High Temperature Engine Rotative Parts ». In *12th International Symposium on Superalloys, Superalloys 2012, September 9, 2012 - September 13, 2012*. (Seven Springs, PA, United states), p. 911-919. Coll. « Proceedings of the International Symposium on Superalloys »: Minerals, Metals and Materials Society.

Doi, M., et T. Miyazaki. 1992. « Effect of Elastic Interaction Energy on the Distribution of Coherent Precipitate Particles in Nickel-Base Alloys ». In *Superalloys 1992*. sous la dir. de Antolovich, S. D., R.W. Stusrud, R.A. MacKay, D.L. Anton, T. Khan, R.D. Kissinge et D.L. Klarstrom, p. 537-546. The Minerals, Metals & Materials Society.

Ferro, P. 2013. « A Dissolution Kinetics Model and its Application to Duplex Stainless Steels ». *Acta Materialia,* vol. 61, nº 9, p. 3141-3147.

Ferro, P., et F. Bonollo. 2012. « A Semiempirical Model for Sigma-Phase Precipitation in Duplex and Superduplex Stainless Steels ». *Metallurgical and Materials Transactions A: Physical Metallurgy and Materials Science,* vol. 43, nº 4, p. 1109-1116.

Fuchs, G. E. 2001. « Solution Heat Treatment Response of a Third Generation Single Crystal Ni-Base Superalloy ». *Materials Science and Engineering A,* vol. 300, nº 1-2, p. 52-60.

Giraud, R., Z. Hervier, J. Cormier, G. Saint-Martin, F. Hamon, X. Milhet et J. Mendez. 2013. « Strain effect on the γ′ dissolution at high temperatures of a nickel-based single crystal superalloy ». *Metallurgical and Materials Transactions A: Physical Metallurgy and Materials Science,* vol. 44, nº 1, p. 131-146.

Hazotte, A., T. Grosdidier et S. Denis. 1996. « γ' Precipitate Splitting in Nickel-Based Superalloys: A 3-D Finite Element Analysis ». *Scripta Materialia,* vol. 34, nº 4, p. 601-608.

Kovačević, I., et B. Šarler. 2005. « Solution of a Phase-Field Model for Dissolution of Primary Particles in Binary Aluminum Alloys by an R-Adaptive Mesh-Free Method ». *Materials Science and Engineering A,* vol. 413-414, p. 423-428.

Laughlin, D. E., et K. Hono. 2014. *Physical Metallurgy*. Elsevier 2960 p.

Le Graverend, J. B., J. Cormier, F. Gallerneau, P. Villechaise, S. Kruch et J. Mendez. 2014. « A Microstructure-Sensitive Constitutive Modeling of the Inelastic Behavior of Single Crystal Nickel-Based Superalloys at Very High Temperature ». *International Journal of Plasticity,* vol. 59, p. 55-83.

Lee, E. S., et Y. G. Kim. 1990. « A Transformation Kinetic Model and its Application to CuZnAl Shape Memory Alloys-I. Isothermal Conditions ». *Acta Metallurgica Et Materialia,* vol. 38, nº 9, p. 1669-1676.

Lifshitz, I. M., et V. V. Slyozov. 1961. « The kinetics of Precipitation from Supersaturated Solid Solutions ». *Journal of Physics and Chemistry of Solids,* vol. 19, nº 1-2, p. 35-50.

Mao, Z., C. K. Sudbrack, K. E. Yoon, G. Martin et D. N. Seidman. 2007. « The Mechanism of Morphogenesis in a Phase-Separating Concentrated Multicomponent alloy ». *Nature Materials,* vol. 6, nº 3, p. 210-216.

Mary, C., et M. Jahazi. 2007a. « Linear Friction Welding of IN-718 Process Optimization and Microstructure Evolution ». In *5th International Conference on Processing and Manufacturing of Advanced Materials - THERMEC 2006, July 4, 2006 - July 8, 2006*. (Vancouver, BC, Canada) Vol. 15-17, p. 357-362. Coll. « Advanced Materials Research »: Trans Tech Publications.

Masoumi, F., M. Jahazi, J. Cormier et D. Shahriari. 2014. « Dissolution Kinetics and Morphological Changes of γ ′ in AD730™ Superalloy ». In *MATEC Web of Conferences*. Vol. 14.

Monajati, H., M. Jahazi, R. Bahrami et S. Yue. 2004a. « The Influence of Heat Treatment Conditions on γ′ Characteristics in Udimet® 720 ». *Materials Science and Engineering A,* vol. 373, nº 1-2, p. 286-293.

Ojo, O. A., N. L. Richards et M. C. Chaturvedi. 2004b. « On Incipient Melting during High Temperature Heat Treatment of Cast Inconel 738 Superalloy ». *Journal of Materials Science,* vol. 39, nº 24, p. 7401-7404.

Patil, R. V., et G. B. Kale. 1996. « Chemical Diffusion of Niobium in Nickel ». *Journal of Nuclear Materials,* vol. 230, nº 1, p. 57-60.

Payton, E. J. 2008. « Superalloys ». *975, Warrendale, PA, the Minerals, Metals & Materials Society,* vol. 43, p. 60.

Philippe, T., et P. W. Voorhees. 2013. « Ostwald Ripening in Multicomponent Alloys ». *Acta Materialia,* vol. 61, nº 11, p. 4237-4244.

Radis, R., M. Schaffer, M. Albu, G. Kothleitner, P. Pölt et E. Kozeschnik. 2009. « Multimodal Size Distributions of γ′ Precipitates during Continuous Cooling of UDIMET 720 Li ». *Acta Materialia,* vol. 57, nº 19, p. 5739-5747.

Ratke, L. 1987. « Simultaneous Coarsening of Dispersions by Growth and Coagulation ». *Journal of Colloid And Interface Science,* vol. 119, nº 2, p. 391-397.

Ratke, L. 1995. « Coarsening of Liquid AlPb Dispersions under Reduced Gravity Conditions ». *Materials Science and Engineering A,* vol. 203, nº 1-2, p. 399-407.

Reed, R. C. 2006a. *The Superalloys Fundamentals and Applications*, 9780521859042. Coll. « The Superalloys: Fundamentals and Applications ». 1-372 p.

Safari, J., et S. Nategh. 2006. « On the Heat Treatment of Rene-80 Nickel-Base Superalloy ». *Journal of Materials Processing Technology,* vol. 176, nº 1-3, p. 240-250.

Sajjadi, S. A., S. M. Zebarjad, R. I. L. Guthrie et M. Isac. 2006. « Microstructure Evolution of High-Performance Ni-Base Superalloy GTD-111 with Heat Treatment Parameters ». *Journal of Materials Processing Technology,* vol. 175, nº 1-3, p. 376-381.

Semiatin, S. L., R. C. Kramb, R. E. Turner, F. Zhang et M. M. Antony. 2004. « Analysis of the Homogenization of a Nickel-Base Superalloy ». *Scripta Materialia,* vol. 51, nº 6, p. 491-495.

Shahriari, D., M. H. Sadeghi et A. Akbarzadeh. 2009. « γ' Precipitate Dissolution during Heat Treatment of Nimonic 115 Superalloy ». *Materials and Manufacturing Processes,* vol. 24, nº 5, p. 559-563.

Shahriari, D., M. H. Sadeghi, A. Akbarzadeh et M. Cheraghzadeh. 2009b. « The Influence of Heat Treatment and Hot Deformation Conditions on γ′ Precipitate Dissolution of Nimonic 115 Superalloy ». *International Journal of Advanced Manufacturing Technology,* vol. 45, nº 9-10, p. 841-850.

Siddall, R. J., et J. W. Eggar. 1986. « Production and Quality Control of Superalloy Forging-Quality Billet ». *Materials Science and Technology (United Kingdom),* vol. 2, nº 7, p. 728-732.

Singh, A. R. P., S. Nag, S. Chattopadhyay, Y. Ren, J. Tiley, G. B. Viswanathan, H. L. Fraser et R. Banerjee. 2013. « Mechanisms Related to Different Generations of γ′ Precipitation during Continuous Cooling of a Nickel Base Superalloy ». *Acta Materialia,* vol. 61, nº 1, p. 280-293.

Smoluchowski, M. V. 1916. « Drei Vorträge über Diffusion, Brownsche Molekularbewegung und Koagulation von Kolloidteilchen ». *Phys. Z.,* vol. 17, p. 557-585.

Soucail, M., et Y. Bienvenu. 1996. « Dissolution of the γ′ Phase in a Nickel Base Superalloy at Equilibrium and under Rapid Heating ». *Materials Science and Engineering A,* vol. 220, nº 1-2, p. 215-222.

Thomas, G., et M. J. Whelan. 1961. « Observations of Precipitation in Thin Foils of Aluminium +4% Copper Alloy ». *Philosophical Magazine,* vol. 6, nº 69, p. 1103-1114.

Thompson, P. D. 1968. « A Transformation of the Stochastic Equation for Droplet Coalescence ». In *Proceedings of the International Conference on Cloud Physics*. (Toronto, Canada, August 26-30, 1968), p. 115-126. University of Toronto Press.

Umantsev, A., et G. B. Olson. 1993. « Ostwald Ripening in Multicomponent Alloys ». *Scripta Metallurgica et Materiala,* vol. 29, nº 8, p. 1135-1140.

Voorhees, P. W., et M. E. Glicksman. 1984. « Solution to the Multi-Particle Diffusion Problem with Applications to Ostwald Ripening-II. Computer Simulations ». *Acta Metallurgica,* vol. 32, nº 11, p. 2013-2030.

Wagner, C. 1961. « Theorie der Alterung von Niederschlägen durch Umlösen ». *Z. Elektrochem.,* vol. 65, nº 7-8, p. 581-591.

Wang, G., D. S. Xu, N. Ma, N. Zhou, E. J. Payton, R. Yang, M. J. Mills et Y. Wang. 2009. « Simulation Study of Effects of Initial Particle Size Distribution on Dissolution ». *Acta Materialia,* vol. 57, nº 2, p. 316-325.

Wang, T., G. Sheng, Z. K. Liu et L. Q. Chen. 2008. « Coarsening Kinetics of γ′ Precipitates in the Ni-Al-Mo System ». *Acta Materialia,* vol. 56, nº 19, p. 5544-5551.

Wen, Y. H., B. Wang, J. P. Simmons et Y. Wang. 2006. « A Phase-Field Model for Heat Treatment Applications in Ni-Based Alloys ». *Acta Materialia,* vol. 54, nº 8, p. 2087-2099.

Whelan, M. J. 1969. « On the Kinetics of Precipitate Dissolution ». *Metal Science Journal,* vol. 3, nº 1, p. 95-97.

CHAPITRE 4

ARTICLE 2: KINETICS AND MECHANISMS OF γ′ REPRECIPITATION IN A NI-BASED SUPERALLOY

F. Masoumi[a], D. Shahriari[a], M. Jahazi[a], J. Cormier[b], A. Devaux[C]

[a] Department of Mechanical Engineering, École de Technologie Supérieure (ETS), H3C 1K3, Montreal, QC, Canada
[b] Institute Pprime, UPR CNRS 3346, Physics and Mechanics of Materials Department, ISAE-ENSMA,
BP 40109, Futuroscope- Chasseneuil Cedex 86961, France
[c] Aubert & Duval, Site des Ancizes, BP1, 63770 Les Ancizes Cedex, France

This article was published in the Scientific Reports in June, 2016

4.1 Abstract

The reprecipitation mechanisms and kinetics of γ′ particles during cooling from supersolvus and subsolvus temperatures were studied in AD730^{TM} Ni-based superalloy using Differential Thermal Analysis (DTA). The evolution in the morphology and distribution of reprecipitated γ′ particles was investigated using Field Emission Gun Scanning Electron Microscopy (FEG-SEM). Depending on the cooling rate, γ′ particles showed multi or monomodal distribution. The irregularity growth characteristics observed at lower cooling rates were analyzed in the context of Mullins and Sekerka theory, and allowed the determination of a critical size of γ′ particles above which morphological instability appears. Precipitation kinetics parameters were determined using a non-isothermal JMA model and DTA data. The Avrami exponent was determined to be in the 1.5-2.3 range, suggesting spherical or irregular growth. A methodology was developed to take into account the temperature dependence of the rate coefficient $k(T)$ in the non-isothermal JMA equation. In that regard, a function for $k(T)$ was developed. Based on the results obtained, reprecipitation kinetics models for low and high cooling rates are proposed to quantify and predict the volume fraction of reprecipitated γ′ particles during the cooling process.

Keywords: Ni-based superalloy; AD730^{TM}; γ′ Phase Reprecipitation; DTA; Morphological Instability; Kinetics Model

4.2 Introduction

AD730^{TM} is a newly developed Ni-based superalloy for turbine disk applications, with reported superior service properties around 700°C when compared to Inconel 718 and several other alloys (Devaux et al., 2012c). This alloy is a γ′ strengthened alloy produced by the cast and wrought processes. In manufacturing processes such as rolling, forging, machining, friction welding and repair processes of turbine disks, different zones of the component experience temperatures above or below the solvus temperature of γ′ particles. Therefore, dissolution and subsequent γ′ reprecipitation occur during these thermomechanical processes (Shahriari et al., 2009b). In this context, an evaluation of γ′ characteristics and precipitation kinetics after cooling is critical in order to develop optimum process parameters and reach optimal mechanical performance (Payton et al., 2008).

The precipitate size distribution depends strongly on the cooling rate. It has previously been reported (Babu et al., 2001; Huang et al., 2007b; Masoumi et al., 2014; Seidman, Sudbrack et Yoon, 2006; Shahriari, Sadeghi et Akbarzadeh, 2009) that γ′ particles reprecipitate in monomodal morphology at high cooling rates, while multimodal distribution is obtained for slow cooling (Radis et al., 2009; Sarosi et al., 2007; Singh et al., 2013; Singh et al., 2011; Wen et al., 2003; Wen et al., 2006). The formation of multimodal γ′ has been associated with multiple bursts of γ′ at different temperatures (Radis et al., 2009; Singh et al., 2013; Singh et al., 2011; Wen et al., 2003). At lower undercoolings, just below γ′ solvus, higher diffusivity levels result in the formation of a first population of γ′ particles; while higher undercoolings provide supersaturation and thermodynamic driving forces for the formation of other populations of γ′ precipitates (Babu et al., 2001; Wen et al., 2003; Wen et al., 2006). Furthermore, it has been reported that γ′ reprecipitation can be suppressed at high cooling rates in alloys with low volume fractions of γ′ (< 30%) (Huang et al., 2007b; Maldonado et North, 2002; Mary et Jahazi, 2007a; Preuss et al., 2002b). For example, no γ′ reprecipitation was observed in the fusion zone of laser and electron beam or linear friction welded Waspaloy (Chamanfar et al., 2011b; Sekhar et Reed, 2002). This suppression leads to a precipitate-free region adjacent to the interface and, consequently, a pronounced drop in hardness in these regions. However, the influence of process and material parameters, such as

the cooling rate, cooling start temperature, γ′ volume fraction, etc., on the formation of monomodal or multimodal precipitation of γ′ is still not well documented. It should also be noted that most of the reported works on γ′ reprecipitation have been focused on cooling from supersolvus temperatures, while little data (Cormier et al., 2010; Cormier, Milhet et Mendez, 2007b) is available on cooling from subsolvus temperatures.

In addition to the precipitate size distribution, the γ′ morphology is also a function of the cooling rate. Based on Mullins and Sekerka (1963) theory, in a diffusion-controlled process, when a second phase grows in a supersaturated matrix, there is a potential for morphological instability. Several examples of γ′ morphological instability and dendrites are available in the literature (Furrer et Fecht, 2000; Lippard et Jones, 2000; Locq, Marty et Caron, 2000) but few studies (Behrouzghaemi et Mitchell, 2008; Yoo, 2005) have investigated the origin of this instability, and specifically, the role of the cooling rate on inducing such instability. In the present study, the effect of the cooling rate on the morphological instability of γ′ particles in recently developed AD730^{TM} Ni-based superalloy is quantified, and the possible origin of this instability is investigated.

Little quantitative data is available on the kinetics of γ′ reprecipitation reaction in superalloys. Most studies (Ardell et Ozolins, 2005; Bian, 2015; Masoumi et al., 2016a; Meher et al., 2013; Monajati et al., 2004a) have been focused on the effect of different aging heat treatments on the size and morphology or coarsening kinetics of γ′ in superalloys. Rougier et al. (2013) developed a particle size distribution (PSD) model for numerical simulations of γ′ precipitation during isothermal aging of NiCrAl superalloys. They used a multicomponent diffusion model in order to calculate the growth rate. However, their model was fully coupled with CALPHAD (Computer Coupling of Phase Diagrams and Thermochemistry) for the calculation of the nucleation driving force, and this coupling is very expensive computationally. Y. Wang et al. (Sarosi et al., 2007; Wen et al., 2003; Wen et al., 2006) used phase field modeling to visualize the microstructure development and quantify physical phenomena such as impingement, particle coalescence or splitting by solving nonlinear time-dependent phase field equations within the framework of irreversible thermodynamics. However, to obtain accurate results, particularly for a new alloy, extensive

experimental work is needed to set realistic values for the boundary conditions and determine material parameters. Therefore, besides its valuable benefits, its application to new alloys is not straightforward. Bonvalet et al. (2015) recently proposed a numerical model for γ′ precipitation during the isothermal heat treatment of NiCrAl alloys. The model is based on the particle coarsening theory of Philippe et al. (2013), and cannot be directly applied to continuous cooling processes and to transient cooling conditions such as the one used in the present investigation. Olsen et al. (Jou et al., 2012; Olson et al., 2008; Wusatowska-Sarnek et al., 2003) used the PrecipiCalc^{TM} software to develop models for PSD and transformation rates. The software is built around thermodynamic computations and multicomponent diffusional nucleation and growth models to simulate multiphase precipitation. However, since the operation of this software is based on CALPHAD databases, calibration and independent experimental measurements need to determine the model parameters with high fidelity and minimum overfitting for each new alloy. As a consequence, these methods are not easy to apply for industrial applications due to the large computational time required. Many physical constants, such as element diffusion coefficients, surface energies, interface kinetic coefficients and driving forces for phase transformations, are also needed for obtaining reliable results in numerical models; this data is not always readily available for alloys with complex compositions (Kovačević et Šarler, 2005). The situation becomes even more complicated when a new alloy, such as the one used in the present investigation, is considered.

In order to overcome the limitations of numerical methods, semi-analytical models calibrated by experiments may be used. The Johnson-Mehl-Avrami (JMA) model (1941) is one of the most important semi-analytical models available, and plays a central role in transformation studies, where nucleation and growth mechanisms operate. The model has been widely applied to γ′ volume fraction evolution during isothermal dissolution and aging treatments (Cormier, Milhet et Mendez, 2007a; Giraud et al., 2013; Masoumi et al., 2016a). However, to the knowledge of the authors, no such model exists for the quantification of the kinetics of reprecipitation reaction and its mechanisms during the continuous cooling process of Ni-based superalloys. The JMA model holds some constraints in the case of isochronal transformations. Mittemeijer et al. (1992) extended the JMA equation to non-isothermal

transformations. However, the applicability of the model to complex alloy systems, such as Ni-based alloys, has not been reported.

On the basis of the above analysis, the objectives of this study are:
1- To analyze the size distribution and morphology of multiple populations of γ′ precipitates formed during continuous and interrupted cooling from supersolvus and subsolvus temperatures.
2- To develop and validate a semi-analytical model to predict γ′ reprecipitation kinetics at low and high cooling rates.
3- To develop a better understanding of fundamental mechanisms governing γ′ reprecipitation and its morphological instability as a function of the cooling rate.

4.3 Precipitation Kinetics

For the analysis of precipitation kinetics, a physical property such as specific volume/length or enthalpy of the material can be investigated as a function of time and temperature. Then, the fraction of transformation, Y, can be described by following JMA equation, which is applicable to both isothermal and non-isothermal analysis (Avrami, 1941; Mittemeijer, 1992):

$$Y = 1 - exp(-\beta^n) \tag{4.1}$$

where n is the Avrami exponent which depends on precipitate growth modes. For non-isothermal transformations, β is written as:

$$\beta = \int_0^t k(T)dt \tag{4.2}$$

where $k(T) = k_0(T)exp(-Q/RT)$ is the Avrami rate parameter which depends on the nucleation and growth rate and varies with t. Analytical approximation of the above integral using a limited development as proposed by Mittemeijer et al. (1992) gives:

$$\beta = \frac{RT^2}{\varphi Q} k(T)(1 - 2\frac{RT}{Q}) \tag{4.3}$$

where R is the gas constant, φ the cooling rate and Q the activation energy of the reaction. Values of t, T, Y and the kinetics parameters, n, Q and $k(T)$ representative of the precipitation process can be obtained from DTA measurements using the following procedure.

In a DTA run, the fraction of the precipitation $Y(T)$ at temperature T is given by (Jena, Gupta et Chaturvedi, 1989; Luo et al., 1993) :

$$Y(T) = \frac{A(T)}{A(T_f)} \tag{4.4}$$

where $A(T)$ is the area under the peak between the initial temperature of the peak T_i (i.e. temperature of precipitation onset) and temperature T, and $A(T_f)$ is the area of a peak between T_i and T_f in which T_f is the final temperature of the peak (i.e. temperature of precipitation end).

$A(T)$ is defined as:

$$A(T) = \int_{T_i}^{T} (\delta q) dT \tag{4.5}$$

where δq is obtained during a constant cooling rate test by subtracting the measured heat flow of the sample from that of the inert reference.

The precipitation kinetics, dY/dt, can be related to cooling rate, φ, in DTA scan by:

$$\frac{dY}{dt} = \frac{dY}{dT} \times \varphi \tag{4.6}$$

The growth exponent, n, can be obtained from the transformed fraction, Y_T, attained at a certain value of T, as measured for different cooling rates by (Liu et al., 2007) :

$$-ln[-ln(1-Y_T)] = nln\varphi \tag{4.7}$$

Finally, the activation energy (Q) of the process during non-isothermal cooling can be determined by (Mittemeijer, 1992):

$$-\frac{\partial ln(\frac{T_Y^2}{\varphi})}{\partial\left(\frac{1}{RT_Y}\right)} = Q \tag{4.8}$$

where T_Y is the temperature which is attained at a certain fixed value of Y. Using the above equations, it is possible to determine the kinetics of γ′ precipitation during continuous cooling and to study the governing mechanisms by determining n, $k(T)$ and Q.

4.4 Experimental Procedure

The AD730^{TM} material was provided by the Aubert & Duval company in the form of a forged square bar. The bar had been solutionized at 1080°C for four hours, and then air-cooled to room temperature. The chemical composition of the alloy is given in Table 4-1. The equilibrium volume fraction of γ′ is around 40%.

The DTA technique is a well-established technique for studying the kinetics of precipitation or phase changes in alloy systems (Chen et Jeng, 1997). The continuous cooling tests were carried out using a Diamond TG/DTA PerkinElmer with a Pt crucible and flowing Ar atmosphere. DTA experiments were conducted in order to determine γ′ transformation temperatures, to follow the evolution of the γ′ size, morphology and volume fraction during cooling, and to measure the heat flow. All experiments were conducted using high purity Ar to minimize potential oxidizing effects. The unit was calibrated using pure aluminum and gold, with precise melting points of 660°C and 1064°C, respectively. The samples were 2 mm ×2 mm ×0.5 mm in size, and were heated at rates of 10, 15, 65 and 120°C/min, up to 1200°C, held for one minute, and then cooled down to room temperature by the same rates of

10˚C/min (SC_{10}: Slow Cooling), 15˚C/min (SC_{15}), 65˚C/min (IC: Intermediate Cooling) and 120˚C/min (FC: Fast Cooling). The cooling rates were chosen in order to mimic the quenching of a reasonably large superalloy forged disc in air or oil. The 10˚C/min cooling rate is typical of the conditions encountered in industry for equiaxed solidification.

Table 4-1 Chemical composition of AD730™ (wt%) (Devaux et al., 2012c)

Ni	Fe	Co	Cr	Mo	W	Al	Ti	Nb	B	C	Zr
Base	4	8.5	15.7	3.1	2.7	2.25	3.4	1.1	0.01	0.015	0.03

For accurate and reliable measurements of the heat flow, all the DTA runs were corrected by subtracting the measured heat flow of the sample from that of a DTA baseline obtained from a run with an empty pan. In the DTA plots, the endothermic and exothermic reactions were plotted downward and upward, respectively. In order to validate the equation predicting γ′ size evolution obtained from DTA continuous cooling experiments, samples were heated at a rate of 120˚C/min, up to 1200˚C, held for one minute, and then water-quenched (WQ) to room temperature using the Gleeble™ 3800 thermomechanical simulator. The microstructure of the samples, and particularly the γ′ characteristics, were then examined with FEG-SEM. Discontinuous (interrupted) cooling tests were also carried out to study different nucleation bursts of γ′ during cooling cycles from subsolvus temperatures. For these tests, samples were heated from room temperature to 1100˚C at a rate of 120˚C/min, and held one minute at this temperature. The interrupted cooling consisted in continuous cooling at a constant rate of 120˚C/min, followed by immediate water quenching at 1040˚C or 780˚C.

For microstructure characterization, the specimen surface was prepared following standard metallographic preparation procedures and etched using a mixture of Regia water (2/3) and distilled water (1/3). Microstructural examination of the etched samples was carried out using a Hitachi SU70 FEG-SEM. The characterization of the nanometric size particles and morphology of the precipitates were conducted in secondary electron (SE) and back-scattered electron (BSE) modes. Analyses were carried out using low and high magnification SEM images ranging from 2000 to 100,000 magnifications in order to investigate the γ′

distributions and morphologies. In order to measure the dimensions and volume fractions of the γ′ precipitates, digitized microscopic images and ImageJ analysis software were used. Each reported value for γ′ size or volume fraction is an average of 5 measurements. In each case, area measurements on more than 100 precipitates were carried out using the ImageJ software. The particle radius was then calculated as the radius of a circle whose surface area equaled that of the corresponding particle.

4.5 Results

4.5.1 Continuous Cooling Precipitation from supersolvus Temperature

4.5.1.1 DTA Data Analysis

Figure 4.1 shows DTA diagrams with different endothermic and exothermic peaks showing the dissolution and precipitation in the AD730^{TM} alloy measured for the four investigated heating and cooling rates. Two endothermic peaks can clearly be observed at the 65˚C/min and 120˚C/min heating curves. Peak A occurs around 800˚C, and corresponds to the dissolution of secondary γ′ particles. Peak C is related to the dissolution of primary γ′ and is observed for all heating rates. This peak is around 1080˚C for the 10˚C/min heating rate and 1120˚C for the 120˚C/min heating rate.

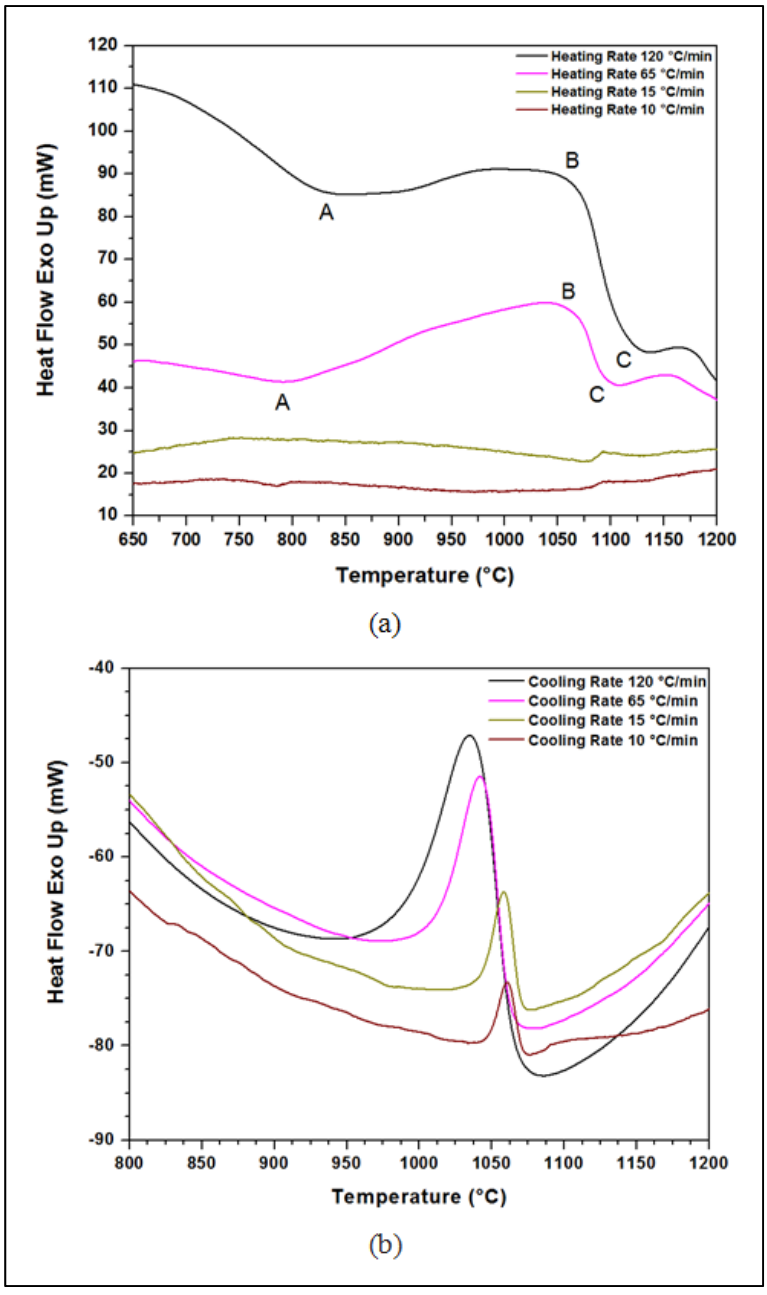

Figure 4.1 DTA curves showing (a) γ′ dissolution and precipitation peaks during heating for different heating rates (b) γ′ precipitation peaks during cooling for various cooling rates.

Figure 4.1 (b) shows the results of the cooling portion of the DTA diagram, and the phase transformation temperatures values obtained during cooling are provided in Table 4-2. It can be seen that the first burst of nucleation initiates at 1075°C for the SC_{10} condition and at

1070°C for the FC condition. Both bursts occur below Peak C (i.e., primary γ′ solvus temperature). As the cooling rate increases, the peak shifts to lower temperatures and undercooling increases. For example, the peak temperature is around 1060°C for the SC_{10} sample, while it drops to 1035°C for the FC condition.

Table 4-2 Values of phase transformations temperatures during cooling for various cooling rates

Cooling Rate (°C/min)	Temperature of maximum precipitation (°C)	Temperature of precipitation end (°C)
10	1060	1039
15	1058	1020
65	1042	980
120	1035	945

Figure 4.2 displays the evolution of the γ′ precipitated fraction (Y) as a function of temperature (T) for the four cooling rates. Figure 4.2 was obtained using Figure 4.1 (b) and Eqs. (4.4) and (4.5). It can be seen that as the cooling rate increases, the curves shift to lower temperatures. For example, for the SC_{10} condition, 25% and 50% of the volume fraction of γ′ particles reprecipitate until 1063°C and 1059°C, respectively. However, these fractions are obtained at up to 1040°C and 1027°C, respectively, for the FC condition. The evolution of the precipitation rate (dY/dt) with temperature, calculated from DTA data (Figure 4.1 (b)), using Eqs. (4.4) and (4.6), is shown in Figure 4.3 for different cooling rates. An analysis of Figure 4.3 indicates that as the cooling rate increases, the maxima of the transformation rate curves shift by 25°C to lower temperatures, going from 1060°C for 10°C/min to 1035°C for 120°C/min.

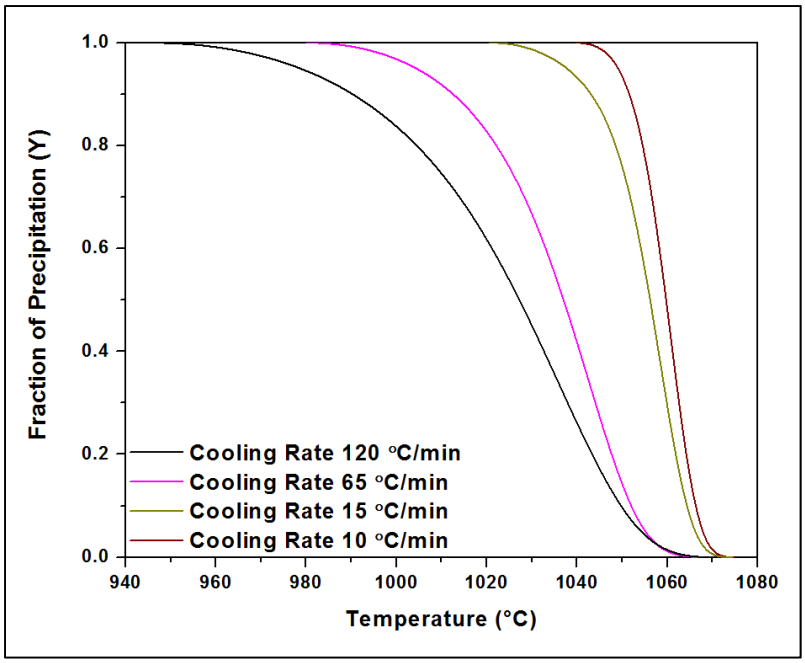

Figure 4.2 Amount of γ′ precipitation as a function of temperature for various cooling rates showing the curves shift to lower temperatures with increasing the cooling rate.

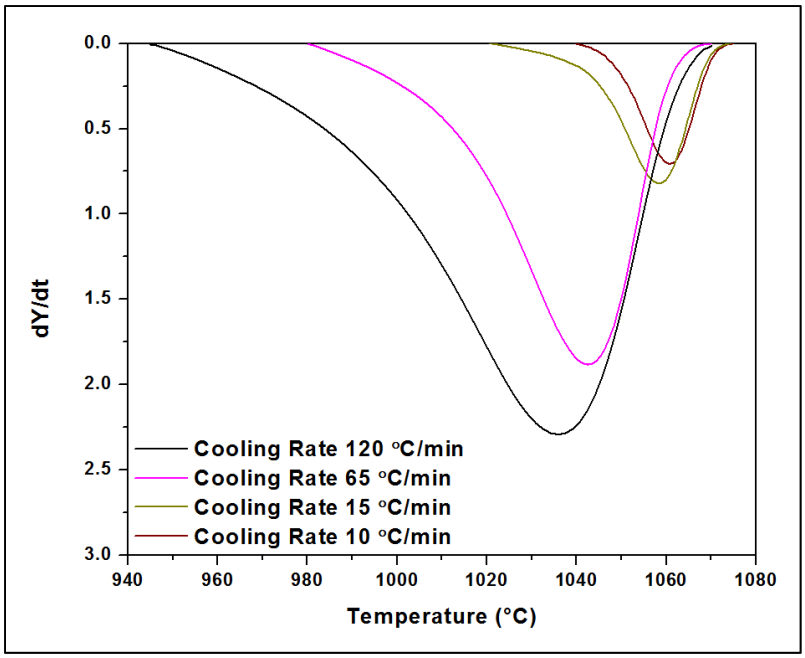

Figure 4.3 γ′ precipitation rate as a function of temperature for various cooling rates showing the shift of the maxima of the transformation rate curves to lower temperatures with increasing the cooling rate.

4.5.1.2 Determination of Precipitation Kinetics Parameters

In order to develop a general precipitation equation, the kinetics parameters of precipitation $(n, Q, k(T))$ can be determined from DTA measurements using the non-isothermal JMA model presented in Eqs. (4.1) to (4.8). The method used in the present investigation is detailed as follows:

A) *Determination of the Avrami coefficient*

The coefficient n can be determined from the slope of the plot $ln[-ln(1-Y_T)]$ versus $ln\varphi$. Using the above procedure, the coefficient n was determined to be in the range 1.5-2.3. In order to avoid displaying similar data, the plot for the minimum value of exponent n (n =1.5) is provided only in Figure 4.4. It must be noted that in order to obtain reliable data, the transformed fraction, Y_T, in Eq. (4.7) should be considered in the same temperature range for all cooling rates. This temperature range is between 1039°C and 1070°C, as shown in Figure 4.2.

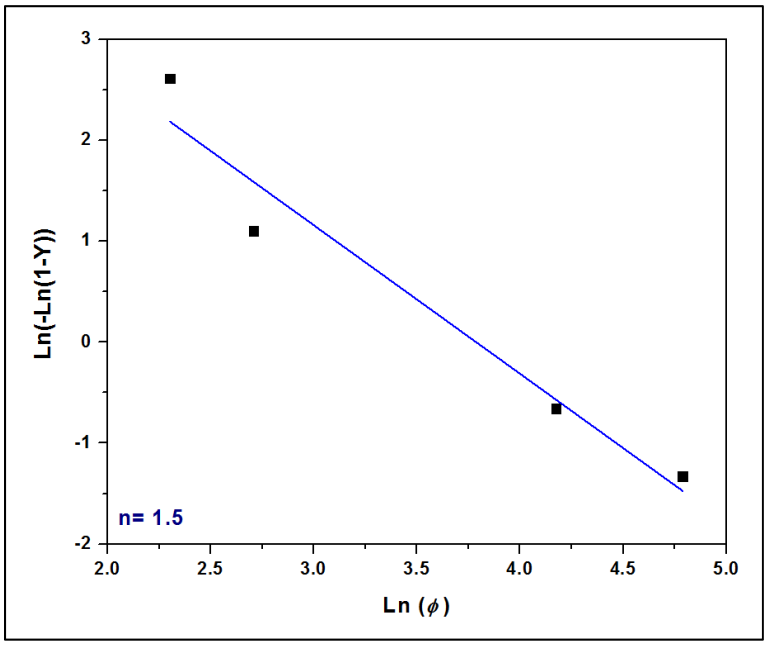

Figure 4.4 The relationship between $ln[-ln(1-Y)]$ and $ln\varphi$ at 1039°C for determining Avrami exponent of γ′ precipitation (R^2= 0.95).

B) Determination of the Activation Energy

Figure 4.5 shows the plot of $\ln(T_\gamma^2/\varphi)$ versus $1000/RT_\gamma$. Based on Eq. (4.8) and using Figure 4.5, the activation energy for γ′ reprecipitation, Q, was obtained as 396 kJ/mol from the slope of the linear fit to the data. The calculated value is close to the activation energy value of γ′ precipitation reported for Waspaloy (398 kJ/mol) (Whelchel, 2011). Rosen et al. (1994) reported an activation energy of 250 kJ/mol for γ′ precipitation in several wrought Ni-based superalloys. This value for activation energy is close to that of nickel self-diffusion. However, the alloys used by Rosen et al. (1994) were of a much simpler composition than the AD730^{TM} alloy used in this study. The smaller number of alloying elements could account for the activation energy being lower than that for AD730^{TM} which has significant amounts of alloying elements.

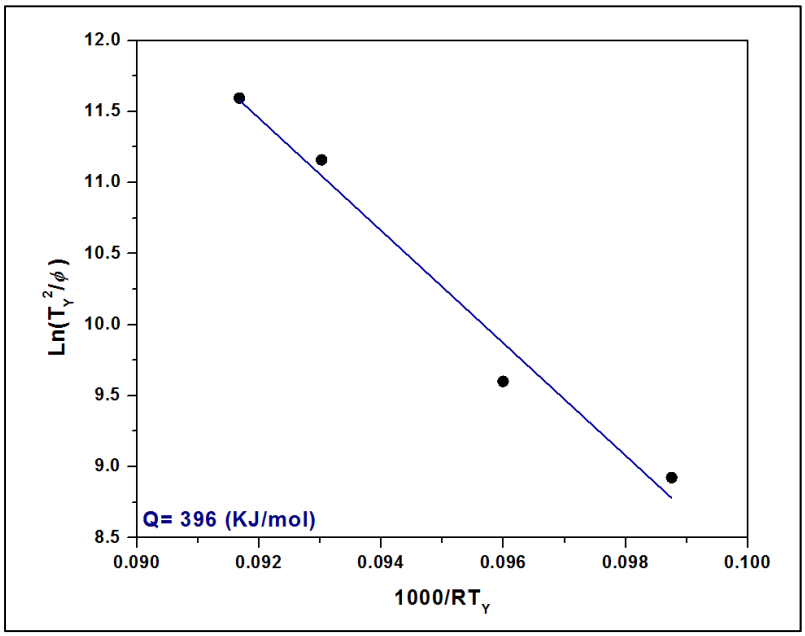

Figure 4.5 The relationship between $\ln(T_\gamma^2/\varphi)$ and $1000/RT_\gamma$ for determining activation energies of γ′ precipitation (R^2= 0.98).

C) Determination of the Avrami Rate Parameter

The rate parameter $k(T)$ can be determined from $k(T) = k_0(T)exp(-Q/RT)$. In order to provide the evolution of $k_0(T)$ with temperature, a function needs to be developed. This function should be defined, in which difference between γ′ precipitated fraction (Y) calculated using the non-isothermal JMA model and that of the experimental data (Figure 4.2) is small. In order to develop this function, MATLAB® was used to optimize the kinetics models for SC_{15} and FC conditions to the experimental values.

Optimization was performed using the Nelder-Mead algorithm as implemented in the MATLAB®, and the experimental data inputs used as initial values. The mean squared error, MSE, which is used as an indicator of the quality of the model (Palavar, Özyürek et Kalyon, 2015), is the average squared difference between experimental data (Figure 4.2) and the calculated values of Y at each of the n time steps (n =80-200).

$$MSE = \frac{1}{n}\sum_{i}^{n}(Y_{model.i} - Y_{exp.i})^2 \tag{4.9}$$

The average difference between the value determined by optimization and the experimental value of the kinetic parameter $k_0(T)$ divided by the actual value is defined as the mean absolute percentage error, $MAPE$.

$$MAPE = \frac{1}{n}\sum_{i}^{n}\left|\frac{\Delta k_0(T)}{k_{0\,exp}}\right| = \frac{1}{n}\sum_{i}^{n}\left|\frac{k_{0\,optimized} - k_{0\,exp}}{k_{0\,exp}}\right| \tag{4.10}$$

On the basis of the optimization process, $k(T)$ is developed as a function of temperature as follows:

$$k(T) = [k_0 + A_1 exp\left(\frac{-(T-T_0)}{t_1}\right) + A_2 exp\left(\frac{-(T-T_0)}{t_2}\right) + A_3 exp\left(\frac{-(T-T_0)}{t_3}\right)]exp(\frac{-Q}{RT}) \quad (4.11)$$

The constants of this function were obtained using experimental data at cooling rates of 15˚C/min (SC_{15}) and 120˚C/min (FC). Then, the evolution of the γ′ precipitated fraction (Y) as a function of temperature was determined using Eqs. (4.1) and (4.3), $k(T)$, Q and n at these cooling rates.

The constants of Eq. (4.11), $k_0,\ T_0,\ A_1,\ t_1,\ A_2,\ t_2,\ A_3,\ t_3$, are given in Table 4-3 for SC_{15} and FC conditions. Figure 4.6 (a) shows the error between the non-isothermal JMA model and the experimental data is negligible.

Table 4-3 The constants of $k_{SC15}(T)$ and $k_{FC}(T)$ equations for SC_{15} and FC conditions, respectively

Cooling Rate (°C/min)	k_0	T_0	A_1	t_1	A_2	t_2	A_3	t_3
15	1.46×10^{15}	1293.99	4.5×10^{15}	1.92	6.09×10^{15}	22.24	7.45×10^{15}	22.24
120	7.07×10^{15}	1220.01	9.3×10^{17}	23.62	2.48×10^{17}	6.57	5.22×10^{16}	1.4

The corresponding differences between input (experimental) values and the optimized value of the kinetic parameter $k(T)$ are given in Table 4-4. It can be seen that the model is able to correctly describe the experimental kinetics, as evidenced by small MSE values for SC_{15} and FC conditions.

The developed equations of $k(T)$ for SC_{15} and FC samples were also validated respectively for the SC_{10} and IC conditions, and the results are shown in Figure 4.6 (b) and Table 4-4.

The results show that MSE and $MAPE$ are respectively less than 7 and 6% for the SC_{10} and IC conditions. Therefore, the equation of $k(T)$ for SC_{15} condition, $k_{SC_{15}}(T)$, is applicable for

slow cooling rates lower than 15˚C/min, and the equation of $k(T)$ for the FC condition, $k_{FC}(T)$, can be applied for cooling rates higher than 65˚C/min.

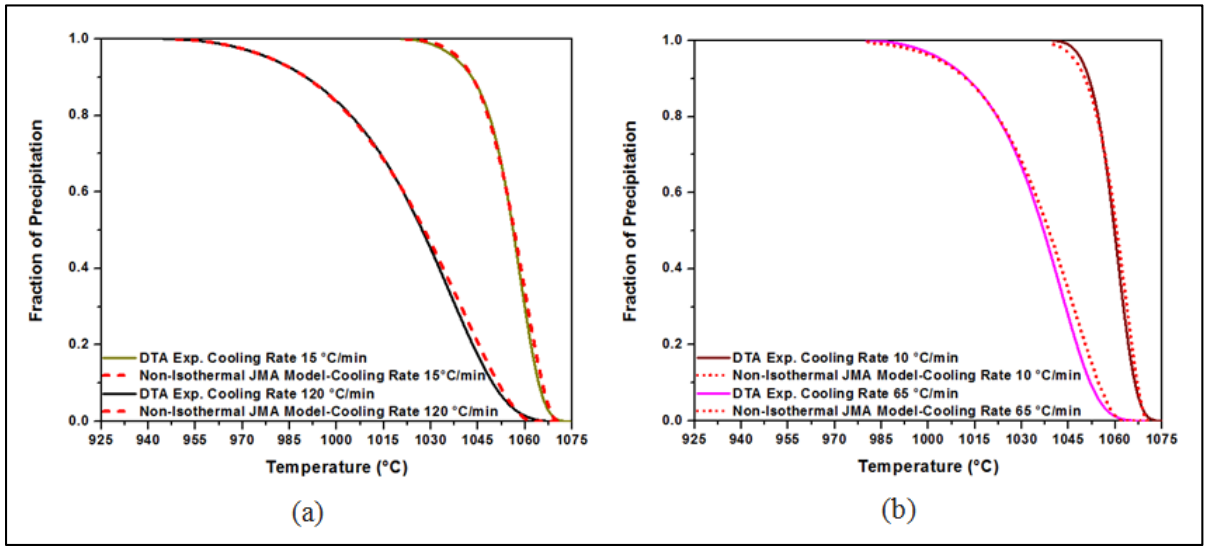

Figure 4.6 (a) Comparison between experimental data of DTA (solid lines) and predictions by the non-isothermal JMA model (dashed lines) using developed k(T) function for SC_{15} and FC conditions (b) Validating developed equations of $k_{SC15}(T)$ and $k_{FC}(T)$ for SC_{10} and IC conditions, respectively. The error between the experimental data (solid lines) and the calculated model (dot lines) is small.

Table 4-4 The results of optimizing kinetics models to the experimental reprecipitation kinetics for SC_{15} and FC conditions and using optimized $k_{SC15}(T)$ and $k_{FC}(T)$ models for SC_{10} and IC conditions, respectively. For the optimized parameter $k_0(T)$, the mean absolute percentage error, MAPE, is given by Eq.(4.10. Additionally, the quality of the optimization is quantified by the mean squared error, MSE (Eq.(4.9).

Cooling Rate: (°C/min)	10	15	65	120
$MAPE$	5.15	1.99	4.1	1.01
$MSE \times 10^4$	6.98	1.86	5.12	0.91

On the basis of the above calculations, and considering an average value of 1.8 for the coefficient n, the kinetics of γ′ reprecipitation in the AD730^{TM} superalloy can be described by the following general equation for both low and high cooling rates:

$$Y = 1 - exp[-(\left(\frac{2.1 \times 10^{-5} T^2}{\varphi}\right) k(T)(1 - 4.2 \times 10^{-5} T))^{1.8}] \quad (4.12)$$

where $k(T) = k_{SC_{15}}(T)$ for low cooling rates and $k(T) = k_{FC}(T)$ for high cooling rates with the various constants provided in Table 4-3. It is important to note that the methodology presented in this study can be applied to other Ni-based superalloys where γ′ reprecipitation may take place.

4.5.1.3 Influence of Cooling Rate on γ′ Characteristics

Slow, intermediate and fast cooling from supersolvus temperatures result in multimodal distribution of γ′ precipitates, as will be shown later in this section. This multimodal distribution of particles can be divided into different groups based on their morphology and size. Fig. 7 shows the morphology and size scale of the first population of γ′ particles for samples cooled under the four investigated cooling rates. The particles' shapes range from relatively round and regular (Figure 4.7 (a)) for the FC condition to fully irregular (Figure 4.7 (d)) for the SC_{10} condition. Papon et al. (2006) and Christian et al. (1975) suggested that when particle growth is spherical or irregular, the Avrami exponent n varies between 1.5 and 2.5. In the present investigation, the n value ranges between 1.5 and 2.3, thus indicating that γ′ growth in the AD730^{TM} alloy follows a diffusion-controlled growth process. This is also confirmed by micrographs in Figure 4.7.

Figure 4.8 shows a correlation between average diameters of the first population of γ′ precipitates with the cooling rate. It can be seen that the average sizes of γ′ particles are about 196 nm for the SC_{10} condition and 61 nm for the FC condition. Since γ′ growth during cooling is a diffusion-controlled process (Vaunois et al., 2010) , a power law relation could describe the evolution of size with the cooling rate using the data presented in Figure 4.8:

$$D_{\gamma'} = 521 \times \varphi^{(-0.44)} \quad (4.13)$$

where $D_{\gamma'}$ is the precipitate diameter in nm and φ is the cooling rate in ˚C/min. The above relation provides a reasonable prediction (R^2 =0.97) of the size evolution over a very broad

range of cooling conditions for the first population of cooling γ′ particles. In order to validate the above equations, a heat treatment cycle, 1200°C/1 minute/ cooling at a rate of 100°C/sec, was performed using Gleeble™ 3800. The morphology and distribution of γ′ precipitates obtained after the above heat treatment cycle were examined using high magnification SEM micrographs, and are presented in Figure 4.9 (a) and (b). The results show that a monomodal size distribution of very fine spherical particles, ranging from 7 to 20 nm, with an average size of 13 nm was obtained. The particle diameter should be 11 nm according to Eq. (4.13), confirming the validity of the proposed equation.

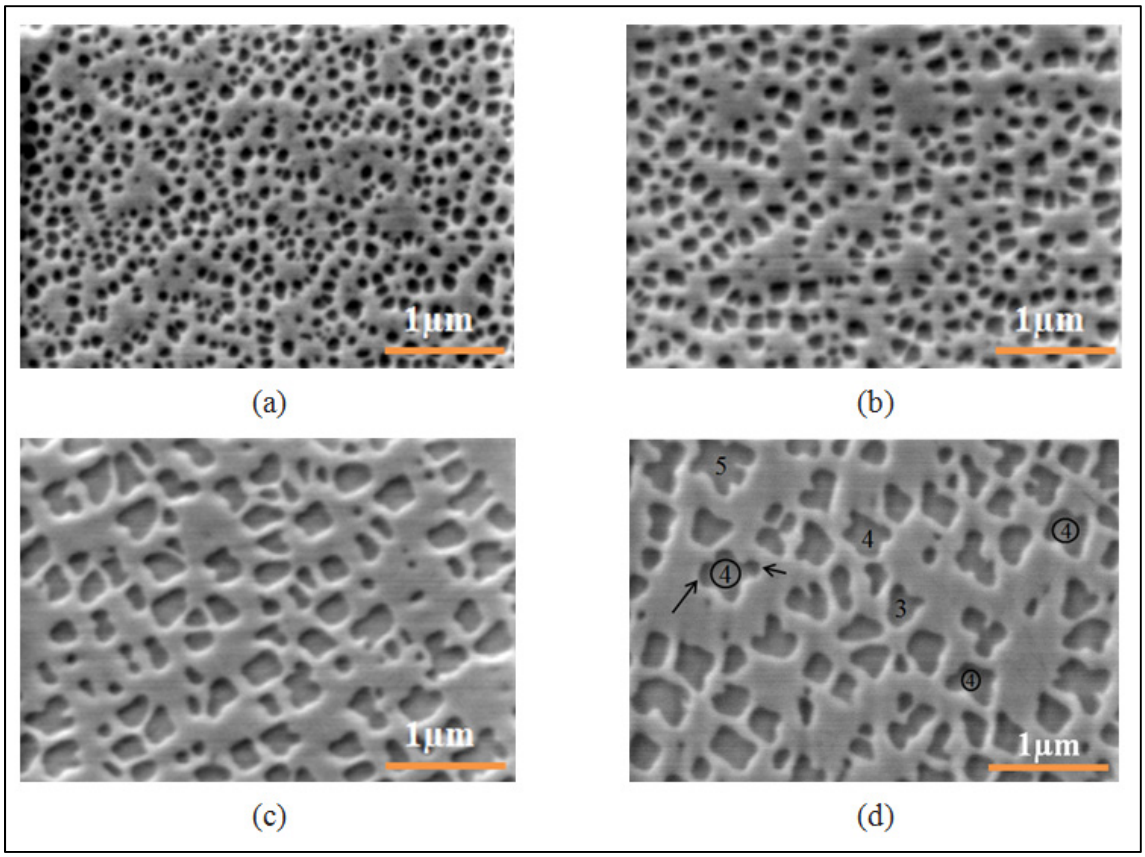

Figure 4.7 Scanning electron microscopy images of the (a) FC (b) IC (C) SC_{15} (d) SC_{10} samples, showing the morphology and size-scale of first generation of γ′ precipitates. Some of protrusions are shown by arrows and their number, l, was indicated inside some particle core areas.

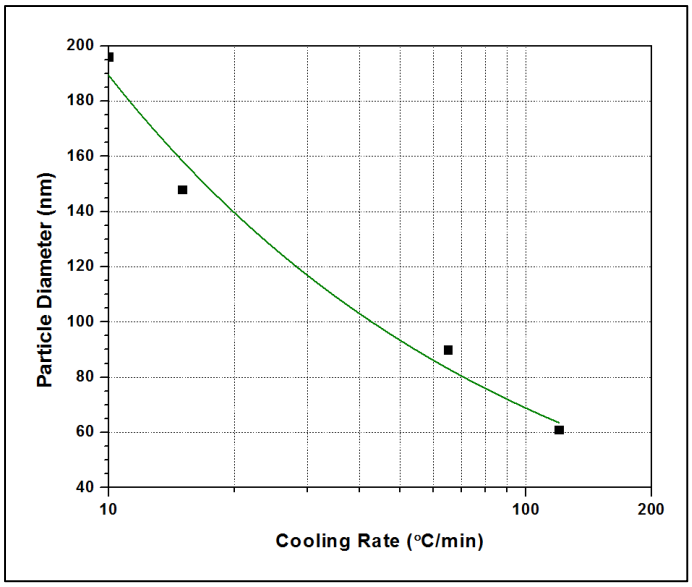

Figure 4.8 Average diameter of first generation of γ′ precipitate as a function of cooling rate (R^2 =0.97).

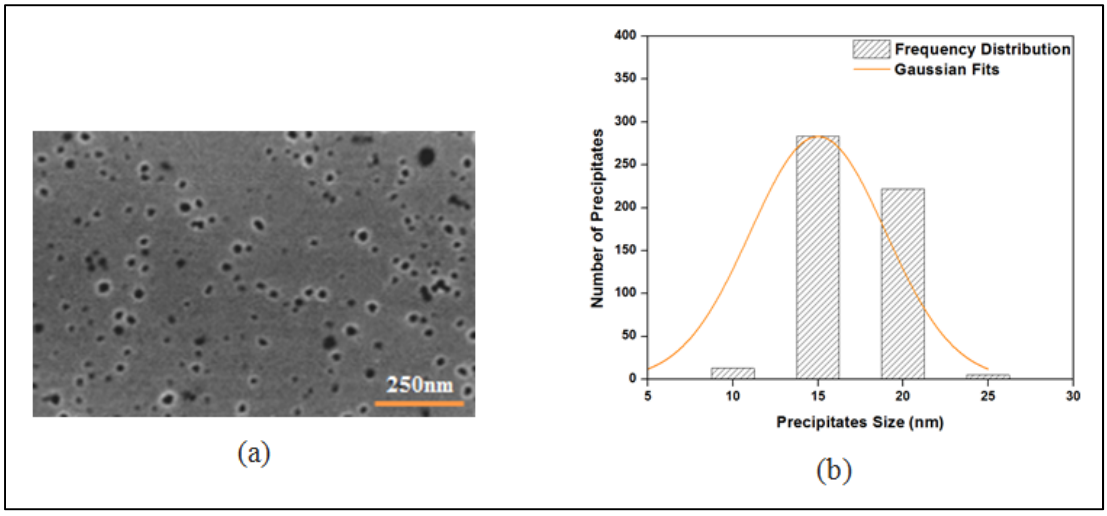

Figure 4.9 (a) Scanning electron microscopy image
(b) Precipitate size distribution plot of the Gleeble™ 3800 sample.

The second population of cooling γ′ particles for the SC_{10} and FC conditions are shown in Figure 4.10 (a) and (b). Particle size measurements indicate that γ′ particles range from 11 to 35 nm for the SC_{10} and from 8 to 12 nm for the FC condition. A detailed particle size distribution analysis carried out over 300 particles clearly reveals a multimodal distribution for the SC_{10} condition as shown in Figure 4.11.

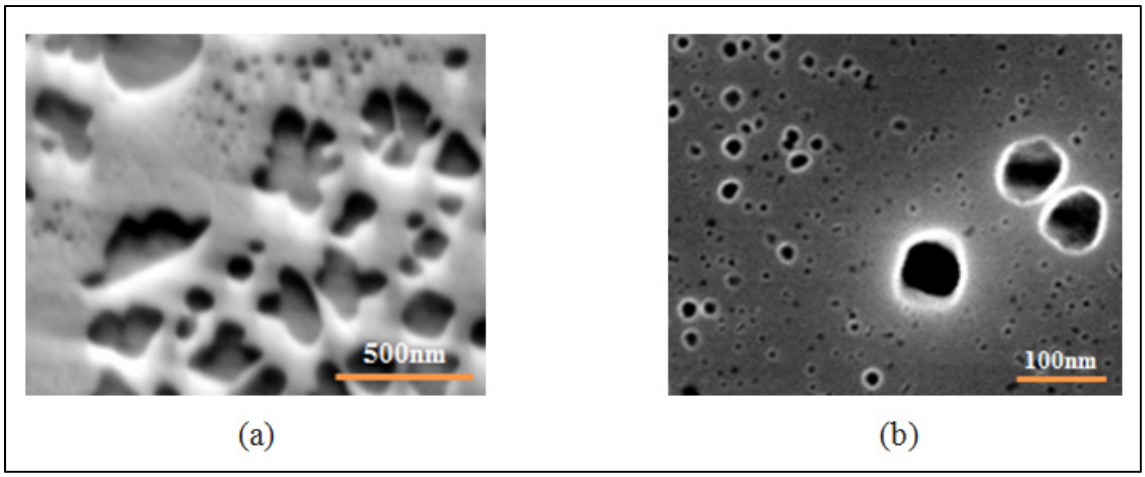

Figure 4.10 BSE and SE images of the (a) SC_{10} (b) FC samples, respectively, showing first and second population of cooling γ′ precipitates.

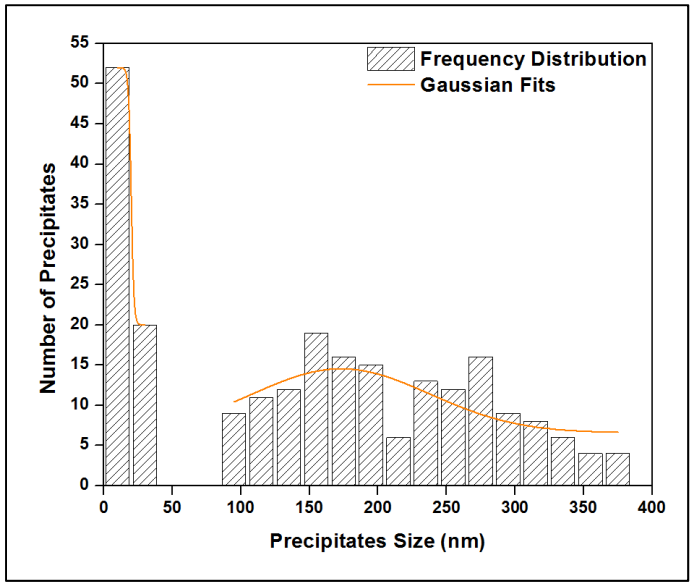

Figure 4.11 Precipitate size distribution plot of SC_{10} sample showing the size difference between the first and second population of cooling γ′ precipitates.

The size distribution of the third population of γ′ precipitates could not be precisely quantified due to their small size (less than 10 nm). A particle volume fraction analysis showed that the volume fraction of γ′ from the first nucleation burst forms about 85% of the total amount of γ′ precipitates in the AD730^{TM} alloy (which is about 40%) for the SC_{10}

condition, indicating that a very small portion of γ′ will be formed as second or third populations of γ′ precipitates.

4.5.2 Precipitation during Discontinuous Cooling from Subsolvus Temperature

Interrupted cooling tests were carried out at a cooling rate of 120°C/min to study the development of γ′ precipitates during a cooling process which represents interpass cooling during forging. It should be noted that the alloy contains around 7% initial primary γ′ when cooling from subsolvus temperature. The distribution of γ′ precipitates, presented in Figure 4.12, reveals a bimodal distribution during cooling from 1100°C interrupted either at 1040°C or 780°C.

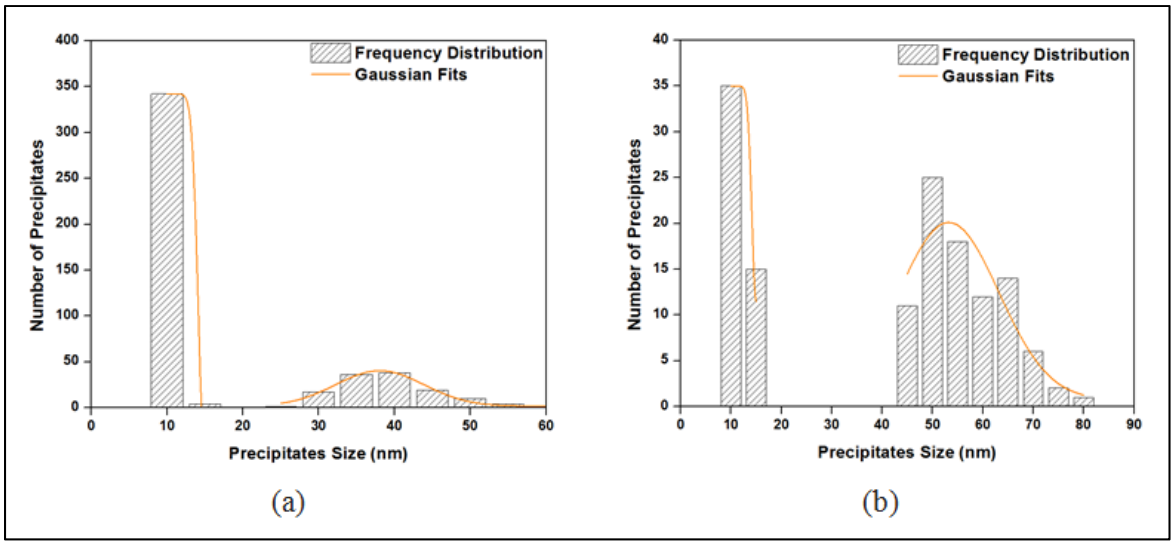

Figure 4.12 Precipitate size distribution plot of (a) high interrupt temperature (b) low interrupt temperature, from 1100°C showing the size difference between the first and second population of γ′ precipitates.

For the interrupt temperature of 1040°C, the first burst of nucleation occurs in the 1100 -1040°C interval (Figure 4.13 (a)), and results in the formation of spherical γ′ particles 25 to 50 nm in size and 13% in volume fraction. The second burst of nucleation occurs during water quenching from 1040°C, and leads to much smaller particles (less than 10 nm), with a small volume fraction of 2.5%. The density of the small particles is about 9 times more than that of the larger precipitates.

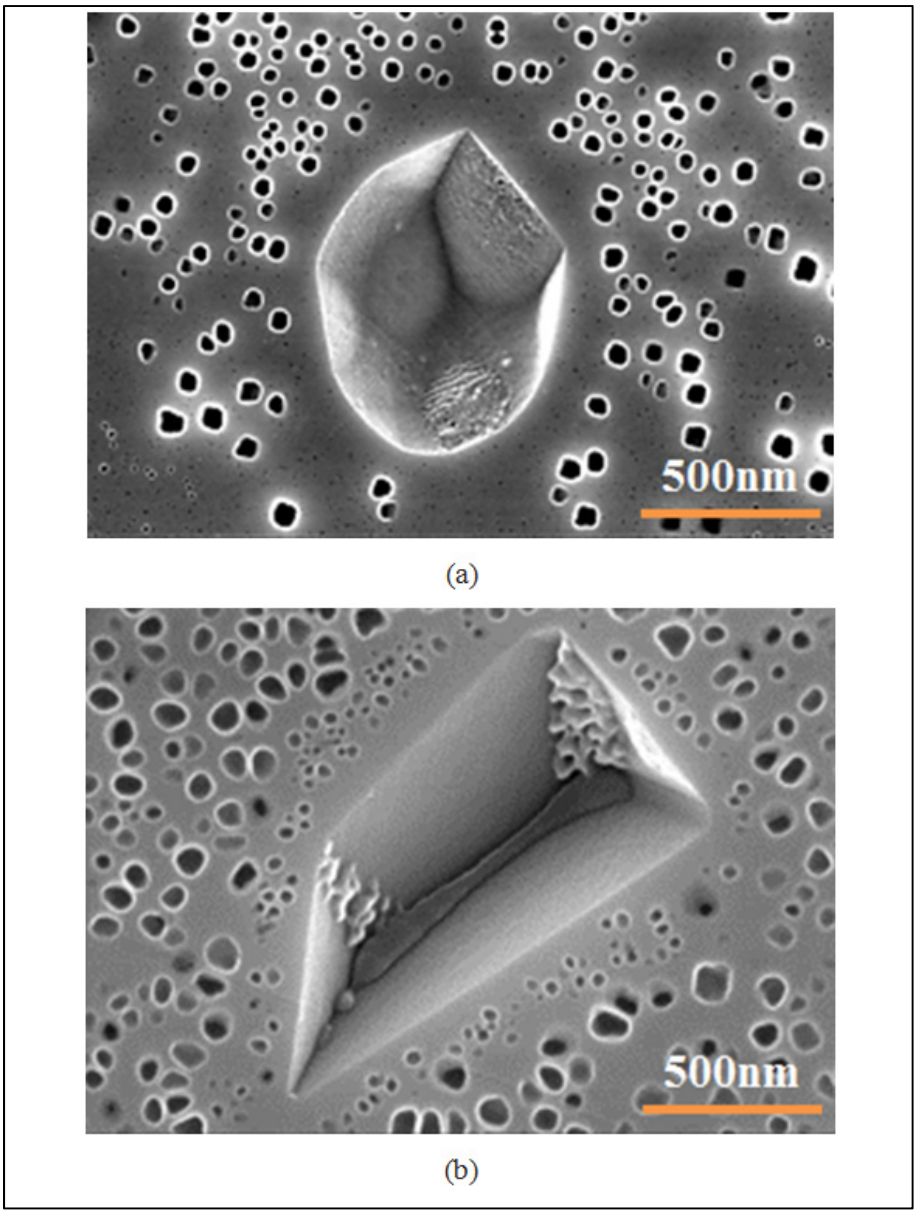

Figure 4.13 Scanning electron microscopy image of the (a) first burst of nucleation at high interrupt temperature (b) coarsening of first generation of γ′ and second burst of nucleation between initial primary and existing γ′ precipitates at low interrupt temperature. The interrupted cooling consisted of continuous cooling from 1100°C at a constant rate of 120°C/min, followed by water quenching at 1040°C (high interrupt temperature) or 780°C (low interrupt temperature).

For the 780°C interrupt temperature, the first population of γ′ particles formed in the 1100°C-780°C interval was 40 to 80 nm in size, with a volume fraction of about 24%. The

average size of these particles is around 60 nm (Figure 4.12 (b)). This value is very close to the one obtained after continuous cooling (FC), as shown in Figure 4.8. This finding indicates that, due probably to low diffusion, very little or no growth of γ′ particles takes place below 780˚C.

Furthermore, as shown in Figure 4.13 (b), a second burst of nucleation takes place in the 1040-780˚C interval. This second nucleation gives rise to precipitates which are much smaller in size (8 to 15 nm) and volume fraction (3%). The average size and volume fraction for the second population of γ′ particles are the same as those after continuous cooling (FC), 10 nm and 3%. This indicates that a second burst occurs between 1040 and 780˚C in AD730^{TM}. This finding is in agreement with DTA results (Figure 4.1 (a)) which showed that the solvus for the secondary γ′ is around 825˚C for a 120˚C/min heating rate.

4.6 Discussion

4.6.1 Analysis of DTA Data during the Heating Cycle

The DTA graphs shown in Figure 4.1 (a) reveal both endothermic and exothermic peaks, indicating that dissolution and precipitation take place during the heating cycle. The peak temperature for precipitation during heating corresponds to the maximum precipitation rate resulting from a competition of two opposing factors: 1) An increase in the diffusivity of the precipitating elements at higher temperatures, which results in an increase in precipitation; 2) A decrease in the driving force for precipitation, due to lower supersaturation, at higher temperatures (Gao, Starink et Langdon, 2009; Masoumi et al., 2016a). The competition between these two phenomena results in the occurrence of various peaks labeled from A to C in Figure 4.1 (a): A- dissolution of secondary γ′ precipitates; B- precipitation of primary γ′ precipitates; C- dissolution of primary γ′ precipitates. The results obtained are in agreement with those reported by other researchers who observed similar dissolution-reprecipitation sequences in precipitation-hardened aluminum alloys (Buha, Lumley et Crosky, 2008; Gao, Starink et Langdon, 2009; Kamp, Sinclair et Starink, 2002). The results also confirm the findings of Boettinger et al. (2006), who observed that the limits of the peaks become more and more visible as the heating rate increases.

The full sequence of precipitations of different populations of γ′ particles is only possible when the alloy is maintained below the γ′ solvus temperature of *that* population. For instance, if the alloy is kept at a temperature above the secondary γ′ solvus, but below the primary γ′ solvus (peak B), only primary γ′ could precipitate.

Based on the classical nucleation theory, the critical free energy for the nucleation of a spherical particle (G^*) is given by (Russell, 1980):

$$G^* = \frac{16\pi\sigma^3}{3(\Delta\, G_v)^2} \tag{4.14}$$

where σ is the interfacial energy between γ and γ′ and $\Delta\, G_v$ is the driving force for precipitation. As shown in Figure 4.10, the second population of cooling γ′ particles is very small in size (10 nm) and spherical in shape. Such characteristics result in highly coherent precipitates with the matrix (i.e., minimum interfacial energy and misfit strains), and consequently, very low values for the nucleation barrier G^* (Reed, 2006b; Sato et al., 2006) DTA results (Figure 4.1 (a)) show that secondary γ′ particles dissolve at around 785°C and 825°C for the SC_{10} and FC conditions, respectively. It has been reported that for each transformation peak in heating, there should be an equal peak for reprecipitation at a few tens of degrees undercooling (Boettinger et al., 2006). Therefore, it is expected that γ′ particles which dissolve during heating will reprecipitate during cooling. This was confirmed in the present investigation by an electron microscopy examination of the microstructure of the samples as shown, for example, in Figure 4.10 (a) and (b).

4.6.2 Effect of Cooling Rate on γ′ Stability during Growth

The morphology of γ′ precipitates is a key factor in determining the properties of superalloys (Papon, Leblond et Meijer, 2006). The irregular growth of precipitates during slow cooling observed in the present work (Figure 4.7 (d)) is analyzed in the context of the Mullins and Sekerka (MS) model (1963). In the model, the critical particle radius (r_{cr}) for the occurrence of morphological instability, defined by the presence of protrusions on spherical particles, is given by:

$$r_{cr} = [\left(\frac{1}{2}\right)(l+1)(l+2)+1]r^* \tag{4.15}$$

where l is the number of protrusions.
The critical radius (r^*) for nucleation is given by:

$$r^* = \frac{2\Gamma_D}{S} \tag{4.16}$$

with $S = \frac{(C_\infty - C_0)}{C_0}$ representing supersaturation, and $\Gamma_D = \frac{\sigma\Omega}{RT}$ showing capillary constant. C_0 is the equilibrium solute concentration at the precipitate/solid solution interface, C_∞ is the initial solute concentration in the supersaturated matrix, σ the matrix-particle interfacial energy, and Ω is the increment of precipitate volume per mole of added solute. Finally, R is the gas constant, and T the absolute temperature.

In order to calculate the precipitate critical radius, an estimation of Γ_D and S must be made. Using σ and Ω values for superalloys reported by Porter (1983), Γ_D was determined to be $9.7 \times 10^{-4}\ \mu m$. Also, using the Thermo-calc® software, C_0 was calculated for AD730™ (Masoumi et al., 2016a), and consequently, a maximum value of 0.4 was obtained for supersaturation constant 'S' when Al and Ti were considered as solutes.

Two-dimensional protrusions on spherical γ′ particles are observed in Figure 4.7 (d), as indicated by the arrows. The number of protrusions, l, was calculated to be 4 for samples slowly cooled from 1200°C. The measurements were made over 100 particles on 15 different high magnification electron micrographs, such as the one shown in Figure 4.7 (d).

Using the above data and Eqs. (4.15) and (4.16), the precipitate critical radius for slow cooling from 1200°C was calculated to be 78 nm. In order to compare the predicted value with experimental findings, the average core radius of particles was measured and determined to be 89 nm. As for the calculation of l, this value represents the average of 100 particles core radii measurements over 15 high magnification SEM micrographs, indicated by circles in Figure 4.7 (d). A relatively good agreement is observed between measured and

calculated values. The difference seen (of about 12%) may be due to the fact that the experimental conditions of Figure 4.7 (d) do not correspond *exactly* to the onset of instability, as it is very difficult to achieve such precisions experimentally.

The variation of precipitate critical radius versus supersaturation is plotted in Figure 4.14 for $l = 4$. It can be observed that precipitates are stable below and unstable above the critical radius r_{cr}. In Figure 4.14, the growth routes of precipitates for slow cooling and water quenching conditions are shown schematically by paths 1 and 2, respectively. In both cases, samples were cooled from above the γ′ solvus temperature (T_s). According to MS theory (Mullins et Sekerka, 1963), morphological instability depends on the domination of either supersaturation or the capillary effect. Once supersaturation is sufficiently built up, spherical particles become unstable. Therefore, the formation of protrusions during slow cooling (path 1) should occur as sufficient supersaturation can build up during a temperature drop (Figure 4.14). Path 1 shows that at the start of nucleation, the shape of the precipitates is mostly spherical due to small supersaturation. As higher supersaturation is present in the case of undercooling, these particles will grow into the unstable zone.

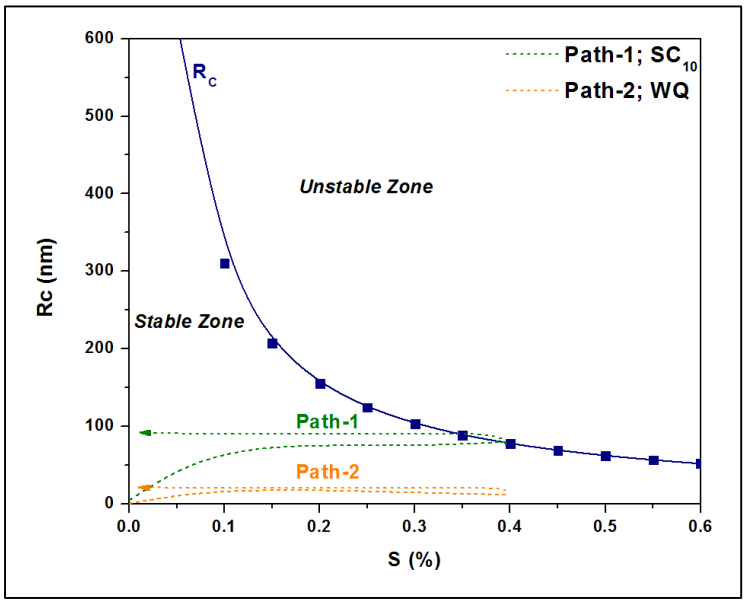

Figure 4.14 The calculated variation of the critical precipitate radius with supersaturation and schematic illustration of possible growth trajectories of spherical precipitates for SC_{10} (path-1) and WQ (path-2).

If multiple bursts of precipitates are considered, then after the first burst of nucleation, few γ′ nuclei will form at high temperatures due to the small undercooling below γ′ solvus (as shown in DTA results in Figure 4.1 (b)). Under these conditions, far from these particles, the γ matrix will remain supersaturated until lower temperatures, i.e., below the peak for the formation of the first population of cooling γ′. Supersaturation will increase further with an additional drop in temperature, such that the second burst of nucleation can occur at these sites (Figure 4.10). The nucleation of this population of cooling γ′ will reduce the supersaturation of solute elements, and with the third nucleation burst, most of the supersaturation is consumed, and the γ matrix reaches equilibrium. While it is expected that once the level of supersaturation is decreased, morphological instability should also decrease (return of path 1 to the stable region), γ′ particles keep their morphological instability, as shown in Figure 4.7 (d). This is probably due to the fact that most of the supersaturation is consumed for the second and third nucleation bursts, rather than for the growth of γ′.

In the light of the above analysis, it can be said that the first population of γ′ particles is formed between 1075°C and 1039°C, and grow rapidly due to high diffusion at high temperatures, and results in an irregular shape or instability (Figure 4.2 and Figure 4.7 (d)). The results also indicate that cooling down to room temperature and reduced supersaturation will not necessarily remove any shape irregularity.

In contrast, when high cooling rates are employed (Figure 4.14-path 2), instability is prevented. This is probably due to the high number of reprecipitated fine γ′ particles, which increases in the presence of high cooling rates. Indeed, as shown in Figure 4.1 (b) and Figure 4.3, higher cooling rates result in increased undercooling below the γ′ solvus temperature, and therefore in higher supersaturation and faster nucleation rates. The proximity of the precipitates results in the overlapping of their diffusion fields and in a rapid reduction of supersaturation around the newly nucleated particles. This overlapping inhibits the instable growth of γ′ precipitates, resulting in the formation of spherical shape particles (Figure 4.9 (a) and Figure 4.10 (b)).

The influence of the cooling rate on the morphology of γ′ precipitates is further illustrated in Figure 4.15. It can be seen that during cooling from supersolvus temperature, the first

population of γ′ precipitates in AD730^{TM} keeps a spherical shape under fast cooling conditions (FC). The particles coarsen, but still keep their spherical shapes during intermediate cooling (IC).

However, with a further decrease in the cooling rate (SC_{15}), they coarsen very rapidly, and develop a cuboidal, and then butterfly, shape. In addition, as shown in Figure 4.7, the density of the first population of γ′ precipitates is higher for the FC condition, at 35/μm^2, compared to 3/μm^2 for the SC_{10} condition. This value for the WQ condition is 85 times higher than that of the SC_{10} condition (Figure 4.7 (d) and Figure 4.9).

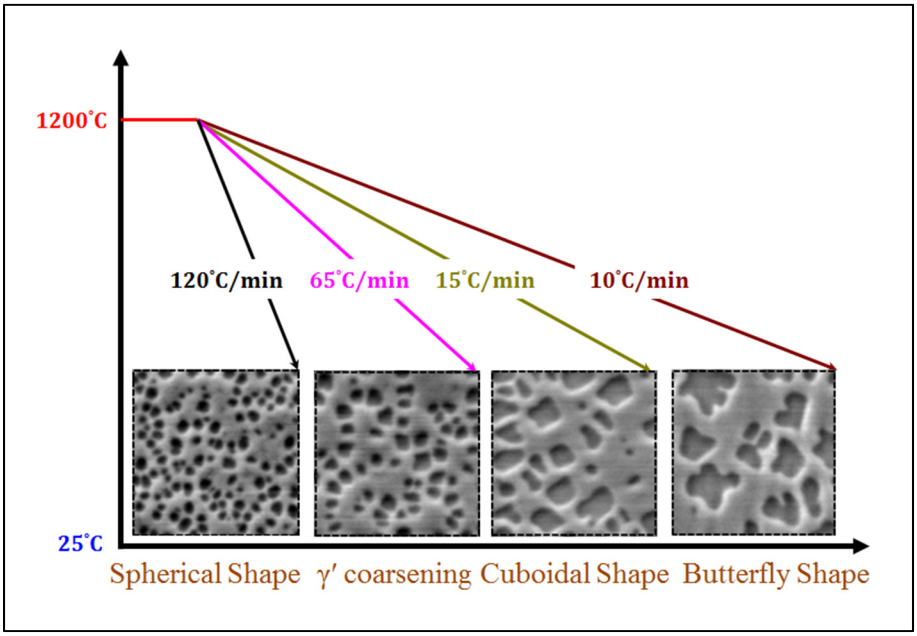

Figure 4.15 Scanning electron microscopy images showing the morphology evolution of first generation of γ′ precipitates during various cooling rates.

The above analysis shows that supersaturation is not the *only* governing mechanism in the formation of γ′ morphological instability during cooling of the AD730^{TM} alloy and most probably other Ni-based superalloys. Low nucleation density and sufficient diffusivity between precipitates and the matrix are other essential factors for irregular growth in Ni-based superalloys. These findings are in agreement with those of Doherty and Yoo (Doherty, 1982; Yoo, 2005), who reported that there should be isotropic interfacial energy, low lattice

mismatch between the two phases, and a low density of nucleation for the formation of protrusions. γ′ precipitates in Ni-based superalloys normally fulfill all these requirements; specifically, the latter condition was satisfied in this work due to the low nucleation density of the first population of cooling γ′ for the SC_{10} condition.

4.6.3 Multiple Precipitation during Cooling

As Table 4-2 and Figure 4.1 show, 20˚C and 85˚C undercooling below the γ′ solvus are necessary to enable subsolvus nucleation for slow and fast cooling rates, respectively. According to Eq. (4.16), at higher supersaturation, the critical radius for nucleation is decreased, and based on the classic nucleation theory (Russell, 1980), the nucleation rate will increase. Consequently, the transformation rate will increase gradually from 0 to 0.7 and 2.3%/min respectively for the SC_{10} and FC conditions, as shown in Figure 4.3. Thus, for the first burst of γ′ nucleation for the SC_{10} condition, only a limited density of γ′ precipitates will be obtained due to the small undercooling at 20˚C (Figure 4.1(b)).

Zener (Christian, 1975) proposed the following model for the precipitates growth rate:

$$\frac{dx_{\gamma'}}{dt} \cong \frac{S\sqrt{D}}{2\sqrt{t}} \tag{4.17}$$

where $x_{\gamma'}$ is the precipitate size, S the supersaturation and D the diffusion coefficient. As the first nuclei are formed and start growing, supersaturation in the matrix is gradually reduced, as does the driving force for nucleation. According to Eq. (4.17), the growth rate will also be reduced due to a decrease in supersaturation and temperature. Therefore, the transformation rate will decrease and reach 0, and the volume fraction of the particles in the system becomes almost constant. However, as the temperature decreases, the redistribution of the solute elements becomes more and more difficult due to their reduced mobility. This leads to a higher supersaturation level in the region free from the first population of γ′ precipitates, which will then become suitable sites for the second and/or third burst of nucleation (Figure 4.10).

For a reprecipitation reaction to occur, the thermodynamics must be favorable (enough driving force), and the kinetics fast enough (small activation energy). Therefore, the transformation rate is proportional to (Kinetic factor) × (Thermodynamic factor). Based on Eqs. (4.14) and (4.16), the critical radius (r^*) is high, and the driving force is small for nucleation near equilibrium. Thus, the nucleation rate will be slow for the first population of γ′ due to small supersaturation at slow cooling rates (SC_{10} and SC_{15} conditions). As a result, the reprecipitation process will not be thermodynamically favorable, and most of the transformation will be controlled by growth. At these cooling rates, supersaturation, S, is small, and the growth rate is controlled by diffusion coefficient, D, according to Eq. (4.17). The growth of first population of γ′ precipitates, which is a diffusion-controlled process, can occur by replacement of the γ atoms at the γ/ γ′ interface with γ′ atoms by normal lattice diffusion involving vacancies. Therefore, the reprecipitation process is kinetically controlled at the SC_{10} and SC_{15} conditions.

As the temperature is lowered during continuous cooling and enough supersaturation and driving force is produced, the probability of nucleation may thus increase rapidly with decreasing temperature, according to Eq. (4.14).

As Table 4-2 and Figure 4.3 show, in the case of samples cooled at a higher cooling rate (FC), most of the transformation seen will occur at a slightly lower temperature (compared to the SC_{10} condition), where both nucleation and growth rates are higher. For the FC condition, the density of the first population of γ′ precipitates is 12 times, and the transformation rate is 3.5 times higher than that of SC_{10}, as shown in Figure 4.3 and Figure 4.7. The reprecipitation process of the first population of γ′ precipitates occurs at high temperatures (1075°C-945°C) for the FC condition, as shown in Figure 4.2. However, a combination of shorter cooling time as compared to the SC_{10} condition, the higher density of particles and therefore overlap of the diffusion fields of precipitates limit the growth rate of γ′ precipitates for the FC condition. This condition will promote a finer size of γ′ precipitates (60 nm) as compared to the SC_{10} condition (196 nm). Thus, the reprecipitation process of the first population of γ′ precipitates is thermodynamically and kinetically favored, and controlled by both nucleation and growth at higher cooling rates (FC).

The experimental results indicate that supersaturation is not uniform at the early stages, when cooling from subsolvus temperature. This is illustrated in Figure 4.16, where it can be seen that during cooling from subsolvus temperature of 1100°C interrupted at 1040°C, γ′ particles nucleate in the supersaturated matrix around the initial primary γ′ precipitates, which remained undissolved during the solutionizing stage, and mostly lie at the γ grain boundaries.

As shown in Figure 4.13 (a), for the interrupt temperature of 1040°C, there is no time for the growth of first generation of precipitates formed during cooling.

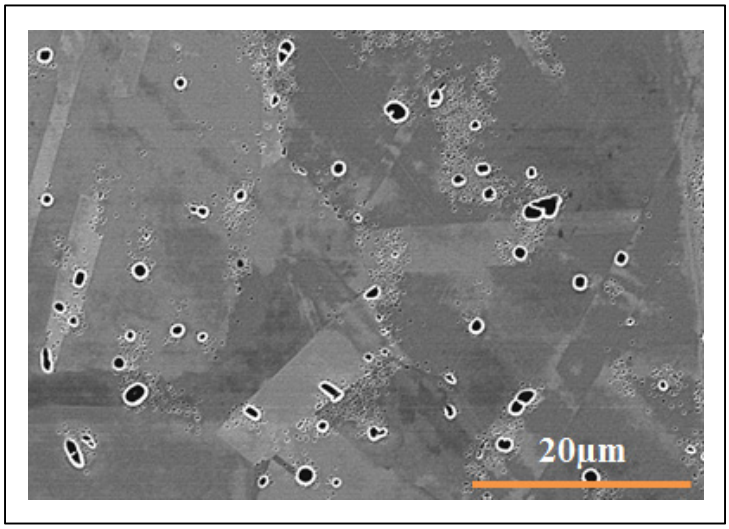

Figure 4.16 Nucleation of γ′ particles around initial primary γ′ at the γ grain boundaries at high interrupt temperature indicating supersaturation is not uniform at the early stages when cooling from subsolvus temperature.

In addition, the high supersaturation buildup in the matrix during water quenching will be the precursor for the second nucleation burst. Conversely, for the 780°C interrupt temperature (Figure 4.13 (b)), existing particles from the first nucleation burst grow by diffusional transfer of atoms toward the precipitates; however, as the temperature is lower, solute diffusivity, and consequently, the growth rate of the precipitates, is slow. Here, the matrix is supersaturated with Al and Ti, and is therefore still in non-equilibrium condition, and thus, a sufficient driving force for a second nucleation burst will be provided at a critical undercooling. This group of precipitates was observed between the initial primary and first

groups of precipitates (Figure 4.13 (b)). It is worth noting that the second group of precipitates is small in size due to the slower movement of solute under these conditions.

4.7 Summary and Conclusion

This study reported the reprecipitation mechanisms and kinetics of γ′ particles in the newly developed AD730^{TM} wrought Ni-based superalloy, with around 40% γ′ particles, but the findings could be also extended to other Ni-based superalloys.

The main conclusions of the present investigation can be summarized as follows:

1- The precipitation of γ′ particles during cooling follows a modified JMA equation, and it was demonstrated that the process is kinetically controlled for the first population of γ′ precipitates at the SC_{10} and SC_{15} conditions. This process is thermodynamically and kinetically favored at the FC condition. The growth parameter (n), the activation energy (Q), the amount of precipitation (Y) and precipitation rate (dY/dt) were determined for the first time for the AD730^{TM} alloy.

2- A function for the kinetic parameter $k(T)$ is developed, and reprecipitation kinetics models for low and high cooling rates were proposed to quantify the volume fraction of reprecipitated γ′ particles.

3- High resolution FEG-SEM indicated that with a decreasing cooling rate, γ′ precipitates show morphological instability going from a spherical shape at high cooling rates to butterfly shapes at slow cooling rates.

4- A new equation is proposed on the basis of experimental correlations between the cooling rate and the γ′ precipitate size for continuous cooling from supersolvus temperatures. The proposed equation was validated experimentally for high cooling rates using Gleeble™ 3800.

5- It was found that supersaturation is not the only determining factor in instability formation. Low nucleation density and enough diffusivity between precipitates and matrix are other essential parameters accounting for an irregular growth of γ′ particles in Ni-based superalloys.

4.8 Acknowledgments

The financial support from the Natural Sciences and Engineering Research Council (NSERC) 261712 of Canada in the form of a Discovery Grant is gratefully acknowledged. The authors express appreciation to Aubert & Duval Co. for providing AD730^{TM} samples.

References

Ardell, A. J., et V. Ozolins. 2005. « Trans-Interface Diffusion-Controlled Coarsening ». *Nature Materials,* vol. 4, nº 4, p. 309-316.

Avrami, M. 1941. « Granulation, Phase Change, and Microstructure Kinetics of Phase Change. III ». *The Journal of Chemical Physics,* vol. 9, nº 2, p. 177-184.

Babu, S. S., M. K. Miller, J. M. Vitek et S. A. David. 2001. « Characterization of the Microstructure Evolution in a Nickel base Superalloy during Continuous Cooling Conditions ». *Acta Materialia,* vol. 49, nº 20, p. 4149-4160.

Behrouzghaemi, S., et R. J. Mitchell. 2008. « Morphological Changes of γ′ Precipitates in Superalloy IN738LC at Various Cooling Rates ». *Materials Science and Engineering A,* vol. 498, nº 1-2, p. 266-271.

Bian, H. 2015. « Regulating the coarsening of the γ′ phase in superalloys Trans-interface diffusion-controlled coarsening ». *NPG Asia Mater.,* vol. 7, p. e212.

Boettinger, W. J., U. R. Kattner, K. W. Moon et J. H. Perepezko. 2006. « DTA and Heat-Flux DSC Measurements of Alloy Melting and Freezing ». *DTA and Heat-flux DSC Measurements of Alloy Melting and Freezing*.

Bonvalet, M., T. Philippe, X. Sauvage et D. Blavette. 2015. « Modeling of Precipitation Kinetics in Multicomponent Systems: Application to Model Superalloys ». *Acta Materialia,* vol. 100, p. 169-177.

Buha, J., R. N. Lumley et A. G. Crosky. 2008. « Secondary Ageing in an Aluminium Alloy 7050 ». *Materials Science and Engineering A,* vol. 492, nº 1-2, p. 1-10.

Chamanfar, A., M. Jahazi, J. Gholipour, P. Wanjara et S. Yue. 2011b. « Mechanical Property and Microstructure of Linear Friction Welded Waspaloy ». *Metallurgical and Materials Transactions A: Physical Metallurgy and Materials Science,* vol. 42, nº 3, p. 729-744.

Chen, S. W., et S. C. Jeng. 1997. « Determination of the Solidification Curve of a Rene N4 Superalloy ». *Metall. Mater. Trans. A,* vol. 28 A, p. 503-504.

Christian, J. W. 1975. *The Theory of Transformation in Metals and Alloys*. Pergamon Press, 586 p.

Cormier, J., M. Jouiad, F. Hamon, P. Villechaise et X. Milhet. 2010. « Very High Temperature Creep Behavior of a Single Crystal Ni-Based Superalloy under Complex Thermal Cycling Conditions ». *Philosophical Magazine Letters,* vol. 90, nº 8, p. 611-620.

Cormier, J., X. Milhet et J. Mendez. 2007a. « Effect of Very High Temperature Short Exposures on the Dissolution of the γ′ Phase in Single Crystal MC2 Superalloy ». *Journal of Materials Science,* vol. 42, nº 18, p. 7780-7786.

Cormier, J., X. Milhet et J. Mendez. 2007b. « Non-Isothermal Creep at Very High Temperature of the Nickel-Based Single Crystal Superalloy MC2 ». *Acta Materialia,* vol. 55, nº 18, p. 6250-6259.

Devaux, A., B. Picqué, M. F. Gervais, E. Georges, T. Poulain et P. Héritier. 2012c. « AD730™-A New Nickel-Based Superalloy for High Temperature Engine Rotative Parts ». In *Proceedings of the International Symposium on Superalloys*. p. 911-919.

Doherty, R. D. 1982. « Role of Interfaces in Kinetics of Internal Shape Changes ». *Metal Science,* vol. 16, nº 1, p. 1-14.

Furrer, D. U., et H. J. Fecht. 2000. « Microstructure and Mechanical Property Development in Superalloy U720LI ». *Superalloys 2000*, p. 415-424.

Gao, N., M. J. Starink et T. G. Langdon. 2009. « Using Differential Scanning Calorimetry as an Analytical tool for Ultrafine Grained Metals Processed by Severe Plastic Deformation ». *Materials Science and Technology,* vol. 25, nº 6, p. 687-698.

Giraud, R., Z. Hervier, J. Cormier, G. Saint-Martin, F. Hamon, X. Milhet et J. Mendez. 2013. « Strain effect on the γ′ dissolution at high temperatures of a nickel-based single crystal superalloy ». *Metallurgical and Materials Transactions A: Physical Metallurgy and Materials Science,* vol. 44, nº 1, p. 131-146.

Huang, Z. W., H. Y. Li, M. Preuss, M. Karadge, P. Bowen, S. Bray et G. Baxter. 2007b. « Inertia Friction Welding Dissimilar Nickel-Based Superalloys Alloy 720Li to IN718 ». *Metallurgical and Materials Transactions A: Physical Metallurgy and Materials Science,* vol. 38 A, nº 7, p. 1608-1620.

Jena, A. K., A. K. Gupta et M. C. Chaturvedi. 1989. « A Differential Scanning Calorimetric Investigation of Precipitation Kinetics in the Al-1.53 wt% Cu-0.79 wt% Mg Alloy ». *Acta Metallurgica,* vol. 37, nº 3, p. 885-895.

Jou, H. J., G. Olson, T. Gabb, A. Garg et D. Miller. 2012. « Characterization and Computational Modeling of Minor Phases in Alloy LSHR ». In *Superalloys 2012*. p. 893-902.

Kamp, N., I. Sinclair et M. J. Starink. 2002. « Toughness-Strength Relations in the Overaged 7449 Al-Based Alloy ». *Metallurgical and Materials Transactions A: Physical Metallurgy and Materials Science,* vol. 33, nº 4, p. 1125-1136.

Kovačević, I., et B. Šarler. 2005. « Solution of a Phase-Field Model for Dissolution of Primary Particles in Binary Aluminum Alloys by an R-Adaptive Mesh-Free Method ». *Materials Science and Engineering A,* vol. 413-414, p. 423-428.

Lippard, H. E., et R. F. Jones. 2000. « Characterization and Thermomechanical Processing of Spray Formed Allvac720 Alloy ». *Superalloys,* vol. 2000, p. 151.

Liu, F., F. Sommer, C. Bos et E. J. Mittemeijer. 2007. « Analysis of Solid State Phase Transformation Kinetics: Models and Recipes ». *International Materials Reviews,* vol. 52, nº 4, p. 193-212.

Locq, D., M. Marty et P. Caron. 2000. « Optimisation of the Mechanical Properties of a New PM Superalloy for Disk Applications ». *Superalloys 2000*, p. 395-403.

Luo, A., D. J. Lloyd, A. Gupta et W. V. Youdelis. 1993. « Precipitation and Dissolution Kinetics in AlLiCuMg Alloy 8090 ». *Acta Metallurgica Et Materialia,* vol. 41, nº 3, p. 769-776.

Maldonado, C., et T. H. North. 2002. « Softened Zone Formation and Joint Strength Properties in Dissimilar Friction Welds ». *Journal of Materials Science,* vol. 37, nº 10, p. 2087-2095.

Mary, C., et M. Jahazi. 2007a. « Linear Friction Welding of IN-718 Process Optimization and Microstructure Evolution ». In *5th International Conference on Processing and Manufacturing of Advanced Materials - THERMEC 2006, July 4, 2006 - July 8, 2006.* (Vancouver, BC, Canada) Vol. 15-17, p. 357-362. Coll. « Advanced Materials Research »: Trans Tech Publications.

Masoumi, F., M. Jahazi, J. Cormier et D. Shahriari. 2014. « Dissolution Kinetics and Morphological Changes of γ ′ in AD730™ Superalloy ». In *MATEC Web of Conferences*. Vol. 14.

Masoumi, F., M. Jahazi, D. Shahriari et J. Cormier. 2016a. « Coarsening and Dissolution of γ′ Precipitates during Solution Treatment of AD730™ Ni-Based Superalloy: Mechanisms and Kinetics Models ». *Journal of Alloys and Compounds,* vol. 658, p. 981-995.

Meher, S., S. Nag, J. Tiley, A. Goel et R. Banerjee. 2013. « Coarsening Kinetics of γ′ Precipitates in Cobalt-Base Alloys ». *Acta Materialia,* vol. 61, nº 11, p. 4266-4276.

Mittemeijer, E. J. 1992. « Analysis of the Kinetics of Phase Transformations ». *Journal of Materials Science,* vol. 27, nº 15, p. 3977-3987.

Monajati, H., M. Jahazi, R. Bahrami et S. Yue. 2004a. « The Influence of Heat Treatment Conditions on γ′ Characteristics in Udimet® 720 ». *Materials Science and Engineering A,* vol. 373, nº 1-2, p. 286-293.

Mullins, W. W., et R. F. Sekerka. 1963. « Morphological Stability of a Particle Growing by Diffusion or Heat Flow ». *Journal of Applied Physics,* vol. 34, nº 2, p. 323-329.

Olson, G. B., H. J. Jou, J. Jung, J. T. Sebastian, A. Misra, I. Locci et D. Hull. 2008. « Precipitation Model Validation in 3rd Generation Aeroturbine Disc Alloys ». In *Proceedings of the International Symposium on Superalloys*. p. 923-932.

Palavar, O., D. Özyürek et A. Kalyon. 2015. « Artificial Neural Network Prediction of Aging Effects on the Wear Behavior of IN706 Superalloy ». *Materials and Design,* vol. 82, p. 164-172.

Papon, P., J. Leblond et P. H. E. Meijer. 2006. *The Physics of Phase Transitions: Concepts and Applications*. Springer, Berlin, Heidelberg.

Payton, E., G. Wang, N. Ma, Y. Wang, M. Mills, D. Whitis, D. Mourer et D. Wei. 2008. « Integration of Simulations and Experiments for Modeling Superalloy Grain Growth ». In *Proceedings of the International Symposium on Superalloys*. p. 975-984.

Philippe, T., et P. W. Voorhees. 2013. « Ostwald Ripening in Multicomponent Alloys ». *Acta Materialia,* vol. 61, nº 11, p. 4237-4244.

Preuss, M., P. J. Withers, J. W. L. Pang et G. J. Baxter. 2002b. « Inertia welding nickel-based superalloy: Part I. Metallurgical characterization ». *Metallurgical and Materials Transactions A: Physical Metallurgy and Materials Science,* vol. 33, nº 10, p. 3215-3225.

Radis, R., M. Schaffer, M. Albu, G. Kothleitner, P. Pölt et E. Kozeschnik. 2009. « Multimodal Size Distributions of γ′ Precipitates during Continuous Cooling of UDIMET 720 Li ». *Acta Materialia,* vol. 57, nº 19, p. 5739-5747.

Reed, R. C. 2006b. *The Superalloys Fundamentals and Applications*, 9780521859042. Cambridge University Press, 1-372 p.

Ricks, R. A., A. J. Porter et R. C. Ecob. 1983. « The Growth of γ′ Precipitates in Nickel-Base Superalloys ». *Acta Metallurgica,* vol. 31, nº 1, p. 43-53.

Rosen, Gad I., S. F. Dirnfeld, Menachem Bamberger et Bruno Prinz. 1994. « In-Situ Electrical Resistivity Measurements for Determining Formation Kinetics of the γ′ Phase in Nickel-Based Wrought Superalloys ». *Zeitschrift fuer Metallkunde/Materials Research and Advanced Techniques,* vol. 85, nº 2, p. 127-130.

Rougier, L., A. Jacot, C. A. Gandin, P. D. Napoli, P. Y. Théry, D. Ponsen et V. Jaquet. 2013. « Numerical Simulation of Precipitation in Multicomponent Ni-Base Alloys ». *Acta Materialia,* vol. 61, nº 17, p. 6396-6405.

Russell, K. C. 1980. « Nucleation in Solids: The Induction and Steady State Effects ». *Advances in Colloid and Interface Science,* vol. 13, nº 3-4, p. 205-318.

Sarosi, P. M., B. Wang, J. P. Simmons, Y. Wang et M. J. Mills. 2007. « Formation of Multimodal Size Distributions of γ′ in a Nickel-Base Superalloy during Interrupted Continuous Cooling ». *Scripta Materialia,* vol. 57, nº 8, p. 767-770.

Sato, J., T. Omori, K. Oikawa, I. Ohnuma, R. Kainuma et K. Ishida. 2006. « Cobalt-Base High-Temperature Alloys ». *Science,* vol. 312, nº 5770, p. 90-91.

Seidman, D. N., C. K. Sudbrack et K. E. Yoon. 2006. « The Use of 3-D Atom-Probe Tomography to Study Nickel-Based Superalloys ». *JOM,* vol. 58, nº 12, p. 34-39.

Sekhar, N. C., et R. C. Reed. 2002. « Power Beam Welding of Thick Section Nickel Base Superalloys ». *Science and Technology of Welding and Joining,* vol. 7, nº 2, p. 77-87.

Shahriari, D., M. H. Sadeghi et A. Akbarzadeh. 2009. « γ' Precipitate Dissolution during Heat Treatment of Nimonic 115 Superalloy ». *Materials and Manufacturing Processes,* vol. 24, nº 5, p. 559-563.

Shahriari, D., M. H. Sadeghi, A. Akbarzadeh et M. Cheraghzadeh. 2009b. « The Influence of Heat Treatment and Hot Deformation Conditions on γ′ Precipitate Dissolution of Nimonic 115 Superalloy ». *International Journal of Advanced Manufacturing Technology,* vol. 45, nº 9-10, p. 841-850.

Singh, A. R. P., S. Nag, S. Chattopadhyay, Y. Ren, J. Tiley, G. B. Viswanathan, H. L. Fraser et R. Banerjee. 2013. « Mechanisms Related to Different Generations of γ′ Precipitation during Continuous Cooling of a Nickel Base Superalloy ». *Acta Materialia,* vol. 61, nº 1, p. 280-293.

Singh, A. R. P., S. Nag, J. Y. Hwang, G. B. Viswanathan, J. Tiley, R. Srinivasan, H. L. Fraser et R. Banerjee. 2011. « Influence of Cooling Rate on the Development of Multiple Generations of γ′ Precipitates in a Commercial Nickel Base Superalloy ». *Materials Characterization,* vol. 62, nº 9, p. 878-886.

Vaunois, J. R., J. Cormier, P. Villechaise, A. Devaux et B. Flageolet. 2010. « Influence of Both γ′ Distribution and Grain Size on the Tensile Properties of UDIMET 720Li at Room Temperature ». In *7th International Symposium on Superalloy 718 and Derivatives 2010*. Vol. 1, p. 199-213.

Wen, Y. H., J. P. Simmons, C. Shen, C. Woodward et Y. Wang. 2003. « Phase-Field Modeling of Bimodal Particle Size Distributions during Continuous Cooling ». *Acta Materialia,* vol. 51, nº 4, p. 1123-1132.

Wen, Y. H., B. Wang, J. P. Simmons et Y. Wang. 2006. « A Phase-Field Model for Heat Treatment Applications in Ni-Based Alloys ». *Acta Materialia,* vol. 54, nº 8, p. 2087-2099.

Whelchel, R. L. 2011. « Characterization of A Nickel-base Superalloy Through Electrical Resistivity Microstructure Relationships Facilitated by Small Angle Scattering ». USA, Georgia Institute of Technology.

Wusatowska-Sarnek, A. M., G. Ghosh, G. B. Olson, M. J. Blackburn et M. Aindow. 2003. « Characterization of the Microstructure and Phase Equilibria Calculations for the Powder Metallurgy Superalloy IN100 ». *Journal of Materials Research,* vol. 18, nº 11, p. 2653-2663.

Yoo, Y. S. 2005. « Morphological Instability of Spherical γ′ Precipitates in a Nickel Base Superalloy ». *Scripta Materialia,* vol. 53, nº 1, p. 81-85.

CHAPITRE 5

ARTICLE 3: ON THE OCCURRENCE OF LIQUATION DURING LINEAR FRICTION WELDING OF NI-BASED SUPERALLOYS

F. Masoumi[a], D. Shahriari[a], M. Jahazi[a], J. Cormier[b], B.C.D. Flipo[c]

[a] Department of Mechanical Engineering, École de Technologie Supérieure (ETS), H3C 1K3, Montreal, QC, Canada
[b] Institute Pprime, UPR CNRS 3346, Physics and Mechanics of Materials Department, ISAE- ENSMA, BP 40109, Futuroscope- Chasseneuil Cedex 86961, France
[c] TWI Ltd, Granta Park, Great Abington, Cambridge CB21 6AL, UK

This article was published in the Metallurgical and Materials Transactions A in June, 2017

5.1 Abstract

A combination of experimental and analytical methods were used to study the possible occurrence of liquation during LFW of the newly developed AD730^{TM} Ni-based superalloy. LFWed joints were produced using a semi-industrial size facility and the interfaces of the joints as well as the ejected flash were examined using optical and Field Emission Gun Scanning Electron Microscopy (FEG-SEM). Physical simulation of the LFW thermal cycle, using thermomechanical simulator Gleeble™ 3800, showed that incipient melting started from 1473K (1200°C). The analytical model, calibrated by experiments, predicted that the highest temperature of the interface was about 1523K (1250°C). The constitutive equations based on lattice and pipe diffusion models were developed to quantify the self-diffusivity of the elements and control the extent of liquation by considering the effect of LFW process parameters. Analytical results show that the application of compressive stresses during LFW results in 25 times increase in the diffusion of Ni atoms at the weld interface. Therefore, no presence of re-solidified phases, i.e. occurrence of liquation, was observed in the microstructure of the weld zone or the flash in the present study. Based on the obtained results, a methodology was developed for designing the optimum pressure above which no liquation, and hence cracking, will be observable.

Key Words: Linear friction welding; Ni-based superalloy; Liquation temperature; Liquation mechanisms; Diffusion mechanisms.

5.2 Introduction

AD730^{TM} is a recently developed Ni-based superalloy for turbine disk applications (Devaux et al., 2012c); however, many of its properties, especially its weldability, are still unknown for advanced manufacturing applications such as LFW. LFW is an emerging manufacturing technology for joining of blades to disks or repairing turbine disks in gas turbines and jet engines. This process presents significant advantages over the traditional mechanical assembly techniques by providing quality and performance improvements or weight reduction and economic benefits. The LFW process is in essence a hot deformation process and in this regard the material undergoes a severe thermomechanical process which brings substantial microstructural changes (Bhamji et al., 2011; Mary et Jahazi, 2007a; Uday et al., 2010).

One of the on-going questions in LFW is whether liquation and consequently cracks occurs during this process (Chamanfar et al., 2012b; Ola et al., 2011c). The possibility of liquation during LFW plays a key role in controlling the mechanical properties of the joint as micro-cracks can be produced due to weakness of liquid film against thermal and mechanical stresses induced during cooling. Although bulk melting and consequently solidification cracking does not occur in LFW (Mary et Jahazi, 2007a), the occurrence of local melting and possible micro-cracks are still imaginable. Re-solidified eutectic micro-constituent and constitutional liquation of γ' precipitates were observed in thermo-mechanically affected zone (TMAZ) of LFWed IN 738 material (Ola et al., 2011c) while no liquation was observed in the LFWed Waspaloy components (Chamanfar et al., 2012b). Constitutional liquation of second phase particles occurs due to the formation of intergranular liquid films along the particle-matrix interface through a eutectic-type reaction with the surrounding matrix (Ojo, Richards et Chaturvedi, 2004a). Having a good understanding of liquation mechanisms is critical for reliable prediction of microstructure evolution and mechanical properties of

LFWed joints and correlating it to process parameters for the optimum design of weld parameters.

Extensive studies have investigated different mechanisms of grain boundary (GB) liquation during fusion welding of Ni-based superalloys (Danis et al., 2010; Dye, Hunziker et Reed, 2001; Mousavizade et al., 2009; Nakkalil, Richards et Chaturvedi, 1992; Ojo, Richards et Chaturvedi, 2004a; Zhang, Ojo et Chaturvedi, 2008). These reports suggest that some metallurgical and mechanical factors affect liquation cracking susceptibility. The main metallurgical factors are the amount of borides, carbides and γ' precipitates, grain and particle size, heat input and segregation of boron, phosphorous and sulfur. The mechanical factors are thermally induced strains, stresses and base alloy hardness (Dye, Hunziker et Reed, 2001; Mousavizade et al., 2009; Ojo, Richards et Chaturvedi, 2004a; Zhang, Ojo et Chaturvedi, 2008). However, no quantitative data is available on the possibility of constitutional liquation and subsequent cracking of superalloys under non-equilibrium thermal cycles such as those encountered in LFW.

In order to have a better insight on microstructure development during LFW, the influences of the two most important process parameters (i.e. temperature and external imposed pressure) need to be quantified. Experimental measurement of temperature evolution during LFW of superalloys has been carried out by few research groups (Chamanfar et al., 2011a; Mary et Jahazi, 2007a). However, it is nearly impossible to experimentally obtain the exact temperature at the interface during welding due to the highly dynamic nature of the process. Varis and Frost (2000b) developed a numerical model to obtain temperature history in the initial stage of LFW. Li et al. (2010) formulated a model, using ABAQUS, for temperature prediction during LFW of Ti alloys. Having estimated the interface heat generation rate, a one-dimensional temperature distribution in the case of inertia friction welding has been calculated (Li et al., 2016; Shinoda et al., 2000; Soucail et al., 1992; Yilbas et Sahin, 2014). However, in none of the above works, the predicted interface temperatures were not validated experimentally. In this study, in order to predict the weld interface temperature, an analytical approach based on solving one-dimensional thermal energy conservation equation (Bateman, 1932; Bergman et al., 2011; Xiong et al., 2013) is used. The obtained results were

then validated using a semi-analytical model, developed previously for γ′ dissolution kinetics (Masoumi et al., 2016a) , and measured temperatures by thermocouples or infrared thermal camera for Ni-based superalloys in the literatures (Chamanfar et al., 2011a; Yang et al., 2015).

LFW is fundamentally a hot deformation process. While extensive data is available on hot deformation and creep of Ni-based superalloys (Cormier, Milhet et Mendez, 2007b; Giraud et al., 2013; Ola, Ojo et Chaturvedi, 2013a; Shahriari et al., 2009b; Viswanathan et al., 2015; Wang et al., 2011a), few of them could be used for analyzing the LFW process. The reason is that the applied stress, deformation and temperatures used for these experiments are much lower than those occurring during the LFW process even though the fundamental mechanisms governing microstructure evolution are similar. The glide and climb of dislocations and the diffusive flow of individual atoms can cause plastic flow during creep or hot deformation (Cormier, Milhet et Mendez, 2007b; Giraud et al., 2013; Porter et Easterling, 1992). Glide and climb of dislocations are controlled by lattice or pipe diffusion (Giraud et al., 2013; Viswanathan et al., 2015). Therefore, from a fundamental point of view, it is important to quantify the contribution of the LFW process parameters on lattice and pipe diffusion processes on microstructure development during LFW.

The present research has been defined in this context and has the objective to evaluate the possible occurrence of liquation during LFW of Ni-based superalloys, determine the conditions under which liquation could take place during LFW, and discuss possible governing mechanisms.

5.3 Experimental Procedure

The AD730^{TM} material was a forged square bar provided by Aubert & Duval. A post forge heat treatment consisting in solutionizing at 1353K (1080°C) for four hours followed by air cooling had also been conducted on the material. The chemical composition of the alloy is given in Table 5-1. The equilibrium volume fraction of γ′ particles was around 40% in the as received material.

Table 5-1 Chemical composition of AD730^{TM} (wt%) (Devaux et al., 2012c)

Ni	Fe	Co	Cr	Mo	W	Al	Ti	Nb	B	C	Zr
Base	4	8.5	15.7	3.1	2.7	2.25	3.4	1.1	0.01	0.015	0.03

For LFW experiments, rectangular blocks 26 mm × 13 mm × 37 mm (length × width × height), were machined by wire electro-discharge machining (EDM). The LFW process was conducted using the FW34-E20 LFW machine at TWI, Cambridge, UK. This process generally consists in three major phases (Bhamji et al., 2011; Chamanfar, Jahazi et Cormier, 2015a). The schematic of the processing stages and the details of the processing parameters are shown in Figure 5.1. The axial shortening after welding was 1.7 mm.

In order to determine the range of non-equilibrium liquation temperature of the alloy during LFW, the thermal cycle of the LFW process was reproduced using Gleeble™ 3800 physical simulator. Specifically, the experiments consisted in heating at a fast heating rate of 400K/s to temperatures ranging from 1423K (1150˚C) to 1573K (1300˚C), holding for 3 seconds at the target temperature, followed by compressed air cooling at a rate of 150K/s.

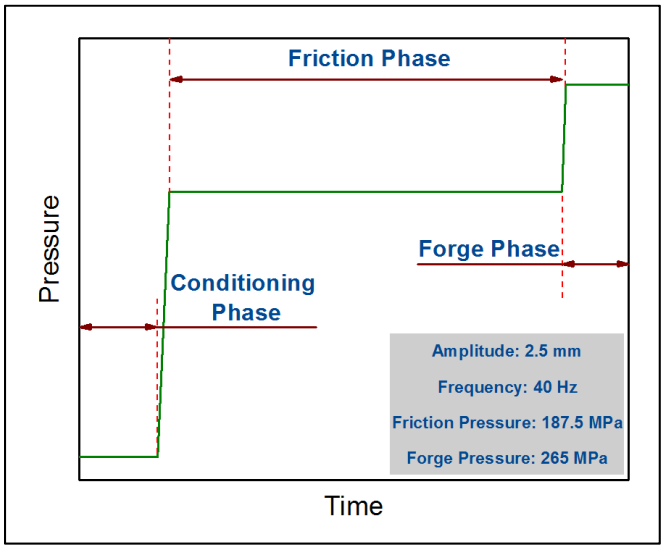

Figure 5.1 Processing phases and parameters during LFW of AD730^{TM}.

The microstructure of the LFWed samples from the parent material to the weld interface, and Gleeble samples, particularly the characteristics of the γ′ particles and their constitutional liquation, were investigated. For microstructural studies, the samples were mounted and polished using standard metallographic techniques and etched using two different etchants. The first was composed of 170cc H_3PO_4, 10cc H_2SO_4 and 15gr Cro_3, the second a mixture of Regia water (2/3) and distilled water (1/3). After etching, the specimens' microstructures were observed using optical and FEG-SEM. Characterization of the nanometric size particles were conducted using Hitachi SU823 SEM in the secondary electron (SE) imaging mode. The back-scattered electron (BSE) images were recorded from polished cross sections by use of a backscattered electron detector attached to the SEM.

Furthermore, distribution mappings and chemical composition of the different chemical elements constituting various phases in the specimen were obtained by EDS. Analyses were carried out at microscopic scale using small and high magnification SEM images such as 2000, 50,000 and 100,000 magnifications to investigate γ′ characteristics. In order to measure the dimensions and volume fractions of the γ′ precipitates, digitized microscopic images and ImageJ analysis software were used. Each reported value for γ′ size or volume fraction is an average of 5 measurements. In each case, area measurements on more than 100 precipitates were carried out. The particle radius was then calculated as the radius of a circle whose surface area equaled that of the corresponding particle.

5.4 Results and Discussion

5.4.1 Macroscopic and Microscopic Examination of the Joint after LFW

Visual examination of the flash (Figure 5.2 (a)) revealed that the material extruded symmetrically from four sides of each weld, and developed curly swirl shape. The flash, formed due to the applied pressure and material plastic flow, was connected around the corners of the specimen. Therefore, the flash shape implies that the entire area of the interface was plasticized as a result of high temperature and stress applied during the LFW process. The presence of a continuous flash is often considered as an indication for a sound weld (Chamanfar, Jahazi et Cormier, 2015a; Chamanfar et al., 2011a; Mary et Jahazi, 2008)

as oxides present at the interface are ejected out, and therefore “fresh” atoms from both sides of the joint come into contact. Higher magnification of flashes (numbered 1 and 2 in Figure 5.2 (b)) showed that they are 1.7 mm in thickness and 3.3 mm in height, as shown by arrows in Figure 5.2 (c). Oxide particles which are observed in flash number 3, arrowed in Figure 5.2 (b), are expelled oxides from the interface. Examination of the weld by optical microscopy (Figure 5.2 (b)) revealed no microcracks or microvoids in the weld interface.

Parent material, AD730^{TM} alloy, has around 10 % primary γ′, 26% secondary and 3% tertiary γ′, and around 1% MC, $M_{23}C_6$ carbides and M_3B_2 borides, with M being the metallic element (Ti, Nb, Cr, Mo and W) (Masoumi et al., 2016a). Figure 5.3 shows the evolution in volume fraction of primary and secondary γ′ as a function of the distance "L" from the weld interface. For instance, as shown in Figure 5.3, primary and secondary γ′ particles are mostly dissolved at L = 0.4 mm and L = 1.5 mm, respectively. Figure 5.4 shows that primary γ′ particles are dissolved in the central zone and at the corners. Noticeable changes occur in the microstructure of the LFWed alloy from its original condition (parent material) within 4-4.5 mm thick layer on both sides from the weld interface, with a total width of the TMAZ and heat affected zone (HAZ) of 8-9 mm, as shown in Figure 5.3. The absence of primary or secondary γ′ particles and the presence of MC carbides at the weld line indicate that the temperature in this zone was above the γ′ solvus and below the carbide solvus temperature. The above observations confirms the presence of a strong temperature gradient across the LFWed joint with the highest temperatures existing in the weld zone and the flash as reported by other authors (Chamanfar et al., 2011a; Li, Ma et Li, 2010; Mary et Jahazi, 2007a; Vairis et Frost, 2000b).

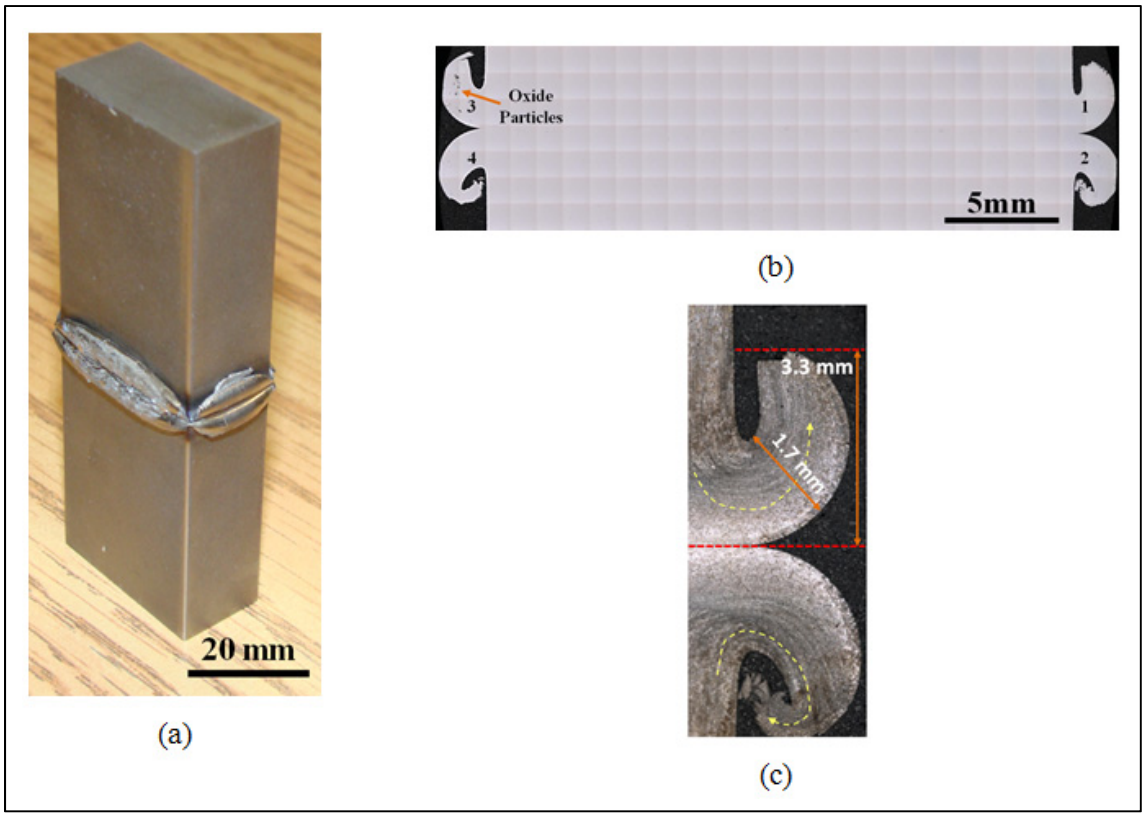

Figure 5.2 (a) A photograph of LFWed sample (b) a low magnification optical image of the welded sample showing oxide particles in flash 3, as shown by arrow (C) higher magnification of flash 1 and 2 (defined in (b)) showing formation of flashes with thickness 1.7 mm and height 3.3mm due to material flow, as shown by arrows, near the LFW interface.

In the microstructure examination of the flash, as shown in Figure 5.4 (a), no indication of liquation or γ/γ′ eutectic product was observed. Examination by electron microscopy indicated that TMAZ was also free from resolidified products, and no γ/γ′ eutectic phase was observed at the γ/γ′ interface (Figure 5.4 (b)). However, flash is formed from the expulsion of material subjected to the highest temperature out of the interface. In addition, coarse second phase particles such as γ′ particles, carbides and borides that formed along the grain boundaries in the microstructure of the as received material have a high tendency for constitution liquation at high temperatures (Mousavizade et al., 2009).

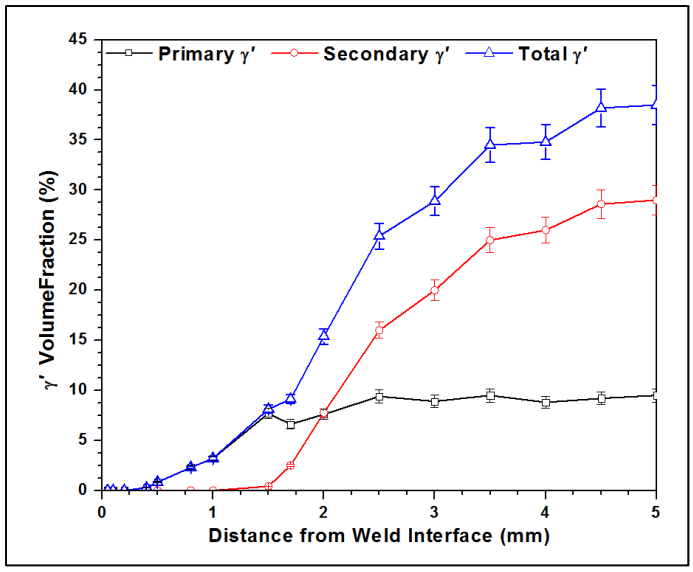

Figure 5.3 Variation in γ′ volume fraction as a function of distance from the weld interface.

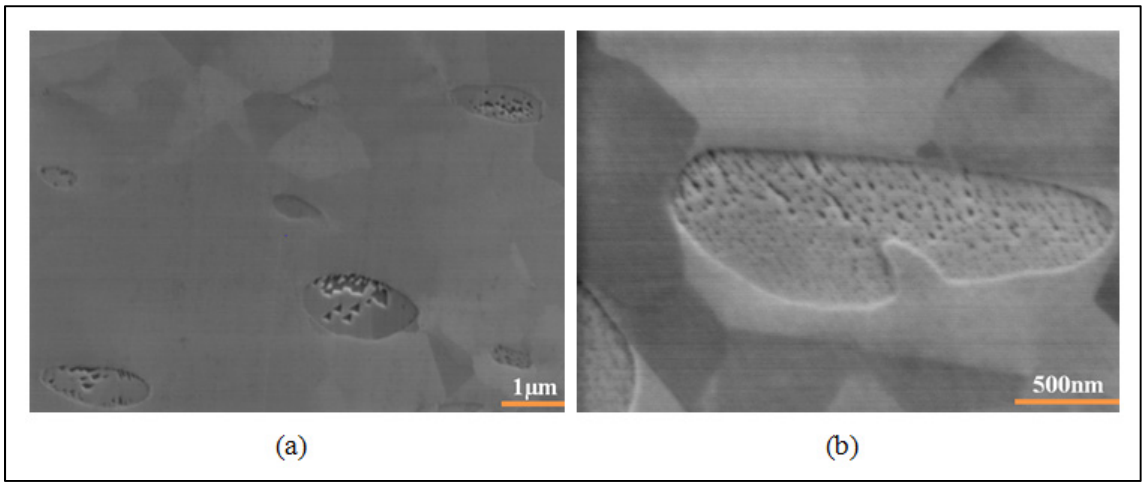

Figure 5.4 SEM micrographs of the: (a) flash (b) TMAZ at 500 μm from the weld interface. No indication of liquation or γ/γ′ eutectic product was observed at the γ/γ′ interface at the flash or TMAZ.

Thus, two assumptions could be made on the possibility of γ′ liquation during LFW of this alloy and most probably other Ni-based superalloys: 1) Processing conditions (temperature, friction and forge pressures, strain and strain rate) are such that no liquation occurs during LFW, and 2) liquation is produced but disappeared before eutectic re-solidification.

The thermal cycle (heating rate, temperature, and holding time) in addition to accumulated plastic strain and applied stress paly significant role in the microstructural evolution during LFW. Out of the parameters listed above, the heating stage is the most important factor in contributing to the occurrence of liquation. Therefore, in order to elucidate the observed microstructural development during LFW of AD730^{TM}, the non-equilibrium liquation temperature of the investigated alloy is predicted through physical simulation using the Gleeble™ 3800 equipment. The microstructure examinations are described in the following section.

5.4.2 Physical Simulation of the LFW Thermal Cycle

Samples were heated at a rate of 400K/s to temperatures ranging from 1423K (1150˚C) to 1573K (1300˚C) followed by air cooling at a rate of 150K/s. Figure 5.5 (a) and (b) show the microstructure of the samples after heat treatment at 1423K (1150˚C) and 1493K (1220˚C), respectively. As shown in Figure 5.5 (a), the microstructure mainly consisted of primary and small volume fraction, 0.4 %, of fine spheroidal secondary γ′ particles which remained undissolved during heat treatment at 1423K (1150˚C), and dispersed non-uniformly in the matrix. Therefore, the solvus temperature of secondary γ′ precipitates is considered to be 1423K (1150˚C). Primary γ′ particles were 1.2 μm in size and 7 % in volume fraction which is comparable to the values of average size and volume fraction of these particles in the as-received material. Therefore, no indication of primary γ′ dissolution was observed while 99% of secondary γ′ have been dissolved after heat treatment at 1423K (1150˚C). Figure 5.5 (b) shows primary γ′ particles have somewhat reduced in size, from 1.4 μm to 800 nm, due to solid-state diffusion, during heat treatment at 1493K (1220˚C) but not totally dissolved. There are still 0.4 % undissolved primary γ′ particles after this heat treatment probably due to the short time for diffusion of Al and Ti. As a result, the solvus temperature of primary γ′ precipitates is considered to be 1493K (1220˚C). In the case of AD730^{TM} alloy, under equilibrium conditions, γ′ solvus is around 1073K (800˚C) for secondary γ′ precipitates and 1383K (1110˚C) for the primary γ′ particles (Masoumi et al., 2016a). In contrast, at a heating rate of 400K/s, this temperature is around 1423K (1150˚C) for secondary and 1493K

(1220˚C) for primary γ′ particles (Figure 5.5). Thus, there is clearly a large departure from thermodynamic equilibrium for the dissolution of the γ′ particles during rapid heating.

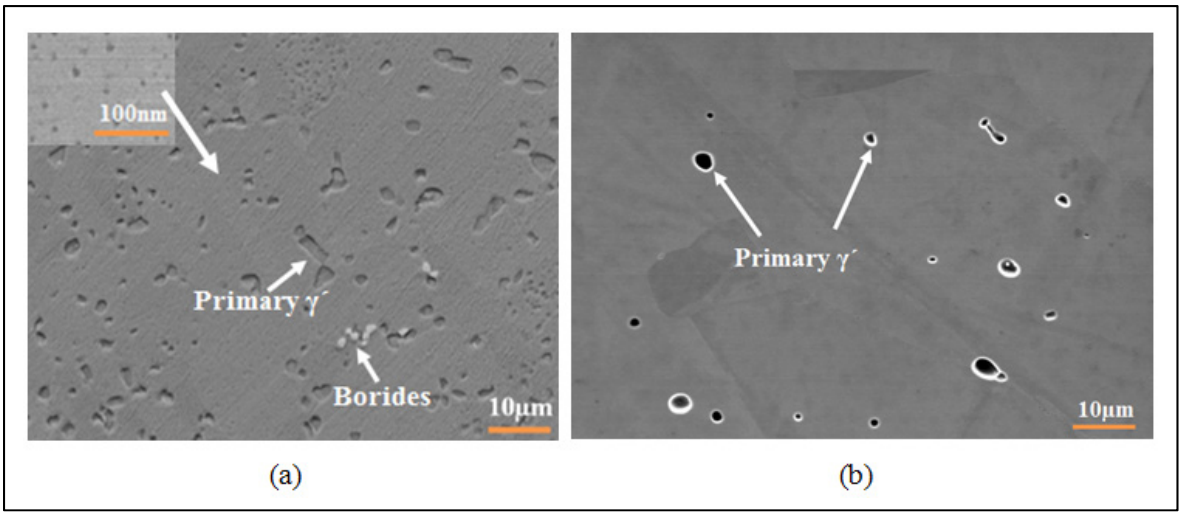

Figure 5.5 SEM micrographs of Gleeble-simulated materials under rapid thermal cycle (heating rate of 400K/s) and 3 s holing time at peak temperatures of : (a) 1423K (1150˚C) and (b) 1493K (1220˚C) showing the presence of some undissolved secondary γ′ particles at 1423K (1150˚C) (see zoom area in (a)) and primary γ′ particles at 1493K (1220˚C) (with only 0.4 % remained undissolved).

Dissolution kinetics of γ′ particles depends strongly on the time experienced at high temperature, accumulated plastic strain and the initial γ′ characteristics (size, morphology and chemical composition) (Cormier, Milhet et Mendez, 2007a; Giraud et al., 2013; Masoumi et al., 2016a; Soucail et Bienvenu, 1996). Under equilibrium conditions, both coarse and fine γ′ precipitates dissolve by diffusional transfer of γ′ forming elements toward the γ matrix. The dissolution rate is much faster for secondary γ′ precipitates than for primary γ′ particles due to their smaller sizes and the lower amounts of γ′ forming atoms. Therefore, their solvus temperature is lower than that of primary γ′ particles (Masoumi et al., 2016a; Masoumi et al., 2016c; Milhet et al., 2013; Wang et al., 2009).

In comparison to the deformation cycle, the thermal cycle (heating rate, temperature, and holding time) plays the most important role in the occurrence of liquation during LFW. High heating rates, such as those applied during LFW, can induce non-equilibrium liquation of second phase particles (Ojo, Richards et Chaturvedi, 2004a). Therefore, it is important to

quantify the impact of the LFW thermal cycle on liquation and separate it from the deformation cycle.

On the other hand, the application of deformation has two separate effects: 1) it will increase the temperature by internal heating, and 2) enhances the atomic diffusion which at the end could impact the extent of liquation as will be discussed in the section 3.4.

Temperature increase due to deformation, including the effect of strain rate, was calculated according to the equation proposed by Altan et al. (2005). This value was estimated to be about 25.5K (25.5°C) at 1473K (1200°C). Details regarding the influence of deformation on internal heating and estimation of the strain rate value during LFW are provided in Appendix I. Also, diffusion enhancement due to the application of compressive strain has been reported in different alloy systems (Lesuer et al., 2001; Samantaray et al., 2011; Xu, 2003). For example, a three orders of magnitude increase in the diffusion coefficient of impurity-vacancy complex of low carbon steels has been reported by Xu (2003). Such acceleration of the atomic diffusion would contribute to the reduction of the liquation 'footprint' in the microstructure and hinder its detection. Therefore, in order to accurately determine the liquation temperature, it is better not to apply pressure during the heating cycle.

Based on the applied thermal cycles in the present investigation, no liquation was observed at 1423K (1150°C) while rosette shaped phases, which is commonly called as γ-γ′ eutectics start to form at γ/γ′ interface at 1473K (1200°C), as shown in Figure 5.6.

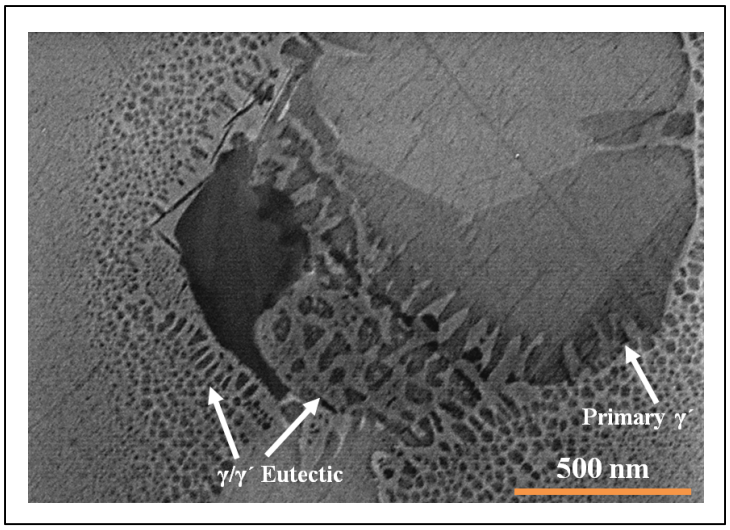

Figure 5.6 SEM micrographs showing the formation of γ-γ′ eutectic at γ/γ′ interface after constitutional liquation of primary γ′ particle. Heating rate of 400K/s + 3 s holing time at 1473K (1200˚C) followed by compressed air cooling.

Therefore, if the weld zone reaches this temperature, liquation should occur. γ-γ′ eutectics can be morphologically characterized by coarse γ′ particles embedded in a narrow γ channel. Large areas of fine γ′ particles are formed around the incipient melted zone. On the basis of the above analysis, the constitutional liquation temperature of this alloy can be considered to be around 1473K (1200˚C) during fast heating (e.g. the thermal cycle of LFW). This result confirms Thermo-calc® simulation results (Masoumi et al., 2016a) which predict a solidus temperature of 1493K (1220˚C) for AD730^{TM} alloy. The necessary conditions for constitutional liquation are: slow phase dissolution, rapid heating and microscopic equilibrium at the particle/matrix interface (Ojo, Richards et Chaturvedi, 2004a). Primary γ′ particles "survive" until 1493K (1220˚C), as shown in Figure 5.5 (b). Since there is not enough time for the accommodation of the solute into the matrix and homogenization by diffusion during rapid heating, the solid in contact with the γ′ particles would become solute rich with a diffusion gradient compared to the matrix. At the eutectic temperature, the particles would be smaller yet, but now a eutectic reaction between the solid at the interface and the particles would form liquid phase around the particles. Again, a diffusion gradient would be present in the solid. When temperature is increased, the particles will be in contact

with the solute rich liquid phase. Upon solidification, this will lead to an excess of solute in the solid.

SEM micrograph and EDS mapping results presented in Figure 5.7 show eutectic products formed close to Nb-Ti carboborides and Cr-Mo-W-Nb rich borides during cooling from 1493K (1220˚C). γ-γ′ eutectics, as shown by arrows in Figure 5.7 (a), take the form of lamellar rosettes in which γ′ particles are separated by γ ribbons in fan like shapes. As shown in Figure 5.7 (b), EDS spectrum of samples heat treated at 1493K (1220˚C) indicated that the platelet shape phase is rich in Ni, Ti and Nb. It has also been reported that the eutectic temperature of the Nb-Ni-Ti ternary system varies between 1336K (1063˚C) and 1553K (1280˚C) depending on the mole fraction of each element suggesting the formation of Ni-Ti-Nb compound/γ eutectic in the liquated areas during heat treatment at 1493K (1220˚C) (Matsumoto et al., 2005).

Moreover, Thermo-calc® simulation shows MC carbide particles start dissolving at 1118K (845˚C), and are totally dissolved at 1553K (1280˚C) while M_3B_2 particles dissolve much earlier at around 1493K (1220˚C) (Masoumi et al., 2016a). The dissolution of Nb-Ti-rich carboborides provides a source of Nb and Ti elements.

High amounts of Ti make γ′ unstable and platelet shape Ni-Ti-Nb intermetallic (η) phase is formed during degeneration of Nb-Ti carbides or carboborides instead of γ′. These findings are in agreements with those obtained by Choi et al. (2004) who found that Ni-Ti intermetallic formation was mostly accompanied by MC decomposition and the release of Ti. In addition, it is well known that Ni and Al promote the formation of Ni_3Al γ′ phase in which Al may also be replaced by Ti, Nb and Ta. However, once the sum of Ti+ Nb+Ta exceeds Al, Ni_3(Ti, Nb), η phase would form preferentially (Bouse, 1996). As indicated in Figure 5.7 (b), chemical composition of Ni-Ti-Nb phase shows this situation is susceptible to occur in AD730^{TM} as the (Ti+Nb)/Al ratio is more than 8. Therefore, this phase may have transformed from the γ′ eutectic pools, and is confirmed that this resolidified phase can be η which has been formed in the incipient melted region.

The constituent phase of the eutectic-like products formed during cooling from 1523K (1250°C) are shown in Figure 5.8, and the chemical composition of the three main phases, as determined by EDS, are given in Table 5-2. Significant carbon concentration was detected in Nb-Ti rich particles, phase 1, indicating that they are carbides.

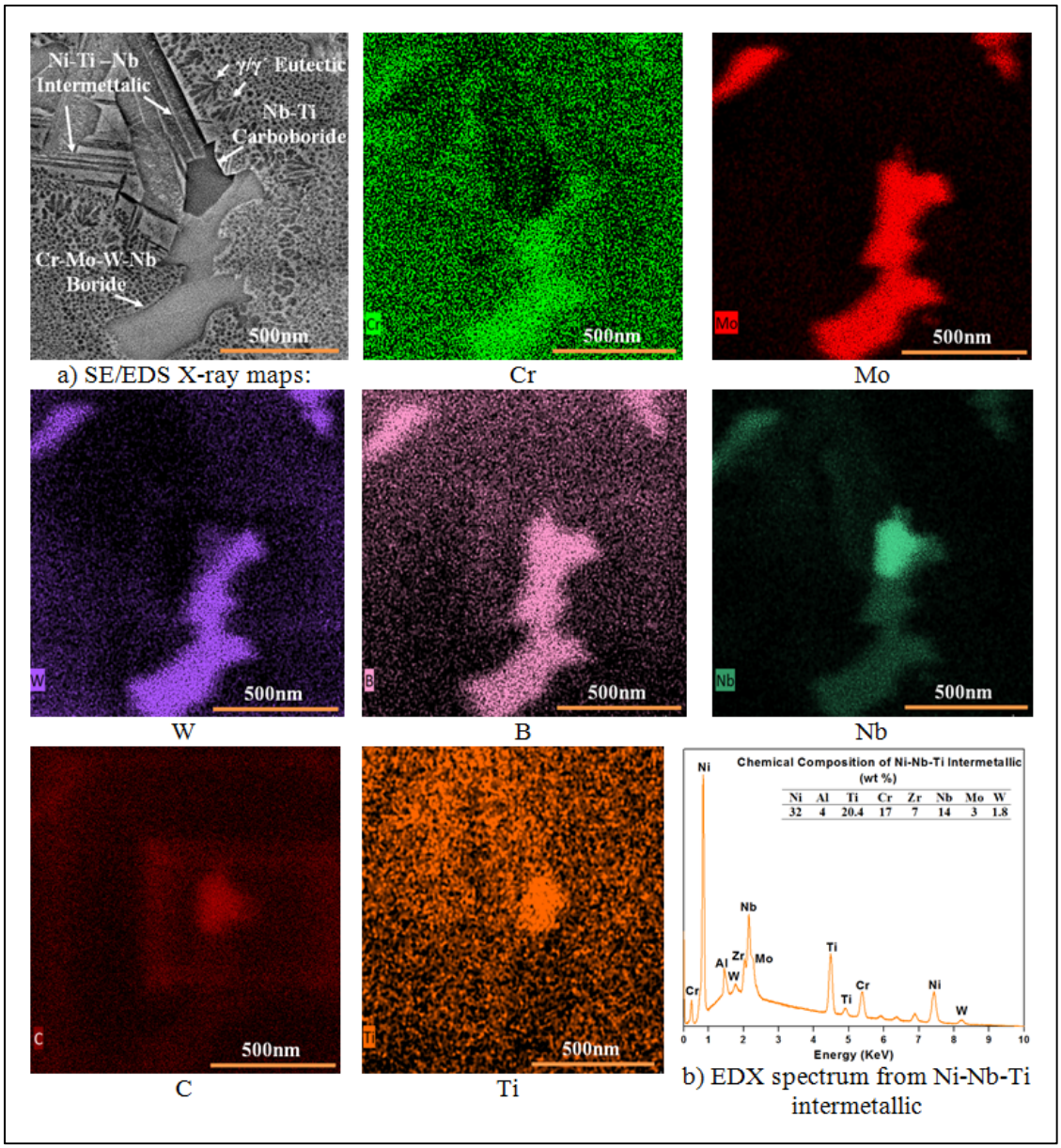

Figure 5.7 a) SE/EDS X-ray maps of simulated material showing the formation of γ-γ′ eutectic and Ni-Ti-Nb intermetallics close to Nb-Ti carboboride and Cr-Mo-W-Nb rich boride particles. b) EDX spectrum from Ni-Nb-Ti intermetallic contain 32 % Ni, 20 % Ti, 14 % Nb, 4 % Al, 17% Cr, 7 % Zr, 3 % Mo, 1.8 % W. samples heated at a rate of 400K/s, 3 s holing time at peak temperature of 1493K (1220°C).

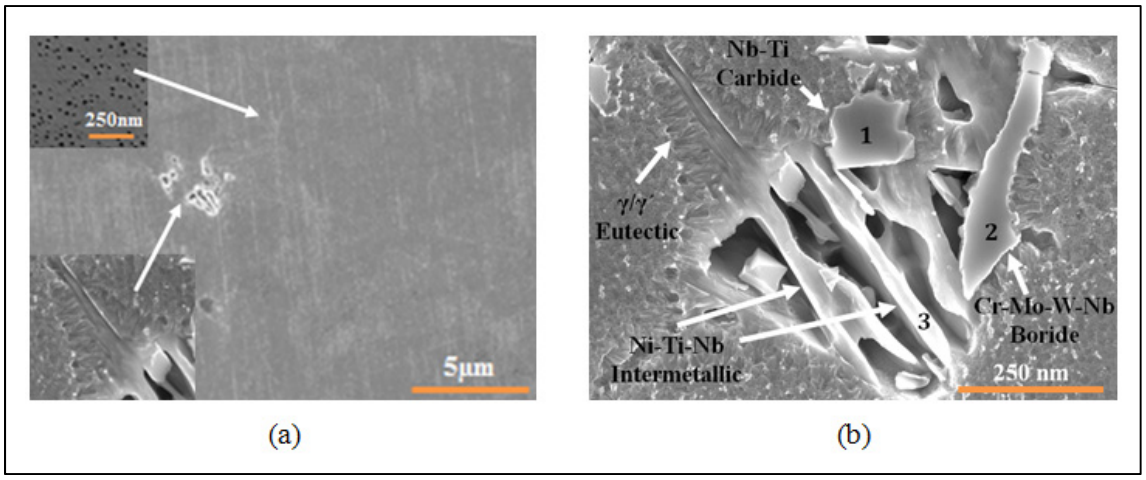

Figure 5.8 a, b) SEM micrographs showing formation of γ-γ′ eutectic and Ni-Ti-Nb intermetallic close to Nb-Ti carbide and Cr-Mo-W-Nb rich boride particles . Samples heated at a rate of 400K/s + 3 s holding time at 1523K (1250°C), followed by air quench.

Table 5-2 Chemical composition of intermetallic constituents (wt%) in the incipient melting zone at samples heated at a rate of 400K/s, held 3 s at peak temperature of 1523K (1250°C)

Elements	Ni-Nb-Ti intermetallic	Nb-Ti carbide	Cr-Mo-W-Nb boride
Al	4.14	0.42	0.24
Ti	21.46	30.81	4.25
Cr	19.46	2.72	38.8
Ni	33.53	1.12	1.98
Zr	4.1	4.73	0.88
Nb	11.18	46	13.09
Mo	3.92	7.48	31.21
W	2.21	6.72	9.53

A significant concentration of boron was detected by EDS in particles of phase 2, which also had a high concentration of Cr and Mo (Table 5-2). High Cr and Mo concentration observed in the EDS chemical analysis in this work is the characteristic feature of the boride phase observed in many Ni-based superalloys (Masoumi et al., 2014; Masoumi et al., 2016a; Reed, 2006a; Shahriari, Sadeghi et Akbarzadeh, 2009). Presence of boride and carbide particles in AD730™ has also been reported in our previous work (Masoumi et al., 2014; Masoumi et al., 2016a). Close to Nb-Ti carbides and Cr-Mo-W-Nb rich boride particles and at grain

boundaries, γ-γ′ eutectics as well as some binary eutectics containing γ phase and Ni-Ti-Nb intermetallics, phase 3, can be seen. The presence of these eutectic products contributes to the formation of liquid "pockets" in these zones via eutectic-type reaction between second phase particles and the surrounding matrix. The width of incipient melted region is around 1.2 µm. As given in Table II, the ratio of (Ti+Nb) /Al is around 8 for Ni-Ti-Nb phase. Therefore, the chemical composition of phase 1, given in Table II, and the platelet like morphology of the phase suggest that this phase is based on intermetallic $Ni_3(Ti, Nb)$, η. Figure 5.7, Figure 5.8 and Table 5-2 show that some degrees of grain boundary liquation can be also attributed to the constitutional liquation of borides during heat treatment between 1473K (1200˚C) and 1523K (1250˚C).

As Figure 5.9 shows although all the primary γ′ precipitates have been dissolved at 1573K (1300˚C), sub-solidus incipient melting of boride and carbide particles is still present. Figure 5.9 (b) shows another type of partially melted, intergranular liquation, observed at this temperature. Alloying elements such as B, C, Zr, Nb, Ti, Mo and Nb have the tendency to segregate at the grain boundaries and form compounds with lower melting temperatures. It is then reasonable to assume that melting takes place for some critical combinations of concentrations and temperature (Ojo, Richards et Chaturvedi, 2004a).

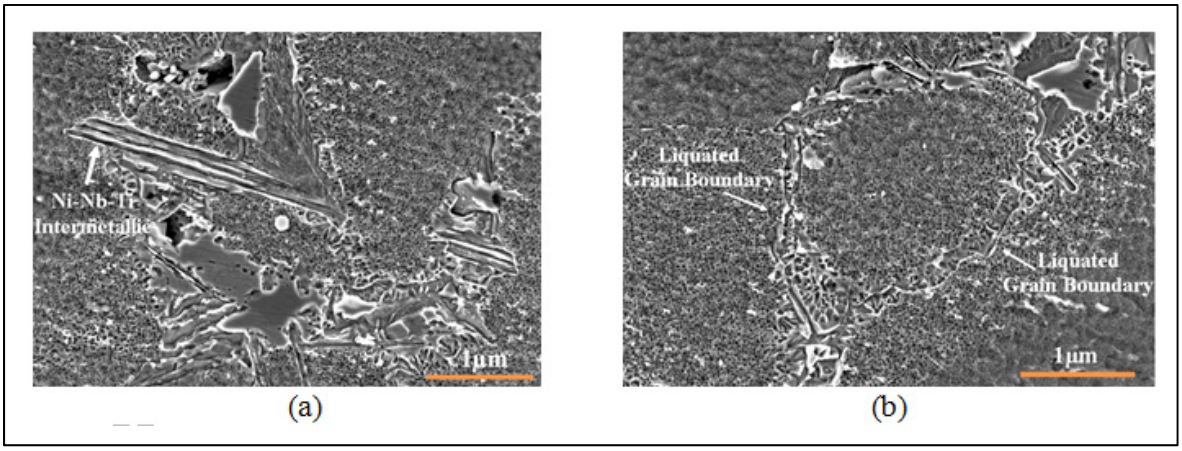

Figure 5.9 SEM micrographs showing: (a) formation of Ni-Nb-Ti intermetallic after sub-solidus incipient melting of boride and carbide particles, and (b) liquated grain boundary. Samples heated at a rate of 400K/s, held 3 s at 1573K (1300˚C), followed by compressed air cooling.

The above findings indicate that liquation may take place at temperatures in the vicinity of 1473K (1200°C). During LFW, in addition to rapid heating, high strain and strain rate will be applied which would increase the tendency of the material to have liquation at different locations. In the following, an analytical model is developed for predicting the temperature of the weld region, and hence to find out whether or not the weld zone experiences temperatures higher than the liquation temperature of this alloy.

5.4.3 Prediction of Temperature in Different Zones of LFWed Sample

The highly dynamic nature of the LFW process characterized by high frequency reciprocal movement of the parts accompanied by sever plastic deformation at the weld interface renders challenging the accurate measurement of the temperature at the interface during LFW. Attempts have been made by several authors to place thermocouples near the joint area (Chamanfar et al., 2011a; Mary et Jahazi, 2007a). However, plasticized material pushed down into thermocouple hole by the applied pressure during LFW, displaces the thermocouple from the desired location. Therefore, thermocouples should be placed far from the weld interface, and the measurement of temperature at the interface or any locations very close to the interface is not possible due to the complexity of the LFW process.

In order to overcome the limitations of experimental methods in temperature measurements at the interface, an analytical method calibrated by experiments is used to approximate the interface temperature and compare with the obtained liquation temperature of the alloy. Assuming that the plastic flow has a uniform thickness, and the stress, strain rate as well as the temperature of the weld interface are uniform and symmetric, friction welding can be modeled as a one-dimensional problem in which the effects of the flash are considered (Xiong et al., 2013). Using the one-dimensional thermal energy conservation analysis (Bateman, 1932; Bergman et al., 2011; Xiong et al., 2013; Yilbas et Sahin, 2014), temperatures at the weld interface and at different distances (L) from the weld line are:

$$T(WI)_i = T_1 + \frac{T_1 - T_2}{e^{-\frac{u}{k_\alpha}L_1} - e^{-\frac{u}{k_\alpha}L_2}} - \frac{T_1 - T_2}{1 - e^{-\frac{u}{k_\alpha}(L_1 - L_2)}} \qquad (5.1)$$

$$T(L) = T_1 + \frac{T_1 - T_2}{e^{-\frac{u}{k_\alpha}L_1} - e^{-\frac{u}{k_\alpha}L_2}} e^{-\frac{u}{k_\alpha}L} - \frac{T_1 - T_2}{1 - e^{-\frac{u}{k_\alpha}(L_1 - L_2)}} \quad (5.2)$$

where T_1 and T_2 are temperatures at L_1 and L_2, k_α is the thermal diffusivity and u the axial shortening rate. Non-equilibrium primary and secondary γ′ dissolution temperatures, determined from section 3.2, are used as boundary conditions to predict temperatures experienced by different weld zones during LFW. As shown in Figure 5.5, primary γ′ and secondary γ′ precipitates are practically totally dissolved at 1493K (1220˚C) and 1423K (1150˚C), respectively. Microstructure evaluation of LFWed samples showed that such volume fraction for primary and secondary γ′ particles is obtained at 0.4 mm and 1.5 mm from the weld interface, respectively. Therefore, considering the axial shortening of 0.21 mm during the forge stage, the temperatures at 0.505 mm and 1.605 mm from the weld line should be respectively 1493K (1220˚C) and 1423K (1150˚C) (according to boundary conditions obtained from the experiments). Based on the experimental data, the rate of axial shortening, u, is around 0.1 mm/s for the LFWed sample. Thermal diffusivity is normally expressed as $k_\alpha = \frac{\lambda}{\rho C_p}$ where λ is the thermal conductivity, ρ is the density and C_p the heat capacity. The values for λ, ρ, C_p and therefore, k_α are 35 W/(m.K), 8353 Kg/m^3, 828 J/(Kg.K) and 5.06×10^{-6} m^2/s , respectively for Ni-based superalloys (Donachie Matthew et Donachie Stephen, 2002). Using the above data, temperature distribution along the moving interface was calculated based on the formulation presented in Eqs. (5.1) and (5.2), and is shown in Figure 5.10, with the interface being the x axis origin. The obtained results indicate that the temperature of the weld zone decreases from 1523K (1250˚C) at the weld line to 1473K (1200˚C) at L= 0.7 mm.

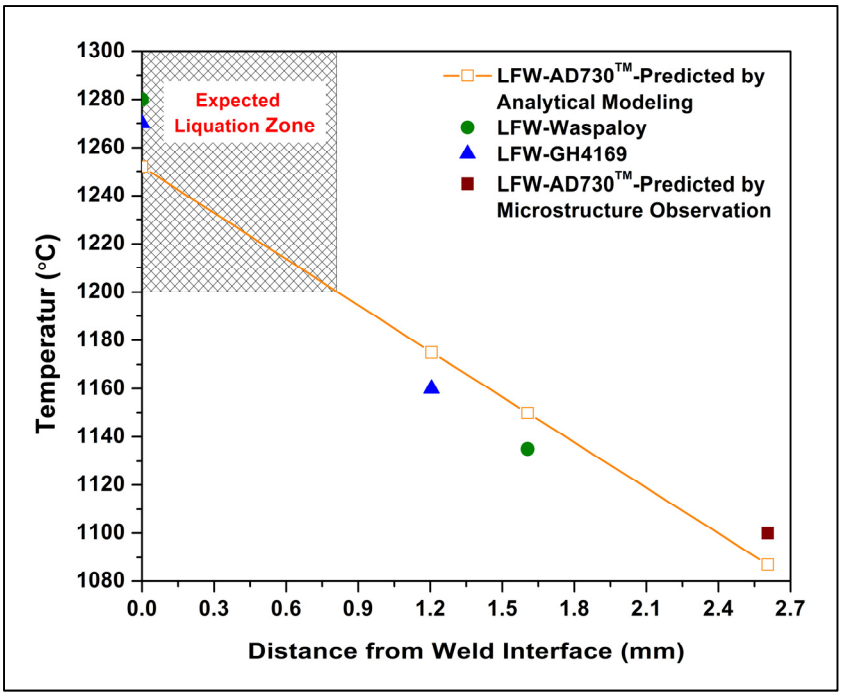

Figure 5.10 Comparison between predicted values using 1D analytical model and measured (thermocouple or infrared camera) temperature distributions in locations near to the LFW line and for two different superalloys, Waspaloy and GH4169. Predicted temperature at one location is also compared with predicted temperature by microstructure observation.

The evolution of the γ′ area fraction ($F_{s\gamma\prime}$) as a function of the processing time (t) for dissolution heat treatment at 1373K (1100°C) for AD730™ superalloy was determined in a previous study and is equal to (Masoumi et al., 2016a):

$$F_{s\gamma\prime} = 2.47 + 34.53\ exp(\frac{-t_e}{0.57}) \tag{5.3}$$

where t_e is the equivalent holding time at 1373K (1100°C) which considers the effects of heating and cooling rates on γ′ evolution in superalloys. t_e was calculated based on the following equation proposed by Soucail and Bienvenu (1996):

$$t_e = \frac{RT_m^2}{Q}\left(\frac{1}{V_h} + \frac{1}{V_c}\right) + t_m \tag{5.4}$$

where R is the gas constant, T_m the holding temperature, Q the activation energy for the dissolution of the γ′ phase, V_h and V_c respectively the heating and cooling rates, and t_m the holding time. Using Eq. (5.4), t_e was calculated to be about 8 sec at 1373K (1100˚C) for Q =270 KJ/mol, V_h= 400K/s, V_c= 50K/s, and t_m= 6.5 sec (Chamanfar et al., 2011a; Mary et Jahazi, 2007a; Masoumi et al., 2016a).

By substituting the obtained value of t_e into Eq. (3), the γ′ surface fraction, $F_{s\gamma\prime}$, was calculated to be about 29 %. Based on microstructure examination, the total area fraction of primary and secondary γ′ precipitates is 25.9 % at 2.5 mm from the weld interface (see Figure 5.3 and Figure 5.11). Therefore, this location which is in the TMAZ should have experienced a temperature around 1373K (1100˚C). On the other hand, using Eq. (5.2), temperature at L= 2.5 mm is calculated to be 1360K (1087˚C). The above analysis confirms that the thermal energy conservation equation can reliably predict the temperature at the weld interface during LFW of AD730™.

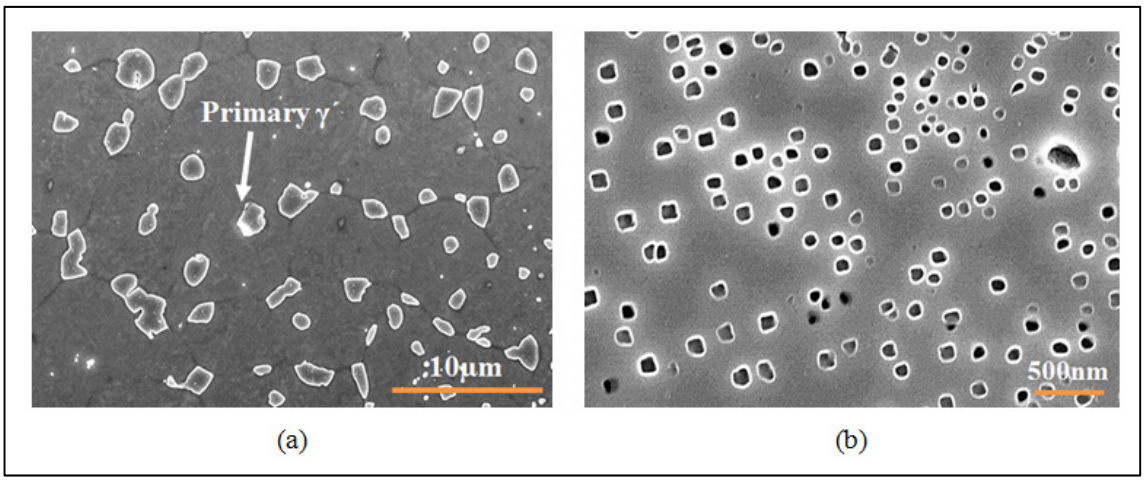

Figure 5.11 SEM micrographs of (a) primary γ′ (b) secondary γ′ precipitates at 2.5 mm from the weld interface.

Figure 5.10 shows a comparison between measured (thermocouple or infrared camera) temperature distributions in locations near to the LFW line and predicted values using the proposed 1D thermal analysis for two different superalloys, Waspaloy and GH4169 (Chamanfar et al., 2011a; Yang et al., 2015). It can be seen that in both cases a reasonable agreement exist between the predicted values and the measured ones (an error of about 3%) thereby confirming the good predictability of the 1D thermal model in the present investigation. For example, in the case of LFWed Waspaloy (Chamanfar et al., 2011a) at 1.5mm far from weld line, the measured temperature was around 1408K (1135˚C) and the predicted one, 1423K (1150˚C). A similar difference between the measured and predicted values was found for the GH4169 superalloy at 1.1 mm location from the weld line. Moreover, in the case of the GH4169 alloy, the authors (Yang et al., 2015) used 2D FEM simulation for predicting the temperature fields at and near the weld line. Their simulation results, confirmed by infrared camera measurement, indicated that temperature maps in the liquation sensitive zone, as shown in Figure 5.10, are approximately equal and their distribution is uniform in both directions (±5K (5˚C) from one end to another of the sample in both directions) which are in agreement with the rational used in the present investigation in considering a uniform temperature distribution.

The above analyses confirm that the proposed 1D analytical thermal conservation equation can be used to predict reasonably well temperature distribution in the liquation sensitive zone (Figure 5.10) during LFW of the AD730 alloy used in this investigation. Finally, it must be noted that for the calculations the same thermal expansion coefficients was used for the three alloys, as no specific data is available for each alloy and very similar heat input values (3000kW/m^2) was used for the three cases.

According to Eqs. (5.1), (5.2) and Figure 5.10, weld zone should experience temperatures higher than 1473K (1200˚C) until L= 0.7 mm. On this basis, the highest temperature reached at the interface is about 1523K (1250˚C), and at L=0.5 mm, it is about 1486K (1213˚C). As shown in Figure 5.6 to Figure 5.9, during the rapid heating process, constitutional liquation of both grain boundaries and second phase particles such as γ' particles, carbides and borides were observed between 1473K (1200˚C) and 1573K (1300˚C). Since weld line and TMAZ

(i.e. very close to the weld interface) experience temperatures higher than 1473K (1200˚C), indications of liquation are expected to be evident in these areas. However, as illustrated in Figure 5.4, no such indications were observed in the microstructure. Therefore, the contribution of other process parameters such as the applied compressive stress, frictional and forge deformation, as well as strain rate needs to be considered. No quantitative data is available on the possible influence of applied frictional and forge pressures on atomic diffusion of precipitates during LFW. However, simulation results showed that atomic diffusion can be enhanced by compressive stress and reduced by tensile stress (Xu, 2003) during hot compression or hot tensile tests in complex alloys. Thus, it is possible that liquation may be produced but disappears due to diffusion assisted pressure during LFW. In order to confirm this possibility, the governing mechanisms need to be determined before their impact could be quantified.

5.4.4 Possible Micromechanisms Controlling Diffusivity during LFW

Considering that AD730^{TM} would be fully austenitic at 1523K (1250˚C), the effect of stress will therefore be evaluated on the diffusion of Ni atoms. It is well known that lattice and pipe diffusion are the two most important mechanisms describing the diffusion of solutes to or away from stacking faults (Viswanathan et al., 2015). Transport of matter via dislocation pipe diffusion contributes significantly to the overall diffusive transport of matter, and under certain circumstances becomes the dominant transport mechanism (Robinson et Sherby, 1969). This contribution is included by defining the effective diffusion coefficient:

$$D_{eff} = D_L f_L + D_p f_p = D_{L_{eff}} + D_{p_{eff}} \tag{5.5}$$

where D_L and D_P are, respectively, the lattice and dislocation pipe diffusion coefficients, while f_L, essentially is equal to unity, and $f_p = a_p \rho$ are, respectively, the fraction of atoms participating in lattice and pipe diffusion processes (Robinson et Sherby, 1969). a_p is the cross-sectional area of the dislocation pipe in which fast diffusion is taking place, and ρ is the dislocation density.

Argon and Frost et al. (Ashby et Verrall, 1977; Frost et Ashby, 1982) reported that under an applied stress of σ_S, the dislocation density is given by $\rho = \frac{10}{b^2}\left(\frac{\sigma_s}{\mu}\right)^2$ with b the Burger's vector, and μ the shear modulus of the material. In the present investigation, the values of applied frictional and forge pressures (i.e. σ_S) during linear friction welding were 187.5 and 265 MPa, respectively.

Ashby and Frost (1977; 1982) have proposed relations for obtaining the values of b and μ under applied stress. These equations are identified as A3 and A5 in Appendix II. Also, the general expressions for calculating D_L and D_p according to Eqs. (A7) and (A8) are reported in this Appendix. Finally, all the variables that are needed for the calculation of D_L and D_p in Ni alloys are listed in Table 5-3. The reported data were obtained from the literature (Donachie Matthew et Donachie Stephen, 2002; Frost et Ashby, 1982; Masoumi et al., 2016a; Reed, 2006a).

Temperature measurements at different distances from the interface for Waspaloy (Chamanfar et al., 2011a) and IN 718 superalloys (Mary et Jahazi, 2007a) have shown that holding time at the highest temperature for each location close to the weld line is around 3 seconds. Combination of load and temperature measurements during the process (Chamanfar et al., 2011a; Mary et Jahazi, 2007a) showed that frictional pressure takes about 65 % of this time, and forge pressure the remaining, 35%. Therefore, since the applied pressures are different in each phase during LFW, the corresponding diffusion coefficient should be obtained separately.

Table 5-3 Temperature, pressure coefficients and material data for Ni alloys (Lesuer et al., 2001; Li et al., 2016; Milhet et al., 2013; Wang et al., 2009)

Bulk modulus, K_0, MPa	1.27×10^5
Shear modulus, , μ_0, MPa	5.3×10^4
Pressure dependence, $\frac{d\mu}{d\sigma_s}$	1.8
Pressure dependence, $\frac{dK}{d\sigma_s}$	5.1
Temperature dependence, $\frac{T_M dK}{K_0 dT}$	0.26
Temperature dependence, $\frac{T_M d\mu}{\mu_0 dT}$	-0.64
Activation Volume V_p^*, (m^3/mole)	6.9×10^{-6}
Burger's vector, b_0, m	2.5×10^{-10}
Pre exponential of pipe diffusion, $a_p D_{0p}$ (m^4/s)	3.1×10^{-23}
Activation energy of pipe diffusion, Q_p (kJ/mole)	170
Pre exponential of lattice diffusion for nickel, D_{0L} (m^2/s)	1.9×10^{-4}
Activation energy of lattice diffusion for nickel, Q_{0L} (kJ/mole)	284
Melting point of AD730^{TM}, T_M, K (°C)	1623 (1350)

Based on Eq. (A8), there is no pipe diffusion when there is no applied stress, and only lattice diffusion is taking place. On this basis, using Eqs. (A3) to (A9) and the data provided in Table 5-3, the value of $D_{L\,eff}$ is determined to be 3.45×10^{-14} m^2/s under no stress, and the values of $D_{p\,eff}$ were determined to be respectively 3.9×10^{-13} and 8.2×10^{-13} m^2/s under frictional and forge pressures at 1523K (1250°C). Therefore, the application of compressive stress during LFW results in 25 times increase in the value of D_{eff}. The findings indicate that the applied stress during LFW results in a minor increase (about 16 %) of the lattice diffusion while pipe diffusion ($D_{p\,eff}$) is about 23 times faster than lattice diffusion, $D_{L\,eff}$. The results are in agreement with the simulation results reported by Xu (2003) who showed that for low carbon steels, under applied stress, the diffusion coefficient of impurity-vacancy complex is three orders of magnitude larger than that of under no applied stress conditions.

In order to estimate the length scales over which diffusion of Ni element may realistically take place in the core of the liquated phase during LFW at the weld interface, a plot of diffusion length, x, vs. t is shown in Figure 5.12 for lattice and pipe diffusion coefficients following $x = \sqrt{Dt}$.

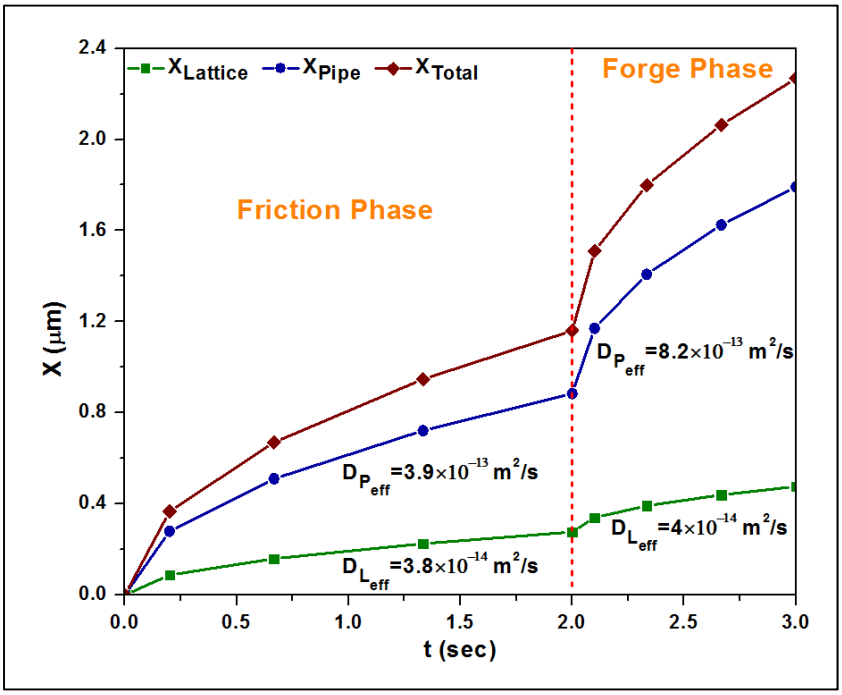

Figure 5.12 Diffusion distance, $x = \sqrt{Dt}$, vs. time for lattice, pipe and total diffusion coefficients at 1523K (1250˚C) for LFWed AD730^{TM} superalloy.

The calculated pipe diffusion coefficient would correspond to a diffusion distance of about 1.8 μm over the course of the 3 sec friction and forge pressures period at 1523K (1250˚C). In contrast, if only lattice diffusion had been considered, the distance Ni atoms have diffused would have been only 0.5 microns (i.e. 3.6 times shorter). These findings indicate that the governing mechanism controlling the diffusion of elements from the liquated zone at the weld interface is dislocation pipe diffusion. Similar behavior has been observed on the diffusion mechanisms during hot deformation of steels (Lesuer et al., 2001; Samantaray et al., 2011).

As shown in Figure 5.12, the total diffusion length of Ni atom (due to lattice and pipe diffusion) under compression is around 2.3 μm at 1523K (1250˚C). Therefore, the maximum diameter of the liquated phase that can disappear by the applied stress is 4.6 μm. Otherwise, some traces of the liquidated zone will remain after the end of the welding. SEM results (Figure 5.8) show that the maximum length (or diameter) of the liquated phase is around 1.2 μm at 1523K (1250˚C). Thus, it is reasonable to consider that the liquated phase at the interface can be eliminated by the imposed pressure and that is probably the reason why no trace of liquated phase was observed at the weld interface in our experiments.

Ola et al. (2011c) reported intergranular and intragranular liquation in the TMAZ experiencing 1503K (1230˚C) during linear friction welding of IN 738.The frictional and forge pressures reported by the authors were identical and equal to 90 MPa (Ola et al., 2011c). To analyze this apparent discrepancy with the results obtained in the present work, lattice and pipe diffusion coefficients of Ni atoms were calculated using the process data provided by the authors. These values were determined to be 2.7×10^{-14} (lattice diffusion) and 3.3×10^{-14} m^2/s (pipe diffusion), and the results are presented in Figure 5.13. It can be seen that a diffusion length of 0.4 μm for lattice and pipe diffusion coefficient under the above mentioned conditions is obtained. A comparison between Figure 5.12 and Figure 5.13 show that although lattice diffusion lengths are almost the same for IN 738 and AD730^{TM}, the pipe diffusion length for IN 738 is 4.5 times shorter than the one for AD730^{TM}. This result is in agreement with those of Leuser (2001) and Samantaray (2011) who found that pipe diffusion is much faster at higher temperatures and higher applied stresses.

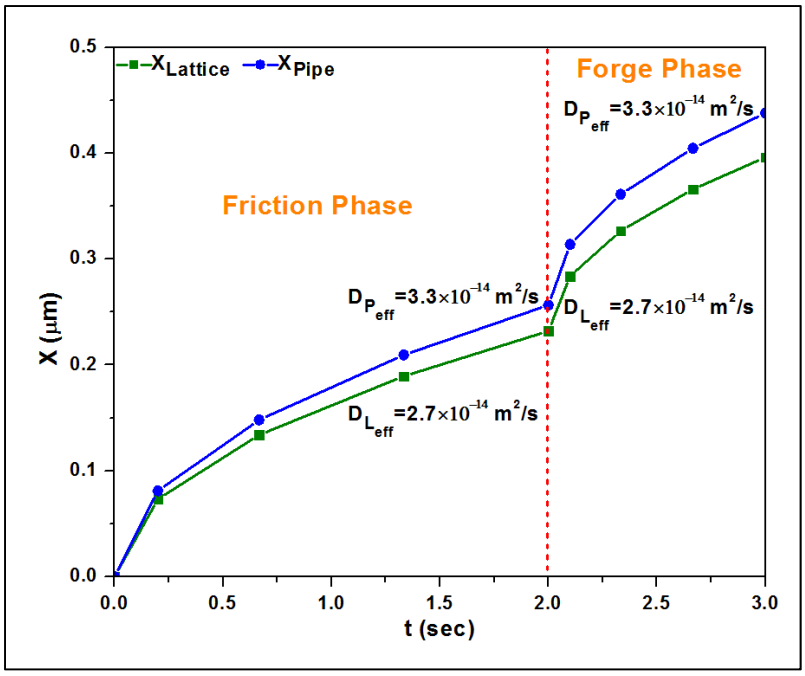

Figure 5.13 Diffusion distance, $x = \sqrt{Dt}$, vs. time for lattice and pipe diffusion coefficients at 1503K (1230˚C) for LFWed IN738 superalloy.

Also, the total diffusion lengths over the course of the 3 seconds peak temperature of 1503K (1230˚C) are compared for different pressures of 90 and 187.5 and 265 MPa in Figure 5.14 for AD730^{TM} and IN 738.

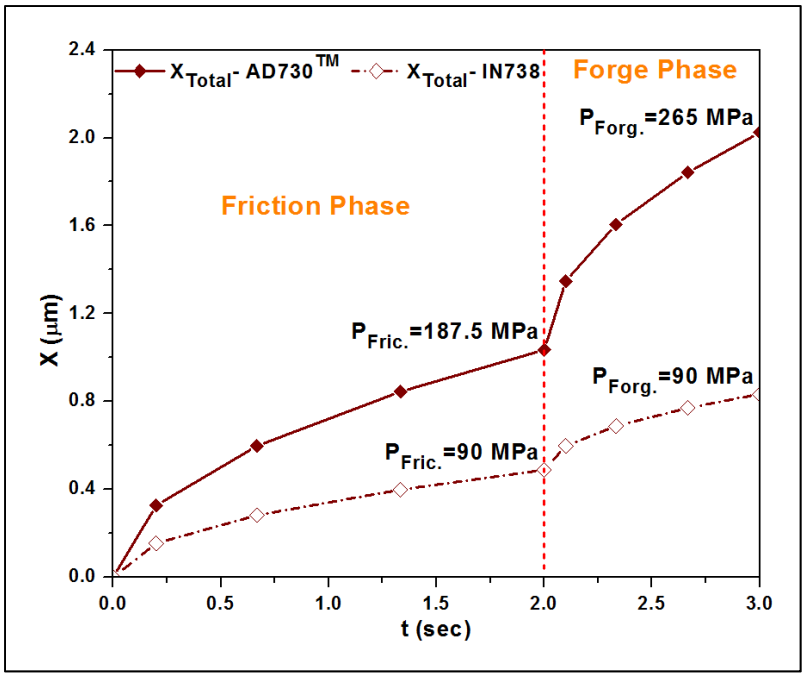

Figure 5.14 Comparison of diffusion distance, $x = \sqrt{Dt}$, vs. time for total diffusion coefficients at 1503K (1230˚C) for LFWed AD730^{TM} and IN738 superalloys.

It can be seen that the higher is the applied pressure, the faster would be the diffusion of atoms during LFW. Specifically, the total diffusion length is around 2 µm for the frictional pressure of 187.5 MPa and forge pressure of 265 MPa while this value is only 0.8 µm under constant friction and forge pressures of 90 MPa. Therefore, only a liquated zone with a maximum diameter of 1.6 µm can be eliminated by the applied pressure of 90 MPa. However, the size of the observed liquated phase is around 3 µm for IN 738 (Ola et al., 2011c). Therefore, the liquated phase cannot be eliminated during the LFW process and will be detectable upon post weld microscopic examination as reported by the authors. In order to eliminate this liquation, pressures higher than 90 MPa should have to be applied during linear friction welding.

The above proposed methodology can be used for the design of optimum LFW processes and accurate determination of the applied frictional and forge pressures in order to obtain sound and crack free LFW joints of Ni based superalloys.

5.5 Summary and Conclusions

In the present study, the influence of high temperature and pressure on liquation occurrence during LFW of wrought Ni-based superalloy was investigated. The effect of each parameter was studied and quantified separately. A combination of LFW welding, Gleeble thermomechanical testing and analytical modeling allowed us to determine the liquation temperature of the investigated alloy and to propose a methodology for optimum design of LFW of Ni-based superaloys. By considering the influence of kinetic parameters, the governing mechanisms responsible for the possible observation or not observation of resolidified phases were identified and discussed.

The main conclusions of the present investigation are as follows:

1- Noticeable changes occur in the microstructure of the LFWed AD730^{TM} from parent material within 4-4.5 mm thick layer on both sides from the weld interface. The volume fraction of primary and secondary γ' particles decrease with a decrease in the distance from the weld interface, and they are totally dissolved until respectively 0.4 mm and 1.5 mm from the weld interface.

2- Constitutional liquation of primary γ', Cr-Mo-W-Nb borides, and Nb-Ti carbides were the predominant liquation mechanisms in AD730^{TM} between 1473-1573K (1200-1300˚C).

3- Analytical modeling results indicated that the peak temperature in the weld interface reached 1250˚C. However, no liquation was observed in the weld zone or flash.

4- The compressive stress increases the diffusion coefficient of the Ni atoms by about 25 times.

5- The combination of high temperature, frictional and forge pressures during LFW can result in liquation and crack resistant microstructure in LFWed superalloy.

5.6 Acknowledgments

The financial support from the Natural Sciences and Engineering Research Council (NSERC) 261712 of Canada in the form of a Discovery Grant is gratefully acknowledged. The authors express appreciation to Aubert & Duval Co. and to Dr. Alexandre Devaux for providing AD730^{TM} samples and for invaluable discussions, and to TWI Ltd. for welding the samples.

Appendix I

Strain rate in LFW

There is still debate on the actual strain rate value during the LFW process. Due to the very dynamic nature of the process, most of the estimations are done indirectly or using simulation. Grant et al. [55] using 2D FEM simulation reported that the maximum strain rate during inertia friction welding process of Ni-based superalloy RR1000, which could be considered similar to LFW is about 4.5 s^{-1}. Wang et al. (2017) and Vairis et al. (1999a) estimated a strain rate of 4.3 s^{-1} for linear friction welding of titanium alloys. Vairis and Frost proposed the following equation for estimating the strain rate in the LFW process (Vairis et Frost, 1998):

$$\dot{\varepsilon} = \frac{af}{l} \tag{A1}$$

where a is the amplitude of the oscillation, f is the frequency and l is the length of specimen in the direction of oscillation. Since then, changes to this equation have been proposed by other authors but essentially the equation remained the same. Using the above equation, the strain rate during LFW of superalloys (considering the process parameters used for these alloys) is in the range 3-18 s^{-1}. Turner et al. (2011a) carried out by a 2D numerical simulation of LFW for Ti-6Al-4V alloy. The authors predicted a peak strain rate of 2500 s^{-1} in some region along the weld line. However, the stress-strain curves used in the simulation were obtained using the JMatPro software till strain rate values of 1000 s^{-1}. Considering the

microstructural evolution and the greater deformation in LFW joint, the strain rate has been estimated to be around 70 s^{-1} (Jing et al., 2015).

Based on Eq. (A1), and the LFW parameters used in the present investigation, the strain rate during LFW of AD730^{TM} was determined to be 3.85 s^{-1}. This value was then used for calculating the adiabatic effect during LFW. In order to cover a wider range of strain rate values, the temperature rise due to internal heating during deformation was estimated for strain rates of 1s^{-1} and 20 s^{-1} at 1473K (1200˚C) providing a lower and upper limit for temperature variations.

Temperature increase during LFW

The following equation was used for calculating the extra increase in temperature (ΔT) due to deformation (Altan, Ngaile et Shen, 2005):

$$\Delta T = \frac{0.95\eta}{\rho C_p}\int_0^{\varepsilon} \sigma d\varepsilon \qquad \text{(A2)}$$

where ρ is the density of the alloy (8353.86 Kg/m^3 at 1473K(1200˚C)), C_p the specific heat (828 J/(Kg.K) at 1473K(1200˚C)), σ the flow stress, ε the true strain, and η the thermal efficiency which is function of strain rate, and can be expressed as η= 0.95 for $\dot{\varepsilon} \geq 1$ s^{-1}. σ and ε values were obtained for similar Ni-based superalloys from literature (Guo et al., 2012; Jiang et al., 2016; Liu et al., 2008).

The temperature increases at strain rates 1 s^{-1} and 20 s^{-1} are about 13.5K (13.5˚C) and 25.5K (25.5˚C) at 1473K (1200˚C), respectively. This indicates that a 20 times increase in strain rate results in a temperature increment of about 12K (12˚C) showing a relatively slow increase in temperature with the strain rate. Little experimental data is available on the impact of high strain rate (100 s^{-1} and more) on temperature increase; however, it is generally accepted that as the strain rate increases the temperature increase reaches almost the steady state value (Guo et al., 2012; Oluwasegun et al., 2014; Zhao, 1993).

Appendix II

$$b(\sigma_s) = b_0 exp(-\frac{\sigma_s}{3K}) \tag{A3}$$

$$K(T, \sigma_s) = K_0[1 + \frac{T_M dK}{K_0 dT}\left(\frac{T - 300}{T_M}\right) + \frac{\sigma_s}{K_0}\frac{dK}{d\sigma_s} \tag{A4}$$

$$\mu(T, \sigma_s) = \mu_0[1 + \frac{T_M d\mu}{\mu_0 dT}\left(\frac{T - 300}{T_M}\right) + \frac{\sigma_s}{\mu_0}\frac{d\mu}{d\sigma_s} \tag{A5}$$

$$Q_p = Q_{p0} + \sigma_s V_p^* \tag{A6}$$

$$D_L = D_0\, exp\left(-\frac{Q_L}{RT}\right) \tag{A7}$$

$$D_{p_{eff}} = \frac{10}{b^2}\,(\frac{\sigma_s}{\mu})^2 a_p D_p \tag{A8}$$

$$a_p D_p = a_p D_{0p}\, exp\left(-\frac{Q_p}{RT}\right) \tag{A9}$$

References

Altan, T., G. Ngaile et G. Shen. 2005. *Cold and Hot Forging: Fundamentals and Applications*. ASM International, 342 p.

Ashby, M. F., et R. A. Verrall. 1977. « Micromechanisms of Flow and Fracture, and Ttheir Relevance to the Rheology of the Upper Mantle ». *Philosophical Transactions of the Royal Society A: Mathematical, Physical and Engineering Sciences,* vol. 288, p. 59-95.

Bateman, H. 1932. *Partial Differential Equations of Mathematical Physics*. Coll. « Cambridge University Press and The Macmillan Co ». 338-345 p.

Bergman, T. L., A. S. Lavine, F. P. Incropera et D. P. Dewitt. 2011. *Fundamentals of Heat and Mass Transfer*, 7 Edition John Wiley & Sons, 1072 p.

Bhamji, I., M. Preuss, P. L. Threadgill et A. C. Addison. 2011. « Solid State Joining of Metals by Linear Friction Welding: A Literature Review ». *Materials Science and Technology,* vol. 27, nº 1, p. 2-12.

Bouse, G. K. . 1996. « Eta and Platelet Phases in Investment Cast Superalloys ». In *Superalloys 1996*. sous la dir. de Kissinger, R. D., D. J. Deye et D. L. Anton, p. 163-172. The Minerals, Metals & Materials Society.

Chamanfar, A., M. Jahazi et J. Cormier. 2015a. « A Review on Inertia and Linear Friction Welding of Ni-Based Superalloys ». *Metallurgical and Materials Transactions A: Physical Metallurgy and Materials Science,* vol. 46, nº 4, p. 1639-1669.

Chamanfar, A., M. Jahazi, J. Gholipour, P. Wanjara et S. Yue. 2011a. « Mechanical Property and Microstructure of Linear Friction Welded Waspaloy ». *Metallurgical and Materials Transactions A,* vol. 42, nº 3, p. 729-744.

Chamanfar, A., M. Jahazi, J. Gholipour, P. Wanjara et S. Yue. 2012b. « Suppressed Liquation and Microcracking in Linear Friction Welded Waspaloy ». *Materials and Design,* vol. 36, p. 113-122.

Choi, B. G., I. S. Kim, D. H. Kim, S. M. Seo et C. Y. Jo. 2004. « Eta Phase Formation during Thermal Exposure and its Effect on Mechanical Properties in Nickel-Base Superalloy GTD 111 ». In *Superalloys 2004*. sous la dir. de Green, K. A., T. M. Pollock, H. Harada, T. E. Howson, R. C. Reed, J. J. Schirra et S. Walston, p. 163-171. The Minerals, Metals & Materials Society.

Cormier, J., X. Milhet et J. Mendez. 2007a. « Effect of Very High Temperature Short Exposures on the Dissolution of the γ′ Phase in Single Crystal MC2 Superalloy ». *Journal of Materials Science,* vol. 42, nº 18, p. 7780-7786.

Cormier, J., X. Milhet et J. Mendez. 2007b. « Non-Isothermal Creep at Very High Temperature of the Nickel-Based Single Crystal Superalloy MC2 ». *Acta Materialia,* vol. 55, nº 18, p. 6250-6259.

Danis, Y., C. Arvieu, E. Lacoste, T. Larrouy et J. M. Quenisset. 2010. « An Investigation on Thermal, Metallurgical and Mechanical States in Weld Cracking of Inconel 738LC Superalloy ». *Materials and Design,* vol. 31, nº 1, p. 402-416.

Devaux, A., B. Picqué, M. F. Gervais, E. Georges, T. Poulain et P. Héritier. 2012c. « AD730™-A New Nickel-Based Superalloy for High Temperature Engine Rotative Parts ». In *Proceedings of the International Symposium on Superalloys*. p. 911-919.

Donachie Matthew, J., et J. Donachie Stephen. 2002. *Superalloys-A Technical Guide* 2nd Edition. ASM International: ASM International, 439 p.

Dye, D., O. Hunziker et R. C. Reed. 2001. « Numerical Analysis of the Weldability of Superalloys ». *Acta Materialia,* vol. 49, nº 4, p. 683-697.

Frost, H. J., et M. F. Ashby. 1982. *Deformation-Mechanism Maps: The Plasticity and Creep of Metals and Ceramics*. Pergamon Press, Oxford, 166 p.

Giraud, R., Z. Hervier, J. Cormier, G. Saint-Martin, F. Hamon, X. Milhet et J. Mendez. 2013. « Strain effect on the γ′ dissolution at high temperatures of a nickel-based single crystal superalloy ». *Metallurgical and Materials Transactions A: Physical Metallurgy and Materials Science,* vol. 44, nº 1, p. 131-146.

Guo, S., D. Li, Q. Guo, Z. Wu, H. Peng et J. Hu. 2012. « Investigation on Hot Workability Characteristics of Inconel 625 Superalloy Using Processing Maps ». *Journal of Materials Science,* vol. 47, nº 15, p. 5867-5878.

Jiang, H., J. Dong, M. Zhang et Z. Yao. 2016. « A Study on the Effect of Strain Rate on the Dynamic Recrystallization Mechanism of Alloy 617B ». *Metallurgical and Materials Transactions A,* vol. 47, nº 10, p. 5071-5087.

Jing, L., R. D. Fu, Y. J. Li, Y. Shi, J. Wang et D. X. Du. 2015. « Physical Simulation of Microstructural Evolution in Linear Friction Welded Joints of Ti-6Al-4V Alloy ». *Science and Technology of Welding and Joining,* vol. 20, nº 4, p. 286-290.

Lesuer, D. R., C. K. Syn, J. D. Whittenberger, M. Carsi, O. A. Ruano et O. D. Sherby. 2001. « Creep Behavior of Fe-C Alloys at High Temperatures and High Strain Rates ». *Materials Science and Engineering A,* vol. 317, nº 1-2, p. 101-107.

Li, W., A. Vairis, M. Preuss et T. Ma. 2016. « Linear and Rotary Friction Welding Review ». *International Materials Reviews,* vol. 61, nº 2, p. 71-100.

Li, W. Y., T. Ma et J. Li. 2010. « Numerical Simulation of Linear Friction Welding of Titanium Alloy: Effects of Processing Parameters ». *Materials and Design,* vol. 31, nº 3, p. 1497-1507.

Liu, Y., R. Hu, J. Li, H. Kou, H. Li, H. Chang et H. Fu. 2008. « Deformation Characteristics of As-Received Haynes230 Nickel Base Superalloy ». *Materials Science and Engineering: A,* vol. 497, nº 1, p. 283-289.

Mary, C., et M. Jahazi. 2007a. « Linear Friction Welding of IN-718 Process Optimization and Microstructure Evolution ». In *5th International Conference on Processing and Manufacturing of Advanced Materials - THERMEC 2006, July 4, 2006 - July 8, 2006.* (Vancouver, BC, Canada) Vol. 15-17, p. 357-362. Coll. « Advanced Materials Research »: Trans Tech Publications.

Mary, C., et M. Jahazi. 2008. « Multi-Scale Analysis of IN-718 Microstructure Evolution during Linear Friction Welding ». *Advanced Engineering Materials,* vol. 10, nº 6, p. 573-578.

Masoumi, F., M. Jahazi, J. Cormier et D. Shahriari. 2014. « Dissolution Kinetics and Morphological Changes of γ ′ in AD730™ Superalloy ». In *MATEC Web of Conferences*. Vol. 14.

Masoumi, F., M. Jahazi, D. Shahriari et J. Cormier. 2016a. « Coarsening and Dissolution of γ′ Precipitates during Solution Treatment of AD730™ Ni-Based Superalloy: Mechanisms and Kinetics Models ». *Journal of Alloys and Compounds,* vol. 658, p. 981-995.

Masoumi, F., D. Shahriari, M. Jahazi, J. Cormier et A. Devaux. 2016c. « Kinetics and Mechanisms of γ′ Reprecipitation in a Ni-Based Superalloy ». *Scientific Reports,* vol. 6.

Matsumoto, S., T. Tokunaga, H. Ohtani et M. Hasebe. 2005. « Thermodynamic analysis of the phase equilibria of the Nb-Ni-Ti system ». *Materials Transactions,* vol. 46, nº 12, p. 2920-2930.

Milhet, X., M. Arnoux, V. Pelosin et J. Colin. 2013. « On the Dissolution of the γ′ Phase at the Dendritic Scale in a Rhenium-Containing Nickel-Based Single Crystal Superalloy after High Temperature Exposure ». *Metallurgical and Materials Transactions A: Physical Metallurgy and Materials Science,* vol. 44, nº 5, p. 2031-2040.

Mousavizade, S. M., F. M. Ghaini, M. J. Torkamany, J. Sabbaghzadeh et A. Abdollah-zadeh. 2009. « Effect of Severe Plastic Deformation on Grain Boundary Liquation of a Nickel-Base Superalloy ». *Scripta Materialia,* vol. 60, nº 4, p. 244-247.

Nakkalil, R., N. L. Richards et M. C. Chaturvedi. 1992. « Grain Boundary Liquid Film Migration during Welding of Incoloy 903 ». *Scripta Metallurgica et Materiala,* vol. 26, nº 10, p. 1599-1604.

Ojo, O. A., N. L. Richards et M. C. Chaturvedi. 2004a. « Contribution of Constitutional Liquation of Gamma Prime Precipitate to Weld HAZ Cracking of Cast Inconel 738 Superalloy ». *Scripta Materialia,* vol. 50, nº 5, p. 641-646.

Ola, O. T., O. A. Ojo et M. C. Chaturvedi. 2013a. « Effect of Deformation Mode on Hot Ductility of a γ' Precipitation Strengthened Nickel-Base Superalloy ». *Materials Science and Engineering A,* vol. 585, p. 319-325.

Ola, O. T., O. A. Ojo, P. Wanjara et M. C. Chaturvedi. 2011c. « Analysis of Microstructural Changes Induced by Linear Friction Welding in a Nickel-Base Superalloy ». *Metallurgical and Materials Transactions A: Physical Metallurgy and Materials Science,* vol. 42, nº 12, p. 3761-3777.

Oluwasegun, K. M., J. O. Olawale, O. O. Ige, M. D. Shittu, A. A. Adeleke et B. O. Malomo. 2014. « Microstructural Characterization of Thermomechanical and Heat-Affected Zones of an Inertia Friction Welded Astroloy ». *Journal of Materials Engineering and Performance,* vol. 23, nº 8, p. 2834-2846.

Porter, D. A., et K. E. Easterling. 1992. *Phase Transformations in Metals and Alloys*. CRC Press.

Reed, R. C. 2006a. *The Superalloys Fundamentals and Applications*, 9780521859042. Coll. « The Superalloys: Fundamentals and Applications ». 1-372 p.

Robinson, S. L., et O. D. Sherby. 1969. « Mechanical Behavior of Polycrystalline Tungsten at Elevated Temperature ». *Acta Metallurgica,* vol. 17, nº 2, p. 109-125.

Samantaray, D., C. Phaniraj, S. Mandal et A. K. Bhaduri. 2011. « Strain Dependent Rate Equation to Predict Elevated Temperature Flow Behavior of Modified 9Cr-1Mo (P91) Steel ». *Materials Science and Engineering A,* vol. 528, nº 3, p. 1071-1077.

Shahriari, D., M. H. Sadeghi et A. Akbarzadeh. 2009. « γ' Precipitate Dissolution during Heat Treatment of Nimonic 115 Superalloy ». *Materials and Manufacturing Processes,* vol. 24, nº 5, p. 559-563.

Shahriari, D., M. H. Sadeghi, A. Akbarzadeh et M. Cheraghzadeh. 2009b. « The Influence of Heat Treatment and Hot Deformation Conditions on γ′ Precipitate Dissolution of

Nimonic 115 Superalloy ». *International Journal of Advanced Manufacturing Technology,* vol. 45, nº 9-10, p. 841-850.

Shinoda, T., Y. Mizuno, J. Li et T. Saito. 2000. « Friction Welding Phenomena of Aluminium ». *Welding International,* vol. 14, nº 6, p. 425-430.

Soucail, M., et Y. Bienvenu. 1996. « Dissolution of the γ′ Phase in a Nickel Base Superalloy at Equilibrium and under Rapid Heating ». *Materials Science and Engineering A,* vol. 220, nº 1-2, p. 215-222.

Soucail, M., A. Moal, E. Massoni, C. Levaillant, L. Naze et Y. Bienvenu. 1992. « Microstructural Study and Numerical Simulation of Inertia Friction Welding of Astroloy ». In *Superalloys 1992*. p. 847-856. The Minerals, Metals & Materials Society.

Turner, R., J. C. Gebelin, R. M. Ward et R. C. Reed. 2011a. « Linear friction welding of Ti-6Al-4V: Modelling and validation ». *Acta Materialia,* vol. 59, nº 10, p. 3792-3803.

Uday, M. B., M. N. A. Fauzi, H. Zuhailawati et A. B. Ismail. 2010. « Advances in Friction Welding Process: A Review ». *Science and Technology of Welding and Joining,* vol. 15, nº 7, p. 534-558.

Vairis, A., et M. Frost. 1998. « High Frequency Linear Friction Welding of a Titanium Alloy ». *Wear,* vol. 217, nº 1, p. 117-131.

Vairis, A., et M. Frost. 1999a. « On the Extrusion Stage of Linear Friction Welding of Ti 6A1 4V ». *Materials Science and Engineering A,* vol. 271, nº 1-2, p. 477-484.

Vairis, A., et M. Frost. 2000b. « Modelling the Linear Friction Welding of Titanium Blocks ». *Materials Science and Engineering A,* vol. 292, nº 1, p. 8-17.

Viswanathan, G. B., R. Shi, A. Genc, V. A. Vorontsov, L. Kovarik, C. M. F. Rae et M. J. Mills. 2015. « Segregation at Stacking Faults within the γ′ Phase of two Ni-Base Superalloys Following Intermediate Temperature Creep ». *Scripta Materialia,* vol. 94, p. 5-8.

Wang, G., D. S. Xu, N. Ma, N. Zhou, E. J. Payton, R. Yang, M. J. Mills et Y. Wang. 2009. « Simulation Study of Effects of Initial Particle Size Distribution on Dissolution ». *Acta Materialia,* vol. 57, nº 2, p. 316-325.

Wang, X. Y., W. Y. Li, T. J. Ma et A. Vairis. 2017. « Characterisation Studies of Linear Friction Welded Titanium Joints ». *Materials and Design,* vol. 116, p. 115-126.

Wang, Y., W. Z. Shao, L. Zhen et B. Y. Zhang. 2011a. « Hot deformation behavior of delta-processed superalloy 718 ». *Materials Science and Engineering A,* vol. 528, nº 7-8, p. 3218-3227.

Xiong, J. T., J. L. Li, Y. N. Wei, F. S. Zhang et W. D. Huang. 2013. « An Analytical Model of Steady-State Continuous Drive Friction Welding ». *Acta Materialia,* vol. 61, nº 5, p. 1662-1675.

Xu, T. D. 2003. « Creating and Destroying Vacancies in Solids and Non-Equilibrium Grain-Boundary Segregation ». *Philos. Mag.,* vol. 83, nº 7.

Yang, X., W. Li, J. L. Li, B. Xiao, T. Ma, Z. Huang et J. Guo. 2015. « Finite Element Modeling of the Linear Friction Welding of GH4169 Superalloy ». *Materials & Design,* vol. 87, nº Supplement C, p. 215-230.

Yilbas, B. S., et A. Z. Sahin. 2014. *Friction Welding: Thermal and Metallurgical Characteristics*. Springer Science & Business Media.

Zhang, H. R., O. A. Ojo et M. C. Chaturvedi. 2008. « Nanosize Boride Particles in Heat-Treated Nickel Base Superalloys ». *Scripta Materialia,* vol. 58, nº 3, p. 167-170.

Zhao, D. 1993. « Temperature Correction in Compression Tests ». *Journal of Materials Processing Tech.,* vol. 36, nº 4, p. 467-471.

CHAPITRE 6

ARTICLE 4: HIGH TEMPERATURE CREEP PROPERTIES OF A LINEAR FRICTION WELDED NEWLY DEVELOPED WROUGHT NI-BASED SUPERALLOY

F. Masoumi[a], L. Thébaud[b,c], D. Shahriari[a], M. Jahazi[a], J. Cormier[b], A. Devaux[C], B.C.D. Flipo[d]

[a] Department of Mechanical Engineering, École de Technologie Supérieure (ETS), H3C 1K3, Montreal, QC, Canada
[b] Institute Pprime, UPR CNRS 3346, Physics and Mechanics of Materials Department, ISAE- ENSMA, BP 40109, Futuroscope- Chasseneuil Cedex 86961, France
[c] Aubert & Duval, Site des Ancizes, BP1, 63770 Les Ancizes Cedex, France
[d] TWI Ltd, Granta Park, Great Abington, Cambridge CB21 6AL, UK

This article was published in the Material Science and Engineering A in January, 2018

6.1 Abstract

AD730^{TM} Ni-based superalloy specimens in solution-treated conditions were linear friction welded. Then, post-weld heat treatment (PWHT), consisting of γ′ sub-solvus solution treatments followed by aging, was conducted on the linear friction welded samples. High temperature creep tests were performed on the as-welded and PWHTed joints at two different temperatures: 700°C under 600 and 750 MPa stress levels, and 850°C under 100 and 200 MPa stresses. The creep resistance of the PWHTed joints was higher than that of the as-welded samples. The PWHTed joints exhibited better ductility than that of the base material at 850°C, while they showed slightly lower creep life at 700°C in comparison to the base metal. Microstructure examination showed that cracks initiated at the interface of oxidized particles at 700°C. The decrease in creep resistance of the AD730^{TM} Ni-based superalloy at 850°C was related to a combination of the formation of precipitate-free zones (PFZ) in the vicinity of the grain boundaries (GBs) and microcracking assisted by oxidation. The Larson-Miller Parameter (LMP) was used to correlate the creep strength, temperature and time to failure for the as-welded and PWHTed samples. LMP values varied between 21.5×10^3 and 24.5×10^3. It was found that in the investigated temperature range, the PWHTed AD730^{TM} has similar creep characteristics as Udimet^{TM}720 Li and Inconel 738LC at low values of LMP and better creep properties than those of the Inconel 617 alloy at higher LMP values.

Key words: Linear friction welding, Ni-based superalloy, AD730^{TM}, Mechanical properties at elevated temperatures, Creep mechanisms

6.2 Introduction

Ni-based superalloys are widely used in the hot section of gas turbines, and consequently, are subjected to creep and/or fatigue damage during operation (Cormier, Milhet et Mendez, 2007b; Devaux et al., 2014; Reed, 2006a). Therefore, improving their high temperature performance is of paramount importance for industry. Linear Friction Welding (LFW), which is an emerging technology for manufacturing and repairing of rotating gas turbine components, has many advantages, such as improving service life and reducing weight, over fir tree assembly. It has been reported that slotted blade/disk assemblies are susceptible to fatigue damage since fretting cracks initiate from the fir tree, while LFW joints can be free from such problems (Chamanfar, Jahazi et Cormier, 2015a; Mary et Jahazi, 2007b; Okazaki, Ohtera et Harada, 2004; Preuss, Withers et Baxter, 2006b). Therefore, LFW can be used as an alternative manufacturing technology for fir tree replacement. LFW has already been applied to Ti alloys for compressor (i.e. low temperature) operation applications, but not to high temperature components. Thus, there is a need to understand the properties of LFWed joints at elevated temperatures.

LFW is a solid state joining process free from micro-cracking or porosity defects as the temperature does not reach the fusion point of the alloy during this process. This process is divided into three stages (Chamanfar, Jahazi et Cormier, 2015a): I) the conditioning phase, during which samples are oscillated under a specific frequency and amplitude, and brought together under a small force and time; II) the frictional phase, where friction pressure increases and heat is generated at the interface; the material at the interface then becomes plastic, and is expelled out of the weld interface as a flash (this material loss from the weld interface causes the parts to be shortened); III) the forge phase, during which the amplitude decreases to zero, and the samples are brought and consolidated together.

Thermomechanical processes such as LFW involve substantial microstructural changes in Ni-based superalloys. The occurrence of dissolution and subsequent re-precipitation of γ'

precipitates during LFW play a key role in controlling the mechanical properties of these alloys (Masoumi et al., 2016a; Masoumi et al., 2016c). The dynamic and post-dynamic recrystallization, as well as the dissolution of creep resisting phases during welding, are expected to have some adverse effects on creep properties (Cormier et Cailletaud, 2010a; Cormier, Milhet et Mendez, 2007b; le Graverend et al., 2010a). Damodaram et al. reported that, a reduction in the average size and volume fraction of γ′ precipitates led to a reduction in the mechanical properties of as-welded specimens (Damodaram, Ganesh Sundara Raman et Prasad Rao, 2014b). They studied the tensile properties of as-weld and post-weld heat-treated (PWHT) conditions on continuous drive friction-welded Inconel 718 specimens. The post-welded samples provided better room temperature tensile properties than those of the as-welded samples. Chamanfar et al. (2011b) reported that the post-weld heat treatment of LFWed Waspaloy provides better hardness properties than what is seen in the as-weld condition. However, the tests in that case were performed at room temperature, and consequently, the results cannot be directly applied to creep properties at high temperatures. Therefore, in this study, post-weld heat treatment is performed on the as-welded samples, and their creep properties are compared to those of the as-welded specimens.

Steuer et al. and Shi et al. (Shi et al., 2012; Steuer et al., 2011; 2014) evaluated the creep properties of the transient liquid phase bonding and brazed joints of two different Ni-based superalloys used for blade applications. They reported that an increase in the density of pores, brittle phases and impurities at the grain boundaries resulted in lower creep properties in the brazed samples. In addition, both the volume fraction and morphology of γ′ particles at the grain boundary have significant impacts on the creep rupture life. Thus, a homogenous joint after heat treatment may lead to higher yield strength for bonded samples. To the knowledge of the authors, no study has covered the creep properties of LFWed Ni-based superalloys in as-weld or post-weld heat treated conditions.

This study thus aims to investigate the high temperature creep performance of linear friction welded AD730^{TM} in as-weld and post-weld conditions, in comparison to the base material. In addition, the creep life of LFWed AD730^{TM} is predicted by the Larson-Miller plot. The creep

properties are compared with those of several other Ni-based superalloys, and the underlying damage mechanisms are discussed.

6.3 Experimental Procedures

The material used in this study was a wrought AD730^{TM} (Devaux et al., 2012a) produced by the Aubert and Duval company, Les Ancizes (France) site. Table 6-1 presents the chemical composition of the investigated material. The material was subjected to a post-forge heat treatment consisting in solutionizing at 1080°C for four hours, followed by air cooling. The as-received material had around 40% γ′ particles at room temperature in equilibrium condition (Masoumi et al., 2016a).

Table 6-1 Chemical composition of AD730^{TM} (wt%) (Devaux et al., 2012a)

Ni	Fe	Co	Cr	Mo	W	Al	Ti	Nb	B	C	Zr
Base	4	8.5	15.7	3.1	2.7	2.25	3.4	1.1	0.01	0.015	0.03

For the LFW experiments, rectangular blocks measuring 26 mm × 13 mm × 37 mm (length × width × height) were machined by wire electro-discharge machining (EDM) at the mid-radius of a forged bar having a ~ 150 mm diameter. An FW34-E20 LFW machine at TWI, Cambridge, UK was used for welding. The welding parameters which resulted in a sound joint with axial shortening of 3.8 mm were as follows: frequency of oscillation of 40 Hz, friction pressure of 285 MPa and forge pressure of 580 MPa.

A PWHT consisting of solutionizing and aging was conducted on the LFWed specimens as follows: solutionizing at 900°C for two hours, heating at 0.15°C/s to 1080°C, held at this temperature for four hours followed by air cooling, and aging at 730°C for eight hours followed by air cooling. This last aging heat treatment is known to maximize the tensile strength in the 600-700°C temperature range, without affecting the creep strength of AD730^{TM} at 700°C in the fine grain state (Devaux et al., 2014).

Creep tests were conducted in as-welded and PWHTed conditions on cylindrical samples having a diameter of 4 mm and a gage length of 14 mm. Specimens were machined after

PWHT (if any) by EDM, and then turned. A final mechanical polishing of the gage length up to a 4000 grade SiC was used to limit the surface roughness, and to avoid any surface recrystallization of the specimens due to surface residual stresses. Creep tests were performed in tension under constant load, and elongation was continuously monitored using a Linear Variable Displacement Transducer (LVDT). Creep tests were carried out under initial stresses of 600 MPa and 750 MPa at 700°C (± 1°C), and initial stresses of 100 MPa and 200 MPa at 850°C (± 1°C). These tests were performed at 700°C and 850°C to cover possible applications of AD730™ alloy, such as high pressure turbine disks or seal rings for land-based gas turbine or aero-engines.

Macro and microstructural investigations were conducted after specimens were mounted and polished using standard metallographic techniques. For the microstructure characterization of as-welded samples, a mixture of Regia water (2/3 vol. part) and distilled water (1/3 vol. part) was used as an etchant. Microstructure evolution and fractographic observations were examined by optical microscopy (OM), Field Emission Gun Scanning Electron Microscopy (FEG-SEM) and JEOL 6400 SEM. The welds were investigated by FEG-SEM to examine the changes that occur in the microstructure during post-weld heat treatment, as well as to analyze the fracture surfaces. In order to characterize the nanometric size γ′ precipitates, the secondary electron (SE) mode in Hitachi SU8230 SEM was used. The back-scattered electron (BSE) mode was used to record images from the polished surfaces of the samples. The energy dispersive spectroscopy (EDS) technique was performed to acquire local chemical composition and distribution maps of the different chemical elements constituting various phases along the fractured locations. Grains sizes were evaluated by analyzing EBSD maps obtained for 5 areas in the weld interface in as-welded and PWHT conditions. High angle boundaries in the misorientation range of 15-55° were considered to estimate the grain size.

6.4 Results and Discussion

6.4.1 Macroscopic and Microscopic Evaluation of the Joint after LFW

Visual inspection of the weld interface (Figure 6.1 (a)) showed that a bifurcated flash was formed during LFW, and that the flash is connected around the corners of the specimen, which is indicative of the high integrity of the joint in the LFWed sample. Examination of the weld by optical microscopy revealed that the weld line did not have any microcracks or impurities such as oxides, which can affect the mechanical properties or life of the weld (Figure 6.1 (b)). Higher magnification of the weld revealed no oxide particles, voids or microcracks in the corner of the LFWed sample (Figure 6.1 (c)).

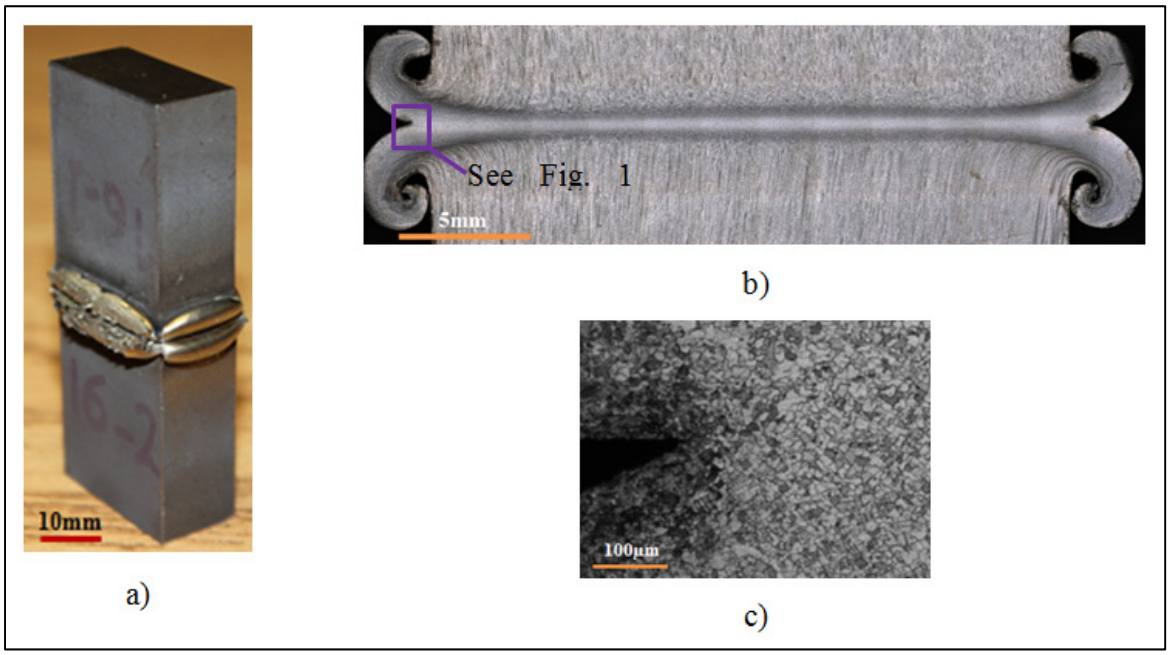

Figure 6.1 (a) A photograph of LFWed sample (b) a low magnification optical image of the welded sample showing integrated joint with no defects or impurities in the weld line (c) higher magnification of flash corner showing no microcracks or oxide particles.

Microstructure examination of the parent material showed a trimodal γ′ size distribution composed of primary, secondary and tertiary γ′ particles with average diameters of 1.4 µm, 30 nm, and less than 10 nm, respectively (Masoumi et al., 2016a). In contrast, a monomodal

re-precipitated γ′ distribution, less than 10 nm in size, was observed in the microstructure of the as-welded specimens in the weld line until 100 µm from the weld interface (Figure 6.2 (a)). As shown in Figure 6.2 (a), primary γ′ and boride particles are mostly dissolved at the weld interface, indicating that the weld interface experiences temperatures higher than boride and γ′ solvus during LFW (Masoumi et al., 2017a).

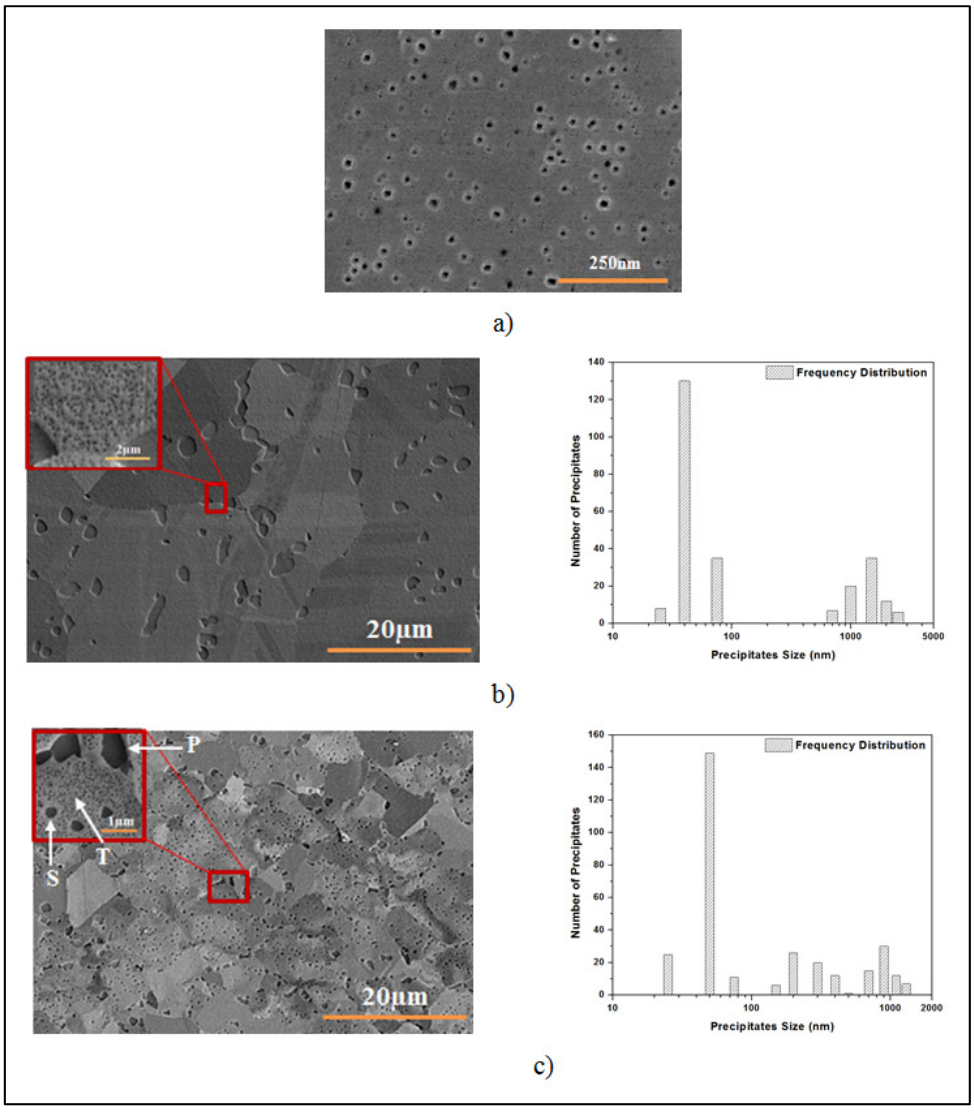

Figure 6.2 Microstructure of LFWed specimens in: (a) weld line in as-welded condition (b) parent material and (c) weld zone (100 µm from the weld interface) in PWHTed condition. Primary (P), secondary (S) and tertiary (T) γ′ precipitates have been shown by white arrows. γ′ size distribution of the parent material and the weld zone after PWHT are presented respectively in (b) and (c).

After post-weld heat treatment, the parent material showed a bimodal precipitate size distribution, containing primary and secondary γ′ particles, having respectively average diameters of 1.5 μm and 40 nm, while the weld zone revealed a trimodal size distribution, as shown in Figure 6.2 (b) and Figure 6.2 (c). The obtained results show that subsolvus post-weld heat treatment led to coarsening of re-precipitated γ′ particles formed during cooling in the weld zone after LFW. The morphology of the coarsened particles is cuboidal, and their average size and volume fraction were determined to be 230 nm and 4%, respectively (Figure 6.2 (c)). Higher magnification (insert in Figure 6.2 (c)) shows that tertiary γ′ particles were formed between the cuboidal precipitates during cooling from 1080°C, and that they coarsened during the aging heat treatment at 730°C, as they were 40 nm in size after PWHT. Finally, grain size measurement revealed that the average grain size of the weld interface was about 8 μm in PWHT condition, which is twice of that in the as-welded condition (Figure 6.3).

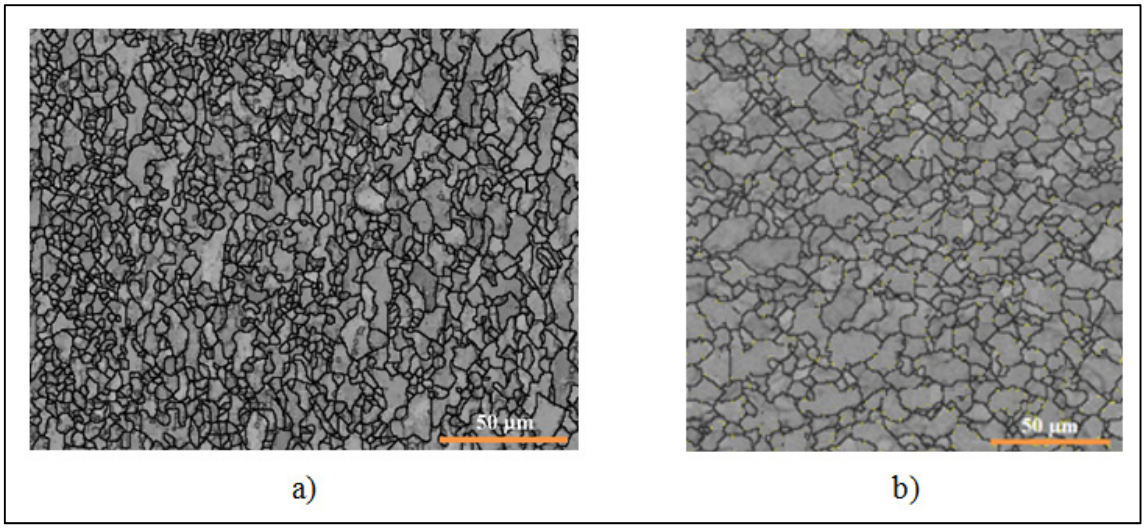

Figure 6.3 Microstructure of a LFWed AD730™ at the weld line in:
(a) as-welded (b) post welded conditions.

6.4.2 Creep Testing of PWHTed Joints at 700°C and 850°C

The creep behavior of specimens tested under 100 MPa and 200 MPa at 850°C and under 600 MPa and 750 MPa at 700°C are compared in Fig. 4 for the base material, as well as in the

as-welded and post-weld heat-treated conditions. As shown in Figure 6.4 (a) and (d), creep properties improved after the welded specimens were subjected to post-weld heat treatment. In order to observe the three stages of creep in uniaxial tension, the creep curves are plotted in the form of the instantaneous strain rate versus strain, as illustrated in Figure 6.4 (b), (c), (e) and (f). The results demonstrate that at 700°C and 850°C, the minimum creep strain rate decreases with decreasing applied stress. In these figures, a noticeable primary creep stage is observed for PWHTed condition at 700°C under both stress levels and at 850°C under stress level 200 MPa, as the strain rate decreases until a minimum true creep strain is reached.

The secondary creep stage is identified where the strain rate is approximately constant. As shown in Figure 6.4 (a), (b) and (c), it is relatively easy to observe this stage for creep tests of the base material and under the PWHT condition at a temperature of 700°C under 600 MPa and 750 MPa stress levels. There is no clear secondary creep domain in the creep curve of the as-welded specimen since there is a continuous increase in the creep rate. This continuous acceleration of creep deformation is expected to result from a dynamic evolution of γ' precipitation during creep deformation.

During stage II, the creep rate is controlled by the balance between the strain hardening of the alloy due to deformation and thermal softening due to dislocations movement (Riedel, 1987). The tertiary creep regime can be seen at 700°C and 850°C as the strain rate begins to increase once again. It is worth mentioning here that the as-welded specimens did not exhibit any primary and secondary creep stages at 850°C creep test conditions. In addition, PWHTed specimens did not reveal any primary and secondary creep stages at 850°C under the 100 MPa stress level. Their creep behavior consisted of continuous creep acceleration up to failure (see Figure 6.4 (b), (c), (e) and (f)). This thus indicates an absence of any strain hardening mechanism, which will be elaborated in section 3.4.1 through microstructure analyses.

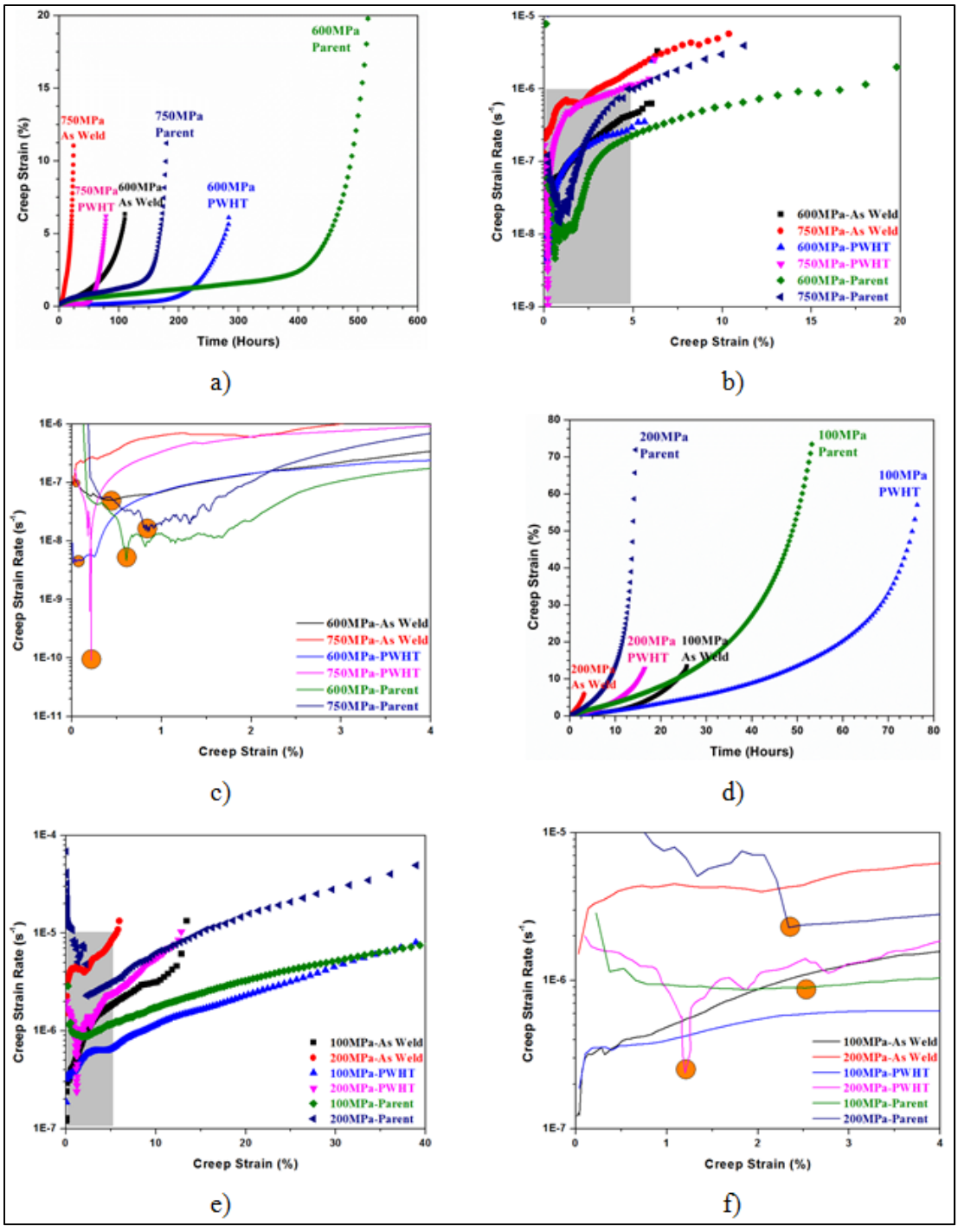

Figure 6.4 Creep curves of base material and LFWed specimens in as-welded and PWHTed conditions at (a) & (b) & (c) 700°C under 600 MPa and 750 MPa (d) & (e) & (f) 850°C under 100 MPa and 200 MPa. Strain rate vs. strain data, shown in (b) & (c) & (e) & (f), are used to reveal various stages of creep tests. Shaded zone is magnified to indicate the absolute minimum of the curves, as shown by filled circles.

Figure 6.5 (a)-(d) show the appearance of the cross section of PWHTed samples after rupture during creep tests at 700˚C and 850˚C. More creep strain accumulation occurs during creep testing at 850˚C compared to that at 700˚C. Microscopic observations showed that the fracture surface was mostly oxidized, especially after testing at 850˚C. In addition, SEM and optical observations showed that the failure initiated in the parent material during testing under 750 MPa at 700˚C and 100 MPa at 850˚C, while it was in the weld zone after testing under 600 MPa at 700˚C and 200 MPa at 850˚C. Although PWHTed samples exhibited failure initiation in the weld zone, their creep life was found to be comparable to that of the parent material, as illustrated in Figure 6.4 (d). The specimens after failure at 850˚C under 100 MPa, had a non-homogenous diameter due to the difference in grain size in the heat-affected area close to the weld joint. At this temperature, diffusion creep is mainly active for fine grain materials, with the grain boundary sliding acting as a rate controlling parameter for creep strains in excess of 1% (Soula et al., 2010; Soula et al., 2009; Thibault et al., 2013). The creep damage mechanisms in the LFWed samples will be discussed in detail in the following sections.

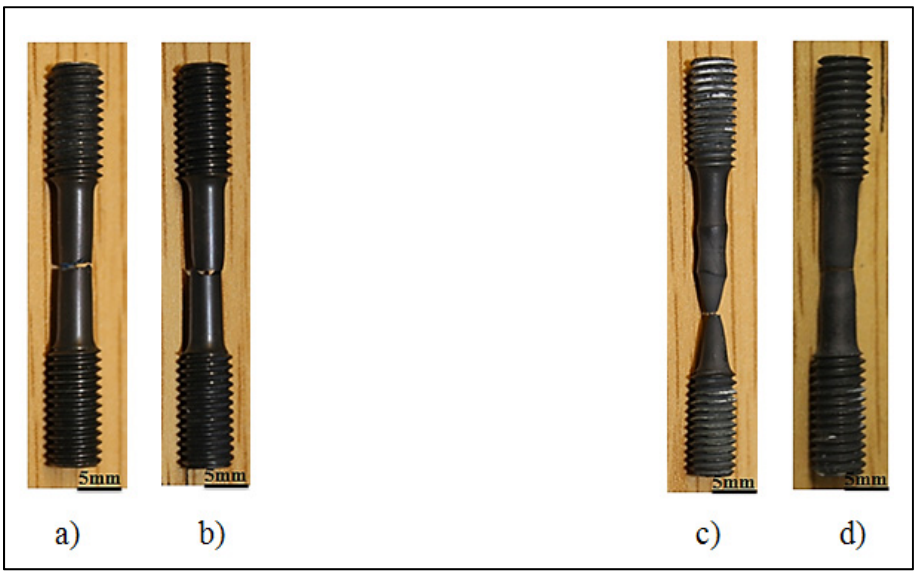

Figure 6.5 Appearance of the cross section of PWHTed samples after rupture during creep tests at (a) 700˚C / 600 MPa (b) 700˚C / 750 MPa (c) 850˚C / 100 MPa (d) 850˚C / 200 MPa.

6.4.3 Effect of PWHT on Larson-Miller Diagram

The creep rupture characteristics of the base, as-welded and PWHTed materials are compared in Figure 6.6 (a) in the form of a Larson-Miller diagram. Eq. (6.1) is used to plot creep strength data as a function of a Larson-Miller Parameter (LMP) (Reed, 2006a):

$$LMP = T[20 + log(t)] \times 10^3 \quad (6.1)$$

where T is the absolute temperature in Kelvin and t is the creep time to failure in hours. The diagram, presented in Figure 6.6, shows that at high values of LMP=23.3×10^3 - 25.3×10^3 (high temperatures, low loads), base and PWHTed materials have similar characteristics. However, at lower values of LMP (low temperatures, high loads), the base material has higher strength than that of as-welded and PWHTed conditions. Testing conditions for the homogeneous fine grain parent AD730^{TM} are 700˚C/950MPa, 700˚C/850MPa, 700˚C/800MPa, 700˚C/750MPa, 700˚C/700MPa, 700˚C/600MPa, 850˚C/250MPa, 850˚C/200MPa, 850˚C/100MPa and 850˚C/50MPa.

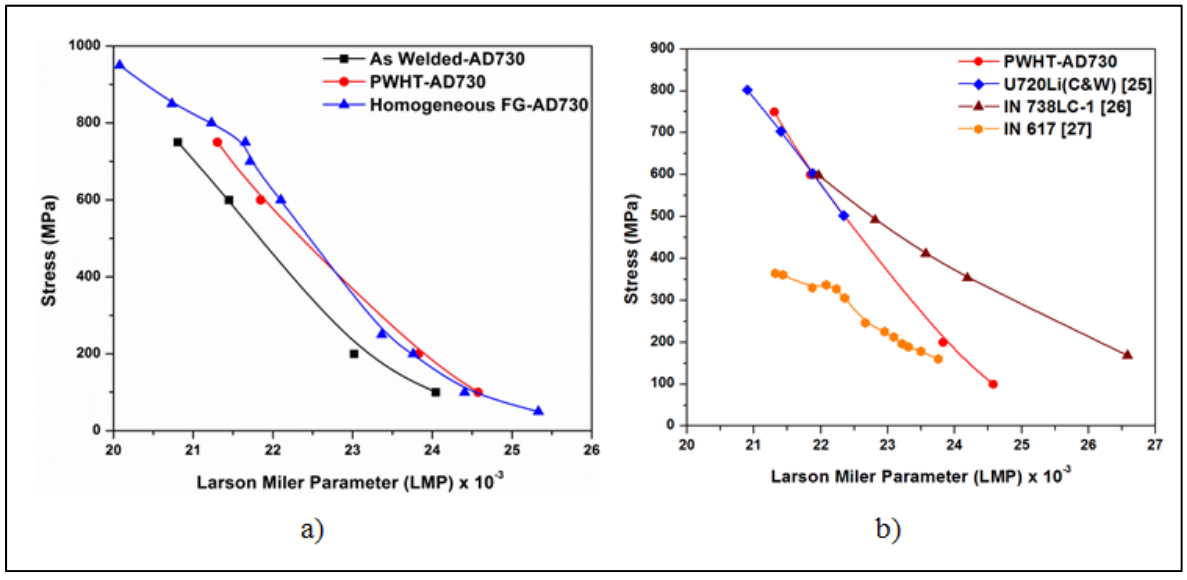

Figure 6.6 Comparison of Larson Miller parameter (LMP) for (a) base metal, as-welded and PWHTed samples of AD730^{TM} (b) PWHTed AD730^{TM}, U720Li, IN 738 LC and IN 617.

The creep life values and creep rupture characteristics obtained in the present study (Figure 6.4 and Figure 6.6) indicate that the PWHTed specimens have higher creep life and strength than those of as-welded specimens for all test conditions and LMP values. Crack propagation is mainly associated with the joint microstructure in as-welded samples. It has been reported that if creep is controlled by diffusion, the creep strain rate is proportional to 1/(grain size)^2 or 1/(grain size)^3, depending on whether the diffusion is along grain boundaries or within the grain bulk during creep tests (Bano, Koul et Nganbe, 2014). Microstructural examination results reported in Figure 6.3 indicate that the average grain size in the weld interface is about 4 μm in the as-welded condition, while it is about 8 μm in the PWHTed condition. Thus, the creep strain rate of the weld interface in as-welded samples will be about four or eight times larger than that of the PWHTed samples, therefore leading to lower creep life for the as-welded samples.

Furthermore, the creep crack growth rate, CCGR is inversely proportional to the grain size, d, as follows (Xu, Koul et Dickson, 2001):

$$CCGR = \frac{AK^2}{d} \tag{6.2}$$

where K is the stress intensity factor and A is a material constant. Therefore, the crack growth rate should be higher in small grain size samples such as the as-welded samples based on Eq. (6.2).

The creep rupture properties of PWHTed AD730^{TM} are compared to those of Udimet^{TM}720Li (U720 Li) (Gu et al., 2009), Inconel 738LC (IN 738LC) (Hou et al., 2004) and Inconel 617 (IN 617) (Nandi, Reddy et Singh, 2014) by a Larson-Miller plot, as shown in Figure 6.6 (b). The plot shows that PWHTed AD730^{TM} has similar characteristics as U720 Li and IN 738LC at low values of LMP (low temperatures and high stresses). The diagram also shows that the PWHTed sample has an advantage over the IN 617 alloy, while the IN 738LC alloy boasts higher LMP characteristics, LMP=22×10^3 - 26×10^3, at high temperatures and low stresses. This could be due to the fact that IN 738LC has a higher γ′ volume fraction than AD730^{TM} in

this temperature range (IN 738LC has a 45% γ′ volume fraction, which is 5% higher than that of AD730^{TM}), and larger grains, since it is a cast alloy, while IN 617 alloy has a lower volume fraction of γ′ as compared to AD730^{TM}. The IN 617 alloy is mainly a solution-hardened Ni- based alloy with a very low γ′ volume fraction of about 4%.

6.4.4 Microstructure Analysis of PWHTed Joints

6.4.4.1 Deformation and Damage Mechanism during Creep

a) 700°C-600 MPa

The fractographic features of the creep-tested specimen at 700°C under 600 MPa are shown in Figure 6.7 and Figure 6.8. Figure 6.7 (a) shows that the fracture surface is almost flat. An analysis of this flat surface at higher magnification (Figure 6.7 (b)) revealed dimples throughout the fracture surface, indicating a ductile fracture. Parallel strips observed on the fracture surface at low magnification (Figure 6.7 (a)) and a multimodal size distribution of γ′ particles on the longitudinal fracture surface (Figure 6.8 (a)) are specific to a fracture at the weld zone.

Cavities initiate preferentially in the weld zone at the grain boundaries due to the nucleation of voids around the primary γ′ or carbide precipitates and the decohesion of these particles, as shown in Figure 6.8. Furthermore, the growth and coalescence of voids, nucleated at grain boundaries connected to the surface, assist surface creep crack growth (Figure 6.7 (c)). As reported in Figure 6.2 (b), primary γ′ precipitates are largely dissolved in the weld zone during LFW. Therefore, grain boundaries have the weakest configuration in the weld region, and microcracks could easily propagate in this zone due to a lack of borides and primary γ′ particles at the grain boundaries (Figure 6.8 (b)). It is worth noting that while grain boundaries are the preferred crack initiation sites, as shown in Figure 6.8 (c), some cavities at the interface of coarse secondary γ′ coalesced and formed continuous intergranular cracks.

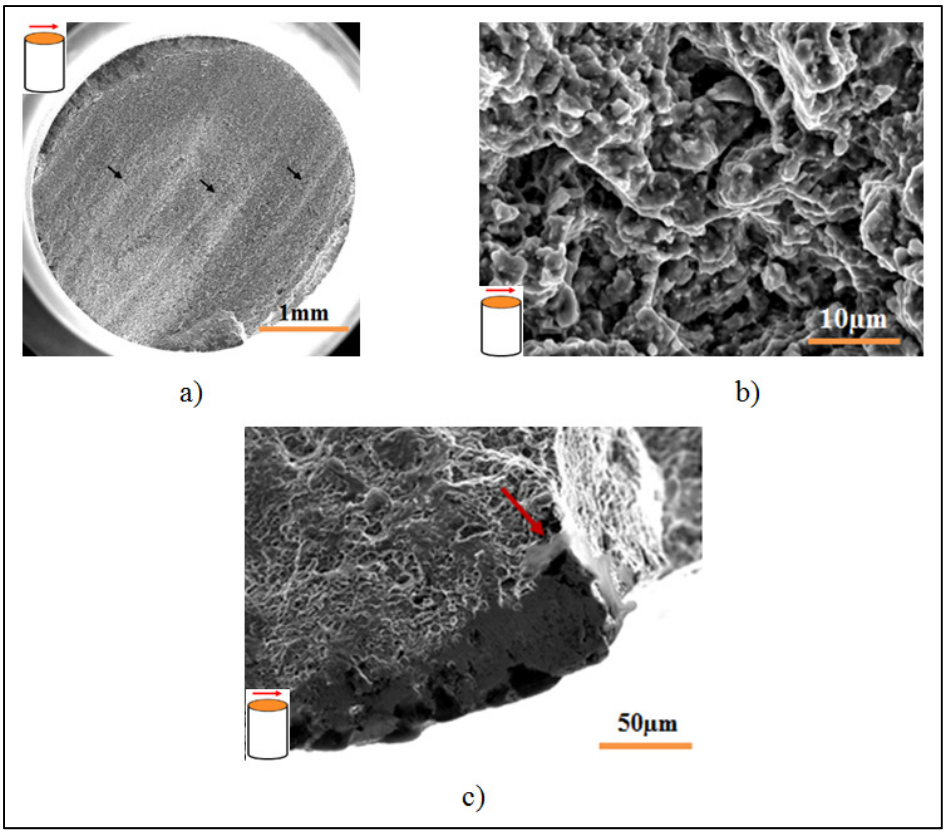

Figure 6.7 Fracture surface of the creep tested specimen at 700˚C under 600 MPa showing (a) parallel strips on flat fracture surface, as marked by black arrows (b) dimples and intergranular fracture (c) oxidized layer at the fracture surface, as marked by red arrow. Transverse direction is shown by brown color.

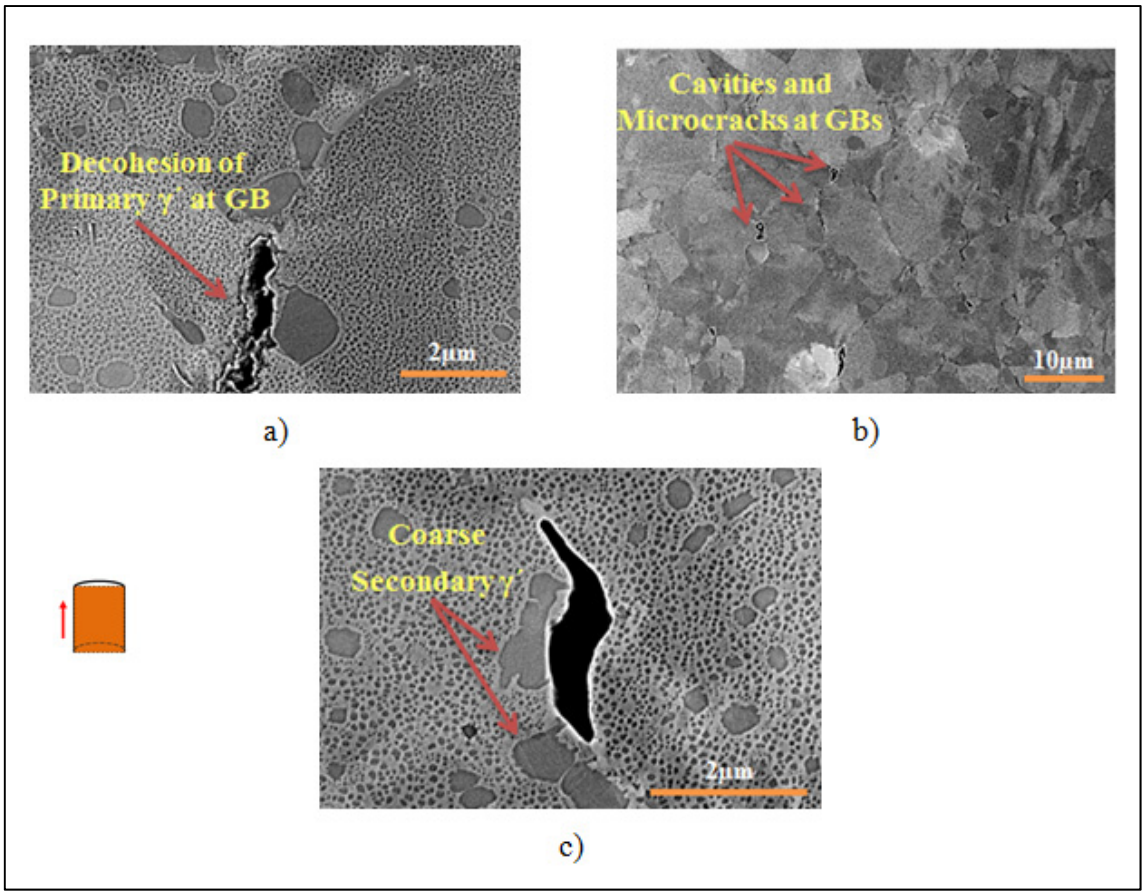

Figure 6.8 Post-failure observations on longitudinal cut from the creep tested samples at 700°C/600 MPa showing (a) decohesion of primary γ′ (b) cavities and microcracks at GB (c) Cavities at the interface of coarse secondary γ′. Longitudinal direction is shown by brown color.

b) 700°C-750 MPa

Figure 6.9 (a) shows the fracture surface of the sample tested at 700°C under the highest stress used in this investigation. The surface is characterized by flat regions of dimpled, ductile appearing fracture in the parent material. In contrast, in the zones adjacent to the weld zone, shiny shear lips are visible, and are formed on bands oriented at ±45° to the sample thickness. An examination of the fracture surface also indicates that cracks initiate mainly from oxidized carbide particles in the parent material at the surface and propagate through grain boundaries (Figure 6.9 (b) and (c)). The presence of primary γ′ particles, as indicated by arrows in Figure 6.9 (d), and oxidized grain boundaries (Figure 6.9 (c)) at the fracture

surface indicate that crack propagation is initially intergranular, and occurs in the parent material. Since oxide particles are brittle, creep cracks could initiate very easily from the interface of oxides located at grain boundaries connected to the surface. Then, oxygen diffusion ahead of the crack can weaken the grain boundary and aid intergranular crack propagation in the early stages.

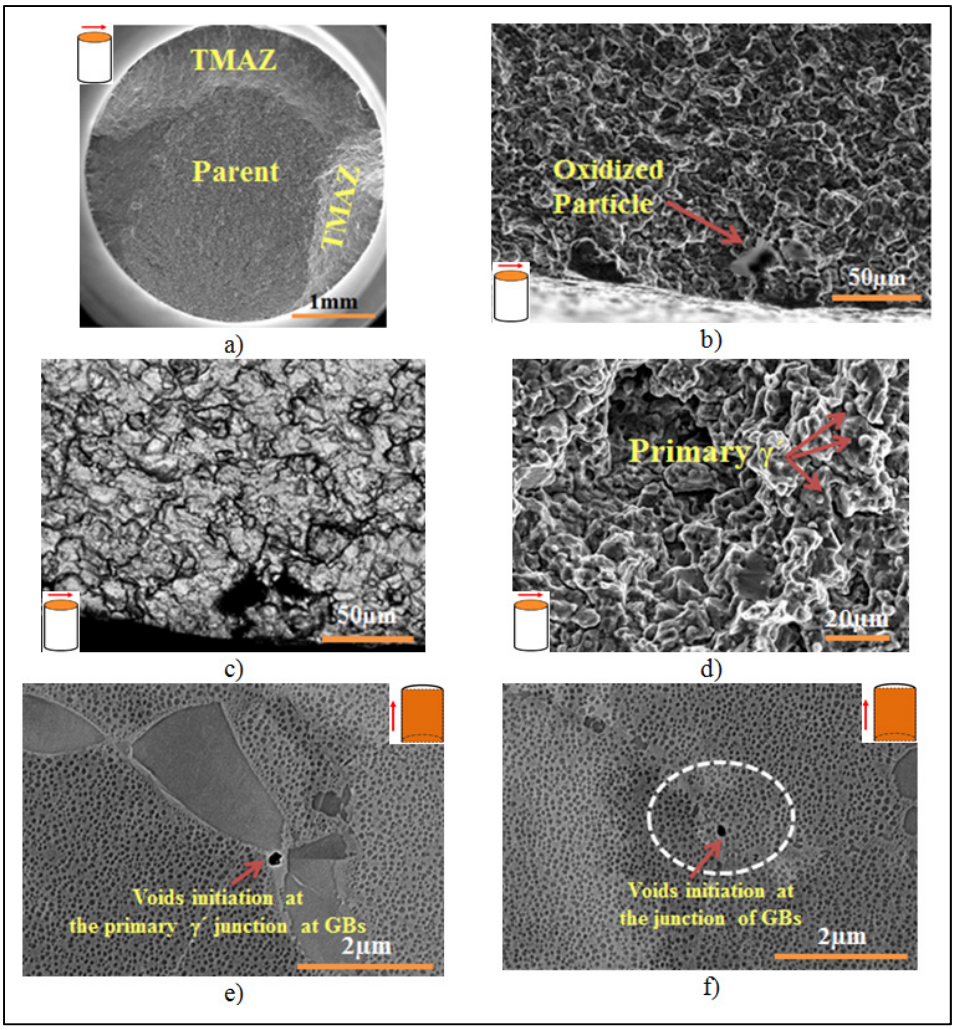

Figure 6.9 Post-failure transverse and longitudinal observations of the creep tested specimen at 700°C /750 MPa test condition showing (a) initiation of crack at parent material and propagation adjacent to the weld zone, at the thermomechanically affected zone (TMAZ) (b) and (c) crack initiation from oxidized secondary particle and intergranular fracture (e) and (f) pore nucleation at the primary γ′ and the matrix interface or at the junction of GB. Transverse and longitudinal directions are shown by brown color.

Thermocalc simulation (Masoumi et al., 2016a) showed that the microstructure of AD730^{TM} contains about 37% γ′ at 700˚C. An examination of the fracture surface in the longitudinal direction revealed that nucleation and growth of pores occurred through diffusion at the interface of the matrix and second-phase particles (Figure 6.9 (e) and (f)). This is generally related to dislocation pile-up at the interface (Frost et Ashby, 1982). Therefore, the first mode of fracture, as shown in Figure 6.9, is grain boundary sliding controlled by diffusion and assisted by oxidation. Testing at 700˚C under 750 MPa stress, compared to that at 700˚C under 600 MPa stress will generate more dislocations, increasing the propensity for transgranular fracture by linkage of these dislocations. Therefore, crack propagation leads to faster fracture of regions at a ±45˚ angle relative to the applied stress direction, as suggested by the shiny zones at the fracture surface, as shown in Figure 6.9 (a).

c) 850˚C-100 MPa

During creep tests at 850˚C under 100 MPa, all specimens fail in the base material far from the weld zone. Fractographic analyses reveal that the specimens neck in the parent material before fracture (Figure 6.10 (a)). As soon as necking starts, deformation is concentrated in the neck, and triaxiality of local applied stress increases due to the geometry of the neck (Rogers, 1968). This causes excessive growth and a coalescence of microvoids at the center of the neck and very high levels of creep elongation, as shown in Figure 6.10 (a) and (b) and Figure 6.5 (c). An analysis of the fracture surface in the longitudinal direction, presented in Figure 6.10 (c) and (d), reveals that cellular γ′ particles and precipitate-free zones (PFZ) are formed adjacent to grain boundaries. The absence of an efficient γ′ precipitation close to the GB probably explains the continuous acceleration of the creep curve (Figure 6.4 (e) and (f)). Cellular or discontinuous coarsening occurs when γ′ particles coarsen perpendicularly to a moving grain boundary (Maldonado et Nembach, 1997). Then, solute diffusion along the grain boundary accelerates the growth of these particles, and as a result, a PFZ is formed. The morphology of γ′ particles is lamellar after coarsening (Figure 6.10 (c) and (d)). An examination of the fracture surface in the transverse and longitudinal directions (Figure 6.10) shows that cracks initiate and propagate inside the PFZ due to strain accumulation in this soft area.

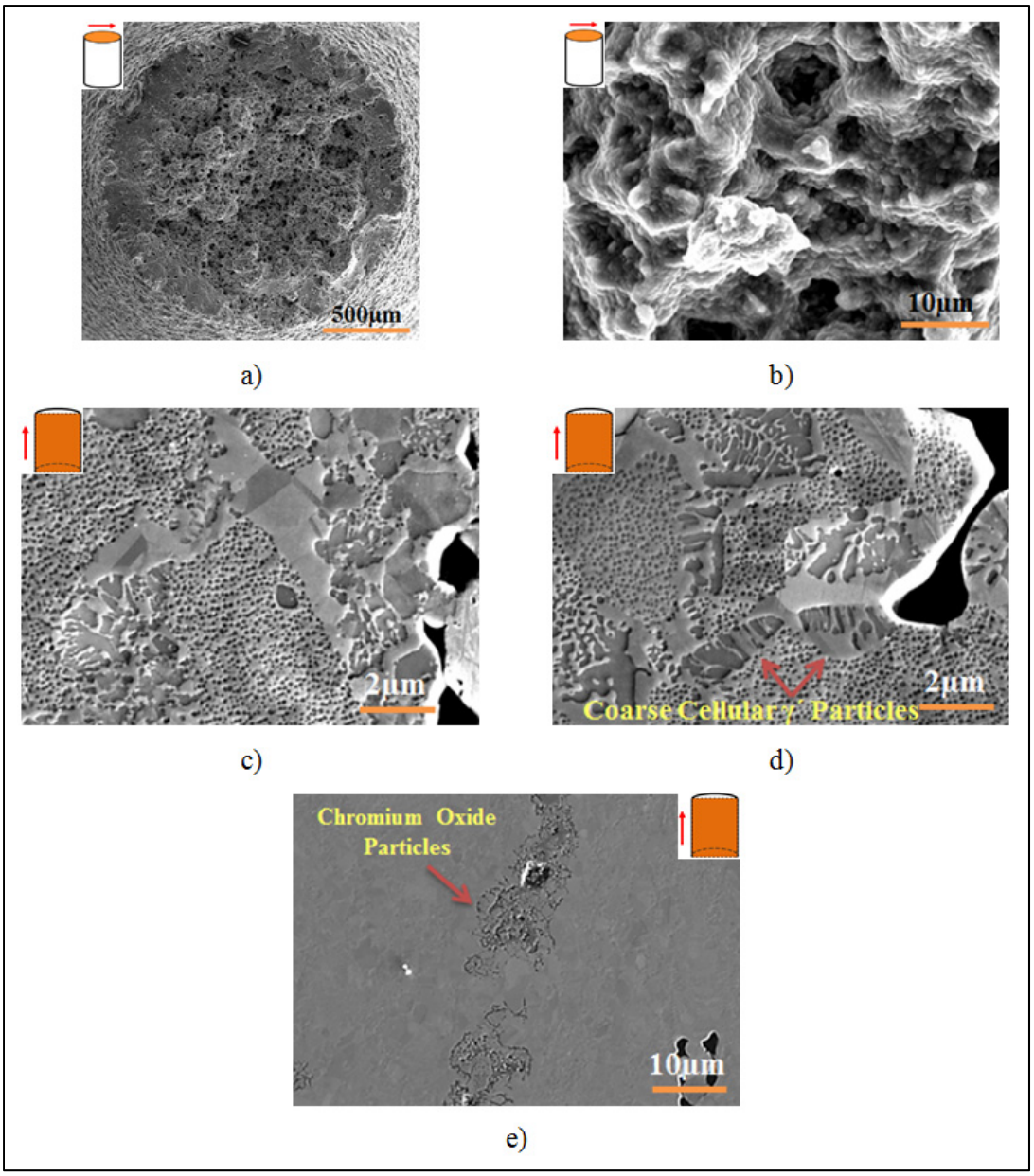

Figure 6.10 Transverse and longitudinal fracture surface of samples tested at 850°C under 100 MPa stress showing (a) necking (b) coalescence of voids at the center of the neck (c) and (d) PFZ formation and lamellar coarsening of γ′ particles, crack and cavity initiation in PFZ (e) chromium oxide particles. Transverse and longitudinal directions are shown by brown color.

Furthermore, EDS mapping results and chemical analyses of the area adjacent to the grain boundary, presented in Figure 6.11, reveal chromium enrichment at the grain boundaries. On the other hand, at such high temperatures, oxygen diffuses very rapidly along grain

boundaries connected to the surface, and with the high affinity of chromium for oxygen, chromium oxides are formed, as shown in Figure 6.10 (e) and Figure 6.11 (c). The low ductility of the oxide layer results in its rupture under loading, which induces crack nucleation, and exposes fresh metallic material to the environment. Crack propagates due to oxide-induced crack growth Therefore, as Figure 6.10 and Figure 6.11 show, the fracture mechanism is intergranular, assisted by diffusion and oxidation. The shape of the specimen after failure (Figure 6.5 (c)) is indicative of the heterogeneity in grain size. A coarser grain area in HAZ leads to slower creep, and thus, to a smaller reduction in the diameter and less elongation in this area. It is also worth mentioning that the increase in grain size has been shown to be very effective in improving the creep strength in the AD730^{TM} alloy at 850°C (Michel et al., 2016; Thébaud et al., 2015).

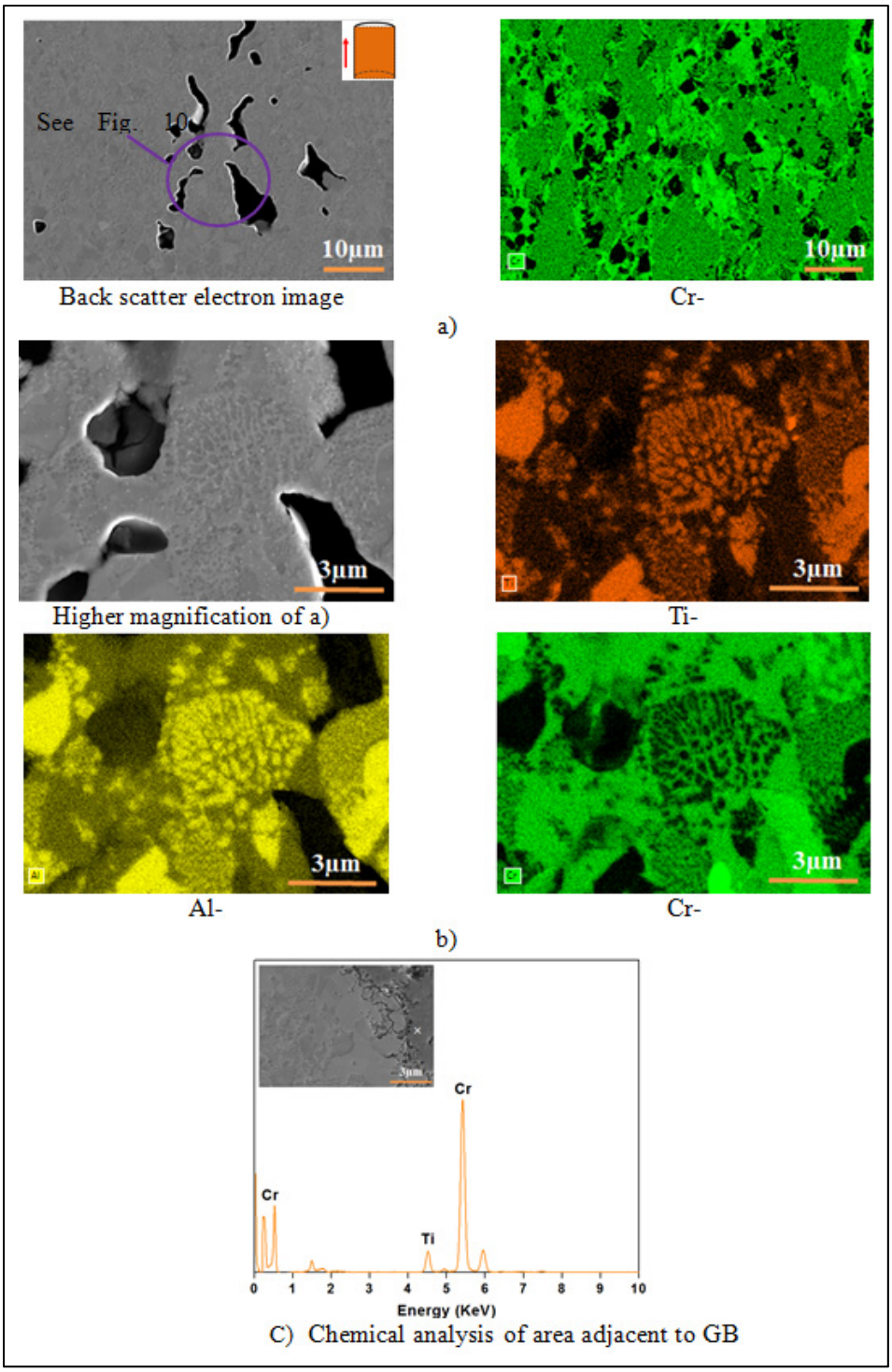

Figure 6.11 EDS mapping results and chemical analysis of the samples tested at 850°C/100 MPa showing Chromium enrichment at the grain boundary. Longitudinal direction is shown by brown color.

d) 850˚C-200 MPa

Multimodal size distribution of γ′ precipitates and parallel strips, shown in Figure 6.12, point to a fracture in the weld zone. However, creep test results (Figure 6.4 and Figure 6.6) show that LMP and creep life of the joints are about 23.8×10^3 and 14 hours, respectively, which are approximately comparable to those of the base metal. Figure 6.12 shows that during creep tests at 850˚C under 200 MPa, PFZ are formed close to grain boundaries. EDS mapping results presented in Figure 6.13 show oxides and cracks formed at the grain boundaries. PFZs are formed due to solute elements absorption by intergranular γ′ precipitates, and are weak and less resistant to oxidation. Thus, cavities, and therefore, chromium oxides (Figure 6.13), are formed more easily in the weak regions than in the matrix. Then, these grain boundary cavities and oxides accelerate the intergranular cracking. Figure 6.12 shows secondary microcracks initiated from the cavities inside the precipitate-free zone, and crack branching develops during propagation due to severe oxidation of the grain boundary. The connection of several grain boundary cracks leads to decohesion of the grain from the matrix, as shown in Figure 6.12 (b).

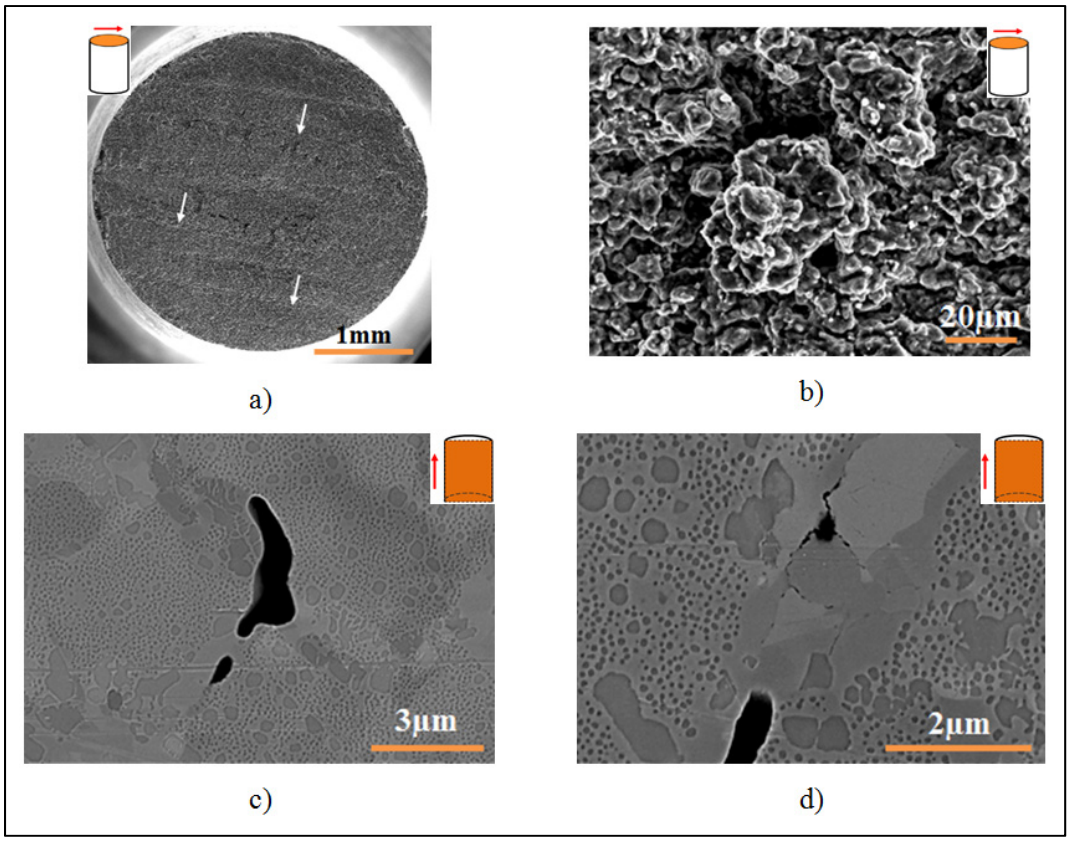

Figure 6.12 Transverse and longitudinal observations of post-failure of samples tested in 850°C under 200 MPa stress showing (a) parallel strips on flat fracture surface, as marked by white arrows (b) decohesion of grain due to crack connection (c) and (d) PFZ and cavity formation adjacent to GB. Transverse and longitudinal directions are shown by brown color.

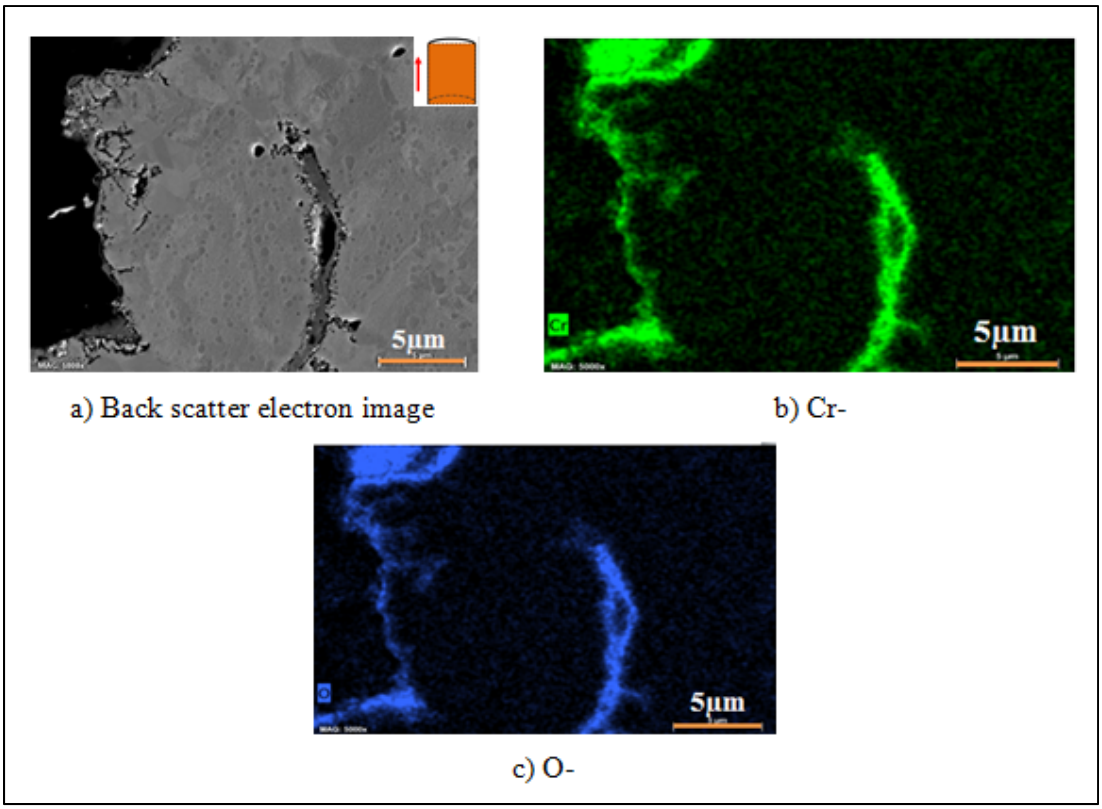

Figure 6.13 EDS mapping results of the creep tested specimen at 850˚C/200 MPa showing oxide and crack formation at GB. Longitudinal direction is shown by brown color.

6.5 Conclusions

The creep behavior of the LFWed AD730^{TM} was investigated in as-welded and PWHTed conditions under 100 MPa and 200 MPa at 850˚C, and 600 MPa and 750 MPa at 700˚C. The findings are summarized as follows:

1- A specific PWHT was developed for an LFWed fine grain AD730^{TM} alloy. It resulted in superior creep strength compared to that of as-welded joints.

2- A high LMP value (24.5×10^3) of the PWHTed AD730^{TM} compared to the IN 617 alloy indicates a good service life under high temperature and low stresses.

3- The nucleation of voids around precipitates and the decohesion of these particles at oxidized grain boundaries connected to the surface assist surface creep crack growth at 700°C.

4- Cracks initiate inside the PFZ at the grain boundaries, and propagate due to oxide-induced crack growth at 850°C.

6.6 Acknowledgement

The financial support from the Natural Sciences and Engineering Research Council (NSERC) 261712 of Canada in the form of a Discovery Grant is gratefully acknowledged. The authors express appreciation to Aubert & Duval Co. for providing AD730™ samples, and to TWI Ltd. for welding the samples.

References

Bano, N., A. K. Koul et M. Nganbe. 2014. « A Deformation Mechanism Map for the 1.23Cr-1.2Mo-0.26V Rotor Steel and its Verification Using Neural Networks ». *Metallurgical and Materials Transactions A: Physical Metallurgy and Materials Science,* vol. 45, nº 4, p. 1928-1936.

Chamanfar, A., M. Jahazi et J. Cormier. 2015a. « A Review on Inertia and Linear Friction Welding of Ni-Based Superalloys ». *Metallurgical and Materials Transactions A: Physical Metallurgy and Materials Science,* vol. 46, nº 4, p. 1639-1669.

Chamanfar, A., M. Jahazi, J. Gholipour, P. Wanjara et S. Yue. 2011b. « Mechanical Property and Microstructure of Linear Friction Welded Waspaloy ». *Metallurgical and Materials Transactions A: Physical Metallurgy and Materials Science,* vol. 42, nº 3, p. 729-744.

Cormier, J., et G. Cailletaud. 2010a. « Constitutive Modeling of the Creep Behavior of Single Crystal Superalloys Under Non-Isothermal Conditions Inducing Phase Transformations ». *Materials Science and Engineering A,* vol. 527, nº 23, p. 6300-6312.

Cormier, J., X. Milhet et J. Mendez. 2007b. « Non-Isothermal Creep at Very High Temperature of the Nickel-Based Single Crystal Superalloy MC2 ». *Acta Materialia,* vol. 55, nº 18, p. 6250-6259.

Damodaram, R., S. Ganesh Sundara Raman et K. Prasad Rao. 2014b. « Effect of Post-Weld Heat Treatments on Microstructure and Mechanical Properties of Friction Welded alloy 718 Joints ». *Materials and Design,* vol. 53, p. 954-961.

Devaux, A., A. Helstroffer, J. Cormier, P. Villechaise, J. Douin, M. Hantcherli et F. Pettinari-Sturmel. 2014. « Effect of Aging Heat-Treatment on Mechanical Properties of AD730™ Superalloy ». In *8th International Symposium on Superalloy 718 and Derivatives 2014, September 28, 2014 - October 1, 2014*. (Pittsburgh, PA, United states), p. 521-535. Coll. « 8th International Symposium on Superalloy 718 and Derivatives 2014 »: John Wiley and Sons Inc.

Devaux, A., B. Picque, M. F. Gervais, E. Georges, T. Poulain et P. Heritier. 2012a. « AD730™-A New Nickel-Based Superalloy for High Temperature Engine Rotative Parts ». In *12th International Symposium on Superalloys, Superalloys 2012, September 9, 2012 - September 13, 2012*. (Seven Springs, PA, United states), p. 911-919. Coll. « Proceedings of the International Symposium on Superalloys »: Minerals, Metals and Materials Society.

Frost, H. J., et M. F. Ashby. 1982. *Deformation-Mechanism Maps: The Plasticity and Creep of Metals and Ceramics*. Pergamon Press, Oxford, 166 p.

Gu, Y. F., C. Cui, D. Ping, H. Harada, T. Fukuda et J. Fujioka. 2009. « Creep Behavior of New Kinds of Ni-Co-Base Superalloys ». *Materials Science and Engineering A,* vol. 510-511, nº C, p. 250-255.

Hou, J. S., J. T. Guo, L. Z. Zhou, C. Yuan et H. Q. Ye. 2004. « Microstructure and Mechanical Properties of Cast Ni-Base superalloy K44 ». *Materials Science and Engineering A,* vol. 374, nº 1-2, p. 327-334.

le Graverend, J. B., J. Cormier, M. Jouiad, F. Gallerneau, P. Paulmier et F. Hamon. 2010a. « Effect of Fine γ' Precipitation on Non-Isothermal Creep and Creep-Fatigue Behaviour of Nickel Base Superalloy MC2 ». *Materials Science and Engineering A,* vol. 527, nº 20, p. 5295-5302.

Maldonado, R., et E. Nembach. 1997. « The Formation of Precipitate Free zones and the Growth of Grain Boundary Carbides in the Nickel-Base Superalloy NIMONIC PE16 ». *Acta Materialia,* vol. 45, nº 1, p. 213-224.

Veuillez sélectionner un type de document autre que « Generic » afin de faire afficher la référence bibliographique.

Masoumi, F., M. Jahazi, D. Shahriari et J. Cormier. 2016a. « Coarsening and Dissolution of γ′ Precipitates during Solution Treatment of AD730™ Ni-Based Superalloy: Mechanisms and Kinetics Models ». *Journal of Alloys and Compounds,* vol. 658, p. 981-995.

Masoumi, F., D. Shahriari, M. Jahazi, J. Cormier et A. Devaux. 2016c. « Kinetics and Mechanisms of γ′ Reprecipitation in a Ni-Based Superalloy ». *Scientific Reports,* vol. 6, p. 1-16.

Masoumi, F., D. Shahriari, M. Jahazi, J. Cormier et B. C. D. Flipo. 2017a. « On the Occurrence of Liquation During Linear Friction Welding of Ni-Based Superalloys ». *Metallurgical and Materials Transactions A: Physical Metallurgy and Materials Science,* vol. 48, nº 6, p. 2886-2899.

Michel, H. T., L. S. Reda, G. E. Santos, J. Cormier, C. Dumont, P. Villechaise, P. Bocher, D. Texier, E. Georges, F. Bridier, F. Hamon et A. Devaux. 2016. « Mechanical Properties of Cast Wrought Hybrid Disks ». In *13th International Symposium on Superalloys, SUPERALLOYS 2016, September 11, 2016 - September 15, 2016*. (Seven Springs, PA, United states) Vol. 2016-January, p. 539-548. Coll. « Proceedings of the International Symposium on Superalloys »: Minerals, Metals and Materials Society.

Nandi, S., G. J. Reddy et K. Singh. 2014. « Microstructural Changes in IN617 Superalloy during Creep at High Temperatures ». In *Procedia Engineering*. Vol. 86, p. 66-70.

Okazaki, M., I. Ohtera et Y. Harada. 2004. « Damage Repair in CMSX-4 Alloy without Fatigue Life Reduction Penalty ». *Metallurgical and Materials Transactions A: Physical Metallurgy and Materials Science,* vol. 35 A, nº 2, p. 535-542.

Preuss, M., P. J. Withers et G. J. Baxter. 2006b. « A Comparison of Inertia Friction Welds in Three Nickel Base Superalloys ». *Materials Science and Engineering A,* vol. 437, nº 1, p. 38-45.

Reed, R. C. 2006a. *The Superalloys Fundamentals and Applications*, 9780521859042. Coll. « The Superalloys: Fundamentals and Applications ». 1-372 p.

Riedel, H. 1987. *Fracture at High Temperatures* Springer Berlin Heidelberg.

Rogers, H. C. 1968. *Ductility*. American Society for Metals, Metals Park, OH.

Shi, D., C. Dong, X. Yang, L. Zhang, J. Hou et Y. Liu. 2012. « Experimental Investigations on Creep Rupture Strength and Failure Mechanism of Vacuum Brazed Joints of a DS Superalloy at Elevated Temperature ». *Materials Science and Engineering A,* vol. 545, p. 162-167.

Soula, A., D. Locq, D. Boivin, Y. Renollet, P. Caron et Y. Bréchet. 2010. « Quantitative Evaluation of High Temperature Deformation Mechanisms: A specific Microgrid Extensometry Technique Coupled with EBSD Analysis ». *Journal of Materials Science,* vol. 45, nº 20, p. 5649-5659.

Soula, A., Y. Renollet, D. Boivin, J. L. Pouchou, D. Locq, P. Caron et Y. Bréchet. 2009. « Analysis of High-Temperature Creep Deformation in a Polycrystalline Nickel-Base Superalloy ». *Materials Science and Engineering A,* vol. 510-511, nº C, p. 301-306.

Veuillez sélectionner un type de document autre que « Generic » afin de faire afficher la référence bibliographique.

Steuer, S., et R. F. Singer. 2014. « Suppression of Boride Formation in Transient Liquid Phase Bonding of Pairings of Parent Superalloy Materials with Different Compositions and Grain Structures and Resulting Mechanical Properties ». *Metallurgical and Materials Transactions A: Physical Metallurgy and Materials Science,* vol. 45, nº 8, p. 3545-3553.

Thébaud, L., P. Villechaise, J. Cormier, C. Crozet, A. Devaux, D. Béchet, J. M. Franchet, A. Organista et F. Hamon. 2015. « Relationships Between Microstructural Parameters and Time-Dependent Mechanical Properties of a New Nickel-Based Superalloy AD730™ ». *Metals,* vol. 5, nº 4, p. 2236-2251.

Thibault, K., D. Locq, P. Caron, D. Boivin, Y. Renollet et Y. Bréchet. 2013. « Influence of Microstructure on Local Intra- and Intergranular Deformations during Creep of a Nickel-Based Superalloy at 700°C ». *Materials Science and Engineering A,* vol. 588, p. 14-21.

Xu, S., A. K. Koul et J. I. Dickson. 2001. « Creep Crack Growth in the Absence of Grain Boundary Precipitates in UDIMET 520 ». *Metallurgical and Materials Transactions A: Physical Metallurgy and Materials Science,* vol. 32, n^{o} 13, p. 795-804.

CONCLUSIONS

In this research, microstructure evolution and the mechanical properties of LFWed AD730^{TM} Ni-based superalloy were studied. This study allowed characterizing this newly developed superalloy for manufacturing processes such as LFW where rapid heating and cooling cycles take place. Moreover, several fundamental aspects related to dissolution, reprecipitation and liquation of γ′ precipitates at the weld interface were identified and discussed. Welded samples at various friction and forge pressures were analyzed, and the effect of pressure in obtaining a defect free LFWed specimen was quantified and a methodology is proposed for rapid determination of optimum LFW process parameters.

From analyses and discussions, provided in each chapter, the main contributions of this thesis are:

1) Friction and forge pressure and time values were estimated to reach a defect free bonding condition. LFWed samples revealed oxides and microcracks below axial shortening of 1.7 mm. Therefore, samples with higher axial shortening of 3.5 mm were chosen for microstructure and mechanical testing. By increasing friction and forge pressure, and thus, axial shortening, the size of TMAZ decreased.

2) EBSD maps showed that LABs fraction significantly increased close to the weld interface while the twin fraction was substantially reduced. Grain boundary bulging and wavy boundaries were also observed in TMAZ indicating occurrence of dynamic recrystallization. HAB fraction drastically increased in the weld interface indicating a substantial increase of recrystallization. From EBSD maps interpretation, the outer edge of weld zone and TMAZ were determined.

3) The volume fraction of primary and secondary γ′ particles reduced with a decrease in the distance from the weld interface, and they were totally dissolved at the weld interface. However, re-precipitated γ′ precipitates (less than 10 nm in size) were formed during cooling at the weld interface.

4) The microhardness evaluation of LFWed samples showed there was a drop in hardness in TMAZ due to dissolution and 90 % reduction of secondary γ′ volume fraction. On the other

hand, with a decrease in distance from LFW interface, the microhardness gradually increased due to partially refined structure.

5) Tensile properties of LFWed specimens improved after PWHT for room temperature and 650˚C test conditions. As-welded samples failed in HAZ region during tensile test at 650˚C due to dissolution of γ′ particles in this region. Weld zone was stronger than TMAZ and HAZ due to finer grain microstructure. PWHT led to re-precipitation of γ′ precipitates at HAZ and TMAZ and restored tensile properties of LFWed joints.

6) A multi-particle semi-analytical dissolution model was proposed to quantify and predict γ′ dissolution kinetics. The comparison of the proposed model with the existing single particle model indicated that the proposed multi-particle model has a better prediction of γ′ dissolution kinetics. Then, an equation based on experimental correlations between the cooling rate and the γ′ precipitate size was proposed for continuous cooling from supersolvus temperatures. The proposed equation was validated experimentally for high cooling rates using Gleeble™ 3800. These dissolution and re-precipitation kinetics models were used to predict temperature or γ′ volume fraction in different zones of the LFWed samples.

7) Simulation of LFW thermal cycle using Gleeble™ 3800 physical simulator revealed constitutional liquation of primary γ′, Cr-Mo-W-Nb borides. Nb-Ti carbides were the predominant liquation source in AD730^{TM} between 1200-1300˚C. Peak temperature in the weld interface was estimated to be around 1250˚C using an analytical model. However, no liquation was observed in the weld zone or flash. The results showed a combination of high temperature, frictional and forge pressures during LFW could result in the elimination of liquation and formation of crack resistant microstructure in LFWed superalloy.

8) PWHT improved creep properties of LFWed specimens due to increasing weld interface grain size. Comparison of LMP values for these specimens with other Ni-based superalloys revealed good service life under high temperature and low stresses for LFWed AD730^{TM}.

9) Nucleation of voids around precipitates at the grain boundaries and decohesion of them contributed to creep crack growth at 700˚C while forming precipitate free zones at the grain boundaries and crack initiation from these regions assisted by oxidation were identified as the main damage mechanisms at 850˚C.

RECOMMENDATIONS

In this study, the LFW of the AD730^{TM} Ni-based superalloy was studied for the first time. Following recommendations are suggested for future investigations in continuing the present PhD thesis:

1) Tensile testing at room temperature and 650˚C on defect free and sound LFWed joint revealed ultimate tensile strength of the joint is more than that of the base material. In addition, the joint revealed better creep life at 850˚C while slightly lower creep life at 700˚C than that of the base material. The tensile and creep damage mechanisms were investigated in details. However, fatigue resistance is one of the other properties desired for disk materials. Therefore, it is suggested to investigate fatigue resistance and damage mechanisms during fatigue for LFWed joint.

2) The precipitation of γ' phase was discussed based on classical nucleation theory. It is recommended that the occurrence of γ' precipitation is also examined through non-classical nucleation or spinodal decomposition mechanism.

3) Joining of polycrystal (PC) to single crystal (SC) presents an important technological interest for the gas turbine industry as it will allow increasing the efficiency of gas turbines. To this end, not only LFW of PC to SC superalloys is of great interest from an industrial point of view but also presents many scientific challenges. For example, successful bonding is still challengeable as there should be the ability to activate major slip systems in both workpieces. It may require favorable orientation of the primary slip system of the SC to the principle axes of the pressure force. Furthermore, recrystallization may occur during joining in SC superalloy which will have some effects on mechanical properties.

4) In order to determine the range of liquation within a material, there are several quantifiable parameters. In this study, rang of liquation was found through physical simulating of the thermal cycle of LFW process using Gleeble physical simulator machine. Another method which is suggested by the author is determining characteristic temperatures: nil ductility temperature (NDT) and the nil strength temperature (NST) using Gleeble machine. As the alloy is heated from the NDT, the liquid film slowly increases in thickness, and thus,

the strength decreases due to reduction in capillary forces holding the grains together. These temperatures can be compared with the results obtained in the present study.

5) In this thesis, the effect of stress/strain on increasing diffusion was quantified and discussed in details. It is recommended that the possibility of strain rate enhanced solute diffusivity on preventing the resolidification products is analyzed.

LIST OF REFERENCES

Amegadzie, M. Y. 2012. « Effect of Forging Pressure on the Microstructure of Linear Friction Welded Inconel 738 Superalloy ». Canada, University of Manitoba.

Bhamji, I., M. Preuss, P. L. Threadgill et A. C. Addison. 2011. « Solid State Joining of Metals by Linear Friction Welding: A Literature Review ». *Materials Science and Technology,* vol. 27, nº 1, p. 2-12.

Chamanfar, A., M. Jahazi, J. Gholipour, P. Wanjara et S. Yue. 2011a. « Mechanical Property and Microstructure of Linear Friction Welded Waspaloy ». *Metallurgical and Materials Transactions A,* vol. 42, nº 3, p. 729-744.

Chamanfar, A., M. Jahazi, J. Gholipour, P. Wanjara et S. Yue. 2012a. « Maximizing the Integrity of Linear Friction Welded Waspaloy ». *Materials Science and Engineering: A,* vol. 555, p. 117-130.

Chamanfar, A., M. Jahazi, J. Gholipour, P. Wanjara et S. Yue. 2012b. « Suppressed Liquation and Microcracking in Linear Friction Welded Waspaloy ». *Materials and Design,* vol. 36, p. 113-122.

Cormier, J., et G. Cailletaud. 2010b. « Constitutive Modeling of the Creep Behavior of Single Crystal Superalloys under Non-Isothermal Conditions Inducing Phase Transformations ». *Materials Science and Engineering: A,* vol. 527, nº 23, p. 6300-6312.

Cormier, J., X. Milhet et J. Mendez. 2007b. « Non-Isothermal Creep at Very High Temperature of the Nickel-Based Single Crystal Superalloy MC2 ». *Acta Materialia,* vol. 55, nº 18, p. 6250-6259.

Dalgaard, E., P. Wanjara, J. Gholipour, X. Cao et J. J. Jonas. 2012. « Linear Friction Welding of a Near-β Titanium Alloy
». *Acta Materialia,* vol. 60, nº 2, p. 770-780.

Damodaram, R., S. G. S. Raman et K. P. Rao. 2013. « Microstructure and Mechanical Properties of Friction Welded Alloy 718 ». *Materials Science and Engineering A,* vol. 560, p. 781-786.

Devaux, A., B. Picque, M. F. Gervais, E. Georges, T. Poulain et P. Heritier. 2012b. « AD730™ -A New Nickel-Based Superalloy for High Temperature Engine Rotative Parts ». In *12th International Symposium on Superalloys, Superalloys 2012, September 9, 2012 - September 13, 2012*. (Seven Springs, PA, United states), p. 911-

919. Coll. « Proceedings of the International Symposium on Superalloys »: Minerals, Metals and Materials Society.

Durand-Charre, M. 1997. *The Microstructure of Superalloys*. CRC Press Boca Raton.

Henderson, M. B., D. Arrell, R. Larsson, M. Heobel et G. Marchant. 2004. « Nickel Based Superalloy Welding Practices for Industrial Gas Turbine Applications ». *Science and Technology of Welding and Joining,* vol. 9, nº 1, p. 13-21.

Huang, Z. W., H. Y. Li, M. Preuss, M. Karadge, P. Bowen, S. Bray et G. Baxter. 2007a. « Inertia Friction Welding Dissimilar Nickel-Based Superalloys Alloy 720Li to IN718 ». *Metallurgical and Materials Transactions A,* vol. 38, nº 7, p. 1608-1620.

Karadge, M., M. Preuss, P. J. Withers et S. Bray. 2008. « Importance of Crystal Orientation in Linear Friction Joining of Single Crystal to Polycrystalline Nickel-Based Superalloys ». *Materials Science and Engineering A,* vol. 491, nº 1-2, p. 446-453.

Korsunsky, A. M., G. M. Regino, D. Nowell, M. Karadge, B. Grant, P. J. Withers, M. Preuss et G. Baxter. 2009. « Inertia Friction Welds between Nickel Superalloy Components: Analysis of Residual Stress by Eigenstrain Distributions ». *Journal of Strain Analysis for Engineering Design,* vol. 44, nº 2, p. 159-70.

le Graverend, J. B., J. Cormier, M. Jouiad, F. Gallerneau, P. Paulmier et F. Hamon. 2010b. « Effect of Fine γ′ Precipitation on Non-Isothermal Ceep and Creep-Fatigue Behaviour of Nickel Base Superalloy MC2 ». *Materials Science and Engineering: A,* vol. 527, nº 20, p. 5295-5302.

Mary, C., et M. Jahazi. 2007a. « Linear Friction Welding of IN-718 Process Optimization and Microstructure Evolution ». In *5th International Conference on Processing and Manufacturing of Advanced Materials - THERMEC 2006, July 4, 2006 - July 8, 2006.* (Vancouver, BC, Canada) Vol. 15-17, p. 357-362. Coll. « Advanced Materials Research »: Trans Tech Publications.

McAndrew, A. R., P. A. Colegrove, C. Buhr, B. C. D. Flipo et A. Vairis. 2018. « A Literature Review of Ti-6Al-4V Linear Friction Welding ». *Progress in Materials Science,* vol. 92, p. 225-257.

Murakumo, T., T. Kobayashi, Y. Koizumi et H. Harada. 2004. « Creep Behaviour of Ni-Base Single-Crystal Superalloys with Various γ′ Volume Fraction ». *Acta Materialia,* vol. 52, nº 12, p. 3737-3744.

Nicholas, E. D., et W. M. Thomas. 1998. « Review of Friction Processes for Aerospace Applications ». *International Journal of Materials and Product Technology,* vol. 13, nº 1 /2, p. 45-55.

Ola, O. T., O. Ojo, P. Wanjara et M. Chaturvedi. 2011a. « Crack-Free Welding of IN 738 by Linear Friction Welding ». In *Euro Superalloys 2010*. Vol. 278, p. 446-453. Coll. « Advanced Materials Research »: Trans Tech Publications. < http://dx.doi.org/10.4028/www.scientific.net/AMR.278.446 >.

Ola, O. T., O. A. Ojo, P. Wanjara et M. C. Chaturvedi. 2011b. « Analysis of Microstructural Changes Induced by Linear Friction Welding in a Nickel-Base Superalloy ». *Metallurgical and Materials Transactions A (Physical Metallurgy and Materials Science),* vol. 42, nº 12, p. 3761-77.

Ola, O. T., O. A. Ojo, P. Wanjara et M. C. Chaturvedi. 2012. « A Study of Linear Friction Weld Microstructure in Single Crystal CMSX-486 Superalloy ». *Metallurgical and Materials Transactions A,* vol. 43, nº 3, p. 921-33.

Preuss, M., J. W. L. Pang, P. J. Withers et G. J. Baxter. 2002a. « Inertia Welding Nickel-Based Superalloy. I. Metallurgical Characterization ». *Metallurgical and Materials Transactions A (Physical Metallurgy and Materials Science),* vol. 33A, nº 10, p. 3215-25.

Preuss, M., P. J. Withers et G. J. Baxter. 2006a. « A Comparison of Inertia Friction Welds in Three Nickel Base Superalloys ». *Materials Science & Engineering A (Structural Materials: Properties, Microstructure and Processing),* vol. 437, nº 1, p. 38-45.

Reed, R. C. 2006b. *The Superalloys Fundamentals and Applications*, 9780521859042. Cambridge University Press, 1-372 p.

Rowe, M. D., V. R. Ishwar et D. L. Klarstrom. 2006. « Properties, Weldability, and Applications of Modern Wrought Heat-Resistant Alloys for Aerospace and Power Generation Industries ». *Transactions of the ASME. Journal of Engineering for Gas Turbines and Power,* vol. 128, nº 2, p. 354-61.

Shahriari, D., M. H. Sadeghi, A. Akbarzadeh et M. Cheraghzadeh. 2009a. « The Influence of Heat Treatment and Hot Deformation Conditions on γ′ Precipitate Dissolution of Nimonic 115 Superalloy ». *The International Journal of Advanced Manufacturing Technology,* vol. 45, nº 9, p. 841.

Sims, C. T., N. S. Stoloff et W. C. Hagel (640). 1987. *Superalloys II: High-Temperature Materials for Aerospace and Industrial Power*. Wiley-Interscience.

Thomas, J. P., F. Montheillet et C. Dumont. 2003. « Microstructural Evolutions of Superalloy 718 during Dynamic and Metadynamic Recrystallizations ». *Materials Science Forum,* vol. 426-432, nº 1, p. 791-6.

Threadgill, P. L. 2007. « Terminology in Friction Stir Welding ». *Science and Technology of Welding and Joining,* vol. 12, nº 4, p. 357-60.

Vairis, A., et M. Frost. 1998. « High Frequency Linear Friction Welding of a Titanium Alloy ». *Wear,* vol. 217, nº 1, p. 117-131.

Vairis, A., et M. Frost. 1999b. « On the Extrusion Stage of Linear Friction Welding of Ti 6Al 4V ». *Materials Science and Engineering: A,* vol. 271, nº 1, p. 477-484.

Vairis, A., et M. Frost. 2000a. « Modelling the Linear Friction Welding of Titanium Blocks ». *Materials Science & Engineering A (Structural Materials: Properties, Microstructure and Processing),* vol. A292, nº 1, p. 8-17.